Università degli Studi di Padova

Dipartimento di Ingegneria Civile, Edile e Ambientale - ICEA
CORSO DI DOTTORATO DI RICERCA IN
SCIENZE DELL'INGEGNERIA CIVILE E AMBIENTALE
Ciclo XXXI

DEVELOPMENT OF A MODEL FOR THE ASSESSMENT OF COASTAL FLOODING VULNERABILITY: AN APPLICATION TO THE VENETIAN LITTORAL

Coordinatore: Ch.mo Prof. Marco Marani

Supervisore: Ch.mo Prof. Piero Ruol

Co-Supervisore: Prof. Luca Martinelli

Dottoranda: Chiara Favaretto

Sommario

L'allagamento costiero è una tematica di grande attualità che ha suscitato negli ultimi anni una forte attenzione sia da parte della comunità scientifica che da parte degli amministratori e gestori del territorio. L'innalzamento del livello medio del mare dovuto ai cambiamenti climatici e la maggior frequenza di mareggiate estreme fanno prevedere una più alta probabilità di accadimento di eventi di ingressione marina lungo i litorali.
Tale fenomeno ha evidentemente conseguenze sia di carattere economico che sociale anche in conseguenza del fatto che le zone costiere risultano avere infatti una densità di popolazione molto maggiore dell'entroterra. In Italia, ad esempio, il 30% della popolazione vive nei 646 comuni costieri che coprono solamente il 13% del territorio nazionale. La costa ha inoltre una forte attrattiva sia dal punto di vista turistico/balneare, con numerose attività ricettive e ricreative, che dal punto di vista produttivo e ambientale/naturalistico. Lungo la costa italiana sono situati oltre 500 porti di tipo commerciale, peschereccio, e turistico e in essa sono dunque concentrate moltissime attività economiche.
La crescente urbanizzazione e la sempre più alta percentuale di persone che vivono nei litorali aumentano il valore esposto all'allagamento costiero, che va dunque studiato e approfondito per mitigare il rischio di perdite economiche, di danni al patrimonio artistico/culturale e all'ambiente e per scongiurare pericoli per l'incolumità delle persone presenti in questi territori.
La motivazione di questa ricerca è scaturita dalla necessità, espressa dagli enti gestori e pianificatori della costa Veneta, di redigere mappe di rischio di allagamento che includessero tra le cause dell'alluvionamento non solamente l'esondazione di tipo fluviale, ma anche quella di origine costiera e di avere pertanto uno strumento rapido e scientificamente basato che consenta di rispondere in maniera unitaria e omogenea per tutto il litorale alla Direttiva Alluvioni (2007/60/CE). A tale scopo è stata predisposta una metodologia per definire mappe di rischio di allagamento attraverso un'analisi di diversi scenari a diverse scale temporali e spaziali.
Il primo passo è stato implementare, dopo un articolato studio teorico (Capitolo 2) e una accurata ricerca bibliografica (Capitolo 3), un modello numerico che risolve le equazioni del moto (ovvero le equazioni alle acque basse) in forma semplificata per simulare la propagazione dell'allagamento nell'entroterra (Capitolo 4). Le semplificazioni apportate alle equazioni (in particolare all'equazione della conservazione della quantità di moto) sono essenzialmente due: i) i termini avvettivi sono stati trascurati poiché risultano poco importanti nel tipo di fenomeno analizzato, ii) il termine di attrito, fondamentale per descrivere la propagazione, è stato linearizzato. Per garantire la positività della soluzione e la sua stabilità, evitando quindi la formazione di oscillazioni, sono state implementate alcune tecniche numeriche descritte nel Capitolo 4.
Le equazioni semplificate sono adatte ad un calcolo in parallelo e pertanto il modello proposto

ha come peculiarità l'utilizzo di algoritmi idonei all'uso di GPU, in grado quindi di analizzare grandi mappe in tempi di calcolo ridotti e di lavorare direttamente alla scala del pixel (utilizzando "Digital Elevation Model" DEM ad alta risoluzione) senza la necessità di creare mesh. Le unità di elaborazione grafica (GPUs, graphics processing units) sono una tipologia particolare di coprocessori, che si contraddistinguono per essere specializzate nel rendering di immagini grafiche, molto utilizzate nel gaming. Negli ultimi anni, tuttavia, tale tecnologia è stata impiegata in diversi campi di ricerca, quali ad esempio elaborazioni di immagini e dati, ambiti medici e calcoli scientifici. Traendo vantaggio dalla possibile parallelizzazione del codice che risolve le equazioni semplificate del moto, nel presente studio è stata utilizzata la GPU Nvidia Tesla K80 con 4992 core e 12 GByte di memoria, ottenendo tempi di calcolo, per domini molto estesi, pari al 3% di quelli necessari utilizzando una classica CPU.
Il modello numerico di allagamento è stato esaminato (Capitolo 5) attraverso il confronto con quattro benchmark molto noti in letteratura (due soluzioni analitiche delle equazioni alla acque basse e due prove sperimentali). Inoltre è stato applicato ad un caso reale di allagamento costiero avvenuto a Caorle (VE) nel Dicembre 2008, confrontando i risultati ottenuti con una mappa di aree allagate ricostruita grazie ad un video ripreso durante l'evento estremo. Il modello è risultato in buon accordo con le soluzioni analitiche, le misure di laboratorio e le informazioni disponibili.
Utilizzando un modello di trasformazione dell'onda dal largo a riva (il modello proposto da Dally et al. 1985), che tiene conto dei fenomeni di rifrazione, shoaling e della dissipazione di energia causata dal frangimento, è possibile valutare la condizione al contorno per il modello di allagamento. Tale condizione è composta dal valore del livello del mare, dal valore di set-up e dall'altezza dell'onda alla linea di riva in condizioni di medio mare.
La metodologia è stata infine applicata alla costa della Regione Veneto (Capitolo 6), traendo vantaggio dall'ampia conoscenza geomorfologica e idraulica del territorio maturata nello svolgimento di una approfondita ricerca eseguita ed elaborata sui più recenti dati e misure disponibili per la zona costiera (Ruol et al.,2016 & 2018). A partire dai dati di altezza d'onda e livello misurati alla Torre CNR "Acqua Alta" è stata condotta un'analisi statistica bivariata che ha permesso di valutare la probabilità di superamento associata a coppie di altezza d'onda e livello.
L'obiettivo finale, ossia la redazione di mappe di allagamento, si avvale di una analisi di affidabilità di livello II (FORM, descritta nel paragrafo 2.4). I risultati sono pertanto i valori di probabilità di superamento di un determinato livello idrico per ciascun pixel del DEM disponibile. Questo si traduce in un risultato di estremo interesse scientifico e pratico, ovvero la predisposizione di mappe di pericolosità all'allagamento costiero nell'arco temporale di 1 e 10 anni. Sono stati analizzati tre tratti che appartengono alla costa Veneta (in provincia di Venezia) e che hanno lunghezza compresa tra i 4 e i 15 km: il litorale di Valle Vecchia (Figg. 6.29 – 6.34), il litorale di Caorle (Figg. 6.39 – 6.44) e il litorale di Cavallino (Figg. 6.48 – 6.53).
Le realizzazione di queste mappe e la conseguente individuazione delle zone più critiche vuole fornire un valido supporto per la programmazione e progettazione degli interventi che riguardano la protezione costiera dal rischio di ingressione marina lungo il litorale.

Abstract

In the recent years, marine flooding and its impacts have become a question of growing interest in the scientific community as well as in managing authorities, since coastal areas are the most heavily populated and developed land zones in the world. Under climate change, sea levels are rising and even storm surge intensity is possibly increasing. Therefore, it is expected that the occurrence probability of extreme coastal flooding events will increase. This major hazard requires urgent adaptations in order to increase the resistance and resilience of an area to coastal floods.

The motivation of this research arises from the practical need highlighted by local managers of the Veneto region that require (possibly GIS-integrated) rapid tools to simulate the whole complexity of the problem of mapping the risk of coastal flood by wave over-topping in an urban area at large scale. The aim of this thesis is to develop a methodology in order to define flood risk maps by analysing different scenarios at a different time and spatial scales, combining both marine forcing and flood propagation in the hinterland.

After an articulated theoretical study (Chapter 2) and an accurate bibliographic research (Chapter 3), a flood propagation numerical model was implemented. In Chapter 4 the key features of the proposed model are presented. In order to use GPU acceleration, i) the domain Shallow Water Equations are simplified by linearising bottom friction and neglecting advection, and ii) an appropriate vectorization method is considered.
The numerical model for coastal flooding propagation was tested (Chapter 5) against four well-known benchmarks (two analytical solutions of the SWEs and two experimental tests) and applied to a real case of coastal flooding occurred at Caorle (VE) in December 2008.

The methodology was finally applied to the coast of the Veneto Region (Chapter 6), thanks to an extensive geomorphological and hydraulic knowledge of the area (Ruol et al.,2016 & 2018). Combining i) a bivariate statistical analysis of marine forcing (waves and sea levels), ii) a model of wave transformation from offshore to onshore and iii) a reliability analysis, Coastal Flooding hazard maps were produced for three stretches of the Veneto littoral: Valle Vecchia (Figs. 6.29 – 6.34), Caorle (Figs. 6.39 – 6.44) and Cavallino-Treporti (Figs. 6.48 – 6.53).

Contents

List of Figures

List of Tables

List of Symbols and Acronyms

a	$[m]$	wave amplitude
α	$[rad]$	wave direction (or weighting factor in Chapter 4)
β	$[-]$	beach slope
c	$[m/s]$	wave celerity
c_g	$[m/s]$	wave group celerity
d	$[m]$	water depth ($= d_0 + \zeta_A + \zeta_S + \zeta_R = d_0 + \zeta$)
γ_b	$[-]$	wave breaking parameter
d_0	$[m]$	mean sea level (MSL)
d_{50}	$[mm]$	median sediment diameter
Dir	$[^oN]$	wave direction
$\Delta x, \Delta y$	$[m]$	grid size
Δt	$[s]$	time step
ζ_A	$[m]$	astronomical tide
ζ_S	$[m]$	storm surge
ζ_R	$[m]$	residual component of d due to seiches or other contributions
E	$[J/m^2]$	wave energy ($=E_P+E_K$=potential + kinetic energy)
$\eta(x)$	$[m]$	surface elevation with respect to the water level
θ	$[-]$	model parameter
f	$[Hz]$	wave frequency
$f(x)$ or $p(x)$	$[-]$	probability density function
F	$[W/m]$	wave energy flux
$F(x)$	$[-]$	cumulative distribution function
g	$[m/s^2]$	gravitational acceleration ($= 9.81\ m/s^2$)
$g(x)$	$[-]$	performance function
h	$[m]$	water level ($d + Z$)
H	$[m]$	wave height
H_0	$[m]$	wave height at deep water
H_{rms}	$[m]$	root-mean-square wave height
h_F	$[m]$	flooding value
H_S	$[m]$	significant wave height
$\mathbf{I}$	$[-]$	marker image
$\mathbf{J}$	$[-]$	mask image
j	$[-]$	friction term
k	$[m^{-1}]$	wave number
K_D	$[-]$	diffraction coefficient
K_H	$[-]$	linearised turbulent friction coefficient
K_R	$[-]$	refraction coefficient
K_S	$[m^{1/3}/s]$	Gauckler Strickler coefficient

L	$[m]$	wave length
$L(\theta)$	$[-]$	Likelihood function
$l(\theta)$	$[-]$	log-transformation of the Likelihood function
N	$[-]$	total number of variables (or shape function in 2.2.4)
ξ	$[-]$	surf similarity parameter
ϕ	$[m]$	velocity potential
p	$[N/m^2]$	pressure
p_f	$[-]$	probability of failure
Q	$[m^3/s]$	discharge
q	$[m^2/s]$	discharge per unit width
R	$[-]$	reliability index
ρ	$[kg/m^3]$	water density
S	$[N/m]$	radiation stress tensor
$S(f, \alpha)$	$[m^2 s/rad]$	directional wave spectrum
t	$[s]$	time in the physical domain
T	$[s]$	wave period
T_P	$[s]$	peak wave period
t_P	$[hour]$	storm peak duration
T_R	$[year]$	return period
t_S	$[hour]$	storm duration
u, v, w	$[m/s]$	velocity components in the x, y and z directions
U	$[-]$	independent standard normal random variable
w	$[m]$	flooding water depth
w_F	$[m]$	maximum available water depth
x, y, z	$[m]$	Cartesian coordinate system (z is the vertical axis)
X	$[-]$	random variables = $(X_1, \ldots, X_N)$
y_O	$[-]$	observation
y_P	$[-]$	prediction
z	$[m]$	discharge per unit width
Z or Z_{up}	$[m]$	wave set-up
Z_{down}	$[m]$	wave set-down
ω	$[rad/s]$	angular frequency

CPU	Central processing unit
DEM	Digital Elevation Model
DTM	Digital Terrain Model
GIS	Geographic Information System
GPU	Graphic processing unit
$SWEs$	Shallow Water Equations
V_M	Morphological Vulnerability
V_{SE}	Socio-Economic Vulnerability
CFL	Courant-Friedrichs-Levy condition
D	Wilmott Coefficient
$FORM$	First Order Reliability Method
NSE	Nash Sutcliffe coefficient
PoT	Peak over Threshold
$RMSE$	Root Mean Square Error
$ZMPS$	"Zero Mareografico Punta della Salute" local datum

Chapter 1

Introduction

1.1 Generalities

Coastal areas are subject to the threat of erosion and flood risk. These zones are more densely populated than the hinterland (Small and Nicholls 2003): in Italy, 30% of the entire population lives in the 646 coastal municipalities, which covers 13% of the national territory (from ISTAT data). The rates of population growth, the development and the urbanization of coastal zones have greatly increased during the recent decades and this trend is expected to continue in the future (Neumann et al. 2015). Merkens et al. (2016) show that, compared to the year 2000 (638 million), the population living in the low elevated coastal zone (which includes all land areas up to 10 m elevation connected to the sea) increases by 58% to 71% until 2050 and exceeds one billion in all the shared socio-economic pathways. Consequently, the vulnerability connected to coastal hazards need to be investigated in order to mitigate the risk to human health, economic activities, cultural heritage and environment.

Coastal flooding occurs in low-lying coastal areas when high water levels due to tides and storm surges, together with waves (e.g. wind waves, tsunamis), over-top or breach coastal defences and inundate the hinterland. Very frequently, coastal flooding is associated also to extreme meteorological conditions (such as hurricanes, typhoons, cyclones), flooding caused by river overflows, morphological changes, problems/collapse of the drainage system, etc. Therefore, significant coastal floods take place when these multiple factors coincide, depending also on the local topographic characteristics (Fig. 1.1). In fact, flooding can be enhanced by the potential occurrence of natural subsidence (falling land levels) that is often exacerbated by additional human-induced subsidence due to drainage and/or excessive groundwater withdrawal, especially in urban centres.
The total sea water level is due to several rather independent factors and it is not uniform in space and time, depending on both global and regional processes. In the Northern Adriatic Sea (Italy), the most significant are: 1) the Astronomical tide (ζ_A), the water levels rise and fall along the coast every day due to the gravitational pull of the moon and sun; 2) the Meteorological contribution (storm surge, ζ_S) caused by wind and pressure effects; 3) the Mean sea level rise, i.e. the increase of the global mean sea level that is usually attributed to global climate change and 4) the Wave contribution, i.e. breaking waves contribute to the water level rise through wave run-up and wave set-up (Z). While astronomic tide is a deterministic component of sea surface elevations, storm surges and waves are stochastic in nature gener-

ated by storm events.
Under climate change, sea-levels are rising (Cazenave and Cozannet 2014) and storm surge intensity increasing (Pomaro et al. 2017; Rahmstorf 2017). Therefore, it is expected that the probability of flooding and inundation for low-lying coastal areas will increase and, since the coastal population will grow, the connected risk will be more serious (Nicholls and Cazenave 2010). This major hazard requires urgent adaptations in order to increase the resilience of an area to coastal floods.

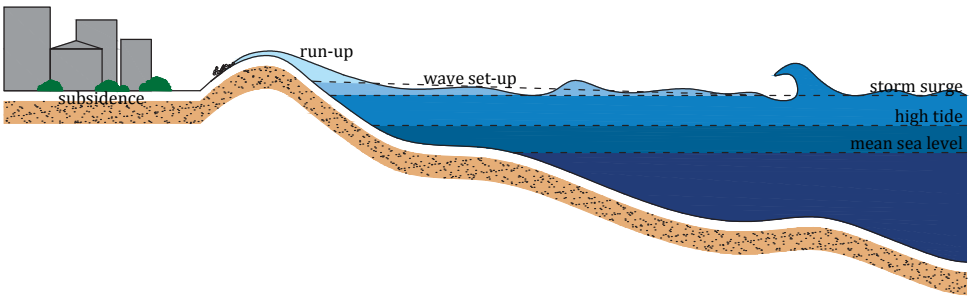

Figure 1.1: *Marine and topographic factors that induce Coastal flooding*

Flood management has evolved over the last 50 years with key areas of advance including developments of flood hazard maps, hydrological/hydraulic models, flood warning systems, evacuation procedures, and flood insurance programs. The reliability of these actions is in part based on accurate and rapid flood modelling. In fact, complete flood inundation analysis requires: i) the estimation of flood flows (e.g. Formentin and Zanuttigh 2018), ii) hydraulic modelling to route the flow, compute water surface elevations and flow velocities, and iii) analysis tools to delineate the flood inundation extent and assess impacts (Kalyanapu et al. 2011).

Two types of tools are commonly employed for the establishments of hazard maps: i) Geographic Information Systems (GIS) or, more in general, static models and ii) hydrodynamic models. The first ones determine the areas vulnerable to flooding through a basic and rapid calculation procedure that identifies land that is lower than the inundation level. The latter enforce the laws of physics to describe the flow of water in the coastal environment by solving the governing equations of fluid flow (i.e. the shallow water equations). Considering the differences in approaches, it is likely that the precision of flood prediction from hydrodynamic models will be higher than those produced by a GIS, which is primarily based on topography and does not account for hydraulic connectivity. However, hydrodynamic models involve a high computational cost in terms of time and memory.

These tools, together with a reliability analysis, help to evaluate the occurrence probability of flood events, namely the morphological vulnerability V_M connect to coastal flooding. Ruol et al. (2018)) defined Risk (or priority) as the product between V_M and the Socio-Economic vulnerability V_{SE}, i.e. an index that specifies the value of the coastal area: frequency and financial investments, presence of natural areas, number of tourist/year, presence of cities, type of inland, presence of production activities, cultural heritage, etc. Therefore, in order to establish coastal flooding risk maps also this information is needed.

1.2 Motivations

Many available studies (e.g. Hinkel et al. 2014; Weisse et al. 2014) including the most recent Stocker et al. (2013) show that European coasts are threatened by the aforementioned risk. The total value of economic assets located within 500 metres of the European coastline, including beaches, agricultural land and industrial facilities, is estimated at € 500 to 1,000 billion (`www.eurosion.org`). Therefore, within the EU water flood directive (2007/60/EC), stakeholders need to establish flood maps to determine the risk to present and future levels of inundation, in order to adopt the most effective flood management:

> ***Directive 2007/60/EC, Article no. 2:***
> *"Flood" means the temporary covering by water of land not normally covered by water. This shall include floods from rivers, mountain torrents, Mediterranean ephemeral water courses, and* ***floods from the sea in coastal areas****, and may exclude floods from sewerage systems.*
>
> *"Flood risk" means the combination of the probability of a flood event and of the potential adverse consequences for human health, the environment, cultural heritage and economic activity associated with a flood event.*
>
> ***Directive 2007/60/EC, Article no. 6:***
> *Member States shall, at the level of the river basin district, or unit of management referred to in Article 3(2)(b), prepare flood hazard maps and flood risk maps, at the most appropriate scale for the areas identified under Article 5(1).*

In the absence of a complete framework for the assessment of coastal flooding hazard, the maps are frequently based on simple indexes that typically combine topographic information (usually available to the coastal managers within GIS database) to sea level and wave run-up. For example, in Italy Aucelli et al. (2017) recently studied the inundation hazard and risk in Volturno coastal plain in Campania (Italy). Di Luccio et al. (2018) focused on the effect of different run-up lumped formulas on the index for coastal vulnerability assessment of a microtidal beach located along the southern Ionian coast of Calabria (Italy). Di Risio et al. (2017) assessed coastal hazard to wave-induced flooding at the national scale. In other cases, the mapping of areas potentially exposed to inundation is carried out by a chain of models (e.g. Gallien 2016; Lerma et al. 2018), solving the wave transformation problem in the sea area and the flow propagation in the inland area.

The issue is particularly relevant also for the Venetian littoral, where local managers require (possibly GIS-integrated) rapid tools to simulate the whole complexity of the problem of a coastal flood by wave over-topping in an urban area at regional scale. The Northern Adriatic coast is subject to rapidly evolving pressures from a range of drivers, including natural and anthropogenic ones: e.g., rapid morphological evolution of Po River Delta (Simeoni and Corbau 2009), human-induced subsidence caused by fluid withdrawal (Carbognin et al. 2004), changing wave climate (Pomaro et al. 2017).
In order to investigate the Venetian littoral and to propose mitigation measures against coastal erosion and flooding, the coastal plan of the Veneto region was established in 2016 (Ruol

et al. 2016), thanks to a balanced combination of scientifically rigorous approach and expert, discussion-based, assumptions (more details in Ruol et al. 2018).
The thesis here presented originates from the practical need to fill a lack in the coastal flooding assessment in the Veneto region, until now studied with simplified approaches, for example considering as flooded areas the ones comprise between the sea and existing dunes/bank/dikes.

1.3 Objectives and scope of the study

The objective of this thesis is to develop a flood propagation model and to establish a methodology, that has the ambition to help the coastal managers and stakeholders in producing flooding hazard maps required under the EU water floods directive. The expected result is a scientifically based approach that helps decision makers to scope optimal strategies to mitigate the associated risks.
The thesis presents a dynamic reduced-complexity model of coastal flooding, that includes sufficient shallow-water physics, using the forcing data available (sea-level characteristics) to simulate flows over high-quality terrain (Digital Elevation Model).
Beyond the implementation of this model, both a model for the evaluation of the boundary conditions to be imposed at the shoreline and a II-level reliability method are implemented in order to carry out coastal flooding hazard maps. The results are the exceedance probability values of a given inundation level (e.g. 0.5 m) for each pixel of the domain (i.e. DEM). The considered failure mechanism is the flooding caused by over-topping.
The scheme of the steps done to achieve the objectives of this thesis is presented in Fig. 1.2.

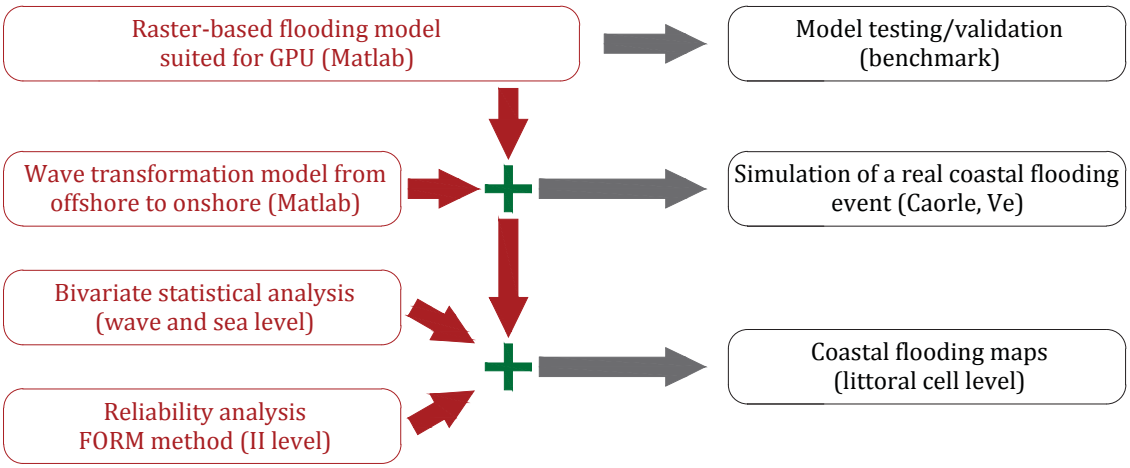

Figure 1.2: *PhD thesis steps*

This study is differentiated from most flood risk research by focusing upon analysis of inundation over a large area where coastal floodplains are relatively small, and water flowing over defences (overflow and wave overtopping) may be more significant compared to breaching. This single failure mechanism taken into account is suited to represent coastal flooding in areas with "rigid boundaries", for example an area with concrete sea walls or with paved coastal roads that typically are not subject to local damage or collapse. However, it should be stressed that the maps proposed by this work require an integration before they may be used for coastal management purposes, for instance other boundaries conditions (e.g river contri-

bution, hydrological conditions), other failure mechanisms (e.g. breaching) and information on the exposed value.

1.4 Novelty of the study

High resolution datasets and numerical tools are currently available for many coastal areas, although are not routinely integrated; particularly where risks are not obvious or recently experienced. The peculiarity of this work concerns the ability of the model to handle large maps on a regional scale in limited time, since specific algorithms and simplifications on the governing equations are considered to obtain a formulation ideal for GPU acceleration. This formulation takes advantage of a grid-based vectorization and a positivity preserving scheme. In the proposed model, the boundaries conditions could be easily updated with the results coming from other models, such as river or hydrological modelling, allowing to study the flooding for a more general perspective. Since flood processes are complex multivariate events characterized by correlated random variables (waves, sea level, river level, duration, etc.), multivariate probabilistic approach, such as the FORM methods used in this work, offers an improved understanding of the entire problem.

1.5 General overview

To achieve the general objective, the following tasks and milestones are identified and described in the following chapters of the thesis:

Chapter 2: Theoretical background of all the methods and analysis used in this work: wave modelling in the coastal area, extreme value statistics, reliability methods and image analysis

Chapter 3: Review of the state-of-the-art of hydrodynamic and simple conceptual models able to simulate the coastal flooding over a topography

Chapter 4: Description and development of a new model able to propagate the flooding over large-scale raster maps together with its implementation suited for the use of a GPU

Chapter 5: Inundation model testing and validation through some analytical solutions for the shallow water equation and some experiments that represent benchmarks in hydraulic modelling and through the simulation of a real flooding event occurs in Caorle (Venice – IT)

Chapter 6: Description of the coast of the Veneto region and analysis of the marine drivers acting on this coast and Application of the whole methodology to some stretches of the Venetian littoral

Chapter 7: Conclusions and possible future development of this research.

Chapter 2

Theoretical Background

2.1 Introduction

The coast is the region that separates the sea (71% of the earth surface) from the land (29% of the earth surface). The complexity of coastal systems needs to be studied through a homogeneous and multidisciplinary approach with reference to large spatial and temporal scales in order to examine a wide range of phenomena and topics. Coastal zones are analysed from several points of view (e.g. geophysical, biological, socio-economic, cultural, historical) and with different approaches (e.g. research, planning, operational purposes). Successful management requires a thorough understanding of the physical processes impacting on the coast and a planning of the effective ways to best secure the desired uses of the coastal land. The coast may be classified into three types: rocky coast, cohesive coast and sandy coast (the latter is the type of coast that characterizes the Venetian littoral). The beach can be defined as the zone, in the coastal region, extending shoreward from the location of the maximum water depth relative to significant sea bottom change to the landward limit of sea ingression under storm action, or the dunes (if present). The features that appear on a beach profile are shown in Fig. 2.1 and are defined as follows:

- **Shoreline**: the line of land, sea and air interface;
- **Bar**: a submerged bar usually lying parallel to the shoreline;
- **Trough**: a depression located immediately landward of a bar;
- **Beach face**: the seaward sloping section of the beach that is exposed to swash action;
- **Berm**: a sub-aerial bar having its crest backed by a nearly horizontal slope.

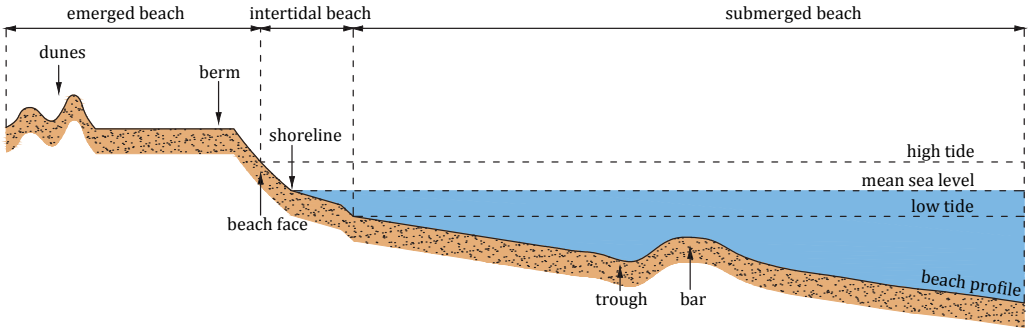

Figure 2.1: *Typical beach profile*

This chapter presents the main characteristics of wave modelling in the coastal area, together with a brief description of extreme value statistics, useful to analyse wave or, more generally marine dataset. The theoretical background of a reliability analysis is also described, that will be applied to establish coastal flooding hazard maps. In the last paragraph, the Image analysis is described, useful to manipulate big raster data (e.g. digital terrain model).

2.2 Wave modelling in coastal areas

The physical system within the coastal region is composed primarily of the motion of the sea, which supplies energy to the system, and the shore, which absorbs this energy. Since the shoreline is the intersection of the air, land, and water, the physical interactions which occur in this region are unique, very complex, and difficult to fully understand.
The motions of the sea which contribute to the beach and near-shore physical system include waves, tides, currents, storm surges, and tsunamis. Wind waves are by far the largest contribution of energy from the sea to the beach and to the near-shore physical system. As winds blow over the water, waves are generated in a variety of sizes from ripples to large ocean waves, that can reach heights of 30 meters. Wind waves, which are also known as oscillatory waves, are usually defined by their height (H distance from the top of the crest to the bottom of the trough), length (L horizontal distance between successive crests), and period (T time between successive crests passing a given point).

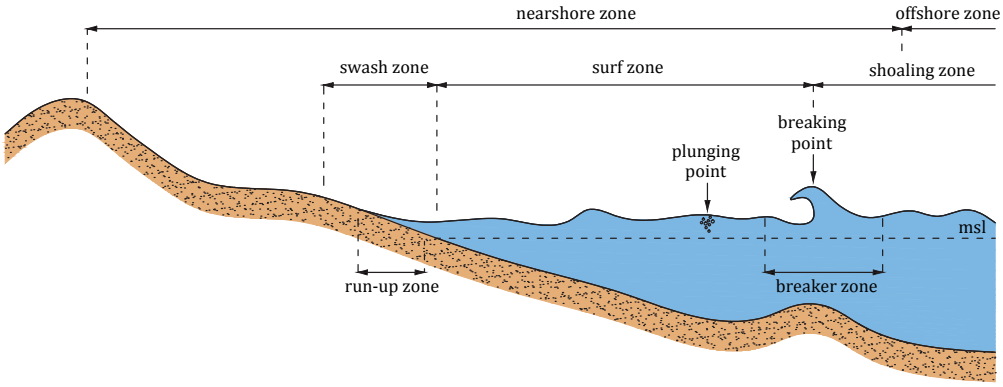

Figure 2.2: *Definition of near-shore zone*

The waves propagate across the ocean and, approaching to the coast, they transform into swells which are typically two-dimensional in shape, with nearly uniform period and long crest lines. The shallow water transformation begins when the influence of the sea bottom to the wave motion starts to be relevant. This zone is called shoaling zone (Fig. 2.2) and here the main wave transformations are refraction and shoaling. Since the wave height is proportional to the square root of the wave energy, it must increase as the wave advances into the shallower depths (conserving its energy). A shoaling wave finally breaks at the location where the wave height is approximately equal to the water depth. This point (zone) is called breaking point and marks the beginning of the surf zone (Fig. 2.2). After the breaking, the waves enter an area of dynamic, complex fluid motions and great energy dissipation. A great amount of sediment movement occurs in this zone, resulting in significant bathymetric changes. Beyond the shoreline, there is the run-up zone, which is alternately wet and dry. The swash zone is

defined to include the run-up zone and its adjacent area where the run-up is generated and the run-down is terminated. Fig. 2.2 shows the different zones associated with waves on the beach. This paragraph describes the basic properties of waves and, more in general, of the fluid in the coastal area.

2.2.1 Linear wave theory

Water wave motion is usually described by the potential theory requiring the fluid to be inviscid, incompressible and irrotational. The velocity field could be related to a potential ϕ:

$$u = \frac{\partial \phi}{\partial x} \qquad v = \frac{\partial \phi}{\partial y} \qquad w = \frac{\partial \phi}{\partial z} \tag{2.1}$$

where x and y are the horizontal coordinates, and z is the vertical coordinate. Origins of the coordinate system is located on the seabed. u, v and w are the velocity components in the x, y and z directions. At a fixed point the governing equations are the continuity equation (Eq. 2.2) and the Euler equation of motion.

$$\frac{\partial u}{\partial x} + \frac{\partial v}{\partial y} + \frac{\partial w}{\partial z} = 0 \tag{2.2}$$

Substituting Eq. 2.1 into the continuity equation and into the Euler equation, the Laplace equation (Eq. 2.3) and the Bernoulli equation (Eq. 2.4) are obtained .

$$\frac{\partial^2 \phi}{\partial x^2} + \frac{\partial^2 \phi}{\partial y^2} + \frac{\partial^2 \phi}{\partial z^2} = 0 \tag{2.3}$$

$$gz + \frac{p}{\rho} + \frac{1}{2}(u^2 + v^2 + w^2) + \frac{\partial \phi}{\partial t} = 0 \tag{2.4}$$

To obtain a solution for surface water motion, boundary conditions must be given at the bottom and free surface. The boundary conditions are:

1. Kinematic bottom boundary condition: at the seabed, if the water depth d is constant, the flow velocity perpendicular to the bed is zero;

$$\frac{\partial \phi}{\partial z} = 0 \tag{2.5}$$

2. Kinematic free surface boundary condition: a fluid particle located at the free surface must remain at the free surface (Fig. 2.3);

$$\frac{\partial \phi}{\partial z} = \frac{d\eta}{dt} \tag{2.6}$$

3. Dynamic free surface boundary condition: the pressure at the water surface must be equal to the atmospheric pressure.

$$\frac{\partial \phi}{\partial t} + g\eta = 0 \tag{2.7}$$

If the wave is two-dimensional and periodic with a wave period T and a direction of propagation in the x direction, the continuity equation can be solved as a boundary value problem. As the maximum surface elevation is assumed small compared to a typical dimension (L, wave

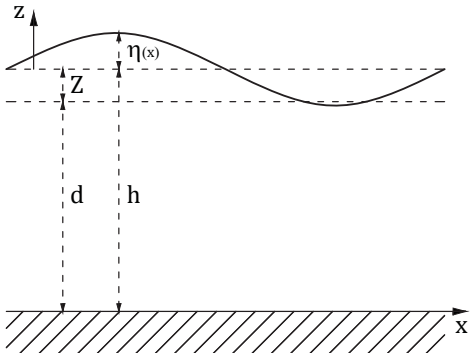

Figure 2.3: *Definition sketch for h, d and η*

length) the solution for waves propagating without deformation can be linearised and solved analytically. This solution is the linear wave solution, also called the Airy wave or the Stoke first order wave. The velocity potential and the wave profile are given by:

$$\phi = -\frac{HL}{2T}\frac{\cosh kz}{\cosh kh} sin(\omega t - kx) = 0 \tag{2.8}$$

$$\eta = a\cos(\omega t - kx) = \frac{H}{2}\cos(\omega t - kx) \tag{2.9}$$

where a is the wave amplitude ($= H/2$), $\omega = 2\pi/T$ is the angular frequency, $k = 2\pi/L$ is the wave number and $c = L/T$ is the wave celerity. The horizontal and vertical components of the water particle velocity are:

$$u = \frac{\pi H}{T}\frac{\cosh kz}{\sinh kh} cos(\omega t - kx) = 0 \tag{2.10}$$

$$v = \frac{\pi H}{T}\frac{\sinh kz}{\sinh kh} sin(\omega t - kx) = 0 \tag{2.11}$$

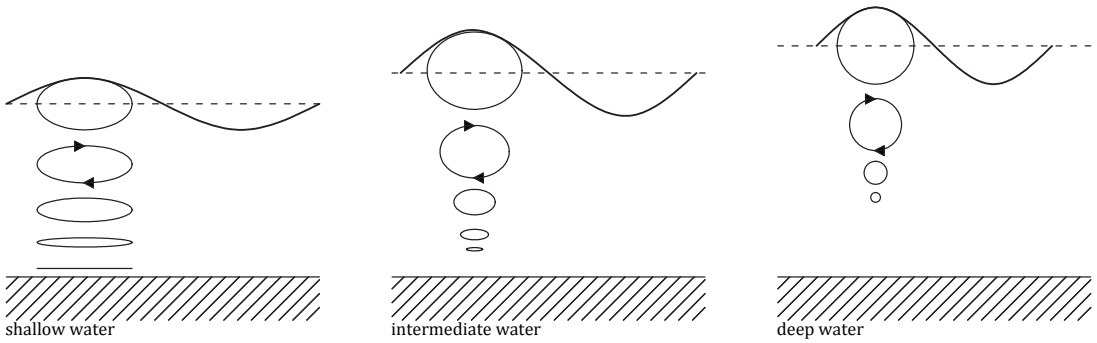

Figure 2.4: *Wave particles orbits in shallow, intermediate and deep water*

In deep water, the particles orbits are circular throughout the water column but decrease in diameter with increasing distance below the water surface, to approximately become zero at a distance of $L/2$. In transitional to shallow water, the orbits reach the bottom and become elliptical with the ellipses becoming flatter near the bottom. At the bottom the particles follow a reversing horizontal path (Fig. 2.4).

In conclusion, the following dispersion relation could be introduced, in order to determine the angular frequency and, consequently, the wave celerity:

$$c^2 = \left(\frac{\omega}{k}\right)^2 = \frac{g}{k}\tanh(kh) \tag{2.12}$$

In deep water, since $h \to \infty$, $\tanh(kh) \approx 1$, the celerity and the wave length (L_0, where the subscript 0 indicates the value in deep water) reduce to:

$$c = \sqrt{\frac{gL}{2\pi}} \qquad L_0 = \frac{gT^2}{2\pi} \tag{2.13}$$

In very shallow water, since $h \to 0$, $\tanh(kh) \approx kh$, the celerity becomes:

$$c = \sqrt{gh} \tag{2.14}$$

For small amplitude wave theory, wave energy consists of two part, potential and kinetic energy, and is given by Eq. 2.17:

$$E_P = \frac{1}{L}\int_0^{L/2} \rho g \eta^2 dx = \frac{1}{16}\rho g H^2 \tag{2.15}$$

$$E_K = \frac{1}{2L}\rho g \int_0^L \left[\int_0^z (u^2 + v^2) dz\right] dx = \frac{1}{16}\rho g H^2 \tag{2.16}$$

$$E = E_P + E_K = \frac{1}{8}\rho g H^2 \tag{2.17}$$

2.2.2 Irregular waves

The wave, described in the preceding theory, are assumed to be regular (i.e. periodic in time and space). However, real sea state are represented by irregular waves. There are two main ways to describes irregular waves: i) spectral analysis, that considers irregular waves as a superposition of infinite component waves and describes their characteristics on the basis of the energy distribution of the component waves, ii) individual wave analysis, the wave characteristics are describes by a distribution of H and T, defined by the zero-crossing methods. Considering the first method, as aforementioned, irregular waves can be described by a superposition of an infinite number of component regular waves, with different wave periods (Fig. 2.5). The water surface elevations can be expressed:

$$\eta = \sum_i a_i \cos(\omega_i t - k_i x) \tag{2.18}$$

The directional wave spectrum $S(f, \alpha)$ is defined as the expected energy density in terms of frequency and directions. The frequency spectrum $S(f)$ is a one dimensional spectrum defined as the energy density in terms of frequency only:

$$S(f)\Delta f = \sum_i \frac{a_i^2}{2} \tag{2.19}$$

The directional spectrum and the frequency spectrum are linked with the following expression:

$$S(f) = \int_0^{2\pi} S(f, \alpha) d\alpha \tag{2.20}$$

In the Joint North Sea Wave Project (JONSWAP), Hasselmann et al. (1980) proposed the well-know Jonswap spectrum of the form:

$$S(f) = \frac{\alpha g^2}{\omega^5} exp\left\{-1.25\left(\frac{\omega_P}{\omega}\right)^4\right\}\gamma_F^r \tag{2.21}$$

where $\gamma_F = 3.3$ and the coefficients α, ω_P and r depend on the wind speed velocity at the 10 m elevation U_{10} and on the fetch length F.

Considering the second way, individual waves in an irregular wave field can be defined by, for

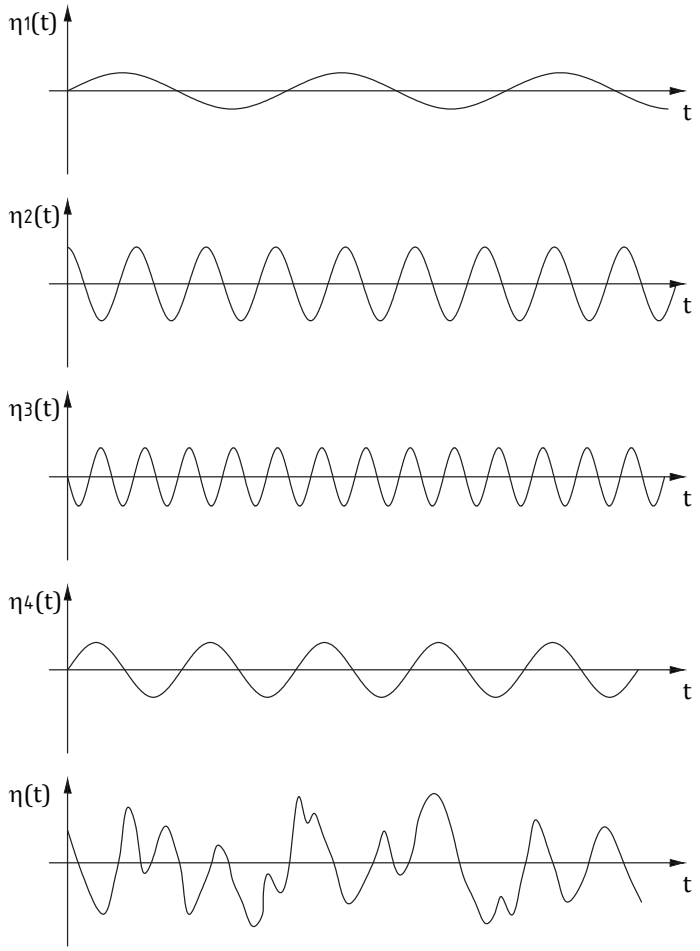

Figure 2.5: *Superposition of component regular waves, with different wave periods*

instance, the zero-crossing methods. It has been found that the distribution of wave heights follows the Rayleigth distribution (Longuett-Higgins 1952):

$$f(H) = \frac{2H}{H_{rms}^2} exp\left[\left(-\frac{H}{H_{rms}}\right)\right]^2 \tag{2.22}$$

Based on this distribution, various representative wave heights can be found:

$\overline{H} = \frac{1}{N}\sum_i^N H_i$	mean wave height
$H_S = H_{1/3} = 1.6\overline{H}$	average of the highest one-third wave heigths
$H_{rms} = 0.706 H_S$	root-mean square wave heigth

2.2.3 Waves in shallow water

In shallow water, waves transform under: i) the influence of the sloping bottom, ii) the shoreline direction respect to the wave direction and iii) the presence of coastal structures. In the following, three wave transformations are describes:

a) Wave shoaling: if waves have an incident direction normal to the beach, with straight and parallel bottom contours, changes in the wave profile are due solely to changes in water depth. The wave profile changes are calculated with reference to the energy flux. Neglecting energy loss, the energy flux can be taken constant. Considering a wave train propagating over a slopping bottom, the energy flux for waves in an infinite depth is equal to the energy flux in intermediate depth:

$$c_g E = cost \Rightarrow E_0 c_{g0} = \frac{1}{8}\rho g H_0^2 c_{g0} = E c_g = \frac{1}{8}\rho g H^2 c_g \tag{2.23}$$

where c_g is the group celerity, that can be obtained from:

$$c_g = c + k\frac{dc}{dk} = \frac{c}{2}\left[1 + \frac{2kh}{\sinh(2kh)}\right] = \frac{c}{2}\left[1 + G\right] \tag{2.24}$$

In deep water, since $h \to \infty$, $c_{g0} = c_0/2$ (subscript 0 indicates deep water). Substituting the group celerity and the Eq. 2.13 in the Eq. 2.23, the wave height in intermediate wave affecting by shoaling can be evaluated as:

$$H = H_0 \left[(1 + G)\tanh(kh)\right]^{-1/2} = K_S H_0 \tag{2.25}$$

b) Wave refraction: the celerity distribution is distorted by the change in water depth and by local currents, if exists in the fluid (Fig. 2.6). A gradient in the wave celerity results in a change of the direction of wave propagation. Refraction follows Snell's law, which states that:

$$\frac{\sin(\alpha)}{c} = \frac{\sin(\alpha_0)}{c_0} \Rightarrow K_R = \sqrt{\frac{\cos\alpha_0}{\cos\alpha}} \tag{2.26}$$

c) Wave diffraction: wave fronts change their shape when wave encounters an obstacle, for instance a breakwater or a groin. The Sommerfeld (1896) solution (Eq. 2.27) of optical diffraction was applied to water waves by Penney and Price (1944). Fig. 2.8 shows the coefficient of diffraction K_D computed for 6 values of R/L and α in the range of 0 - 180°.

$$K_D = \left| f(u) exp\left(-2\pi i (R/L)\cos(\theta)\right)\right| \tag{2.27}$$

$$f(u) = \frac{1+i}{2}\int_{-\infty}^{u} exp\left(\frac{-i\pi u^2}{2}\right) du \tag{2.28}$$

$$u = -\sqrt{8R/L}\sin(\theta/2) \tag{2.29}$$

where θ e R/L are the polar coordinates of the point where the diffraction coefficient K_D is evaluated, α and L are the wave length and the wave direction:

$$\theta = \alpha - \beta = \alpha - atan\left(\frac{x - x_P}{y - y_P}\right) \qquad \frac{R}{L} = \frac{y - y_P}{L\cos\alpha}$$

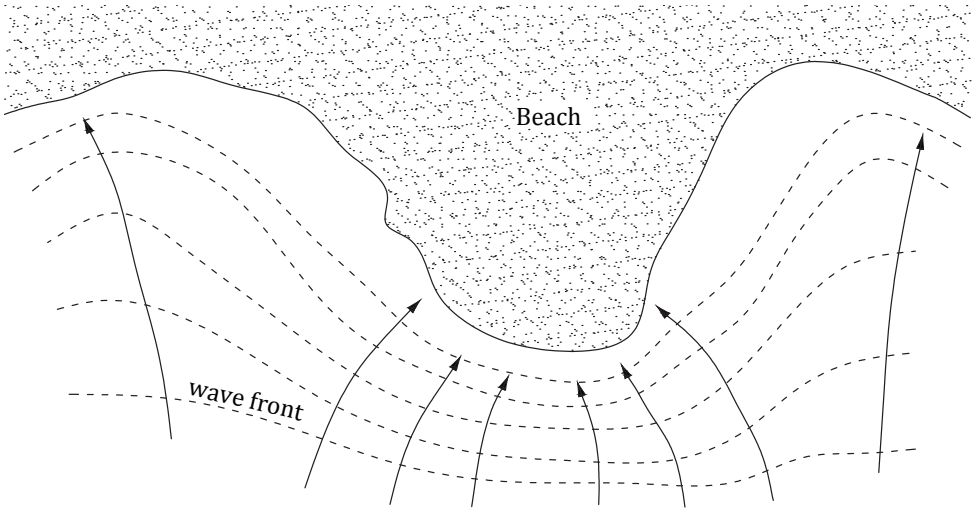

Figure 2.6: *Example of refraction*

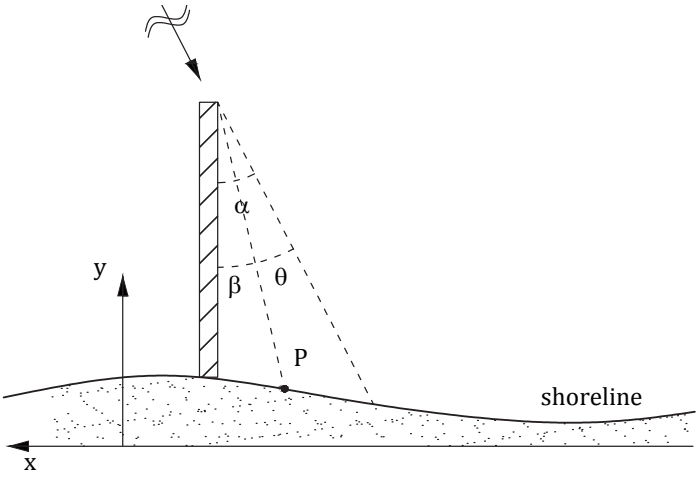

Figure 2.7: *Definition sketch for diffraction*

2.2.4 Waves and currents in the surf zone

Waves break when their height reaches a certain limiting value relative to their length or depth. The surf zone is the area where waves break and with the most intense sediment transport (due to turbulence). Furthermore, the wave breaking generates strong currents that transport the sediment along the coast. As waves propagate into shallower water, the process of shoaling leads to increasing wave height. This process cannot continue and the waves break because their steepness becomes very large as the depth becomes shallower. This phenomenon is associated with a very large loss of wave energy and, due to the strong dissipation, the wave height decreases toward the shore in the surf zone.
The breaking waves can be characterized by the surf similarity parameter ξ_0, which is the ratio between the beach slope β and the square root of the wave steepness.

$$\xi_0 = \frac{\tan\beta}{\sqrt{H_0/L_0}} \tag{2.30}$$

According to this parameter, breaking waves can be divided into 4 different types:

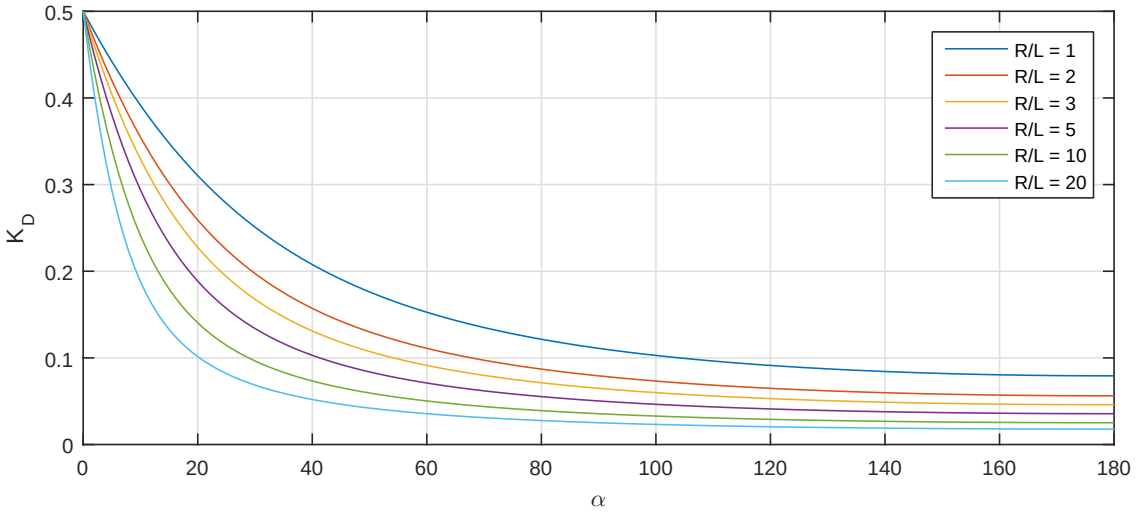

Figure 2.8: *K_D for different values of R/L and α (bottom)*

1. Surging breakers ($\xi_0 > 5$): observed when waves of small steepness propagate onto a steep sloping beach. the foot of the steep front becomes unstable and rushes forward, causing the wave crest to decrease and disappear;

2. Collapsing breakers ($3.3 < \xi_0 < 5$): observed on medium sloping beaches. The breaking is less evident than in the other cases;

3. Plunging breakers ($0.5 < \xi_0 < 3.3$): observed on relatively steep beach slopes. Waves become asymmetric in the crest, which exhibits a sharpening of the wave crest with an almost vertical front face;

4. Spilling breakers ($\xi_0 < 0.5$): observed when waves of large steepness are incident to a gently sloping beach. These breakers are characterized by the forward slope of the wave becoming unstable. A plume of water and air slides down the slope from the crest.

The wave height at the breaking point can be obtained through a criterion involving local parameters, such as wave period and wave height. Miche (1951) derived the following equation describing breaking waves based on parameters in the breaking point (subscript b):

$$\frac{H_b}{L_b} = 0.142 \tanh \frac{2\pi h_b}{L_b} \tag{2.31}$$

In deep water, since $h \to \infty$, $\tanh(kh) \approx 1$, $H_b/L_b = 0.142$, in very shallow water the limit of the Miche (1951) equation becomes:

$$H_b = \gamma_b h_b \tag{2.32}$$

where γ_b is normally taken equal to 0.78. Eq. 2.32 states that the wave height is proportional to the water depth. However, the decay of the wave height, even on a constant bed slope, is more complex than indicated by Eq. 2.32. When more complex bed topography are considered, it is necessary to develop a model which includes more complex phenomena. The water surface elevation can be determined by the solution of the energy equation and the momentum equation. For stationary conditions, the energy equation is:

$$\frac{dE}{dx} = \frac{\partial E}{\partial x} + \frac{\partial F}{\partial x} = \frac{\partial F}{\partial x} = -D \tag{2.33}$$

Dally et al. (1985) developed a model for the breaker decay. They assumed that, when a wave starts breaking, it continues until the height reaches a value of about 0.4 times the water depth (namely stable wave height H_{stab}). The dissipation terms in Eq. 2.33 depends on the wave energy flux and on a stable wave energy flux (corresponding to H_{stab}).

$$D = -0.15\frac{F - F_{stab}}{h} = -\frac{0.15}{h}\left(\rho g\frac{H^2}{8}c_g b - \rho g\frac{H_{stab}^2}{8}c_g b\right) \tag{2.34}$$

Various currents exist in the near-shore region, such as ocean currents, tidal currents and wind and wave induced currents. Assuming that wave near-shore current varies slowly in space and time on a scale that is large compared with typical wave length, the governing equation are the depth integrated mass and momentum balance equations:

$$\frac{\partial \rho z}{\partial t} + \frac{\partial \rho Q_x}{\partial x} + \frac{\partial \rho Q_y}{\partial y} \tag{2.35}$$

$$\frac{\partial}{\partial x}\left(\frac{\rho Q_x Q_x}{h} + S_{xx} + R_{xx}\right) = -\rho g h\frac{\partial z}{\partial x} + \tau_a - \tau_b \tag{2.36}$$

$$\frac{\partial}{\partial x}\left(S_{xy} + R_{xy}\right) = -\tau_b \tag{2.37}$$

where h is the water level, $Q_x = uh$ and $Q_y = uh$, The radiation stress S is an excess flow of momentum induced by the presence of waves and formed by two contributions: the first due to the wave velocities of the particles and the second due to pressure. The radiation stress tensor can be evaluated through:

$$S = \begin{pmatrix} S_{xx} & S_{xy} \\ S_{yx} & S_{yy} \end{pmatrix} = \frac{E}{2}G\begin{pmatrix} 1 & 0 \\ 0 & 1 \end{pmatrix} + \frac{E}{2}(1+G)\begin{pmatrix} \cos^2\alpha & \cos\alpha\sin\alpha \\ \cos\alpha\sin\alpha & \sin^2\alpha \end{pmatrix} \tag{2.38}$$

The strong energy dissipation in the surf zone and the associated decrease of wave height towards the shore give a gradient in the radiation stress. This decrease is balanced by a slope in the mean water surface: the set-up in the surf zone and the set-down outside the surf zone (shoaling produces a variation in the wave height). Assuming that $Q_x = cost = 0$, R_{xx} is negligible, τ_a and τ_b are null due to considering null the velocity orthogonal to the shore, and z is small in the breaker zone, the Eq. 2.36 becomes:

$$\frac{\partial}{\partial x}\left(S_{xx}\right) + \rho g h\frac{\partial z}{\partial x} = \frac{\partial}{\partial x}\left(S_{xx} + +\rho g dz\right) = 0 \tag{2.39}$$

The term inside the brackets is constant along the x-direction. Therefore, equating this term evaluated in the offshore zone and in the breaking point, it is possible to obtain the equation for the set-down:

$$Z_{down} = \frac{1}{\eta_b}\left[\frac{H_0^2}{16}(1+2G_0) + \frac{H_0^2}{16}\frac{c_{g0}}{c_g}(1+2G)\right] \approxeq 4\%H \tag{2.40}$$

where $H^2 = H_0^2 c_{g0}/c_g$ (from dispersion equation). In the surf zone the wave height is proportional to the water depth and $G = 1$. The equation of set-up is:

$$Z_{up} = Z_{down} + \frac{3/8\gamma_b^2}{1 + 3/8\gamma_b^2}\eta_b \approxeq 10\%H \tag{2.41}$$

Eq. 2.37 is the momentum balance equations in the y-direction. The equation, for a steady uniform long-shore current, express the equilibrium between radiation stress gradient, bed shear stress and redistributing forces. Long-shore current velocities can be evaluated solving this equation. Assuming that the current velocity V is very small compared to the particles wave velocity U_{1m} and:

$$R_x x = -\rho \nu_t h \frac{\partial V}{\partial x} \qquad \nu_t = Ch\sqrt{gh}$$
$$\tau_b = \frac{1}{\pi}\rho f_w U_{1m} V \qquad U_{1m} = w\frac{H}{2\sinh(kh)}$$

where C is a coefficient (0.045-1.8) r is the bed roughness and f_w is the friction coefficient, Eq. 2.37 becomes:

$$\frac{\partial}{\partial x}\left(S_{xy}\right) + \frac{1}{\pi}\rho f_w U_{1m} V - \frac{\partial}{\partial x}\left(\rho \nu_t h \frac{\partial V}{\partial x}\right) = \frac{\partial}{\partial x}\left(S_{xy}\right) + kV - \frac{\partial}{\partial x}\left(A\frac{\partial V}{\partial x}\right) = 0 \tag{2.42}$$

Eq. 2.42 can be solved with the finite element methods. Considering $V = \sum_i v_i N_i$ and $S = \sum_i s_i N_i$, where N are the shape functions ("roof function"), and integrating along the profile, the equation becomes:

$$\int_1^L \left[\frac{\partial S_{xy}}{\partial x} + kV - \frac{\partial}{\partial x}\left(A\frac{\partial V}{\partial x}\right)\right] N_j dx = \tag{2.43}$$
$$\int_1^L \frac{\partial S_{xy}}{\partial x} N_j dx + \int_1^L kV N_j dx - \int_1^L A\frac{\partial^2 V}{\partial x^2} N_j dx = 0$$

After some operations and substituting V and S:

$$\underbrace{\int_1^L A\frac{\partial\left(\sum_i v_i N_i\right)}{\partial x}\frac{\partial N_j}{\partial x}dx}_{1} + \underbrace{\int_1^L k\left(\sum_i v_i N_i\right) N_j dx}_{2} - \underbrace{\int_1^L \frac{\partial\left(\sum_i s_i N_i\right)}{\partial x} N_j dx}_{3} = 0 \tag{2.44}$$

1. The first term of the momentum equation is:

$$\int_1^L A\frac{\partial\left(\sum_i v_i N_i\right)}{\partial x}\frac{\partial N_j}{\partial x}dx = \int_1^L A\left(\sum_i v_i \frac{\partial N_i}{\partial x}\right)\frac{\partial N_j}{\partial x}dx = \tag{2.45}$$
$$= \sum_i \left(\int_1^L A\frac{\partial N_i}{\partial x}\frac{\partial N_j}{\partial x}dx\right) v_i = \sum_i f_{i,j} v_i = \underline{F}V$$

   using FEM methods, the terms inside the matrix $\underline{F}$ are:

   a) i = j - 1: $f_{j-1,j} = -A\frac{1}{x_j - x_{j-1}}$ b) i = j + 1: $f_{j+1,j} = -A\frac{1}{x_{J+1} - x_j}$

   c) i = j = 1: $f_{1,1} = A\frac{1}{x_2 - x_1}$ d) i = j = L: $f_{L,L} = A\frac{1}{x_L - x_{L-1}}$

   e) i = j: $f_{j,j} = A\left(\frac{1}{x_j - x_{j-1}} + \frac{1}{x_{J+1} - x_j}\right)$ f) elsewhere: $f_{i,j} = 0$

2. The second term of the momentum equation is:

$$\int_1^L \left(\sum_i v_i N_i\right) N_j dx = \sum_i \left(\int_1^L k N_i N_j dx\right) v_i = \sum_i g_{i,j} v_i = \underline{G}V \tag{2.46}$$

using FEM methods, the terms inside the matrix $\underline{G}$ are:

a) i = j - 1: $g_{j-1,j} = \dfrac{k\,(x_j - x_{j-1})}{6}$ b) i = j + 1: $g_{j+1,j} = \dfrac{k\,(x_{j+1} - x_j)}{6}$

c) i = j: $g_{j,j} = \dfrac{k\,(x_j - x_{j-1})}{3} + \dfrac{k\,(x_{j+1} - x_j)}{3}$ d) i = j = 1: $g_{1,1} = \dfrac{k\,(x_2 - x_1)}{3}$

e) i = j = L: $g_{L,L} = \dfrac{k\,(x_L - x_{L-1})}{3}$ f) elsewhere: $g_{i,j} = 0$

3. The third term of the momentum equation is:

$$\int_1^L \frac{\partial}{\partial x}\left(\sum_i s_i N_i\right) N_j dx = \sum_i \left(\int_1^L \frac{\partial N_i}{\partial x} N_j dx\right) s_i = \sum_i b_{i,j} s_i = \underline{B}S \tag{2.47}$$

using FEM methods, the terms inside the matrix $\underline{B}$ are:

a) i = j - 1: $b_{j-1,j} = \dfrac{1}{2}$ b) i = j + 1: $b_{j+1,j} = -\dfrac{1}{2}$ c) i = j: $b_{j,j} = 0$

d) i = j = 1: $b_{1,1} = -\dfrac{1}{2}$ e) i = j = L: $b_{L,L} = \dfrac{1}{2}$ f) elsewhere: $b_{i,j} = 0$

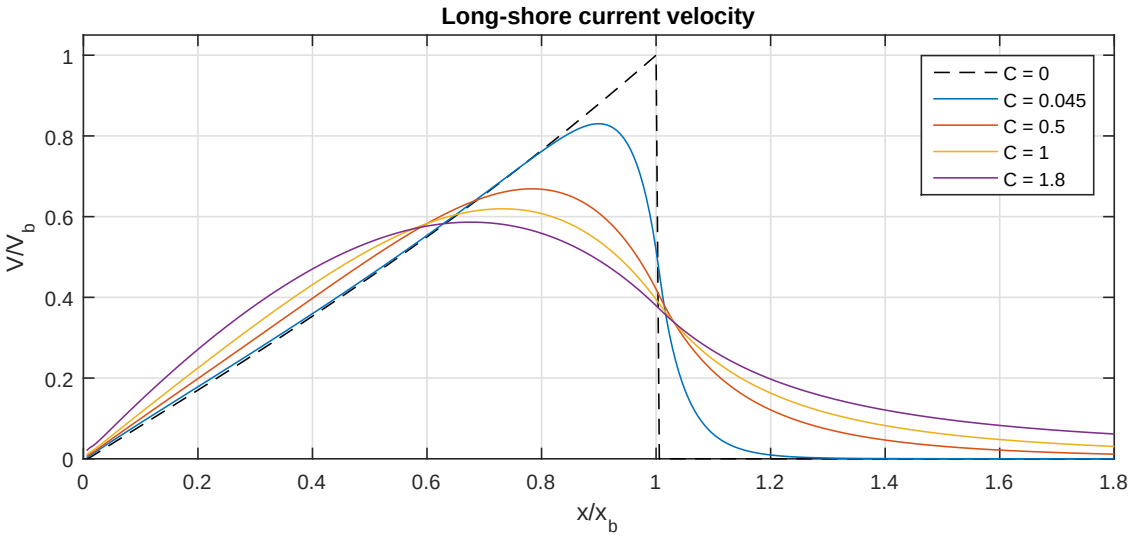

Figure 2.9: *Long-shore current velocities profiles for different values of C*

The momentum equation for the y-direction (Eq. 2.37) becomes:

$$\sum_i f_{i,j} v_i + \sum_i g_{i,j} v_i + \sum_i b_{i,j} s_i = \underline{F}V + \underline{G}V + \underline{B}S \tag{2.48}$$

In conclusion, the long-shore current velocity can be obtained with equation 2.49. The long-shore velocities profiles (divided by the velocity in the breaking point V_b) for different values of parameter C are shown in Fig. 2.9, as a function of x/x_b. The result is similar to the theoretical form proposed by Longuet-Higgins (1970).

$$V = [inv\,(\underline{F} + \underline{G})]\,(-\underline{B}S) \tag{2.49}$$

2.2.5 Shallow water equations

As aforementioned, at the point of wave breaking, the linear theory breaks down and other formulations have to be accounted for explain physics in the surf zone.
The Shallow Water Equations (SWEs) are a system of hyperbolic/parabolic partial differential equations (PDEs) governing fluid flow where the vertical dimension is much smaller than the typical horizontal scale. In this case the equations can be averaged over the depth to get rid of the vertical dimension. Therefore, the Shallow Water Equations can be used to predict tides, storm surge levels, coastline changes from ocean currents and flooding due to river or marine inundation.
The Shallow Water Equations are derived from the Navier-Stokes equations, which describe the motion of fluids. The Navier-Stokes equations are themselves derived from the equations for conservation of mass and linear momentum.

$$\frac{\partial \rho}{\partial t} + \bigtriangledown \cdot (\rho \mathbf{v}) = 0 \tag{2.50}$$

$$\frac{\partial \rho \mathbf{v}}{\partial t} + \bigtriangledown \cdot (\rho \mathbf{v}\mathbf{v}) = \rho \mathbf{b} + \bigtriangledown \cdot \mathbf{T} \tag{2.51}$$

where ρ is the fluid density (kg/m^3), $\mathbf{v} = (u, v, w)$ is the fluid velocity (m/s), $\mathbf{b}$ is the body force density per unit mass acting on the fluid (N/kg) and $\mathbf{T}$ is the Cauchy stress tensor (N/m^2). In order to obtain the Navier-Stokes equations from Eq. 2.50 and Eq. 2.51, some assumptions about the fluid (water), about the density ρ, and about the body forces $\mathbf{b}$ and stress tensor $\mathbf{T}$ have to be made: i) the fluid is incompressible, so ρ does not depend on pressure p; ii) salinity and temperature are assumed to be constant throughout the domain, so ρ can be taken constant; iii) water is a Newtonian fluid. The final form of the Navier-Stokes equations in 3D is:

$$\bigtriangledown \cdot (\mathbf{v}) = 0 \tag{2.52}$$

$$\frac{\partial \rho \mathbf{v}}{\partial t} + \bigtriangledown \cdot (\rho \mathbf{v}\mathbf{v}) = - \bigtriangledown p + \rho g + \bigtriangledown \cdot \overline{\mathbf{T}} \tag{2.53}$$

The following boundary conditions for a water column (η is the elevation of the free surface relative to the mean sea level, d is the bathymetry, measured positive downward from the m.s.l. and $h = \eta + d$ is the total depth) can be used to integrate the Navier-Stokes equations over depth and obtain the Shallow water equations.

1. at the free surface, $z = \eta(x, y)$: $p = 0$ and $\frac{D\eta}{Dt} = \frac{\partial \eta}{\partial t} + u\frac{\partial \eta}{\partial x} + v\frac{\partial \eta}{\partial y} = w$
2. at the bottom, $z = -d$: $u\frac{\partial d}{\partial x} + v\frac{\partial d}{\partial y} + w = 0$

In the momentum equation for z-direction (vertical), all the terms are small compared to the pressure derivative and the gravity term. The z-momentum equation implies that $\partial p/\partial z = \rho g$, so $p = \rho g(\eta - z)$ (hydrostatic pressure distribution). Integrating the continuity equation (Eq. 2.52) for a water column:

$$\begin{aligned} \int_{-d}^{\eta} \bigtriangledown \cdot (\mathbf{v})\, dz &= \int_{-d}^{\eta} \left(\frac{\partial u}{\partial x} + \frac{\partial v}{\partial x} \right) dz + w|_{z=\eta} - w|_{z=-d} \\ &= \frac{\partial}{\partial x} \int_{-d}^{\eta} u dz + \frac{\partial}{\partial y} \int_{-d}^{\eta} v dz - \left(u|_{z=\eta} \frac{\partial \eta}{\partial x} + u|_{z=-d} \frac{\partial d}{\partial x} \right) \\ &- \left(v|_{z=\eta} \frac{\partial \eta}{\partial y} + v|_{z=-d} \frac{\partial d}{\partial y} \right) + w|_{z=\eta} - w|_{z=-d} = 0 \end{aligned} \tag{2.54}$$

Integrating over depth also the x and y momentum equations and defining depth-averaged velocities as:

$$\overline{u} = \frac{1}{h}\int_{-d}^{\eta} u dz \qquad\qquad \overline{v} = \frac{1}{h}\int_{-d}^{\eta} v dz$$

The 2D non-linear Shallow Water Equations in conservative form are:

$$\frac{\partial h}{\partial t} + \frac{\partial h\overline{u}}{\partial x} + \frac{\partial h\overline{v}}{\partial y} = 0 \tag{2.55}$$

$$\frac{\partial h\overline{u}}{\partial t} + \frac{\partial h\overline{u}^2}{\partial x} + \frac{\partial h\overline{u}\overline{v}}{\partial y} = -gh\frac{\partial \eta}{\partial x} + \frac{1}{\rho}\left(\tau_{sx} - \tau_{bx} + F_x\right) \tag{2.56}$$

$$\frac{\partial h\overline{v}}{\partial t} + \frac{\partial h\overline{u}\overline{v}}{\partial x} + \frac{\partial h\overline{v}^2}{\partial y} = -gh\frac{\partial \eta}{\partial y} + \frac{1}{\rho}\left(\tau_{sy} - \tau_{by} + F_y\right) \tag{2.57}$$

where the surface stress τ_s, the bottom stress τ_b and the friction term F must still determined on a case-by-case basis.

2.2.6 Boussinesq equations

In fluid dynamics, the Boussinesq approximation for water waves is valid for weakly non-linear and long waves, so the characteristic depth d_0 is much smaller than the characteristic horizontal length λ in the wave motion. The Boussinesq-type equations incorporate frequency dispersion, differently from the shallow water equations, which are not frequency-dispersive. In coastal engineering, Boussinesq-type equations are frequently used for the simulation of water waves in shallow seas and harbours.
For water waves on an incompressible fluid and irrotational flow in the (x,z) plane (1D), considering the velocities field related to a potential ϕ (Eq. 2.1), the boundary conditions at the free surface elevation $z = \eta(x,t)$ are the kinematic and dynamic conditions:

$$\frac{\partial \eta}{\partial t} + u\frac{\partial \eta}{\partial x} = \frac{\partial \phi}{\partial z} \tag{2.58}$$

$$\frac{\partial \phi}{\partial t} + \frac{1}{2}\left(u^2 + w^2\right) + g\eta = 0 \tag{2.59}$$

In the Boussinesq approximation, the terms of the vertical coordinate are neglected while some influences of the vertical structure of the flow under water waves are retaining. This is useful because the waves propagate in the horizontal plane and have a different behaviour in the vertical direction. Further, in the resulting equations only the linear and quadratic terms with respect to η and u_0 (horizontal velocity at the bottom) are retained. The cubic and higher order terms are assumed to be negligible.
The following partial differential equations, called Boussinesq equations, are obtained:

$$\frac{\partial \eta}{\partial t} + \frac{\partial}{\partial x}\left[u_0\left(d + \eta\right)\right] - \frac{1}{6}d^3\frac{\partial^3 u_0}{\partial x^3} = 0 \tag{2.60}$$

$$\frac{\partial u_0}{\partial t} + \frac{1}{2}\frac{\partial u_0^2}{\partial x} - \frac{1}{2}d^2\frac{\partial^3 u_0}{\partial x^2 \partial t} + g\frac{\partial \eta}{\partial x} = 0 \tag{2.61}$$

2.3 Extreme value statistics

Extreme value theory concerns with probabilistic and statistical questions related to very high values in sequences of random variables and in stochastic processes. The statistics of extremes have played an important role in engineering practice for water resources design and management.
A robust methodology devoted to the return value estimation is crucial in the evaluation of coastal flooding hazard. Indeed, the structural safety must be assessed in the context of a rational evaluation of the wave climate at a specified location. During the past decades, a great deal of effort was put by several researchers to define accurate methodologies for estimating the wave height and the related wave loads used in the design of a maritime and coastal structure. Thus, an inadequate estimation of the design wave may produce either an unsafe structure (if wave loads are underestimated) or an over-designed and uneconomical structure (if wave loads are overestimated).

The common procedure involves the statistical analysis of the wave data obtained from in situ measurements or modelled results. Two issues influence the reliability of this analysis: i) data reliability and ii) limited wave data availability in terms of individual time series length and number of data sources. For instance, assuming that the available data covers a short period (i.e. shorter than 20 years), the return value estimation with low probability level (i.e. $T_R = 50$ years, 100 years) required an extrapolation well beyond the range of available data. Relevant contributions to the development of statistical methods for extreme value prediction of natural random events were given by Fréchet (1927), Weibull (1939) and Gumbel (1958). Several statistical methods that may be applied to carry out extreme value analysis for the marine environment are discussed, for instance, in Goda and Kobune (1991) and Goda (2010).

2.3.1 Univariate analysis

The univariate extreme value analysis can be achieved by making use of two types of extreme series: i) Extreme value distribution (EV); ii) Peaks over Threshold (PoT).
In the first method, the sample is defined by the maximum peak of each time interval (e.g. annual maximum, monthly maximum, daily maximum). However, defining the samples in such a way can result in loss of information. Considering for example a sample of annual maximum, some peaks, that are not the maximum in a year but are still relatively high, are not considered in this analysis.
In the second approach, the PoT sample is defined by all peak values that lie above a certain threshold level. Major difficulties in using this method are assuring the independence of the data series and choosing an appropriate threshold value.

a) Extreme value distribution: The common cumulative distribution function of a series of independent and identically distributed (i.i.d.) random variables is $F(x) = Pr\{X_i \leq x\}$. Denoting $M_n = max(X_1, .., X_n)$ the nth sample maximum of the process, the theoretical exact distribution of the maximum is:

$$Pr\{M_n \leq x\} = F(x)^n \tag{2.62}$$

For non-trivial limit results, F must be renormalised: find $a_n > 0$, b_n such that:

$$Pr\left\{\frac{M_n - b_n}{a_n} \leq x\right\} = F(a_n x + b_n)^n \to H(x) \tag{2.63}$$

the *Three type Theorem* (derived by Fisher and Tippett (1928) and by Gnedenko (1943)) asserts that if H exists, it must be one of three types:

$$\text{Gumbel type: } H(x) = \left\{exp\left(-e^{-x}\right) \quad \text{all x} \right. \tag{2.64}$$

$$\text{Fréchet type: } H(x) = \begin{cases} 0 & \text{x}<0 \\ exp\left(-x^{-\alpha}\right) & \text{x}>0 \end{cases} \tag{2.65}$$

$$\text{Weibull type: } H(x) = \begin{cases} exp\left(-|x|^{\alpha}\right) & \text{x}<0 \\ 1 & \text{x}>0 \end{cases} \tag{2.66}$$

The three types may be combined into a single *Generalised Extreme Value* (GEV) distribution:

$$H(x) = exp\left\{-\left(1 + \xi\frac{x-\mu}{\psi}\right)\right\}^{-1/\xi} \tag{2.67}$$

where μ ia a location parameter, $\psi > 0$ is a scale parameter and ξ is a shape parameter. The limit $\xi \to 0$ corresponds to the Gumbel distribution, $\xi > 0$ to the Fréchet distribution with $\alpha = 1/\xi$, $\xi < 0$ to the Weibull distribution with $\alpha = -1/\xi$.

b) Peaks over thresholds: Consider the distribution of X conditionally on exceeding some threshold u (so $Y = X - u > 0$):

$$F_u(y) = Pr\left\{Y \leq y \mid Y > 0\right\} = \frac{F(u+y) - F(u)}{1 - F(u)} \tag{2.68}$$

As $u \to \omega_F = sup\left\{x : F(x) < 1\right\}$, it could be found a limit $F(y) \approx G(y|k, \xi, \sigma)$, where G is *Generalised Pareto distribution* (GPD), $k(\in \mathbb{R})$, $\xi(\in \mathbb{R})$ and $\sigma(> 0)$ are the shape, location and scale parameters:

$$G(y|k,\xi,\sigma) = \begin{cases} 1 - \left(1 - k\frac{y-\xi}{\sigma}\right)^{1/k} & k \neq 0 \\ 1 - exp\left(-\frac{y-\xi}{\sigma}\right) & k = 0 \end{cases} \tag{2.69}$$

The choice of the most suitable threshold is one of the main issue. Coles et al. (2001) proposed two different methods for threshold selection based on empirical techniques: one is based on the interpretation of the mean excess (ME) plot, which should be approximately linear in proximity of the appropriate threshold, and the other on the stability of shape and scale parameter of GPD in the vicinity of the threshold. The selection of optimal threshold can be done also comparing the modelled and observed distribution using graphical technique or informal indexes (explain in the following).

A problem to be solved regards the optimal choice of Probability Density Function (pdf) parameters (for example the shape, location and scale parameters in the GPD distribution) of a random variable, starting from a sample. The main underlying assumption is that the

available observations constitute a set of realizations of independent and identically distributed (i.i.d.) random variables.
There are several common methods for estimating the parameters of a pdf. The most applied method is the maximum Likelihood (ML) estimation procedure where the parameters of a pdf θ are assumed variable and may be eventually characterized by a certain probability distributions. From this perspective, the choice of the optimal value of the pdf parameters could be based on the maximization (over θ) of the joint pdf of the observations x upon a suitable choice of the parameter values. If we assume that the observations correspond to a sequence of observations of i.i.d. random variables with probability density function $p(x)$, from the statistical independence of the components of the vector x, the likelihood function $L(\theta)$ is defined as the joint pdf of the observations available and evaluated as a function of the model parameters:

$$L(\theta) = p(x|\theta) = p(x_1, .., x_N|\theta) = p(x_1|\theta)p(x_2|\theta)...p(x_N|\theta) = \prod_{i=1}^{N} p(x_i|\theta) \tag{2.70}$$

The optimal choice of the model parameters θ hence relies on the maximization of $L(\theta)$ over θ, leading to the following likelihood conditions:

$$\frac{\partial L(\theta)}{\partial \theta_i} = 0 \text{ i = 1,2,..K} \tag{2.71}$$

In many practical cases it much more straightforward to work with a log transformation of $L(\theta)$, $l(\theta)$:

$$l(\theta) = \ln [L(\theta)] = \sum_{i=1}^{N} p(x_i|\theta) \tag{2.72}$$

which has the noteworthy property of having the same maxima and the same minima of the likelihood function. Hence, the maximization of l is equivalent (and operationally more simple) than the maximization of L.
Statistical analysis have to simulate the behaviour of realistic dataset. The criteria which can be used to identify the model parameters refereed for instance to graphical techniques or informal performance metrics. Plotting position formulas are used in order to graphically compare the distribution of predicted values y_P and observed/measured values y_O. Various formulas exist for different parent distributions:

$$\begin{aligned} p_i &= \frac{i}{N+1} && \text{Weibull (for all distributions)} \\ p_i &= \frac{i-0.44}{N+0.12} && \text{Gringorten (for Exponential and GEV distributions)} \\ p_i &= \frac{i-0.5}{N} && \text{Hazen (for extreme value distributions)} \end{aligned} \tag{2.73}$$

Another way to assess the quality of the model fit is the evaluation of informal performance metrics (or indexes) that provide a quantitative and aggregate estimate of model reliability (y_O versus y_P) and are generally expressed as a function of the simulation errors. The indexes here presented are three: the coefficient of efficiency NSE introduced by Nash and Sutcliffe (1970), the index of agreement D proposed by Willmott et al. (1985) and the root-mean-square error $RMSE$. A perfect agreement between y_P and y_O is reached when NSE and D

are equal to 1 and when $RMSE$ is zero. Regarding the NSE only results larger than zero are acceptable. These indexes can be used also to estimate the reliability between parent distributions and plotting position formulas.

$$NSE = 1 - \frac{\sum_i (y_{Oi} - y_{Pi})^2}{\sum_i (y_{Oi} - < y_{Oi} >)^2} \tag{2.74}$$

$$D = 1 - \frac{\sum_i (y_{Pi} - y_{Oi})^2}{\sum_i (|y_{Pi} - < y_{Oi} > | + |y_{Oi} - < y_{Oi} > |)^2} \tag{2.75}$$

$$RMSE = \sqrt{\frac{\sum_i (y_{Oi} - y_{Pi})^2}{N}} \tag{2.76}$$

2.3.2 Multivariate analysis

A wide variety of situations concerned with extreme events has a multivariate character. In coastal flooding hazard, extreme sea conditions leading to damage are usually a consequence of extreme values jointly in several components. For instance, the simultaneous occurrence of large waves and a high still water level is important in estimating their combined effect on sea defences and over-topping. For each mode of failure, it is important to identify the combinations of sea condition variables which cause the failure. Let $Xi = (X_{i1}, ..., X_{iD}, i = 1, 2, ...)$ be i.i.d. multivariate random vectors and define $M_n = max\{X_{id} : 1 \leq i \leq n\}$ for $1 \leq d \leq D$, it is assumed that exist a sequence of $a_{nd} > 0$ and b_{nd} such that:

$$Pr\left\{\frac{M_{nd} - b_{nd}}{a_{nd}} \leq x_d, 1 \leq d \leq D\right\} = F^n(a_{nd}x_d + b_{nd}) \to G(x_d) \tag{2.77}$$

when $n \to \infty$. G is called multivariate Extreme value distribution function and the univariate margins of G are Extreme Value distributions.
One of the main topic in multivariate extreme events modelling is the problem of how to measure the dependence of random variables. Some well-known measures could quantify the dependence. However, it is worthwhile to use Copula function, that fully captures the dependence structure associated with the joint distribution of two or more random variables.

a) Measures of dependence: Let X_1 and X_2 be random variables with joint distribution function F, marginal distribution functions F_1 and F_2, and positive finite variances. Linear or Pearson correlation is commonly used as a measure of dependence of two random variables.The Pearson correlation of X_1 and X_2 is:

$$\rho(X_1, X_2) = \frac{< [(X_1 - < X_1 >)(X_2 - < X_2 >)] >}{\sqrt{var[X_1]}\sqrt{var[X_2]}} \tag{2.78}$$

and $-1 \leq \rho(X_1, X_2) \leq 1$. An alternative measure of dependence is Spearman's rho:

$$\rho_S(X_1, X_2) = \rho(F_1(X_1), F_2(X_2)) \tag{2.79}$$

$-1 \leq \rho_S(X_1, X_2) \leq 1$. These measures provide an indication of the overall association of two random variables. However, they are essentially a single number that cannot capture very much information about the dependence structure.

b) Copulas: Copulas are functions that describe dependencies among variables, and provide a way to create distributions that model correlated multivariate data. Using a copula, a multivariate distribution could be constructed by specifying marginal univariate distributions, and then choose a copula to provide a correlation structure between variables. A copula C is a joint distribution of standard uniform random variables (indicated with u): $C(u_1, ..., u_d) = Pr\{U_1 \leq u_1, ..., U_d \leq u_d\}$, where $U \sim U(0, 1)$. Copulas allow to characterize the dependence structure of a set of random variables separately from the marginal distributions. Let $X_1, ..., X_d$ be random variables with joint distribution function F and continuous marginal distribution functions $F_i (i = 1, .., d)$. Then there exists a unique copula function given by:

$$C(u_1, ..., u_d) = F(F_1^{-1}(u_1), ..., F_d^{-1}(u_d)) \tag{2.80}$$

where the quantile function F_i^{-1} is defined by $F_i^{-1}(u) = inf\{x : F_i(x) \geq u\}$ (Sklar's theorem discuss in Nelsen (1999)). If C is a copula function, and $F_1, ..., F_d$ are arbitrary distribution functions, then F defined by:

$$F(x_1, ..., x_d) = C(F_1(x_1), ..., F_d(x_d)) \tag{2.81}$$

is a multivariate distribution function with marginal distribution functions $F_1, ..., F_d$. For example, considering the Gumbel's bivariate distribution $\mathbf{F}(x_1, x_2) = (1 + e^{-x_1} + e^{-x_2})^{-1}$ defined in $\mathbb{R}^2$, the marginal distribution are $F_1(x_1) = \int_{\mathbb{R}} \mathbf{F}(x_1, x_2)dx_2 = (1 + e^{-x_1})^{-1}$ and $F_2(x_2) = (1 + e^{-x_2})^{-1}$. The copula function corresponds to:

$$C(u_1, u_2) = \mathbf{F}(\mathbf{F}_1^{-1}(u_1), \mathbf{F}_1^{-1}(u_1)) = \frac{u_1 u_2}{u_1 + u_2 - u_1 u_2} \tag{2.82}$$

Copulas are powerful tool and the modelling problem can be split into two steps: i) the identification of the marginal distributions, ii) the definition of the appropriate copula in order to represent the dependence structure. There are several families of copulas, related to elliptical or non elliptical distributions (i.e Archimedean copulas). The elliptical copulas are symmetric and, for this reason, the tail dependence of the multivariate distribution is not appropriate modelled. Archimedean copulas are more suitable for extreme value analysis and depend on a unique parameter.

1. **Elliptical copulas** are copulas associated with elliptical distributions. Elliptical distributions are a family of multivariate distributions that includes the multivariate normal and multivariate t distributions. For example, the bivariate t copula is given by:

$$C(u_1, u_2) = \int_{-\infty}^{t_v^{-1}(u_1)} \int_{-\infty}^{t_v^{-1}(u_2)} \frac{\Gamma[(\nu + 2)/2]}{\Gamma[\nu/2]\pi\nu\sqrt{1 - \rho^2}} \left(\frac{1 + x' P^{-1} x}{\nu}\right)^{-(\nu+2)/2} dx_1 dx_2 \tag{2.83}$$

   where t_v^{-1} is the quantile function of a univariate t_v distribution and P is the correlation matrix $P = [1\ \rho; \rho\ 1]$.

2. **Archimedean copulas** are copulas associated with non elliptical distribution and are useful to describe dependence in the tails. Archimedean copulas are defined by $C(u_1, u_2) = \varphi^{-1}(\varphi(u_1) + \varphi(u_2))$, where $\varphi(u)$ is a strictly decreasing convex function

with $\varphi(1) = 0$. The function $\varphi(u)$ is called the generator of the copula. Some well-known Archimedean copulas are:

$$\begin{aligned}
&\text{Clayton copula} && C(u_1, u_2) = (u_1^{-\alpha} + u_2^{-\alpha} - 1)^{-1/\alpha} && \alpha > 0 \qquad (2.84)\\
&\text{Gumbel copula} && C(u_1, u_2) = \exp\left\{-[(-\log u_1)^{\alpha} + (-\log u_2)^{\alpha}]^{-1/\alpha}\right\} && \alpha \geq 1\\
&\text{Frank copula} && C(u_1, u_2) = \frac{1}{\alpha}\log\left(1 + \frac{(e^{\alpha u_1} - 1)(e^{\alpha u_2} - 1)}{(e^{\alpha} - 1)}\right) && -\infty < \alpha < \infty
\end{aligned}$$

2.4 Reliability analysis

The reliability of a system is the probability that it meet certain demands under certain conditions (e.g. the probability that a portion of inland is not flooded under certain values of wave height and sea level). Mathematically, reliability is the probability that the random variables $\mathbf{X} = (X_1, X_2, ..., X_N)$ are in the safe region that is defined by $g(\mathbf{X}) > 0$. The probability of failure is defined as the probability $P\{g(\mathbf{X}) < 0\}$ (Du 2005). If the joint probability function distribution of $\mathbf{X}$ is $f_x(\mathbf{X})$, the probability of failure is evaluated as:

$$p_f = P\{g(\mathbf{X}) < 0\} = \int_{g(\mathbf{X})<0} f_x(\mathbf{X}) dX \qquad (2.85)$$

The reliability is computed as $R = 1 - p_f$. One of the most commonly used reliability analysis methods is the First Order Reliability Method (FORM, Hasofer and Lind 1974). The basic idea is to ease the computational difficulties through simplifying the integrand of $f_x(\mathbf{X})$ and approximating the performance function $g(\mathbf{X})$. The probability integrations in Eq. 2.85 are shown in Fig. 2.10 for a 2D case. The Fig. 2.10 (b) shows the joint pdf $f_x(X_1, X_2)$ (as contours) in the X_1-X_2 plane and the integration boundary $g(X_1, X_2) = 0$. The integration for the probability of failure is performed in the region where $g(X_1, X_2) < 0$.

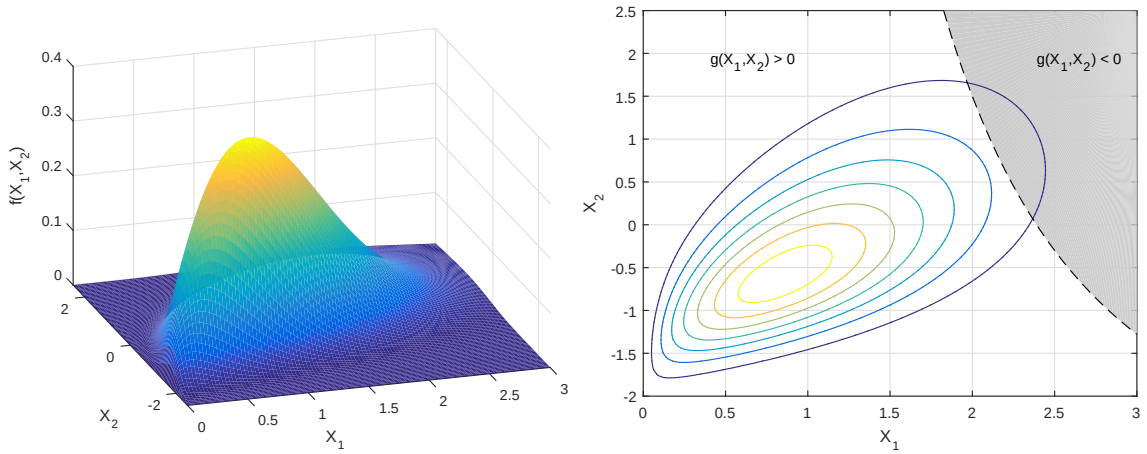

Figure 2.10: *a) Joint pdf $f_x(X_1, X_2)$, b) Joint pdf in X-plane and performance function $g(X_1, X_2) = 0$*

The direct evaluation of the probability integration is extremely difficult (e.g since $f_x(\mathbf{X})$ and $g(\mathbf{X})$ are non-linear multidimensional functions). Approximation methods can be used to compute easily the integration. Two steps are involved: i) simplify the integrand $f_x(\mathbf{X})$,

so that the contours become more regular and symmetric; ii) approximate the boundary $g(\mathbf{X}) = 0$.
The integrand simplification is achieved through transforming the random variables $\mathbf{X}$ to an equivalent independent standard normal random variable space $\mathbf{U} = (U_1, U_2, ..., U_N)$ (mean = 0, standard deviation = 1). This allows taking advantage of the numerous properties of the standard distribution. The transformation from $\mathbf{X}$ to $\mathbf{U}$ is based on the condition that the cumulative distribution functions of the random variables remain the same before and after the transformation $F_x(\mathbf{X}) = \Phi(\mathbf{U})$. There exist several possible transformations from the space of physical variables to the standardized variable space, e.g. Nataf transformation, Rosenblatt transformation (Rosenblatt 1952), etc.
The Nataf transformation (Nataf 1962) describes the joint probability density function of random variables based on their individual marginal distributions and coefficients of correlation using a Gaussian copula. Considering a set of n correlated random variables $\mathbf{X}$ with known marginal cdfs $F_x(\mathbf{X})$ and linear correlation matrix $\mathbf{R}$ with components:

$$\rho_{ij} = E\left[\left(\frac{X_i - \mu_{Xi}}{\sigma_{Xi}}\right)\left(\frac{X_j - \mu_{Xj}}{\sigma_{Xj}}\right)\right] \tag{2.86}$$

where μ_{Xi} and σ_{Xi} are the mean and standard deviation of X_i; the Nataf transformation $T : \mathbf{X} \to \mathbf{U}$ is the composition of two functions $T = T_2 \circ T_1$:

$$T_1 : X_i \longrightarrow \hat{U}_i = \Phi^{-1}\left(F_{Xi}(x_i)\right) i = 1, ..., n \tag{2.87}$$

$$T_2 : \hat{U} \longrightarrow U = \Gamma\hat{U} \tag{2.88}$$

where Φ is the standard normal cdf and Γ is the square root of the inverse of the correlation matrix R_0 (fictive correlation matrix), e.g. a Cholesky factor of R_0^{-1}.
After the transformation, the performance function becomes $g(\mathbf{U})$ and Eq. 2.89 is the new probability integration.

$$p_f = P\left\{g(\mathbf{U}) < 0\right\} = \int_{g(\mathbf{U})<0} \phi(\mathbf{U})dU \tag{2.89}$$

It should be noted that the integration in Eq. 2.89 in the standard space is identical to that in Eq. 2.85 in the physical space without any loss of accuracy, but the contours of the integrand become concentric circles (Fig. 2.11), that are easier to be integrated.
The second step to simplify the probability integration consists on the approximation of the integration boundary $g(\mathbf{U}) = 0$.FORM uses a linear approximation (the first order Taylor expansion):

$$g(\mathbf{U}) \approx L(\mathbf{U}) = g(\mathbf{U}^*) + \bigtriangledown g(\mathbf{U}^*)(\mathbf{U} - \mathbf{U}^*) \tag{2.90}$$

where $L(\mathbf{U})$ is the linearised performance function, $\mathbf{U}^*$ is the expansion point and $\bigtriangledown g(\mathbf{U}^*)$ is the gradient of $g(\mathbf{U})$ at $\mathbf{U}^*$. To minimize the accuracy loss, it is essential to expand the performance function at a point that has the highest contribution to the probability integration. The point that has the highest probability density on the performance $g(\mathbf{U})$ is the one with the shortest distance from the limit state to the origin in the standard space. The minimum distance β is called reliability index and it is shown in Fig. 2.11. In conclusion, the reliability is given by:

$$R = 1 - p_f = 1 - \Phi(-\beta) = \Phi(\beta) \tag{2.91}$$

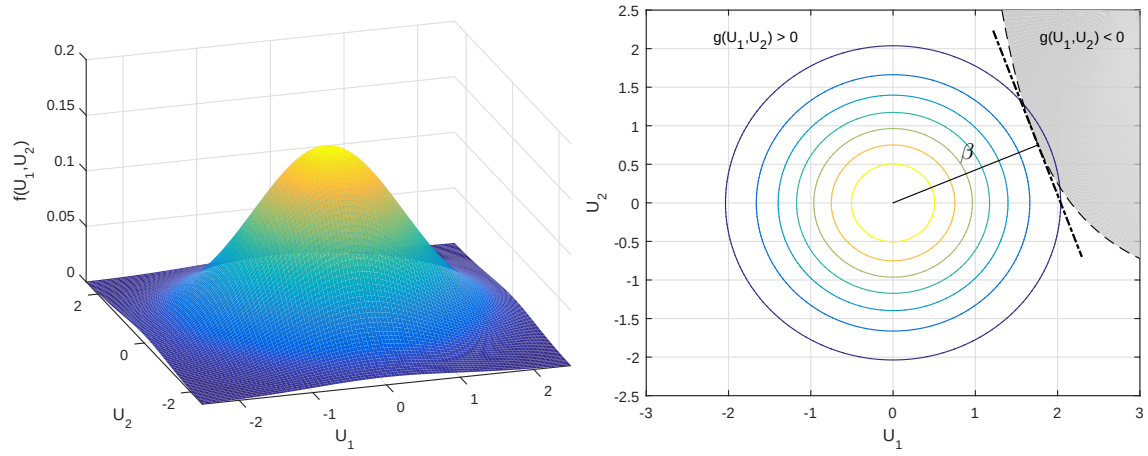

Figure 2.11: *a) Joint pdf $f_u(U_1, U_2)$, b) Joint pdf in U-plane and performance function $g(U_1, U_2) = 0$*

2.5 Image analysis

The use of image in applied science is strongly related to the human being: people look at things to identify and classify them, scan for differences, and obtain information. Image processing involves changing the nature of a digital image in order to either: i) improve its pictorial information for human interpretation; ii) render it more suitable for autonomous machine perception (e.g. for measurement or counting purposes).

Figure 2.12: *Types of digital images*

A digital image can be considered as a large array of discrete dots (x and y ranging from 1 to 256 each), each of which has a brightness $f(x, y)$ associated with it, ranging from 0 (black) and 255 (white). These dots are called pixels and the pixels surrounding a given pixel constitute its neighbourhood. Four basic types of digital images can be considered:

1. Binary: each pixel is just black (0) or white (1), so it is needed only one bit per pixel.

2. Grayscale: each pixel is a shade of grey, normally from 0 (black) to 255 (white). This range means that each pixel can be represented by eight bits, or exactly one byte.

3. RGB: each pixel has a particular colour described by the amount of red, green and blue in it. Therefore, a RGB image consists in a stack of three matrices, representing the red, green and blue values (in the range 0-255) for each pixel (it means that 255^3 different possible colours exist). The total number of bits required for each pixel is 24.

4. Indexed: most colour images only have a small subset of the 255^3 possible colours. For convenience of storage and file handling, the image has an associated colour map which is simply a list of all the colours used in that image. Each pixel has a value which does not give its colour (as for an RGB image), but an index to the colour in the colour map.

Image processing comprises a broad variety of methods mainly subdivided into three classes: i) Image enhancement, processing images so the result is more suitable for a particular application; ii) Image restoration, reversing the damage done to an image by a known cause; iii) Image segmentation, subdividing an image into constituent parts, or isolating certain aspects of an image.
Image processing has an enormous range of applications; almost every area of science and technology can make use of image processing methods.
In coastal flooding, the easiest way to model the inundated area is considering the terrain model (with only the values below the inundation height) and the shoreline position (or more generally the source of flood) as two binary images and extracting from the first only the pixels connected to the second. In order to do this, it is suitable to use the Morphological Grayscale Reconstruction algorithm described by Vincent (1993).

2.5.1 Morphological reconstruction algorithm

In the binary case, reconstruction extracts the connected components of a binary image **I** (the mask) which are marked by a binary image **J**⊆**I**. This transformation can be extended to the grayscale case, where it turns out to be extremely useful for several image analysis tasks, e.g image filtering, segmentation, and feature extraction tasks.

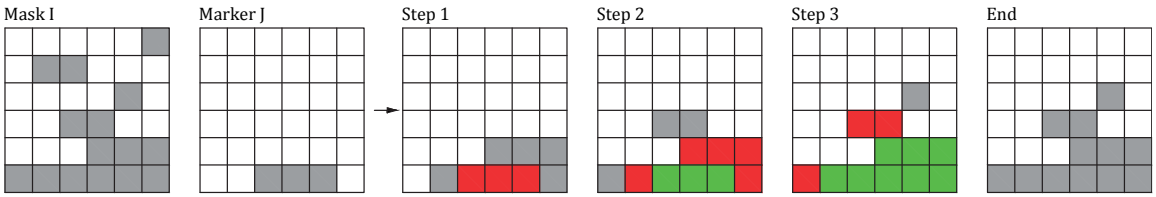

Figure 2.13: *Step in the Binary Reconstruction from markers*

Let **I** and **J** be two binary images defined on the same discrete domain D and such that **J**⊂**I**. In terms of mappings, this means that: $\forall p \in D$, **J**(p) = 1 **I**(p) = 1. **J** is called the marker image and **I** is the mask ($I_1, ..., I_n$ are the connected components of **I**).
The reconstruction $\rho_I(J)$ of mask **I** from marker**J** is the union of the connected components of **I** which contain at least a pixel of **J**:

$$\rho_I(j) = \bigcup_{J \cap I_k \neq 0} I_k \tag{2.92}$$

This simple procedure, illustrated by Fig. 2.13, gives rise to several interesting applications and extensions (erosion, dilatation of images, segmentation, etc.).

2.5.2 GPU graphic cards

Graphics processing units (GPUs) were originally developed to accelerate graphics rendering (e.g for gaming). The hardware architecture of GPUs, capable of massively parallel operations to refresh millions of pixels many times per second, rapidly attracted scientists who saw them as generic maths co-processors that could accelerate certain classes of algorithms that are intrinsically parallel.
Unlike a traditional CPU (central processing unit), which includes no more than a handful of cores, a GPU has a massively parallel array of integer and floating-point processors, as well as dedicated, high-speed memory. A typical GPU comprises hundreds of these smaller processors (Fig. 2.14). A core is a single independent computational unit within a CPU or GPU chip. CPU and GPU cores are not equivalent to each other; GPU cores perform specialized operations whereas CPU cores are designed for general-purpose programs.

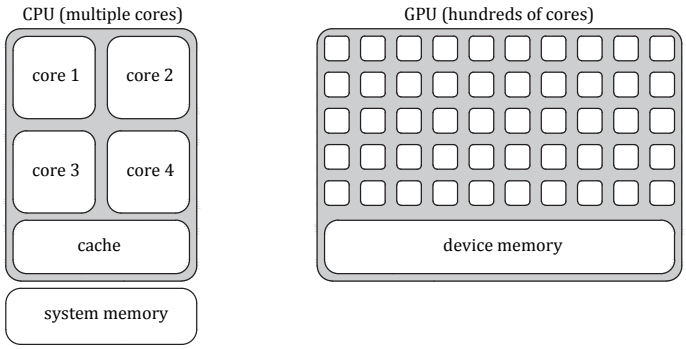

Figure 2.14: *Comparison of the number of cores on a CPU system and a GPU*

The highly parallel structure of a GPU makes them more effective than general-purpose CPUs for algorithms where processing of large blocks of data is done in parallel. Therefore, a GPU can accelerate an application if it fits both the following criteria:

1. Computationally intensive: the time spent on computation significantly exceeds the time spent on transferring data to and from GPU memory.

2. Massively parallel: the computations can be divided down into thousands of independent units of work.

Codes that do not satisfy these criteria might actually run slower on a GPU than on a CPU. In order to achieve a massively parallel code, it is beneficial to apply each computation to whole arrays instead of individual elements. This process of revising loop-based is called vectorization and it is worthwhile for several reasons: the code is easier to understand, shorter and faster. Fig. 2.15 report the execution time needed to obtain an element-wise multiplication between two arrays, i.e. $R = A * B = (a_1, a_2, \ldots, a_n) * (b_1, b_2, \ldots, b_n) = (a_1 * b_1, a_2 * b_2, \ldots, a_n * b_n)$ using a looped code and a vectorized one.

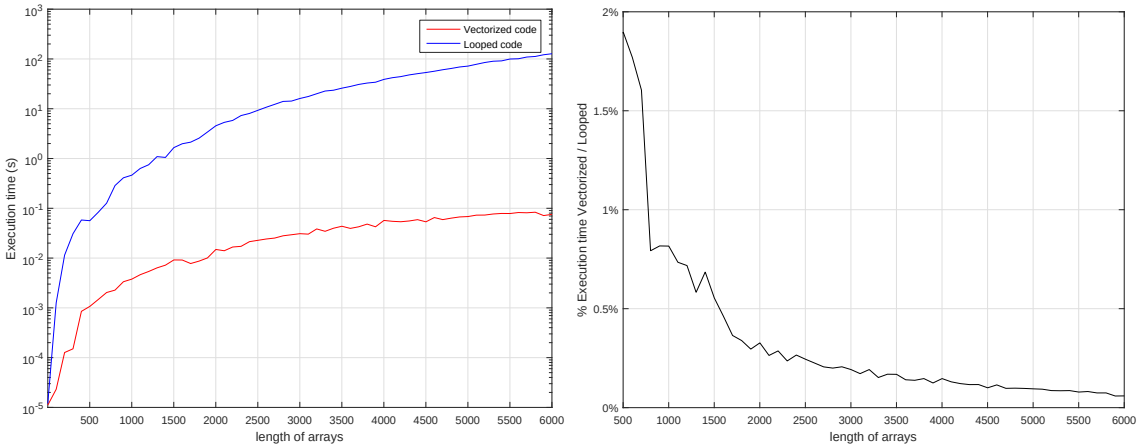

Figure 2.15: *Execution time: comparison between vectorized and looped code*

From the beginning and until now many researchers have attempted to implement GPU by using different techniques for various fields (image processing, scientific computing, health science and biological processing, database processing and signal processing).
The high memory bandwidth and floating-point throughput available in GPUs makes them potentially very attractive also for computational fluid dynamics, however, the adoption of this technology is hampered by the requirement that existing codes be re-written in specialized low-level languages such as CUDA or OpenCL that more closely map to the GPU hardware. MATLAB provides a helpful toolbox (*Parallel Computing Toolbox*, MathWorks 2018) that enable to run the code on a GPU by simply change the data type of function's input (*gpuArray*). To accelerate an algorithm with multiple simple operations on a GPU, it is possible to use $arrayfun$, which applies a function to each element of an array. Because $arrayfun$ is a GPU-enabled function, the memory transfer overhead only incurs on the single call to $arrayfun$, not on each individual operation. These functions help to speed up MATLAB operations without low-level CUDA programming.

Chapter 3

A review of existing inundation models

3.1 Introduction

The available models of varying complexity, able to produce regional scale storm surge flood maps, may be subdivided in static or dynamic. Static models, also called bathtub models, are the simplest ones to map storm surge flooding. The predicted flooded areas are those hydraulically connected to the coast and lower than the elevation of the storm surge. Due to the algorithmic simplicity of these models, the computational demand is low. A static model can be used to estimate simply and quickly storm surge flooding and impact over large regions at hyper-resolutions (Torresan et al. 2012). The model simplicity meets the stakeholder needs for a fast result and it is therefore very popular (Teng et al. 2013; Kovanen et al. 2018). However, static models obviously do not replicate some important processes of coastal flooding (Bates et al. 2005). The most important are the conservation of mass for flows and the effect of landscape roughness on the flood-water spread. The inundation extent, calculated on the basis of static models, is often substantially overestimated when compared to real flood extent observations (Gallien et al. 2014; Vousdoukas et al. 2016).

Dynamic models, also called hydrodynamic models, include a more detailed physical process representation (e.g. TELEMAC 2D, TUFLOW, DIVAST, BreZo). These models can be directly linked to hydrological and river models to provide flood risk mapping, flood forecasting and scenario analysis, and require flow hydrographs and their source locations as input dataset. Martinelli et al. (2010) applied to the Emilia Romagna coast (Italy) a procedure based on a phase-resolving model for the development of coastal flooding risk maps, although very limited in space. The risk did not account for the breaching hazard, which is a critical aspect in coastal flooding. The X-Beach model (Roelvink et al. 2009) couples the non-linear shallow water equations with a morphodynamic model that has the potential to simulate both breaching and subsequent flood propagation together, although it is computationally intensive and limited by the uncertainty related to the knowledge of dune/dike resistance. Le Roy et al. (2015) compare observations of a flooding event to numerical predictions and show the advantages of a time-dependent phase-resolving model that includes an explicit representation of the buildings and the streets, over a simulation based on a more classical approach (a digital

terrain model with no buildings, and a representation of the urban area by an increased soil roughness).

As pointed out by Teng et al. (2017), dynamics models are computationally expensive and are considered as unviable for areas larger than 1000 km^2 when the grid resolution is less than 10 m. The time taken to run simulations for these large domains may be prohibitively long. Several models have been developed aiming at reducing the computational cost by taking into account only water mass conservation (Breilh et al. 2013; Hunter et al. 2005) or some aspects of flooding hydrodynamics (Dottori et al. 2016). With advances in computing science, the performance of flooding models has improved exponentially. A recent approach to improving computational speed is parallelizing the source code (e.g. LISFLOOD-FP by Neal et al. 2009, FloodMap-Parallel by Yu 2010). The limitation of this approach is related of the available number of clusters. An alternative flood model parallelization technique utilizes Graphic Processing Units (GPUs) to achieve a far quicker time speed when compared with CPUs. Kalyanapu et al. (2011) proposed an NVIDIA CUDA GPU-based 2D dynamic flood model (Flood2D-GPU), proving that the computational speed-up ranges between 82X and 88X compared to a CPU model implementing the same numerical algorithms. The limitation of this approach is the size of the domain, due to the time needed to transfer the information between the system memory and the GPU. A simplification of the SWEs is a way to mitigate this issue.
This chapter reviews the state-of-the-art of hydrodynamic and simple conceptual models together with some Decision Support Systems *DSSs* and describes in detail some of these tools.

3.2 Hydrodynamic models

Hydrodynamic models are mathematical models that attempt to replicate/simulate fluid motion, solving equations formulated by applying physics laws. Depending on their spatial representation of the floodplain flow, the models can be dimensionally grouped into 1D, 2D and 3D models. Table 3.1 lists some typical hydrodynamic models and their developers.
The 2D models represent floodplain flow as a two-dimensional field with the assumption that the third dimension — water depth — is shallow in comparison to the other two dimensions. Most approaches solve the two-dimensional shallow water equations (Eq.s 2.55, 2.56, 2.57), which represent mass and momentum conservation in a plane, and can be obtained by depth-averaging the Navier-Stokes equations. In the following five models are briefly described.

a) LISFlood:
LISFLOOD-FP is a simplified 2D finite difference hydrodynamic model developed by Bates and De Roo (2000). The model is based on a structured grid and uses a raster Digital Elevation Model (DEM) and water inflow details to simulate flood dynamics. In the model, hydraulic continuity principles are applied to calculate water depth in each cell of the raster grid and water is routed across the terrain using a simple storage cell algorithm based on the difference in hydraulic head between adjacent cells (Bates et al. 2005). The model uses the height of the water surface above the topographic surface elevation and the Manning friction coefficient to determine flow rates. Although originally developed for riverine flooding, LISFLOOD-FP has been also applied to shallow coastal environments by Bates et al. (2005) and Dawson et al.

(2005). Bates et al. (2010) proposed to modify the LISFLOOD-FP codes to include inertial terms to represent the flow physics in particular environmental settings. This modification may allow the use of a larger stable time step, and hence quicker run times.

Table 3.1: *A review of some existing Hydrodynamic Model*

Model Name	Reference	Solving equation
JFLOW	Bradbrook (2006)	Diffusive wave
LISFLOOD-FP	Bates et al. (2010)	Dynamic wave model without advection
TUFLOW	WBM-BMT (2010)	1D or 2D Shallow water equations (SWE)
MIKE21	DHI	2D SWE
TELEMAC	Galland et al. (1991)	2D SWE or 2D SWE + a solution for vertical velocities using continuity only
BreZo	Begnudelli and Sanders (2006)	2D SWE
Flood2D-GPU	Kalyanapu et al. (2011)	2D SWE
FloodMap-Parallel	Yu (2010)	2D SWE
FLUENT/CFX	Ansys	3D Reynolds averaged Navier-Stokes Equations (NSE)

b) TUFLOW:
TUFLOW (Two-dimensional Unsteady FLOW, `www.tuflow.com`) is a one-dimensional (1D) and two-dimensional (2D) flood and tide simulation software (WBM-BMT 2010). It simulates the complex hydrodynamics of floods and tides using the full 1D St. Venant equations and the full 2D free-surface shallow water equations. TUFLOW is a computational engine that provides 2D and 1D solutions of the free-surface flow equations to simulate flood and tidal wave propagation. The engine is very stable making it a good choice for models with lots of wetting and drying. There are three main numerical models under the TUFLOW software suite:

- TUFLOW 2D: grid based and linked 1D network solver;
- TUFLOW GPU: a 2D only grid based solver using the parallel processing power of the modern GPU for fast simulations;
- TUFLOW FV: a 2D/3D flexible mesh finite volume solution.

TUFLOW is ideally suited to modelling: flooding of rivers and creeks with complex flow patterns; overland and piped flows through urban areas; estuarine and coastal tide hydraulics; inundation from storm tides and tsunamis.
Haines (2013) applied the TUFLOW model at Hexham Swamp (Australia) in order to study

the hydrological behaviour and the wetland inundation extents. Şen and Kahya (2017) employed a model consisting of the combination of Watershed Modelling System (WMS) for peak discharge determination and TUFLOW for floodplain analysis in the Rize province, located in the North-East part of Turkey (between the Black Sea and the North Anatolian Mountains).

c) Mike21:
MIKE 21 Flow Model (`www.mikepoweredbydhi.com`), developed by DHI, is a modelling system based on a flexible mesh approach. The modelling system has been developed for applications within oceanographic, coastal and estuarine environments. The Hydrodynamic module (the basis of the model) is based on the numerical solution of the two-dimensional shallow water equations (the depth-integrated incompressible Reynolds averaged Navier-Stokes equations). Thus, the model consists of continuity, momentum, temperature, salinity and density equations. In the horizontal domain both Cartesian and spherical coordinates can be used. The spatial discretization of the primitive equations is performed using a cell-centred finite volume method. The spatial domain is discretized by subdivision of the continuum into non-overlapping element/cells. In the horizontal plane an unstructured grid is used consisting of triangles or quadrilateral element. An approximate Riemann solver is used for computation of the convective fluxes, which makes it possible to handle discontinuous solutions. For the time integration, an explicit scheme is used. The application areas generally involve problems where flow and transport phenomena are important with emphasis on coastal and marine applications, where the flexibility inherited in the unstructured meshes can be utilized.
Wang et al. (2018) applied the MIKE 21 model to simulate flood magnitudes under multiple scenarios created from combinations of the key environmental factors projected to the year 2030 and 2050, in the coastal areas of Shanghai.

d) TELEMAC:
TELEMAC system (`www.opentelemac.org`) comprises two modules, 2D and 3D (Galland et al. 1991, Hervouet 2000). The first (TELEMAC 2D) solves the so-called shallow water equations, also known as the Saint Venant equations, using the finite-element or finite-volume method and a computation mesh of triangular elements. It can perform simulations in transient and permanent conditions. TELEMAC-2D is used in many fields of application. In the maritime field, particular mention may be made of harbour structure design, studies of the effect of building submersible breakwaters or dredging works, the impact of discharges from a sea outfall, study of thermal plumes; and, with regard to rivers, the impact of various types of construction (bridges, sills, groins), dam breaks, flood studies, transport of dissipating or non-dissipating tracers.
To assess TELEMAC-2D performance, Briere et al. (2007) applied the model to simulate the hydrodynamics of the Adour River and the adjacent beaches of Anglet, France. They found that TELEMAC-2D current predictions, when matched to field measurements, were within the excellent to reasonable category. Bolle et al. (2017) developed an Early Warning & Decision Support System for a port, that combined a spectral wave model, a Boussinesq type wave model and TELEMAC, for the evaluation of the hinterland flooding inside the port of Zeebrugge (Belgian coast).
TELEMAC-3D, uses the same horizontally unstructured mesh as TELEMAC-2D but solves the Navier-Stokes equations, whether in hydrostatic or non-hydrostatic mode so allowing

shorter waves than those in a shallow water context (where wavelengths are required to be at least twenty times the water depth).

e) BreZo:
BreZo (Begnudelli and Sanders 2006, Begnudelli et al. 2008) solves the shallow-water equations using a Godunov-type finite volume algorithm that has been optimized for wetting and drying applications involving natural topography and runs on an unstructured grid of triangular cells. There are several versions of BreZo as a result of an ongoing research process, and we have explored the trade-off between schemes that are formally first and second-order accurate in space and time as well as schemes that solve scalar transport equations in addition to mass conservation and momentum balance equations. This site presents a scheme for flow simulation only that is formally first-order accurate but achieves close to second-order convergence rates in flooding applications involving natural topography because the model retains a second-order representation of terrain. In field-scale applications, the depiction of terrain typically limits model accuracy. Begnudelli and Sanders (2007) present an application of BreZo in a St. Francis dam-break modelling study (California, US).

3.3 Static models

Static models are simplified conceptual models that do not involve any simulation of the physical process of inundation and are based on simplified hydraulic concepts. These models require significantly less computational effort than the hydrodynamic models. They are fast and robust, most desirable for applications that do not require velocity output and have low demands on the accuracy of flow dynamics. However, static models do not take into account either mass conservation or speed representation, producing inaccurate flooding extends.
One of these models is the Rapid Flood Spreading Method RFSM (Lhomme et al. 2008) which divides the floodplain into elementary areas that represent topographic depressions in the pre-processing and spreads the flood volumes by filling these areas using a filling/spilling process.
Teng et al. (2013) proposed another simplified conceptual model (named TVD), based on the so-called theory of "planar method" or "bathtub method". This approach derives the flood extent by intersecting a series of planes at fine intervals with a high-resolution DEM and instantly links the water stage/volume with the flood extent, maximising the usage of topographical details.

3.4 DSS Tools

A DSS is an exploratory tool that allows assessing the conditions of a system under a variety of scenarios and the consequences of different adaptation and mitigation measures. A DSS will generally integrate the relevant environmental models, database and assessment tools within a Graphic User Interface. Based on a review of a range of existing DSSs which deal with coastal areas (Table 3.2), the main objectives of these tools are: i) the analysis of vulnerability, impacts and risks, and ii) the identification and evaluation of related management options, in order to support robust decisions for sustainable management. Specifically, the objectives of the examined DSS tools address three major issues:

- the assessment of vulnerability to natural hazards and climate change;
- the evaluation of present and potential climate change impacts and risks on coastal zones and linked ecosystems, in order to predict how coastal regions will respond to climate change;
- the evaluation or analysis of management options for the optimal use of coastal resources and ecosystems through the identification of feasible measures and adequate coordination of all relevant users/stakeholders.

Table 3.2: *A review of some existing DSS tools*

Model Name	Reference	Processes
DESYCO	Torresan et al. (2016)	Sea level rise, storm surge, flooding,coastal erosion and water quality
DIVA	Hinkel (2005)	Sea level rise, storm surge, flooding, coastal erosion, wetland loss and change, and salinisation
THESEUS	Zanuttigh (2011)	Sea level rise, coastal flooding, coastal erosion and socio-economics scenario
RISK-KIT	Van Dongeren et al. (2017)	Sea level rise, coastal flooding, coastal erosion and socio-economics scenario

a) DESYCO:
The DSS DESYCO (Torresan et al. 2016) is a computerized tool developed in 2010 (as a product of the CMCC-FISR Interministerial Italian Project) with a first software release for the integrated assessment and management of different climate change impacts in coastal areas and related ecosystems (beaches, river deltas, estuaries and lagoons, wetlands, forests, protected areas, urban and agricultural areas), and then upgraded with new modules for groundwater bodies and river basins (GEMINA Interministerial Italian Project).
DESYCO was specifically designed to provide coastal managers with an easy to use software tool that can be applied to produce a spatially explicit scoping of climate risks at the regional scale. The final aim of the tool is to support a preliminary phase of risk assessment (first-pass or screening analysis), providing an integrated view of all the potential threats caused by climate change in the analysed region and fostering decision-makers (and long-term investors) in the identification of a portfolio of adaptation policies and measures.
This tool was applied to three coastal testing areas: Northern Adriatic Sea (Veneto and Friuli Venezia Giulia Regions, Torresan et al. 2012), Gulf of Gabes (Tunisia, Lamon et al. 2014) and the Republic of Mauritius.

b) DIVA:
The DIVA (Dynamic and Interactive Vulnerability Assessment, Hinkel 2005; Vafeidis et al. 2008) model is an integrated model of coastal systems that assesses biophysical and socio-economic impacts of sea-level rise and socio-economic development. One important innovation

introduced by DIVA is the explicit incorporation of a range of adaptation options; impacts do not only depend on the selected climatic and socio-economic scenarios but also on the selected adaptation strategy. Based on the relative sea-level rise, different types of biophysical impacts are assessed: dry land loss due to coastal erosion, flooding and salinity intrusion in deltas and estuaries.
Particular attention must be given to the fact that the scope and scale of the DIVA render it inappropriate for coastal management decisions due to data uncertainties associated in global and regional climate policy analyses. Nevertheless, DIVA can provide a valuable tool for highlighting areas where further in-depth analysis is necessary, thus assisting in the prioritisation of regions where coastal management at local scales is more urgently required.

c) Theseus DSS:
The conceptual model for coastal risk assessment proposed in THESEUS (Zanuttigh 2011; Zanuttigh et al. 2014, `www.theseusproject.eu/dss`) is based on the Source – Pathway – Receptor – Consequence (SPRC). The SPRC model is a simple 1D–2D conceptual model for representing flood systems and processes that lead to particular flooding consequences. Effectively, the SPRC represents how the Sources (in this case, waves, tide, storm surge, mean sea level, river discharge, run-off) through the Pathways (including, coastal defence units) affect the Receptors (buildings, infrastructure, habitats, etc.) generating economic, social and environmental Consequences. Scenarios of change will modify the consequences of flooding and, given adverse trends such as sea-level rise and increasing coastal development, will increase them. Mitigation options from a wide menu of engineering, ecological and social options can offset this increase in Consequences, and keep risk at a socially-acceptable level.
THESEUS adopts a scenario framework that considers the present situation (2010), and three future scenarios: short (2020s), medium (2050s) and long-term (2080s). In THESEUS, the coastal risk assessment is performed at a high spatial resolution using a Digital Elevation Model (DEM) to support detailed coastal management analysis of receptors, consequences and their mitigation.

d) RISK-KIT:
RISC-KIT project (Van Dongeren et al. 2017, `www.risckit.eu`) delivered a set of open-source and open-access methods, tools and management approaches to reduce risk and increase resilience to low-frequency, high-impact hydro-meteorological events in the coastal zone (the "RISC-toolKIT"). These products enhance forecasting, prediction and early warning capabilities, improve the assessment of long-term coastal risk and optimise the mix of PMP-measures. The RISC-KIT project developed the following tools to identify and prioritize the coastal zones which are most at risk:

- the Storm Impact Database of present and historic socio-economic and physical data;
- the Coastal Risk Assessment Framework (CRAF) to identify - at the regional scale (100's km) - present and future hot spot areas of coastal risk;
- the Web-based Management Guide offering innovative, cost-effective, ecosystem-based DRR measures;
- quantitative, high-resolution Hotspot Tool to evaluate the effectiveness of DRR measures

in hot spots (with a scale of 10's km);

- multi-Criteria Analysis Tool (MCA) to assess alternative DRR measures with stakeholders.

The RISC-KIT tools have been applied to 10 case study sites, which are located on each of Europe's regional seas. In particular Armaroli and Duo (2017) describes the results of the implementation of CRAF Phase 1 in the Emilia-Romagna coast (Porto Garibaldi, IT, Northern Adriatic sea).

3.5 Discussion

The review of the state-of-the-art methods presented in this chapter underlines that, over the past years, there has been vast progress in flood inundation modelling and in the availability of high-resolution data. Nevertheless, the key point is that the aim of developing and using very refined models has to be balanced against the computational demand, investment in data collection and model set-up, and the requirements of the end user. The objective highlighted by the stakeholders must be clear and sharp in order to select an appropriate modelling.
The key step is therefore to identify those processes that are relevant to a particular modelling problem and decide how these can be discretised and parametrised in the most computationally efficient manner. While hydrodynamic models are suited to represent detailed flow dynamics, to investigate impacts of tsunamis or flash floods, static models are appropriate for probabilistic flood risk assessment and multi-scenario modelling on a large floodplain.
However, there are still unanswered research questions that warrant addressing in the near future. Faster although more accurate flood propagation model represents a valued demand in this field. Another example of possible future research area includes the assessment of appropriate schemes that are capable of handling dynamic wetting and drying effects over complex, low-lying topography.
The proposed model fulfil a specific practical objective, coupling a simplified hydrodynamic model together with a probabilistic methodology, in order to map at regional scale the coastal flooding vulnerability. The simplifications, that are applied to the governing equations, are balanced with both the requirement of a fast modelling over a large domain and the need for a scientifically based result. In addition, the simplified formulation is suited to GPU acceleration, improving the computational speed.

Chapter 4

Proposed numerical model for coastal flooding

4.1 Introduction

In this chapter, the dynamic reduced-complexity model of coastal flooding is presented, that implements an appropriate vectorization method to take advantage of GPU acceleration and can be applied to hyper-resolution maps over regional scales. This model includes sufficient shallow-water physics, using the forcing data available (sea-level characteristics) to simulate flows over high-quality terrain (Digital Terrain Model). The friction term is linearised and the convective terms are considered negligible, hence the obtained SWEs formulation is ideal for GPU acceleration. The numerical method is positivity preserving, i.e. time-history of flow surface always remains non-negative throughout the simulations, to avoid instability (Khorshid et al. 2017).
Besides the description of this hydrodynamic model, this chapter presents also a static flooding model and a way to evaluate the boundary conditions. As aforementioned, the boundary conditions (i.e. the level to impose at the shoreline) for coastal flooding assessment is represented by the total water level, composed by several independent factors: astronomical tide η_A, meteorological contribution η_S, mean sea level rise and wave contribution η_W. In order to evaluate this last contribution a wave transformation model from offshore to onshore is here presented, based on the Dally et al. (1985) model for breaker decay.

4.2 GIS based wave transformation model

The wave transformation model considers the Dally et al. (1985) model for breaker decay (explained in the paragraph 2.2.4). This model is capable of describing wave transformation across beaches of irregular profile shape, that is essential to an adequate understanding of nearshore hydrodynamics (e.g. littoral currents in both the alongshore and on/offshore directions, wave induced set-down/up) and sediment transport. The wave breaking starts when $H > 0.78d$ (d is the water depth) and continues until some stable wave height is attained (usually $H > 0.4d$). Breaking would be most intense at the beginning and would decrease until the approximate stable wave height is reached.
The model solves, using a finite difference method, the Eq. 2.33 and the rate of energy dis-

sipation per unit plan area is assumed to be proportional to the difference between the local energy flux and the stable energy flux (Eq. 2.34). The numerical scheme (Eq. 4.1) describes the one-dimensional transformation of wave height over bottoms due to shoaling, breaking, reformation, and refraction, including the effects of set-up in mean water level.

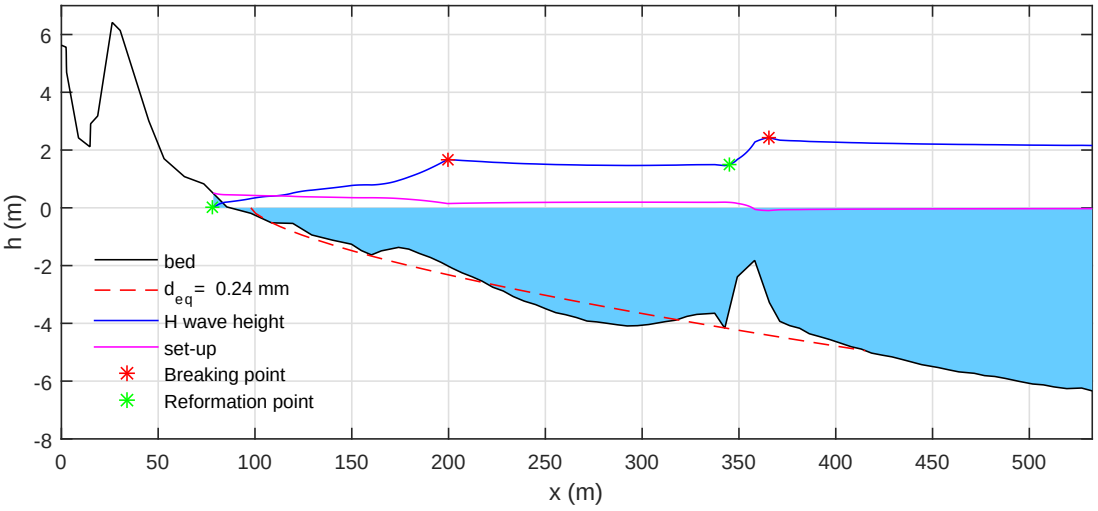

Figure 4.1: *Example of wave breaking decay over a real bottom profile (Pellestrina - Venice, IT)*

$$H_{j+1} = \sqrt{\frac{1}{c_{gj+1}b_{j+1}}\left(H_j^2 c_{gj} b_j - 0.15\frac{H_j^2 c_{gj} b_j - (0.4d_j)^2 c_{gj} b_j}{d_j}\Delta x\right)} \tag{4.1}$$

In order to evaluate the wave celerity, Hunt (1979) proposed an approximation for the dispersion relation (Eq. 2.12):

$$c^2 = gh\left[y + \left(1 + 0.6522y + 0.4622y^2 + 0.0864y^4 + 0.0675y^5\right)^{-1}\right]^{-1} \tag{4.2}$$

where $y = h(2\pi)^2/gT^2$. Fig. 4.1 shows the wave transformation over a real profile (located in Pellestrina - Venice, IT) together with the set-up/down induced by the wave. Red and green dots indicate the location where the wave breaking starts and when the wave becomes again stable (reformation). The figure reports also the "equilibrium profile" proposed by Dean (1977), for which $y = Ax^{2/3}$. The parameter A, according to Hanson and Kraus (1989), is based on the median diameter d_{50} (mm). The formulation could be inverted and adjusted to the bathymetric profile, obtaining an "ideal equilibrium diameter" d_{EQ}.
The wave transformation model has been also developed as an ArcGIS Toolbox (Fig. 4.2), using Python 2.7 and the Geoprocessing Tools from the ArcPy module, incorporating the *spatial* and *3D analysis* ArcMap extensions (ArcMap 10.4).

4.3 Simplified model for coastal flooding

Static models can be used to rapidly predict flooding areas. These tools model the hydrological connectivity to evaluate inundated areas using only raster data, without involving any

simulation of the physical process. The digital elevation model accuracy (grid cell dimension) is considerably increased in the last years, allowing a better recognizing of topographic features (e.g. dunes, structure, etc.) that bound the inundation.
Two main static model approaches (Poulter and Halpin 2008) could be established (Fig. 4.3): 1) "bathtub approach" or "*level 0*", in which a grid cell became flooded if its elevation is less than the flooding value (h_F); 2) "*level 1*", in which a grid cell was flooded only if its elevation is below h_F and it is connected to the source of inundation (i.e the shoreline in coastal flooding assessment). The first approach does not take into account the presence of topographic ridges or other features (e.g. dune or sea walls) that can separate a low-lying area from the source of flooding. Conversely, the second is a more refined approach that takes into account the presence of hydrological disconnection. Two connectivity definitions can be used; a "4-side rule" (connection only with cardinal directions), and an "8-side rule" (connection only with cardinal and diagonal directions).

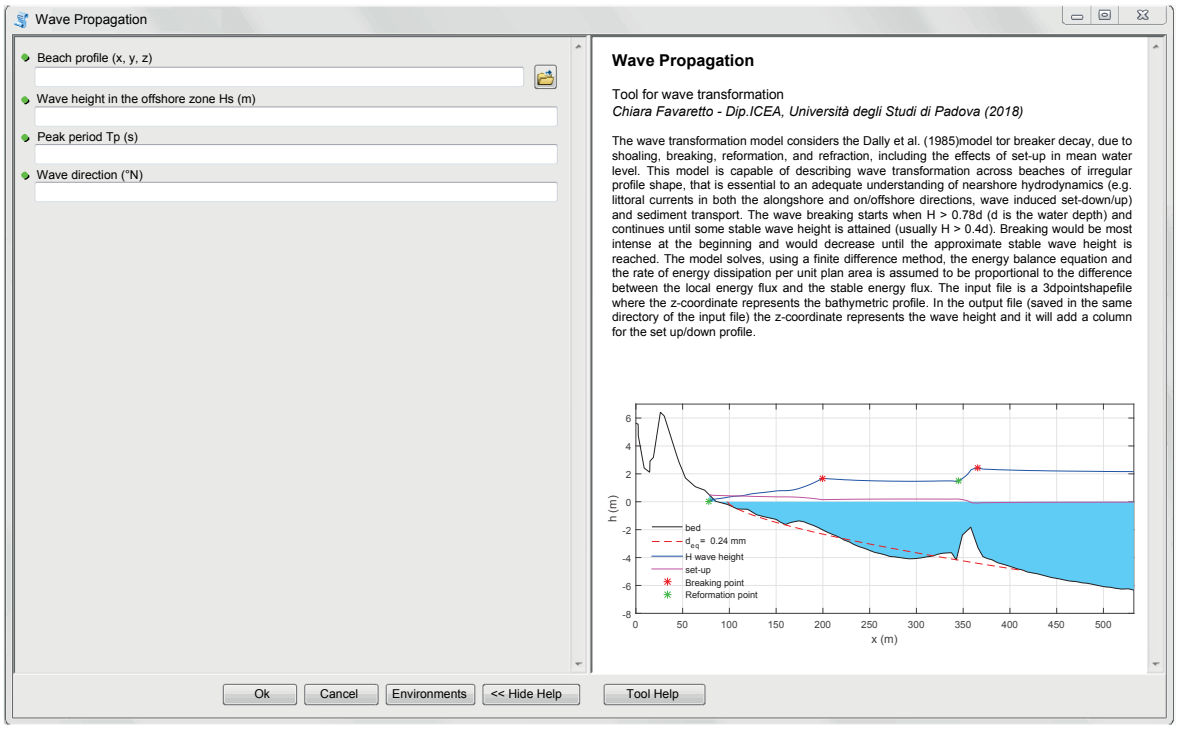

Figure 4.2: *GIS Tool: Wave breaker decay*

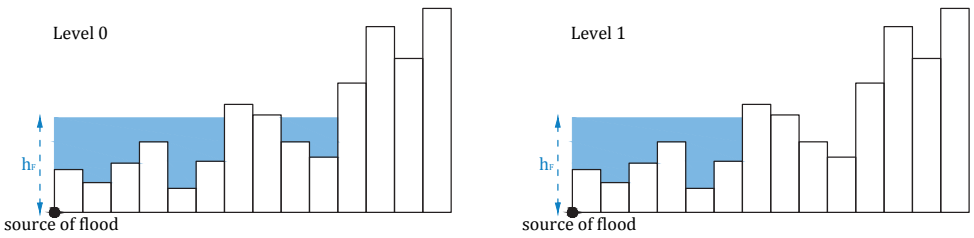

Figure 4.3: *Static model: Level 0 (left) and Level 1 (right)*

Figure 4.4-4 illustrates the flood map obtain with the level 1 approach in a real stretch of coast (Bibione, Venice - IT), including the shoreline position and the digital terrain model.

The Figure 4.4-3 is basically the results of a level 0 approach. The selection of a particular connectivity rule (4 or 8) used for raster-based flood modelling offers a potential solution to enforce connectivity and constrain flood extent. However, the selection of a connectivity routine may result in significant errors in the estimation of flooded area. A "4-sided" rule may underestimate surface flow connections because only cell sides are allowed to be connected. Conversely, the "8-sided" rule may overestimate connectivity by allowing flow to occur across cell corners.

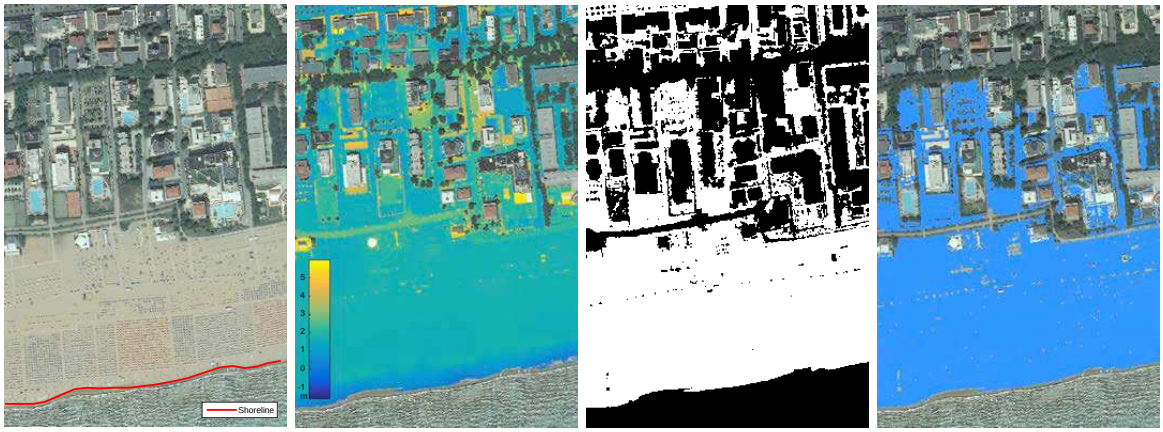

Figure 4.4: *Example of static model for coastal flooding (8-side connectivity), from left to right: 1) Ortophoto and shoreline position (red line), 2) Digital Terrain Model, 3) cell with height less than flooding value h_F equal to 2.15 m, 4) Flood map that includes only cell connected to the shoreline*

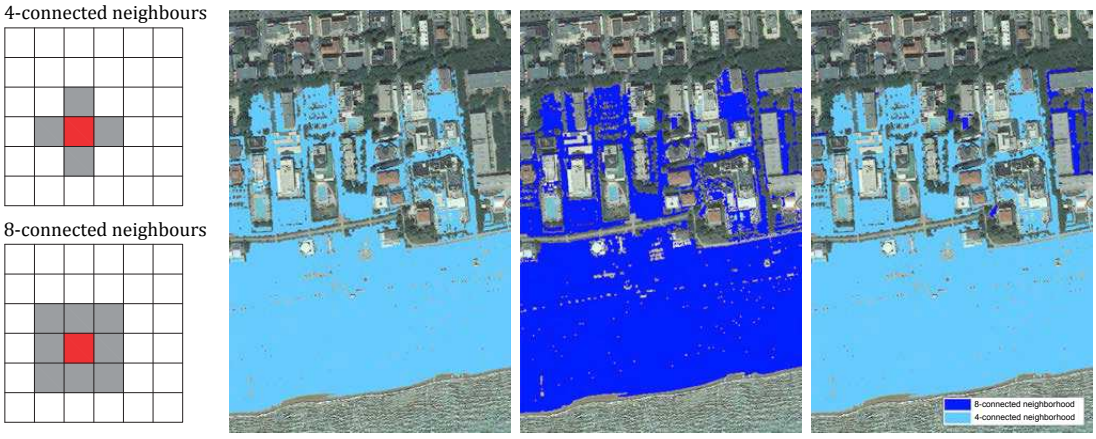

Figure 4.5: *Results considering different connectivity, from left to right:1) different types of connectivity 2) 4-connected neighbours, Area = 116'609 m^2, 3) 8-connected neighbours, Area = 120'338 m^2, 4) differences between the two connectivity*

Figure 4.5 shows the different flooded area evaluated with the 4-side rule (Area = 116'609 m^2) and the 8-side rule (Area = 120'338 m^2). The connectivity rule selected and spatial resolution of the DEM cells act together to influence the accuracy of the depiction of connectivity for different topographic surface features.
Due to the algorithmic simplicity of this model, static model can be used to estimate simply

and quickly flooding and impact over large regions. Moreover, it allows detecting the line beyond which the inland flooding begins. Figure 4.6 shows the procedure for dune and gap detection. The necessary data are the same of the level 1 static model, but it is also essential to highlight some inland point, inside a zone that cannot be inundated (Fig. 4.6-1). The first step consists on evaluating the flooded area for various h_F (Fig. 4.6-2), then it is simple to detect the first value of h_F that inundates one of the inland points. The boundary between this area and the area highlight with a smaller value of h_F is the dune (Fig. 4.6-3). Moreover, the area of the dune that is wet is a gap (Fig. 4.6-4).
Static models do not replicate important processes of storm tide flooding: i) conservation of mass for flows ii) effect of landscape roughness on the spread of flood water; iii) flood propagation only limited by topography and that maximum storm tide water levels are maintained for an infinite duration. These models are orders of magnitude faster to run than 2D or even 1D hydrodynamic models, making them useful tools for large-scale applications.
This static model, like the wave transformation model, has been developed also as an ArcGIS Toolbox (Fig. 4.7).

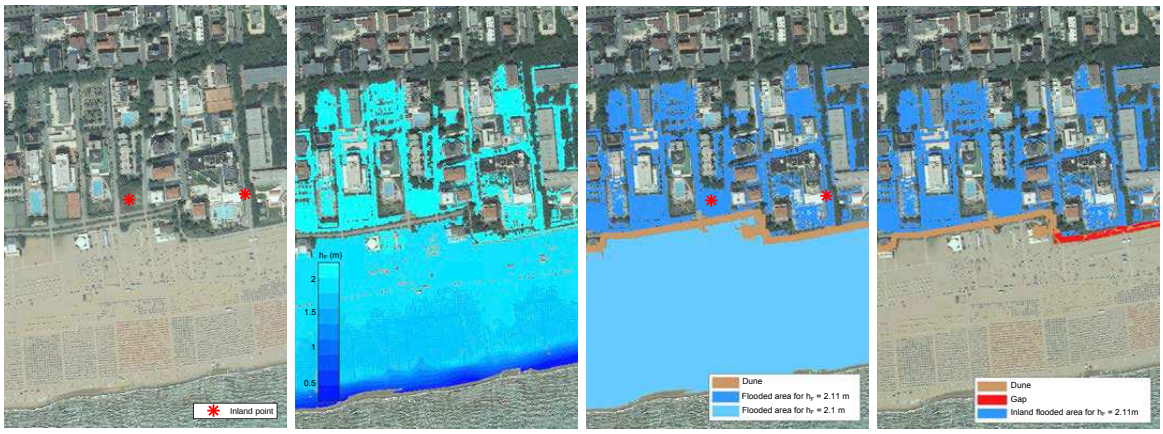

Figure 4.6: *Dune and gap detection, from left to right: 1) inland control point, 2) flooded areas for different values of flooding height h_F, 3) Detection of dune, 4) Detection of gap*

4.4 Raster based model for coastal flooding

The proposed model is a raster-based inundation model (Favaretto et al. 2018) that solves for each cell of the domain a simplified form of the shallow water equations (Eq. 4.3 and Eq. 4.4) applied in the x and y directions to simulate two-dimensional flow over a raster grid.

$$\frac{\partial w}{\partial t} + \frac{\partial q_x}{\partial x} + \frac{\partial q_y}{\partial y} = 0 \tag{4.3}$$

$$\frac{\partial q_\xi}{\partial t} + \frac{\partial (q_\xi^2 / w)}{\partial \xi} = -gh\left(\frac{\partial h}{\partial \xi} + j\right) \tag{4.4}$$

where $\xi = x$ or y. In Eq. 4.3 and Eq. 4.4 $h = w + z$ (w = water depth, z = bed elevation) is the water surface elevation and q (m^2/s) is the discharge per unit width assuming a rectangular channel. In the momentum equation (4.4) the inertial terms are included to avoid overestimated fluxes between adjacent cells and to account for the flooding duration.

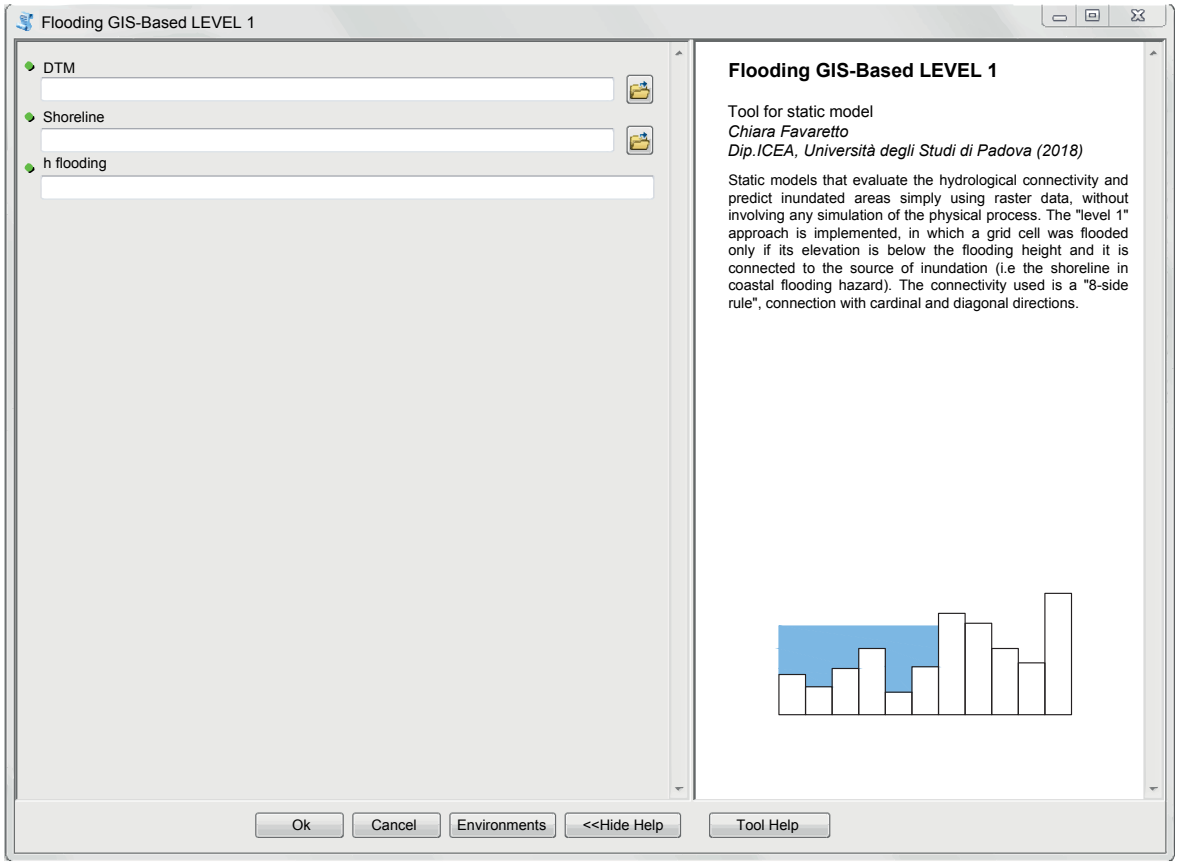

Figure 4.7: *GIS Tool: Static model for coastal flooding*

In addition, the inclusion of inertial effects may also be important to represent the flow physics in particular zones. The friction terms are important for the correct simulation of the flow propagation; however, in order to simplify the equation and to speed up the model, the friction term j is linearised. The selected formula that describes the actual friction is the Gauckler-Strickler Eq. 4.5.

$$j_T = \frac{u|u|}{K_s^2 w_F^{4/3}} = \frac{q|q|}{K_s^2 w_F^{10/3}} \tag{4.5}$$

where K_S is the Gauckler-Strickler friction coefficient ($m^{1/3}/s$). After linearisation, the friction slope j_T becomes proportional to the velocity u, assuming the form of a laminar type friction slope. The linearised friction is described by equation 4.6, a classical formulation based on the Darcy-Weisbach equation, with a coefficient K_H that accounts for the linearised turbulent friction flow.

$$j_L = \frac{K_H}{g}\frac{|u|}{w_F^2} = \frac{K_H}{g}\frac{|q|}{w_F^3} \tag{4.6}$$

where w_F is the maximum available depth that can be flow through two adjacent cells and it is defined, following Bates et al. (2010), as the difference between the highest water free surface in the two cells and the highest bed elevation (Fig. 4.8 a and b). The value of K_H can be found by equating the power lost due to friction ($< \tau q > = < \rho g w_F j q >$) estimated

with j_T (Eq. 4.7) and with the linearised one j_L (eq 4.8) for a sinusoidal wave.

$$< \rho g w_F j_T q >=< \rho g w_F \frac{q^2|q|}{K_s^2 w_F^{10/3}} >= \frac{4 g Q_{MAX}^3}{3\pi K_s^2 w_F^{7/3}} \tag{4.7}$$

$$< \rho g w_F j_D q >=< \rho g w_F \frac{K_H}{g} \frac{q|q|}{w_F^3} >= \frac{K_H}{2 w_F^2} Q_{MAX}^2 \tag{4.8}$$

$$K_H = \frac{8g}{3\pi} \frac{Q_{MAX}}{K_s^2 w_F^{1/3}} \tag{4.9}$$

where Q_{MAX} is the maximum discharge during the sinusoidal oscillation. In practice, the value of Q_{MAX} is assessed as the maximum discharge flowing through the cells.
A dimensionless form of the one-dimensional momentum equation (expressed in terms of the velocity u, Eq. 4.10) for steady state flow in a wide shallow channel can be used to understand when advective terms are significant and when the hypothesis of neglecting them is proper. Considering the friction term described by Eq. 4.5:

$$u \frac{\partial u}{\partial x} + g \frac{\partial w}{\partial x} + g \frac{\partial z}{\partial x} + g \frac{u|u|}{K_s^2 w^{4/3}} = 0 \tag{4.10}$$

Replacing depth-averaged velocity u with $u' = u/u_0$, $w' = w/w_0$, $x' = x/L$, where u_0 and u_0 and w_0 are the mean flow velocity and water depth, and L is the length scale for perturbation, and subdividing all for u_0^2/L, Eq. 4.10 becomes:

$$u' \frac{\partial u'}{\partial x'} + \frac{g w_0}{u_0^2} \frac{\partial w'}{\partial x'} + \frac{g}{u_0^2} \frac{\partial z}{\partial x'} + \frac{g L u'^2}{K_s^2 w_0^{4/3} w'^{4/3}} = 0 \tag{4.11}$$

The relative magnitude of friction to advection forces is given by a dimensionless number equal to $R = gL/K_s^2 w_0^{4/3}$. Forces induced by the advection terms dominate in presence of small scale features (which generate significant velocity spatial derivatives), but in absence, bed friction dominates over the advection terms that may therefore be neglected (Hunter et al. 2007).

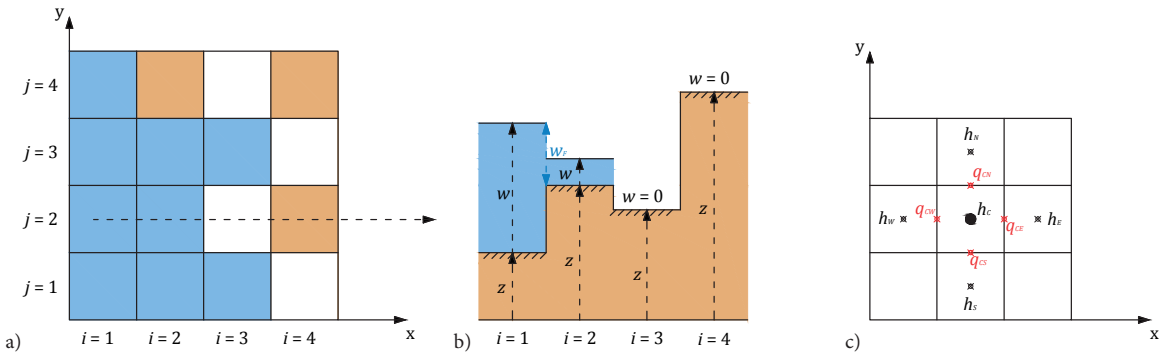

Figure 4.8: *(a) and (b) Definition of maximum available depth between two cells. (c) Water depth grid and discharge staggered grid*

Based on all the above, the final formulation of the momentum equation, only valid where the flow advection is relatively unimportant, becomes:

$$\frac{\partial q_\xi}{\partial t} + g w_F \frac{\partial h}{\partial \xi} + K_H \frac{q_\xi}{w_F^2} = 0 \tag{4.12}$$

4.4.1 Grid-based vectorization and GPU implementation

The discretization method implemented is first order in space and time (Euler scheme minimizes memory requirements), and a semi-implicit treatment is used for the friction term to improve stability. The domain coincides with the DEM, usually subdivided into square cells (area equal to $\Delta x \Delta y$) forming a regular grid; each cell (except for the boundaries cells) is connected with 4 adjacent elements called, for the sake of simplicity, North, South, East and West (N, S, E and W respectively). It is important to notice that the water depth grid is defined in the centre of a cell, whereas the discharge grid is staggered, namely it is defined in the boundaries of the cells (Fig. 4.8 c). Assuming these terminologies, the system formed by equations 4.3 and 4.12 becomes:

$$w_C^{t+\Delta t} = w_C^t - \Delta t \frac{\{(q_{CE}^t - q_{CW}^t)\Delta y + (q_{CN}^t - q_{CS}^t)\Delta x\}}{\Delta x \Delta y} \tag{4.13}$$

$$\frac{(q_{C\beta}^{t+\Delta t} - q_{C\beta}^t)}{\Delta t} = -g w_F \frac{(h_C^t - h_\beta^t)}{\Delta \xi} - K_H \frac{(q_{C\beta}^{t+\Delta t})}{w_F^2} \tag{4.14}$$

Where the subscript C denotes the cell under investigation (central cell) and β = E or W or S or N and ξ = x or y. In order to avoid the formation of oscillations in the solution, artificial diffusion can be added (relaxation technique). The discharge $q_{C\beta}^t$ can be evaluated as follows:

$$q_{C\beta}^t = \alpha q_{C\beta}^t + (1-\alpha)\frac{q_{C(\beta-1)}^t + q_{C(\beta+1)}^t}{2} \longrightarrow \text{ e.g. for } q_{CN}^t = \alpha q_{CN}^t + (1-\alpha)\frac{q_{CS}^t + q_{CNN}^t}{2} \tag{4.15}$$

where α is a weighting factor ($0 \leq \alpha \leq 1$) that adjusts the amount of artificial numerical diffusion. The discontinuities in the solution typically arise as a result of the non-linearity in the system (i.e., shocks). In practical problems, this becomes particularly necessary for low friction surfaces or problems involving fast changes of flow (an example representing a solitary wave run up on a simple beach is shown in Fig 4.9)

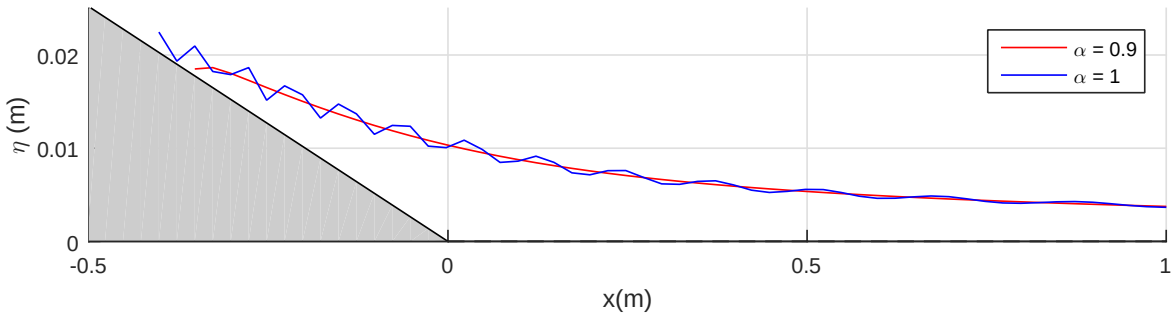

Figure 4.9: *Effect of numerical diffusion*

The numerical model is subject to the Courant–Freidrichs–Levy (CFL) condition: $CFL = V\Delta t/\Delta x < 1$. Since the advection is ignored, the characteristic velocity V is $\sqrt{gh}$.
However, this assumption is not sufficient to ensure model stability and the stable time step is often less than the one indicated by the CFL condition, therefore the flow propagation velocity is less than the simulated one. In order to preserve positivity, it is possible to limit the maximum discharge that can flow between adjacent cells, typically function of the dimension of the cell, the water depth and the time step. The positive preserving property is crucial

when in part of the domain no water is present, or when the water depth is very small, and little oscillations may lead to negative depths, eventually resulting in the simulation to fail (Khorshid et al. 2017).
In the proposed model, the discharge limitation is forced by a two-step approach: if the depth variation Δh evaluated in a cell with equation 4.13 is negative, its absolute value must be obviously less or equal to the currently available depth. If it is not (namely the cell is emptying too much due to the large time step), the "negative" volume is subtracted, to ensure continuity, from the spatially connected cells with positive balance (the procedure is shown in Fig. 4.10). The procedure used to find the connected cells is based on the "Morphological Grayscale Reconstruction algorithm" described by Vincent (1993).

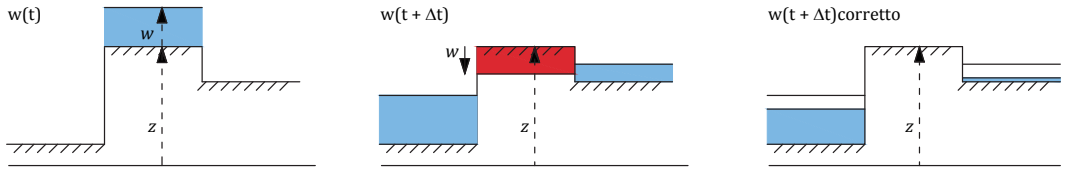

Figure 4.10: *(a) and (b) Definition of maximum available depth between two cells. (c) Water depth grid and discharge staggered grid*

Computational efficiency is one of the key issues in the application of raster-based models (or more refined hydraulic models) with Δx of order 1 – 5 m. Computational speed depends mainly on grid size and, in fact, dynamic models are often applied to coarse grid only ($\Delta x > 100m$). Furthermore, the inundated area evolves throughout the simulation in a manner that is rarely known a priori, meaning that the model domain must be very large to incorporate the flood uncertain extent.
In order to reduce the model runtime (as suggested by Brodtkorb et al. 2012; Liang et al. 2009), it was decided to write a code suitable for a GPU card in order to reduce the model run time through parallelisation. The original code was written in MATLAB and, using the Parallel Computing Toolbox with minimal code changes, the simulation can be run in parallel. The Graphic Processing Unit (GPU), used to execute the simulation, is a Nvidia Tesla K80 (4992 core, 12 GByte memory), shown in Fig. 4.11.
GPUs achieve high performance by calculating many results in parallel since each computation is processed by a different core. Furthermore, matrix and higher-dimensional array operations typically perform much better than operations on vectors or scalars.

One key requirement for using parallel technique is that the individual computations must be independent. This is true for the simplified proposed SW equations in space since each value of the dependent variable at time $t + dt$ can be found based only on the information at time t. One draw-back is that the GPU memory is separated to the system memory and time is needed for the data allocation and retrieval. In order to supply each core with the minimum possible information, it is useful to vectorise the dependent variables: all the C, N, S, E and W variables were ordered in columns of equal length. Eq. 4.16 shows the matrix that includes all the water depth at a time equal to t; vectorizing the code the allocated GPU variables becomes as illustrated below.

$$\mathbf{W}^t = \begin{bmatrix} 0 & 0 & 0 & \dots & \dots & 0 & 0 \\ 0 & w_{1,1} & w_{1,2} & \dots & \dots & w_{1,l} & 0 \\ 0 & w_{2,1} & w_{2,2} & w_{2,3} & \dots & w_{2,l} & 0 \\ 0 & w_{3,1} & w_{3,2} & \dots & \dots & \dots & 0 \\ : & : & : & : & : & : & : \\ 0 & w_{l,1} & \dots & \dots & \dots & w_{l,l} & 0 \\ 0 & 0 & 0 & \dots & \dots & 0 & 0 \end{bmatrix}^t \tag{4.16}$$

$$\mathbf{W}_C^t = \begin{bmatrix} w_{1,1} \\ : \\ w_{2,2} \\ : \\ w_{l,l} \end{bmatrix}^t \quad \mathbf{W}_N^t = \begin{bmatrix} 0 \\ : \\ w_{1,2} \\ : \\ w_{l-1,l} \end{bmatrix}^t \quad \mathbf{W}_S^t = \begin{bmatrix} w_{2,1} \\ : \\ w_{3,2} \\ : \\ 0 \end{bmatrix}^t \quad \mathbf{W}_E^t = \begin{bmatrix} w_{1,2} \\ : \\ w_{2,3} \\ : \\ 0 \end{bmatrix}^t \quad \mathbf{W}_W^t = \begin{bmatrix} 0 \\ : \\ w_{2,1} \\ : \\ w_{l,l-1} \end{bmatrix}^t$$

It is clear that for a hyper-resolution map the GPU efficiency is rather high: for domains smaller than $\sim 100'000$ cells, the CPU is faster than the GPU, conversely for very large domains (10^8 cells, typical of a regional map) the GPU time is 2-3% of the CPU time. It is therefore essential to point out that the proposed model solves the system of equations only in some pixels (extracted by a specific algorithm, based again on the Morphological grayscale algorithm) that are neighbours of wet pixels and below a limit depth (for example the height of a typical building). In this way the domain dimension increases in time but the entire run time is smaller than considering a domain where the equations are solved everywhere.

Specification	
Graphics Engine	2 GPUs - NVIDIA Tesla K80
Interface Type	PCI Express 3.0 x16
API Supported	OpenCL, DirectCompute
n° CUDA Cores	4992
Power Consumption	300 Watt
Memory Size	24 GB
Memory Bandwidth	480 GBps
Memory Technology	GDDR5 SDRAM

Figure 4.11: *Nvidia Tesla K80 GPU*

Chapter 5

Model validation

5.1 Introduction

The present inundation model is tested with two analytical solution of the shallow water equation, that represents benchmarks in the hydraulic modelling; then the model is checked against the experimental investigation of Synolakis (1987) for a solitary wave run-up on a simple beach and the experimental investigation of Briggs et al. (1995) for solitary wave interaction around a circular island. Finally, the model is applied to a real storm occurred in 2008 at the Venetian littoral.
To assess the quality of the model fit, the performance metrics provide a quantitative and aggregate estimate of model reliability. The indexes utilized (and presented in paragraph 2.3.1) are: the coefficient of efficiency NSE (Eq. 2.74, Nash and Sutcliffe 1970), the index of agreement D (Eq. 2.75, Willmott et al. 1985) and the root-mean-square error $RMSE$ (Eq. 2.76).

5.2 Non-breaking wave over a horizontal plane

The full Saint Venant equations (written in 1D from) describing the propagation of a non-breaking wave over a horizontal plane can be simplified to yield an ordinary non-linear differential equation. This is not a true analytical solution to the inertial equation solved by the model although at fine grid resolutions it should be a close approximation.
Basically, imposing the fluid velocity constant ($u = \text{cost}$) equation 4.3 becomes the well-known advection equation in h, with solution $h(x,t) = h(x - ut)$. The equation 4.12, setting the bottom slope equal to zero, becomes an ordinary differential equation that can be solved analytically to provide a test for the numerical model 5.1.

$$w(x,t) = \sqrt[3]{3}\sqrt[3]{C - K_H u(x - ut)} \tag{5.1}$$

C is a constant of integration, which can be fixed by referring to the initial conditions of the problem (i.e. w in $x = 0$ e $t = 0$). The analytical solution is compared with the numerical results (Fig. 5.1) obtained in $t = 60$ min with 6 different grid size ($dx = 2$ m, $dx = 5$ m, $dx = 10$ m, $dx = 25$ m, $dx = 50$ m, $dx = 100$ m).
In Table 5.1 the performance metrics are evaluated for each case, and they show a good agreement with the analytical solution.

Table 5.1: *Performance metrics for the solution of a non-breaking wave over a horizontal plane*

dx	2 m	5 m	10 m	25 m	50 m	100 m
NSE	0.9667	0.9607	0.9467	0.9275	0.9203	0.9261
D	0.9913	0.9893	0.9851	0.9795	0.9776	0.9799
RMSE	0.0355	0.0423	0.0534	0.0728	0.0866	0.0941

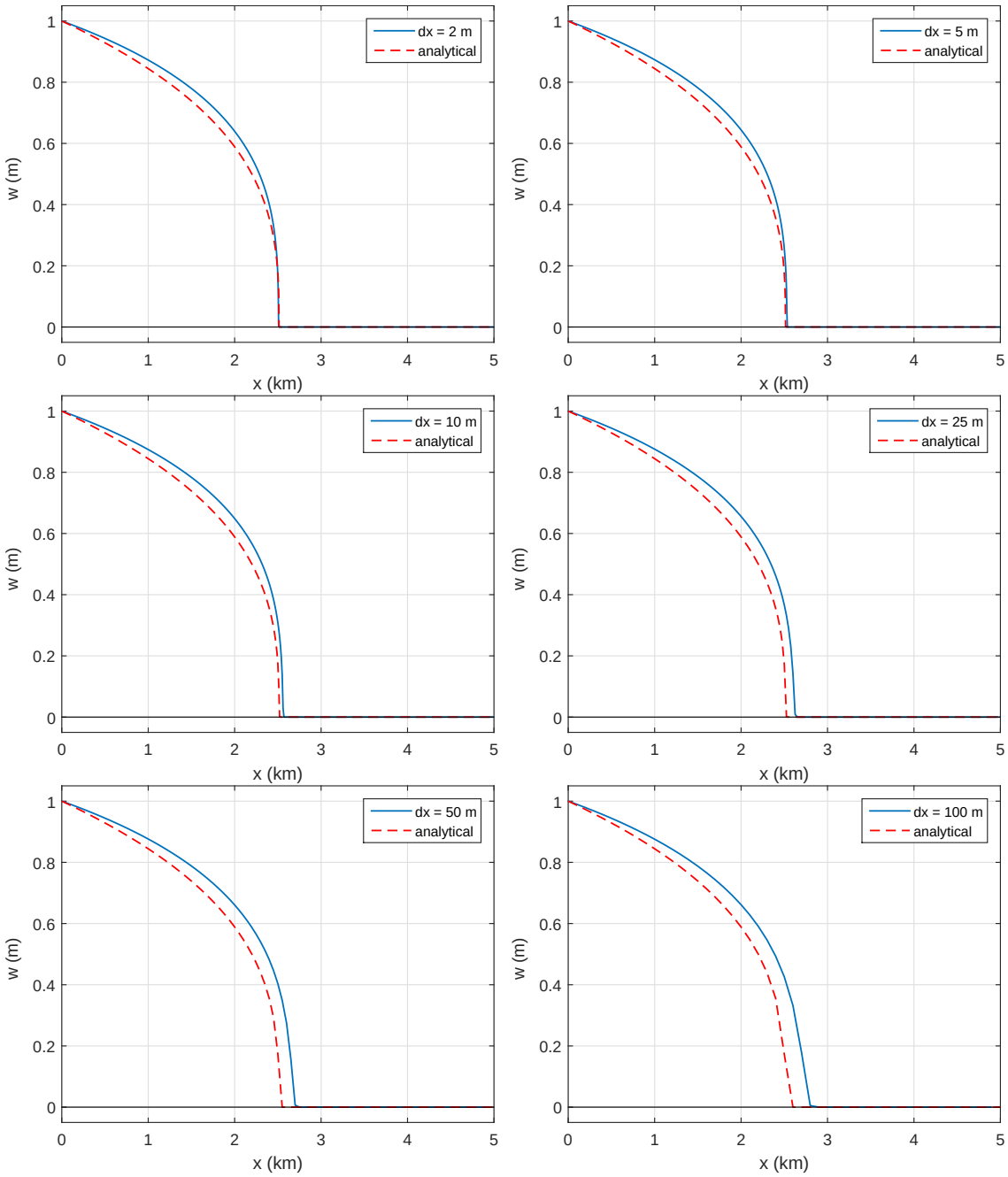

Figure 5.1: *Water-surface profiles for the inundation of a horizontal plane predicted by the model and compared with the analytical solution at t = 60 min, with 4 different grid size*

5.3 Planar surface in a parabola with friction

Considering a linear friction term ($j = u/g$) in the momentum equation 4.12 with Thacker's approach (Thacker 1981), Sampson et al. (2006) got moving boundaries solutions with damping. These solutions provide a set of 1D benchmarks for numerical techniques in wet/dry transitions on varying topographies and with a friction term. One of these solutions regards an oscillatory flow in a parabolic bowl. Wang et al. (2011) extended to 2D the analytical frictional flow. This test case is useful to prove if the model is able to simulate the wet and dry interface over a very large domain (the basin has a diameter equal to 10 km).
The topography is described by Eq. 5.2 where h_0 and a are two parameters and $x \in [-L; L]$. The initial free surface is planar and given by Eq. 5.3:

$$z(x, y) = h_0 \frac{\left(x^2 + y^2\right)}{a^2} \tag{5.2}$$

$$h(x, y, t = 0) = h_0 - \frac{B^2}{2g} - \frac{1}{g} Bsx - \frac{1}{g} B \frac{\tau}{2} y \tag{5.3}$$

where B is a constant, $s = \sqrt{p^2 - \tau^2}/2$ and $p = \sqrt{8gh_0/a^2}$.
The surface remains planar in time and the velocity is assumed uniform. The analytical solution is described by:

$$\begin{aligned} h(x, y, t) =& h_0 - \frac{B^2}{2g} e^{-\tau t} - \frac{B}{g} e^{-\tau t/2} \left(\frac{\tau}{2} \sin st + s \cos st \right) x \\ & - \frac{B}{g} e^{-\tau t/2} \left(\frac{\tau}{2} \cos st + s \sin st \right) y \end{aligned} \tag{5.4}$$

Fig. 5.2 shows the numerical results against the analytical solution in terms of water surface profile along the x-direction centreline at t = 3, 45, 60, 70, 80, 180 min. The computational domain is assumed to be 5000m × 5000m (L = 5000 m) and discretized by a 200 × 200 uniform grid; the constants are set to a = 3000 m, h_0 = 10 m, τ = 0,001 s^{-1}, B = 5 m/s.
The main differences are due to a different assumption in the velocity field: in the numerical model, the velocity is not uniform, in the analytical solution it is uniform. Fig. 5.3 shows the left and right positions of the shoreline during time. The oscillating behaviour is similar to the one described by the analytical solution.
Table 5.2 reports the indexes of performance of this benchmark during time; the worst performance occurs in the first part of the simulation since the run-up is not well reproduced, probably due to friction.

Table 5.2: *Performance metrics for the solution of a planar surface in a parabola with friction*

t	3 min	45 min	60 min	70 min	100 min	180 min	TOT
NSE	0.9961	0.9972	0.9975	0.9986	0.9989	0.9988	0.9978
D	0.9990	0.9993	0.9994	0.9997	0.9997	0.9997	0.9995
RMSE	0.3512	0.2757	0.2628	0.1925	0.1705	0.1834	0.2393

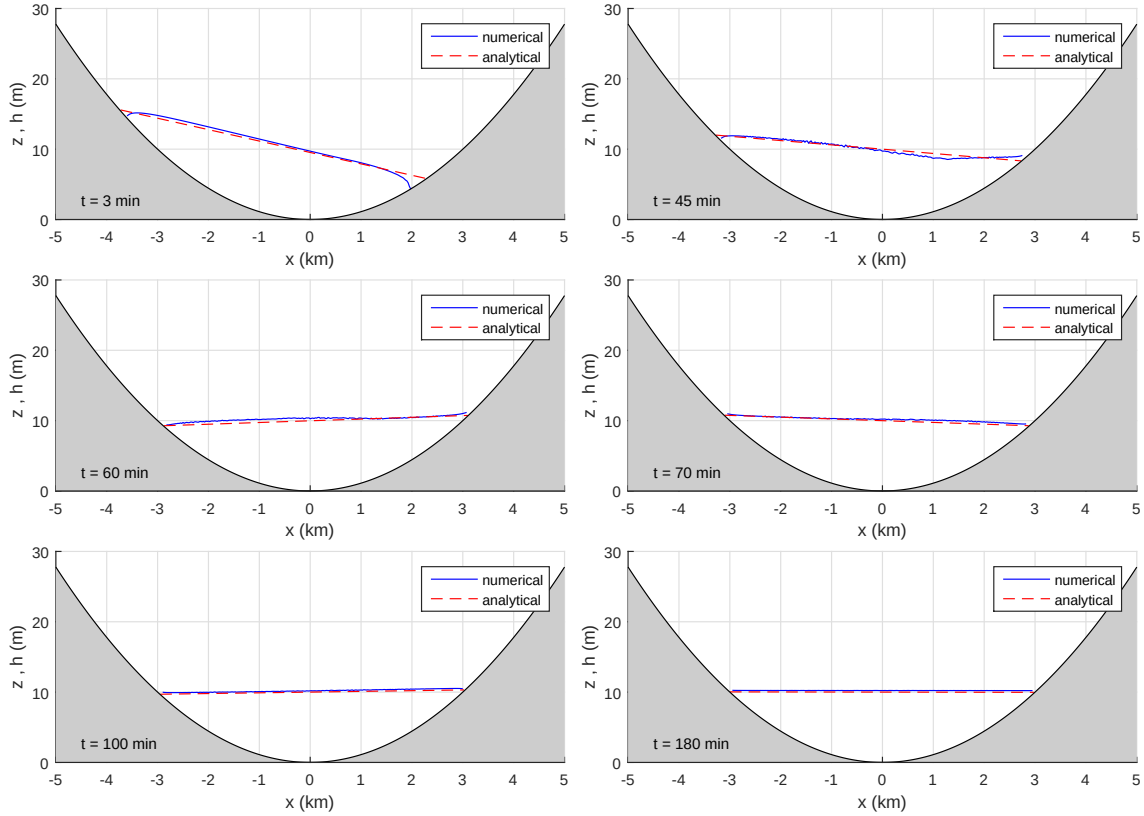

Figure 5.2: *Water-surface profiles of a planar surface in a parabola predicted by the model and compared with the analytical solution at different time*

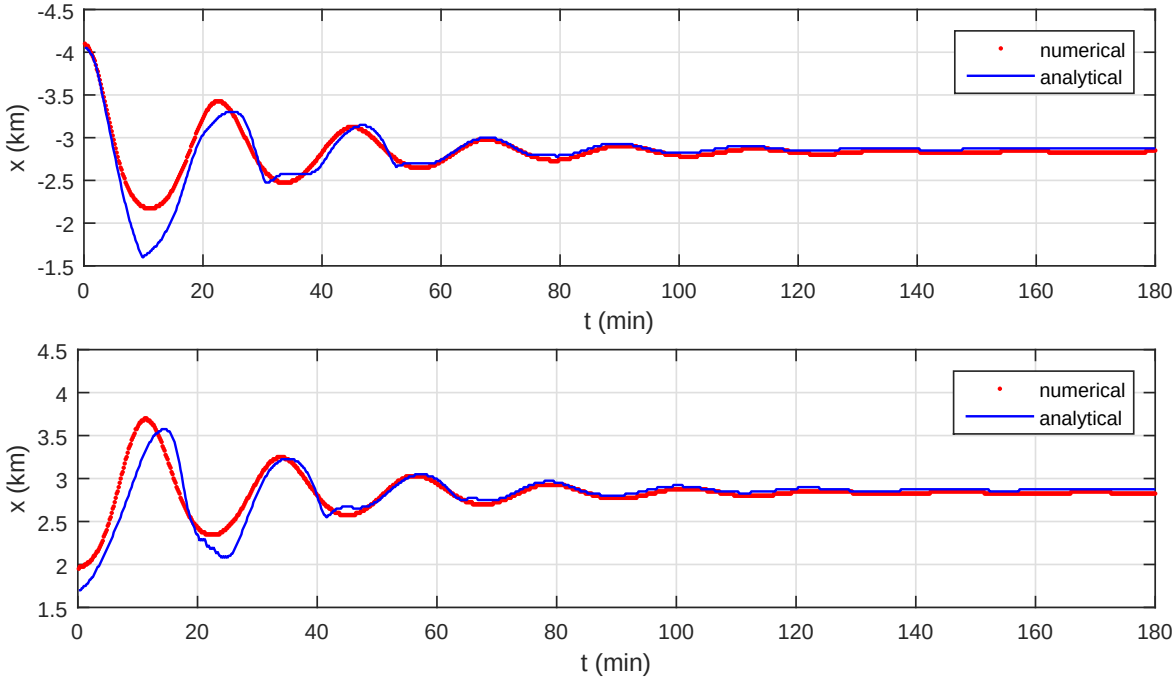

Figure 5.3: *Left and right shoreline position during time of a planar surface in a parabola predicted by the model and compared with the analytical solution*

5.4 Solitary wave on a simple beach

Synolakis (1987) carried out a set of 40 experiments in order to investigate the solitary wave run-up on coastal beaches. This set of laboratory data has been used extensively for code validation, e.g. Synolakis (1987), Grilli et al. (1997), Li and Raichlen (2002), also because the characteristic length scale of the phenomena is small. The common approximate solution for the solitary wave profile by Boussinesq (1871) is:

$$\eta = Hsech^2(\gamma X) \tag{5.5}$$

where H is the wave height, γ is a coefficient equal to $\sqrt{3H/4h^3}$, $X = ct - \xi$ (ξ is the wave-maker position), and the wave celerity is defined as $\sqrt{g(d+H)}$.
The experimental investigation was conducted in a 25 m long wave flume (California Institute of Technology, Pasadena), formed by a 15 m long flat bed and a 10 m long uniform sloping beach with a slope ratio of 1:19.85 as presented in Fig. 5.4.

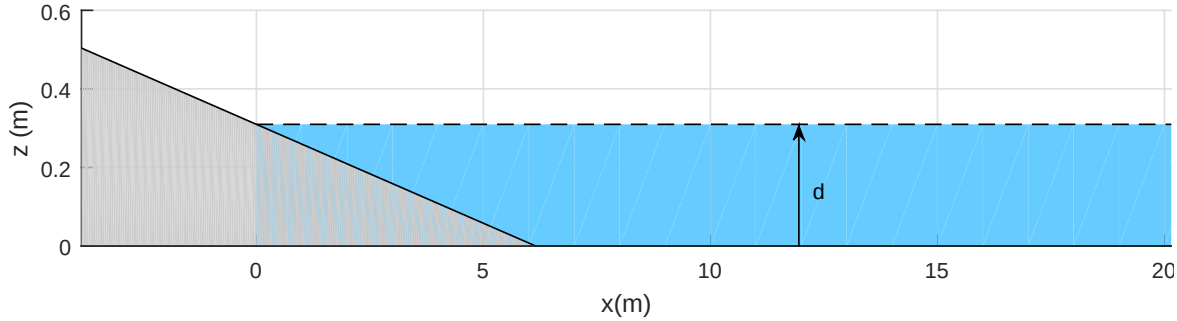

Figure 5.4: *Solitary wave on a simple beach, $H/d = 0.0185$*

For the numerical simulation 15 tests (i.e. all the non-breaking waves) of the 40 experiments carried out by Synolakis (1987) are considered. For the test with $H/d = 0.0185$ and $d = 0.3097$ m, the profile of the solitary wave propagation over the slope for 5 time steps is illustrated in Fig. 5.5, where t^* is a dimensionless time equal to $t/\sqrt{h/g}$. The scale of the figures is enhanced and distorted.
The numerical simulation well predicted the shape of the solitary wave propagation and the wet and dry interface on the sloping beach. The run-up is under-estimated at $t^* = 50$, this difference may be due to the effect of convection that is not included in the proposed numerical model. The wave run-down process begins after the wave reaches its maximum run-up position (at $t^*= 64$). At the beginning of this process the water retreats as the trailing edge of the solitary wave continues to propagate toward the slope. This retreating flow interacts with the wave tail and creates a region of large free surface curvature near the initial shoreline position. In this region, the NLSW assumption that the horizontal velocity is constant with depth is no longer valid. Moreover, in this run-down phase, some oscillations occur after $t^* = 60$ in the numerical solution.
Synolakis (1987) derived a run-up law for non breaking waves, that depends on the water height, wave amplitude, and the angle of the sloping beach.

$$\frac{R_{MAX}}{d} = 2.831(cot\beta)^{1/2}\left(\frac{H}{d}\right)^{5/4} \tag{5.6}$$

where β is the beach angle.

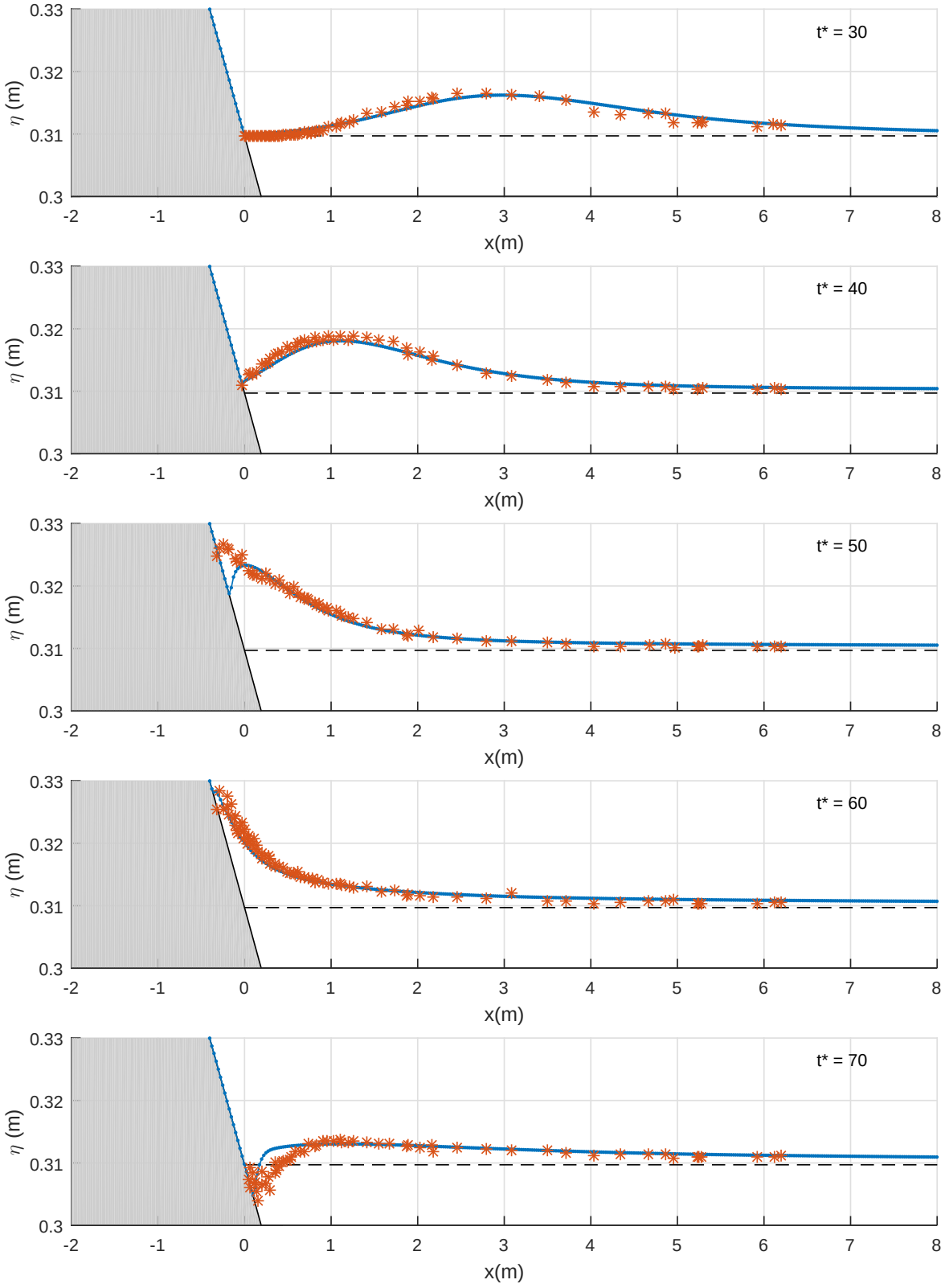

Figure 5.5: *Solitary wave on a simple beach, $H/d = 0.0185$, markers show experimental results of Synolakis (1987), blue lines show numerical solution*

Fig.5.6 shows the relative maximum run-up R_{MAX} of all the 15 non breaking solitary waves, collected by Synolakis (1987). The values plotted in this figure are summarized also in Table 5.3, where R_{Lab} are the laboratory data, R_{num} are the numerical results and R_{Syn} are the results obtained by Synolakis formula.
Close agreement among the run-up law equation (Eq. 5.6), the selected experimental data and the current simulation results is observed.

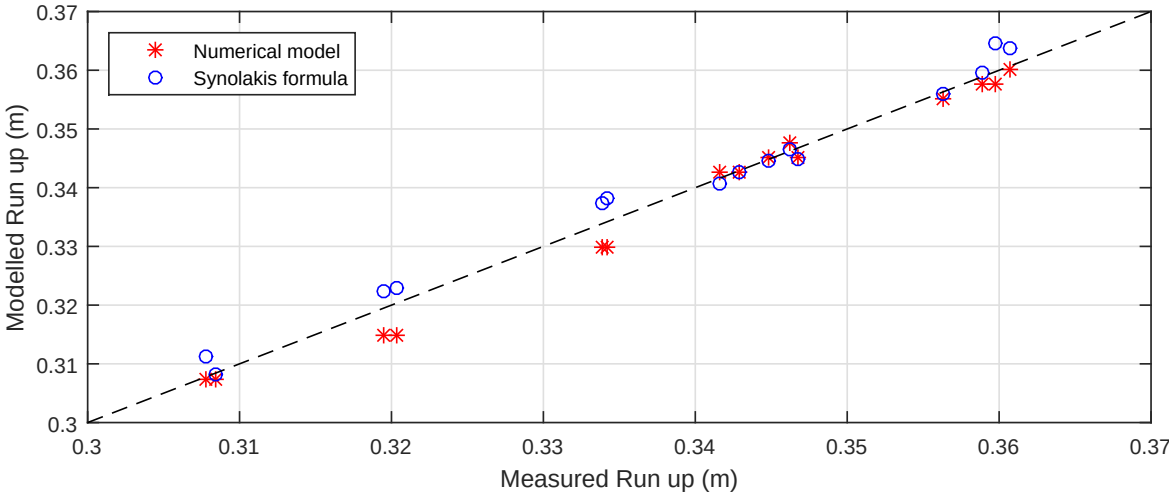

Figure 5.6: *Relative maximum run-up R_{MAX} for non-breaking waves*

Table 5.3: *Laboratory data of runup of solitary waves up a 1 : 19.85 beach, Synolakis (1987)*

H/d	d (m)	R_{Lab} (m)	R_{Num} (m)	R_{Syn} (m)	H/d	d (m)	R_{Lab} (m)	R_{Num} (m)	R_{Syn} (m)
0.014	0.2934	0.3078	0.3073	0.3112	0.006	0.3355	0.3429	0.3426	0.3426
0.018	0.2975	0.3195	0.3149	0.3222	0.007	0.3361	0.3448	0.3451	0.3447
0.009	0.2977	0.3084	0.3073	0.3081	0.008	0.3365	0.3463	0.3476	0.3467
0.018	0.298	0.3203	0.3149	0.3228	0.017	0.3384	0.3597	0.3577	0.3646
0.019	0.3097	0.3339	0.33	0.3373	0.012	0.3424	0.3588	0.3577	0.3596
0.019	0.3106	0.3342	0.33	0.3382	0.014	0.3429	0.3607	0.3602	0.3637
0.009	0.3331	0.3468	0.3451	0.3447	0.009	0.3439	0.3563	0.3552	0.3559
0.005	0.3352	0.3416	0.3426	0.3408					

5.4.1 Evaluation of advection term

In order to evaluate the magnitude and the effects of the advection term in the equation 4.4, this simulation is re-run taking into account this term.

Fig. 5.7 shows the mean relative magnitude $m*$ of the advection term during the propagation of the solitary wave on a slope beach. The $m*$ is defined as follows:

$$m* = \frac{q_{advection}}{q_{inertial} + q_{friction} + q_{bed}} \tag{5.7}$$

Fig. 5.8 shows the maximum value of $m*$ along a portion of the beach profile (near the shoreline). The advection effects occur only during the run up process, in fact it is significant only in the initially dry area.
Fig. 5.9 shows the comparison between the numerical results with and without the advection term. The results obtained considering the advection term simulate more precisely the maximum run-up on the sloping beach, since forces induced by advection and non-linear effects become more important as the run-up process proceeds. The length scale is very small in this test, proving that the improvement including avdective term for larger scale will be not significant.

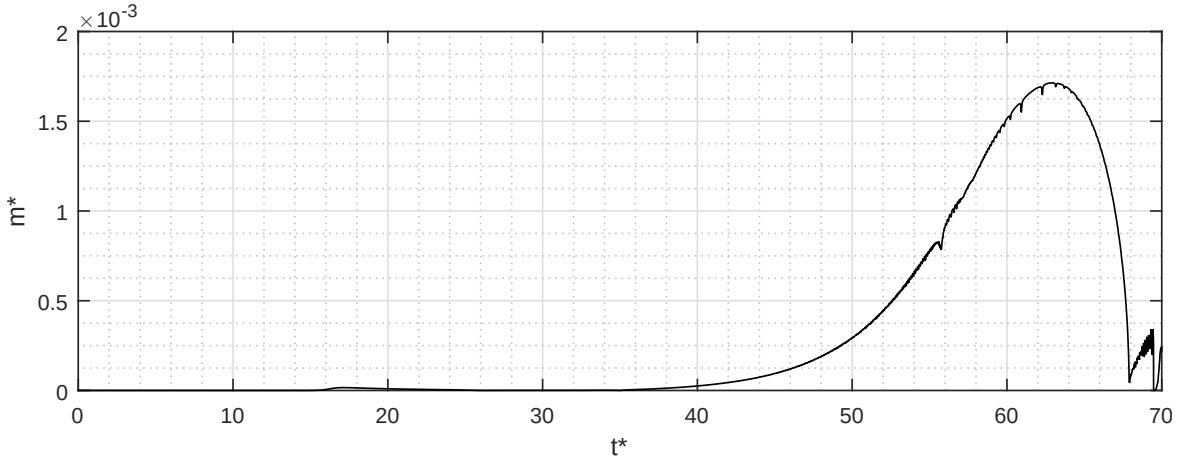

Figure 5.7: *Mean relative magnitude of the advection term in time*

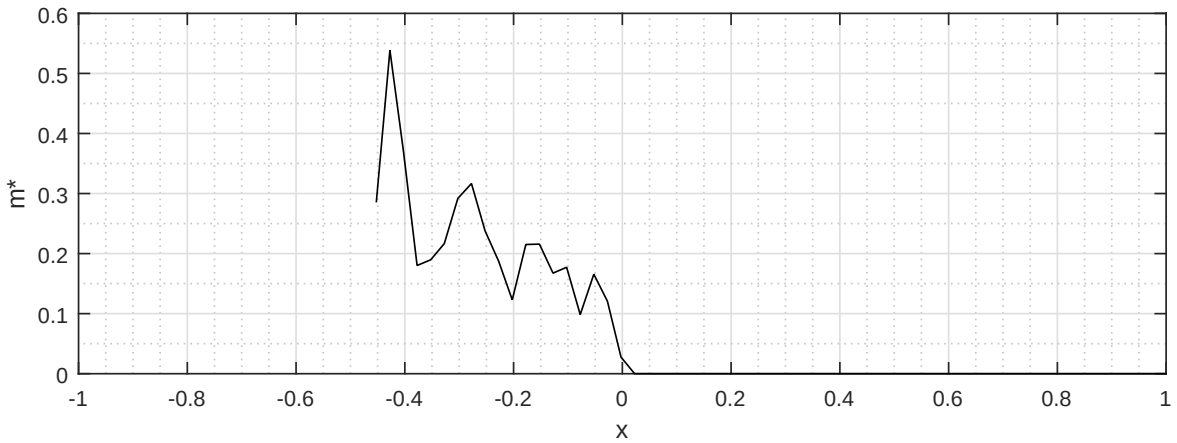

Figure 5.8: *Maximum relative magnitude of the advection term in space*

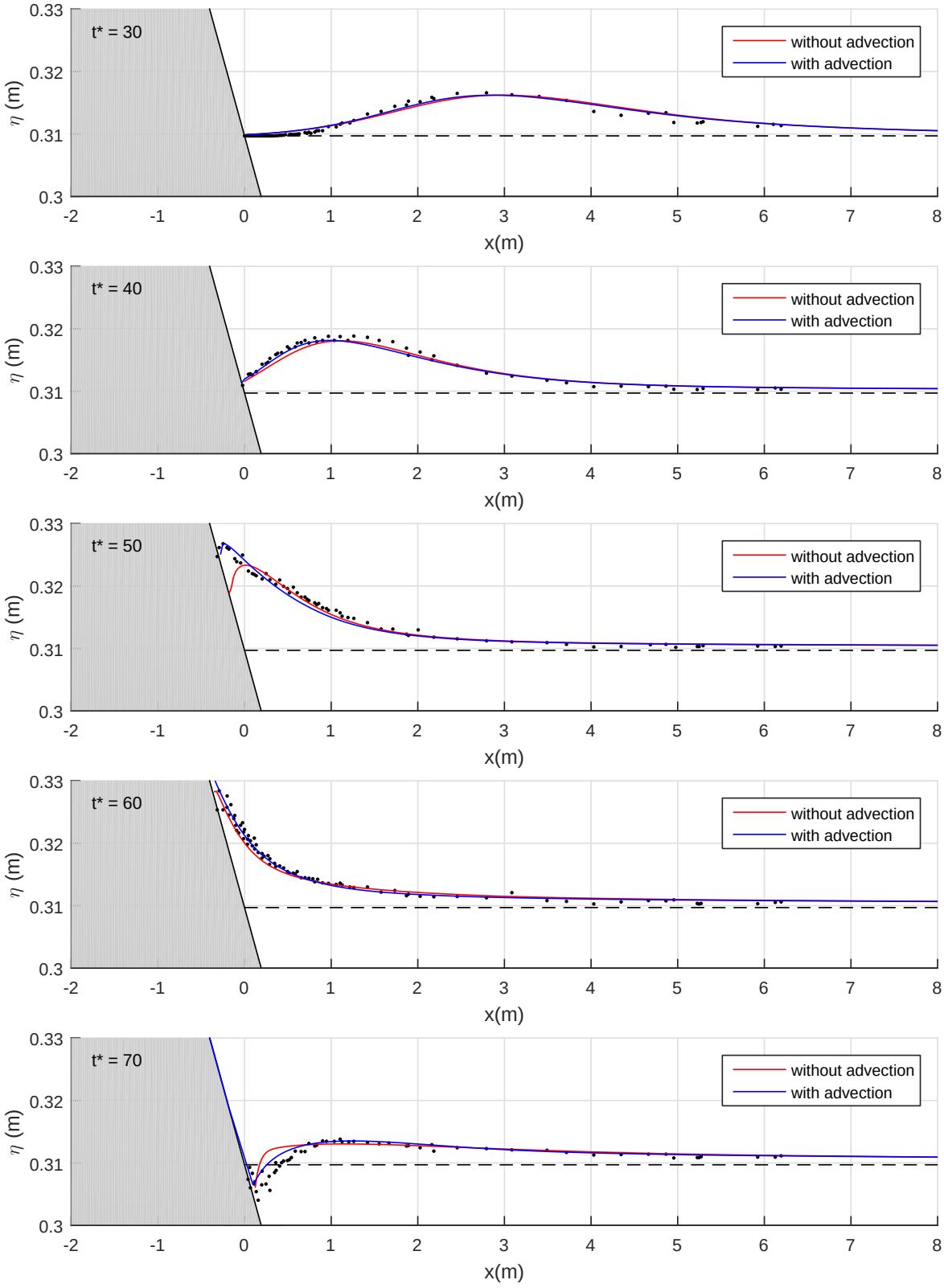

Figure 5.9: *Solitary wave on a simple beach, $H/d = 0.0185$, with and without advection, dots show experimental results of Synolakis (1987)*

5.5 Solitary wave run-up on a conical island

In this paragraph, the model validation with reference to the experiments of Briggs et al. (1995) for solitary wave interaction around a circular island is presented. This test case is frequently used as a benchmark in numerical modelling (Lynett et al. 2002, Tavakkol and Lynett 2017).
The experimental setup is partially shown in Fig. 5.10 (right): a conical island (diameters = 7.2 m at the toe and 2.2 m at the crest) was built in the centre of a 30 m wide by 25 m long flat-bottom wave basin. The slope of the island is 1:4 and the water depth is 0.32 m. Three cases with target relative wave heights of H/d = 0.05, 0.10, and 0.20 were simulated by a directional spectral wave generator and the surface elevation on 27 gauges was recorded (locations of the gauges are shown in Fig. 5.10, right). The numerical domain replicates the same dimensions of the physical model. It is discretized by 1297 x 1382 cells, with a constant time step of 0.002 s. The initial condition in the Southern boundary is the velocity at the wave paddle obtained from the measured displacement of the wave generator (Fig. 5.10, left).

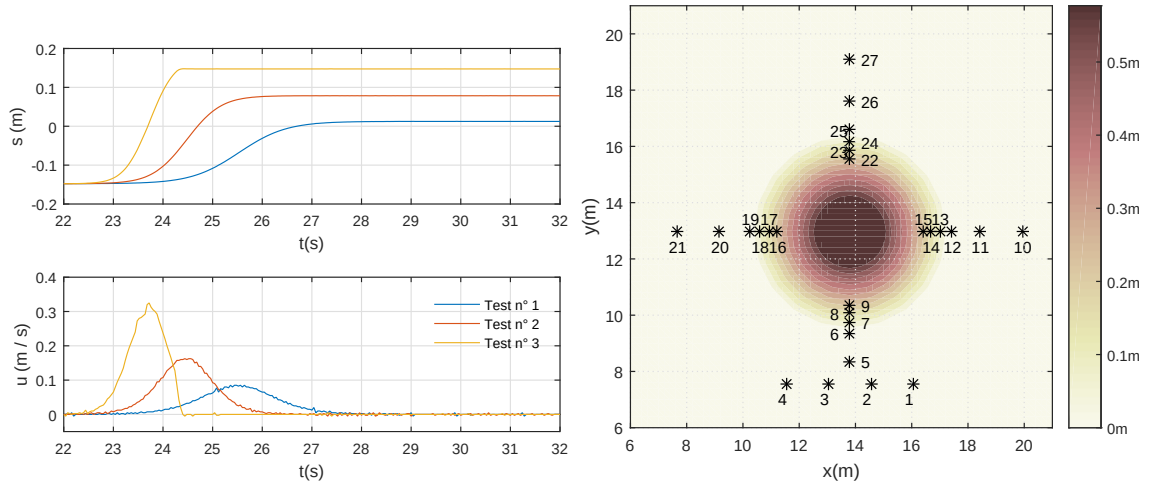

Figure 5.10: *Command for the paddle movement and time histories of velocity at wave paddle (left), top view of the wave basin and location of wave gauges (right)*

Fig. 5.14, Fig. 5.15 and Fig. 5.16 show the numerical surface elevation compared to the experimental results. The wave height, the wave shape and the arrival time are well predicted in all tests, as proved by the performance indexes described in the following. The draw-down is also well simulated for two cases (those with smaller wave heights). The run-up on the back face, generated by the collision of waves wrapping around the island, and the wave elevation at gauge no. 22 are underestimated. Possibly, the discrepancy between experiments and numerical results at wave gauge no. 22 is due to the inaccurate representation of the boundary condition of the experiments, and due to the helicoidal motion of the flow induced by friction at the island, which cannot be well represented by a vertically averaged velocity.
Snapshots of the numerical simulation for the three cases are shown in Fig.s 5.11 - 5.13. The cases a), b) and c) show the wave at different time steps, so that it is possible to visualize the wave propagation behaviour. Due to nonlinear effect, the wave celerity is also larger than for the other cases. The run-up and the reflection/diffraction pattern is also visible.

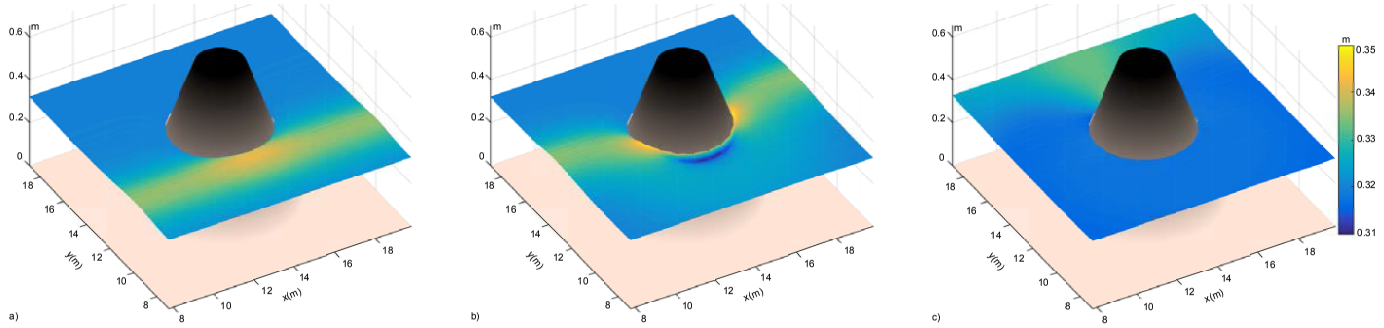

Figure 5.11: *Solitary wave run-up on a conical island, snapshots test n°1: a) front face t = 31s, b) front face t = 33s ,c) back face t = 37s*

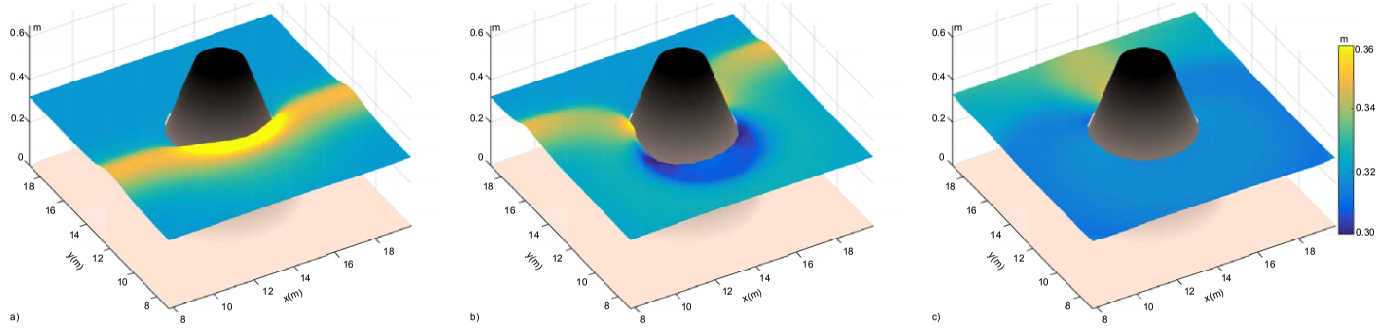

Figure 5.12: *Solitary wave run-up on a conical island, snapshots test n°2: a) front face t = 31s, b) front face t = 33s ,c) back face t = 35.6s*

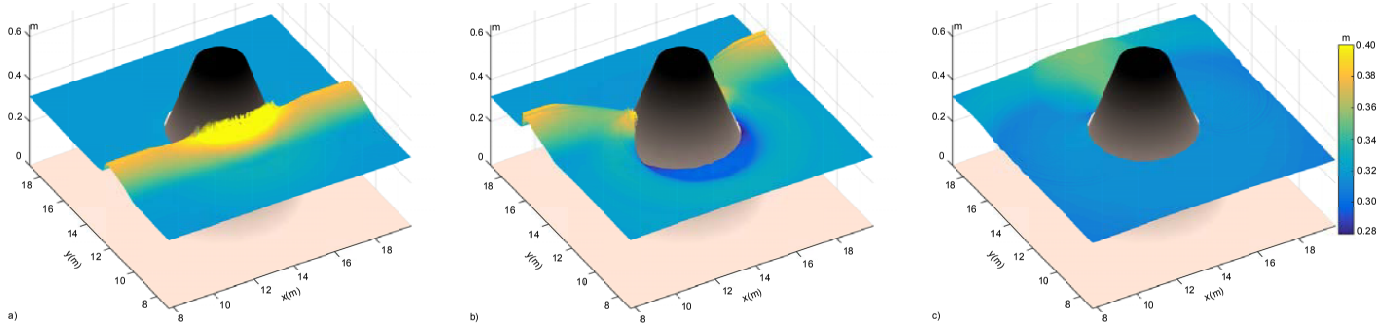

Figure 5.13: *Solitary wave run-up on a conical island, snapshots test n°3: a) front face t = 30s, b) front face t = 32s ,c) back face t = 35s*

Table 5.4: *Index of performance for the Conical island test n°1*

gauge	n° 1	n° 2	n° 3	n° 4	n° 6	n° 9	n° 16	n° 22	TOT.
NSE	0.688	0.668	0.675	0.675	0.817	0.817	0.880	0.762	0.748
D	0.921	0.916	0.917	0.916	0.951	0.952	0.966	0.930	0.933
RMSE	0.003	0.003	0.003	0.003	0.003	0.003	0.002	0.003	0.003

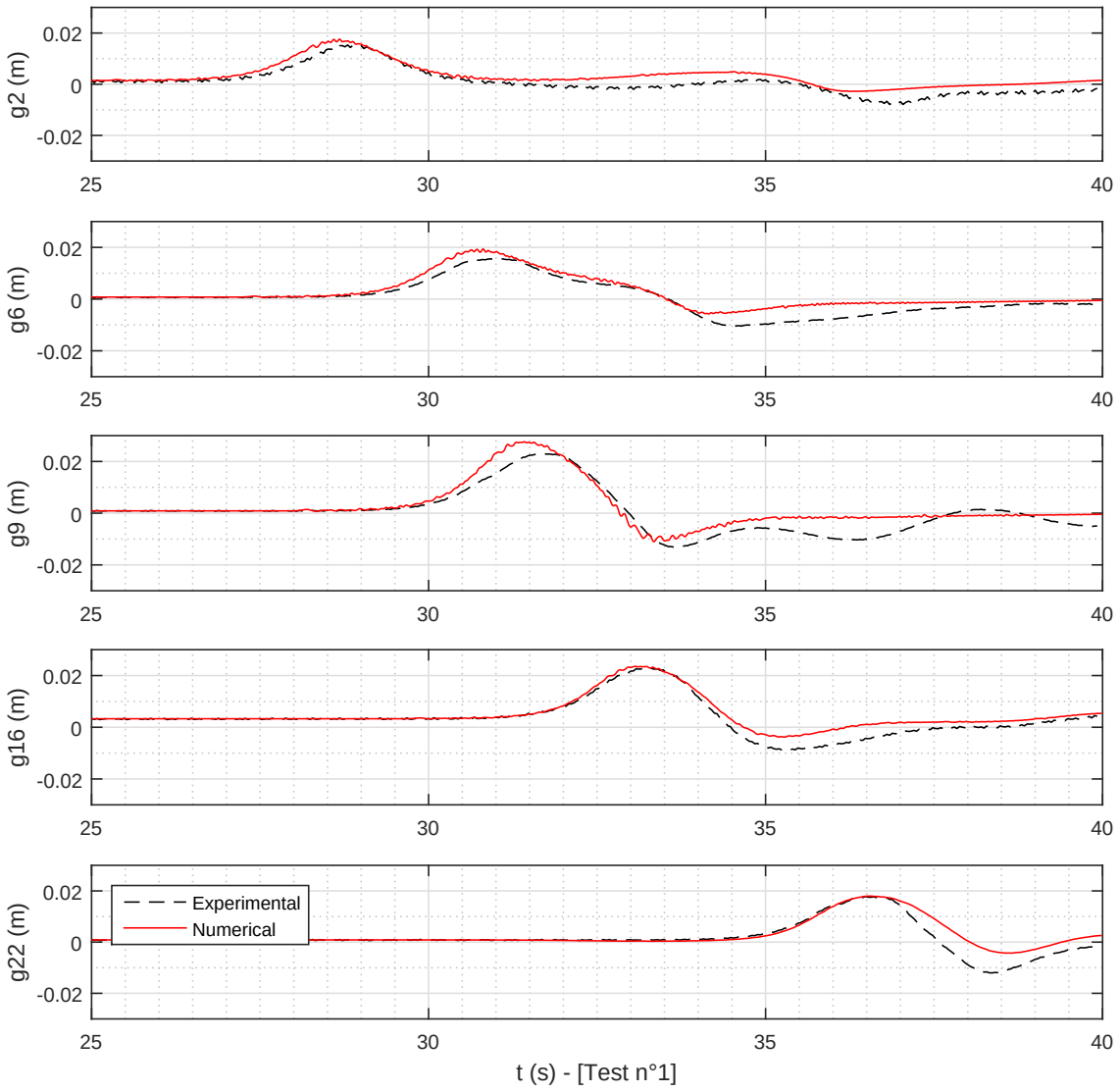

Figure 5.14: *Conical island: comparison experimental and numerical results for test n°1*

Table 5.5: *Index of performance for the Conical island test n°2*

gauge	n° 1	n° 2	n° 3	n° 4	n° 6	n° 9	n° 16	n° 22	TOT.
NSE	0.755	0.789	0.773	0.753	0.828	0.825	0.860	0.437	0.753
D	0.938	0.947	0.941	0.938	0.955	0.955	0.961	0.823	0.932
RMSE	0.004	0.004	0.004	0.004	0.004	0.006	0.004	0.007	0.004

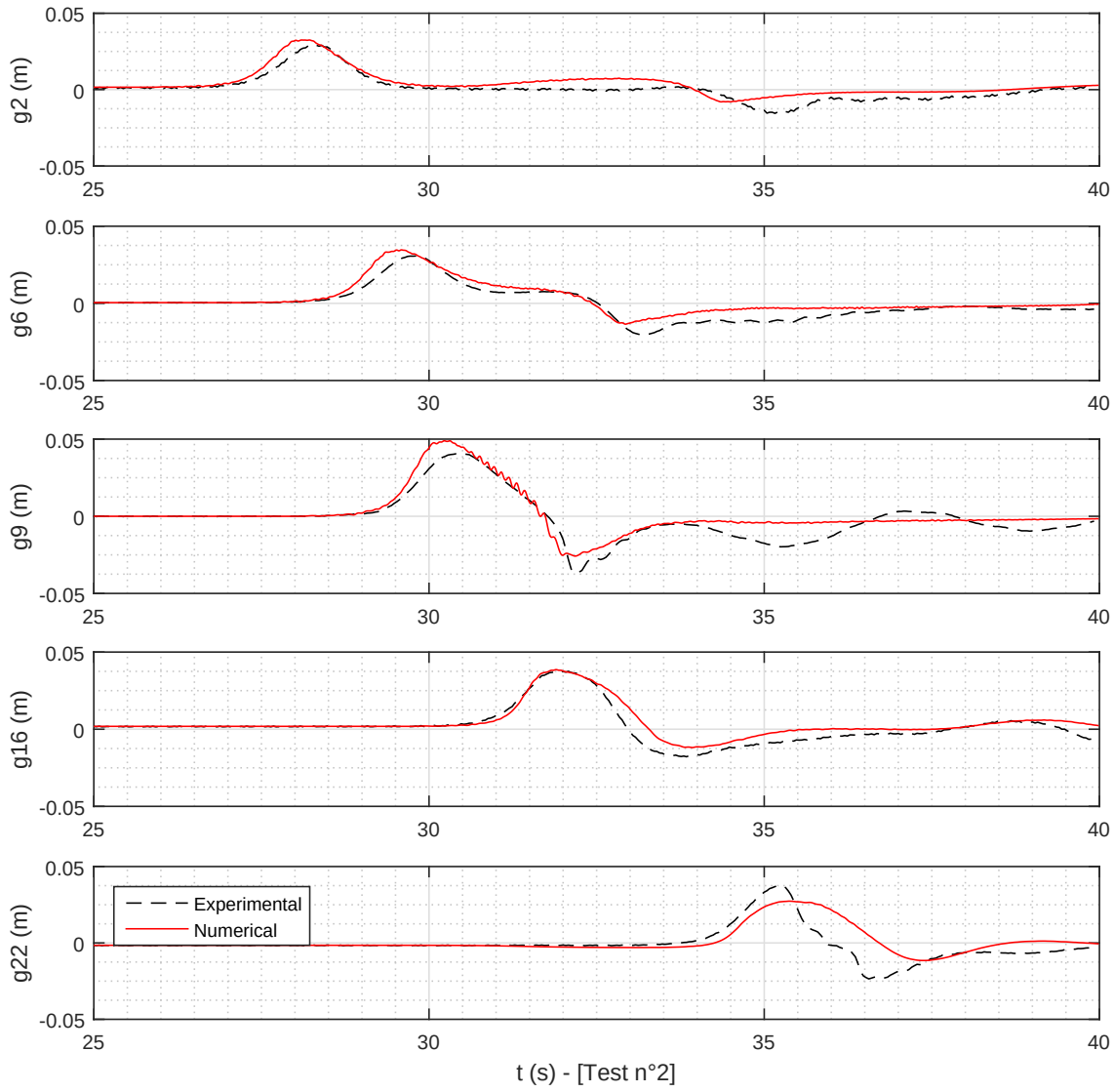

Figure 5.15: *Conical island: comparison experimental and numerical results for test n°2*

Table 5.6: *Index of performance for the Conical island test n°3*

gauge	n° 1	n° 2	n° 3	n° 4	n° 6	n° 9	n° 16	n° 22	TOT.
NSE	0.847	0.827	0.826	0.839	0.865	0.733	0.639	-0.260	0.664
D	0.962	0.954	0.954	0.961	0.966	0.933	0.902	0.483	0.889
RMSE	0.005	0.006	0.006	0.005	0.005	0.010	0.010	0.017	0.008

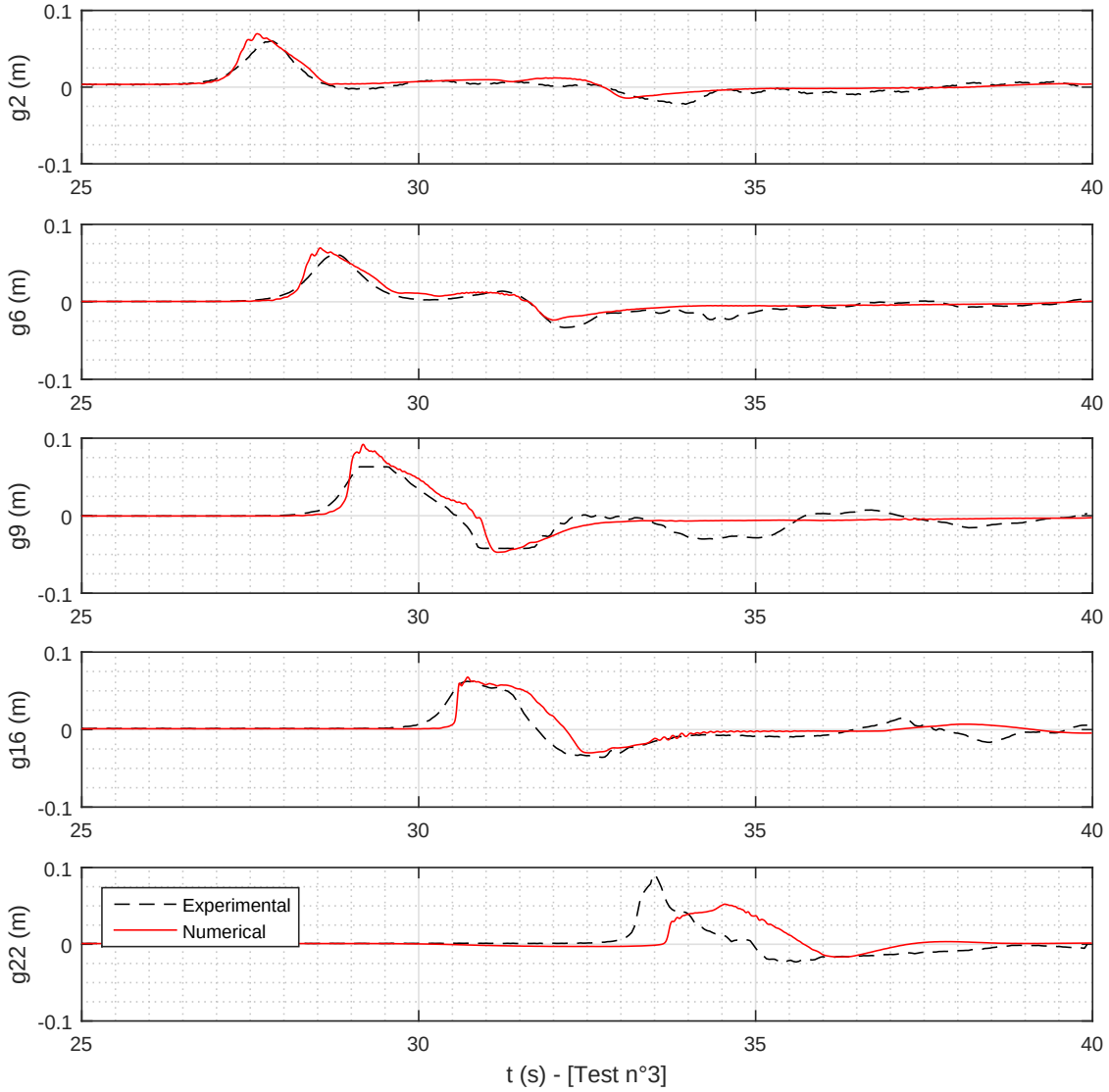

Figure 5.16: *Conical island: comparison experimental and numerical results for test n°3*

Tables 5.4, 5.5 and 5.6 report the performance indexes for the three cases, based on the computed and observed lines shown in Fig. 5.14 - 5.16. Only for the Test n°3, the NSE evaluated for gauge n° 22 is less than zero. However, in all cases, the indexes show a good

agreement between the experimental and numerical results.

5.5.1 GPU performance

This test case is also used to evaluate the performance in terms of runtime using a GPU card and a CPU card, with different dimensions of the domain. The Test n°1 was repeated over 9 domains characterized by different cell size dx = 0.005 m - 1 m, using both the CPU and the GPU card.
Results are reported in Table 5.7 and in Fig. 5.17, in terms of run time (seconds) for every simulated time step Δt, evaluated as $\Delta t = CFL(\Delta x/\sqrt{gh})$, with CFL equal to 0.2 and h equal to the initial water depth (0.32 m). The model speed-up from CPU to GPU is calculated as the ratio of the execution times of CPU to GPU (last column of Table 5.7). As aforementioned, in case of small domains (number of cells $\sim 10^4$), the CPU is faster than the GPU, conversely, for very large domains (10^6 cells), the GPU time is 2-3% of the CPU time. These results can be extended for a more general assessment of the GPU performance, extracting the run time for each Δt for 5 domain dimensions. Considering a typical cell size equal to 1 m (e.g. from DTM data) and a flooding water depth equal to 1 m, it is possible to compute the run time for a 1 hour simulation (Table 5.8 and Fig. 5.18). For a grid composed by 10^6 elements (e.g. a grid of 2 km x 0.5 km) assuming a time step equal to 0.06 s, a 1 hour simulation would take more than 8 hours with a CPU memory, $\sim$ 14 minutes with a GPU memory. As aforementioned, the model solves the system of equations only in some pixels. The domain dimension increases in time but the entire runtime is smaller than considering a domain where the equations are solved everywhere. Frequently, the maximum considered domain is the half of the real domain.

Table 5.7: *Run time (for each Δt) for GPU and CPU card*

n° of pixel	Δx (m)	Δt (s)	CPU run time (s)	GPU run time (s)	GPU/CPU
$7.28*10^2$	1	0.113	0.0016	0.0061	381%
$1.30*10^3$	0.75	0.085	0.0018	0.0064	356%
$2.91*10^3$	0.5	0.056	0.0054	0.0065	120%
$1.15*10^4$	0.25	0.028	0.0075	0.0066	88%
$7.20*10^4$	0.1	0.011	0.0327	0.007	21%
$2.87*10^5$	0.05	0.006	0.1822	0.0082	5%
$1.15*10^6$	0.025	0.003	0.7888	0.0151	2%
$1.79*10^6$	0.02	0.002	1.2764	0.0215	2%
$3.18*10^6$	0.015	0.002	2.1929	0.0355	2%
$1.27*10^7$	0.0075	0.001	7.8698	0.1353	2%
$2.86*10^7$	0.005	0.001	17.79	0.4401	2%

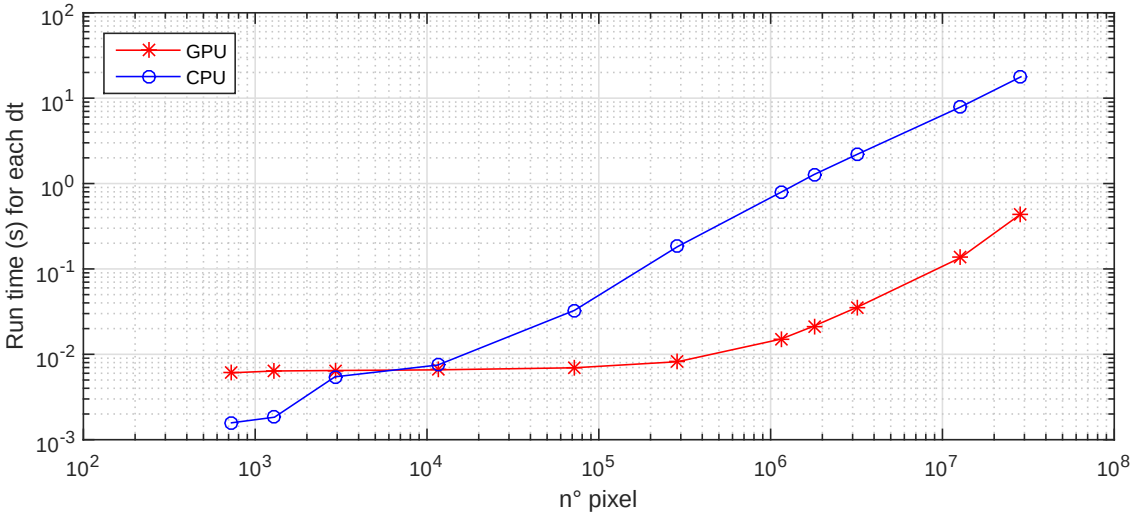

Figure 5.17: *Run time for GPU and CPU card*

Table 5.8: *Run time for GPU and CPU card with dx = 1m and simulated dt = 0.06 s (imposing CFL =0.2 and a typical water depth of 1 m)*

number of pixel	CPU run time (s) for every dt	GPU run time (s) for every dt	1hour simulation with the CPU	1hour simulation with the GPU
10^3	0.0017	0.0062	1 min 42 s	6 min 12 s
10^4	0.0071	0.0066	7 min 6 s	6 min 36 s
10^5	0.0521	0.0071	52 min 6 s	7 min 6 s
10^6	0.6858	0.0139	11 h 25 min 48 s	13 min 54 s
10^7	6.2485	0.1068	104 h 8 min 30 s	1 h 46 min 48 s

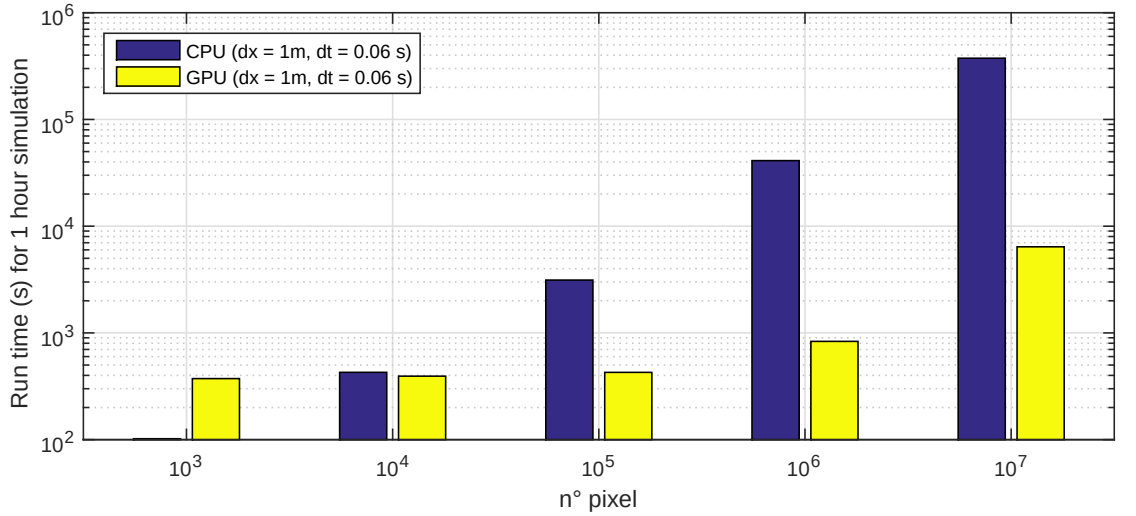

Figure 5.18: *Run time for GPU and CPU card for 1 hour simulation with a typical water depth of 1 m and a dx = 1m*

5.6 Case study: storm event at Caorle (Venice, IT)

A good agreement between analytical solution or experimental data and model results has been carried out in four "idealized" cases (benchmarks). However, the critical test of the model is whether it is able to simulate flood propagation over complex topography and reduce the long run times of codes when applied at fine spatial resolution. The proposed inundation model is applied to a real storm occurred in 2008 along the Venetian littoral; it caused damage to the whole coast and it is the fourth largest surge ever measured in this zone (Ruol et al. 2016). The area under investigation is the Caorle coastline (Fig. 5.19), it is 5 km long and its borders are marked by the Falconera channel to the North-East and the mouth of the River Livenza to the South-West. In order to mitigate the risk to human health, economic activities and cultural heritage, in the central area the shoreline position is stabilized by a seawall, where the historic town is located. The remaining shoreline is formed by wide sandy beaches with a wide range of tourist facilities.

Figure 5.19: *High resolution aerial photo of the study site (Caorle, VE-Italy)*

The Northern part of the Adriatic Sea is characterized by two main wind (and correspondingly wave) regimes that are strongly forced by local orography. Indeed, the prevailing winds in the area under investigation are the North-East and the South-East, the Bora and Scirocco respectively. Further details can be found in Ruol et al. (2015; 2016).
The simulated event is based on a real flood occurred on the 1st of December 2008. The storm characteristics were measured at the CNR Acqua Alta tower (water depth = 16 m), in the Gulf of Venice (Lat 45° 18' 51,27" N, Lon: 12° 30' 29,93" E) and the available information includes water level and wave height, period, and direction. The water level was also measured

in a station placed inside the mouth of the Livenza river.
During the event, extensive wave over-topping took place along the jetty of the Livenza mouth. This caused hinterland flooding, which was documented with a video taken at the Livenza river mouth during the storm event (11.00 am, some video frames are shown in Fig. 5.20). The in-depth viewing of this video allows recognizing the inundated streets and the overtopping locations (Fig. 5.20).
For this area, digital elevation model (DEM) at 1 m resolution was available from a Lidar survey. The domain is 1.0 x 1.5 km (1.5 x 10^6 grid cells) and a portion of it is shown in Fig. 5.21. The runtime for each dt (=0.04 s) is $\sim$ 0.03 s. The Gauckler-Strickler coefficient K_s used to evaluate the value of K_H in Eq. 4.9 is 50 m^3/s.

Figure 5.20: *Frames of the video taken during the storm events (11.00 am) in Caorle (Venice, Italy) and recognized inundated areas/streets*

Fig. 5.22 shows the wave and sea level during the storm event. The maximum significant wave height is Hs = 3.1 m and the direction is mainly 130°N (Scirocco); the maximum water level is equal to 1.25 m at the Acqua Alta tower and 1.46 m at the Caorle station (differently from Acqua Alta, the Caorle station is affected by the river flood contribution).
Two different boundary conditions are necessary:

1. at the shoreline, i.e. sea level elevation plus effects due to waves (set-up and run-up);

2. at the river mouth, i.e. storm surge elevation plus an impulsive signal that mimics the over-topping over the jetty.

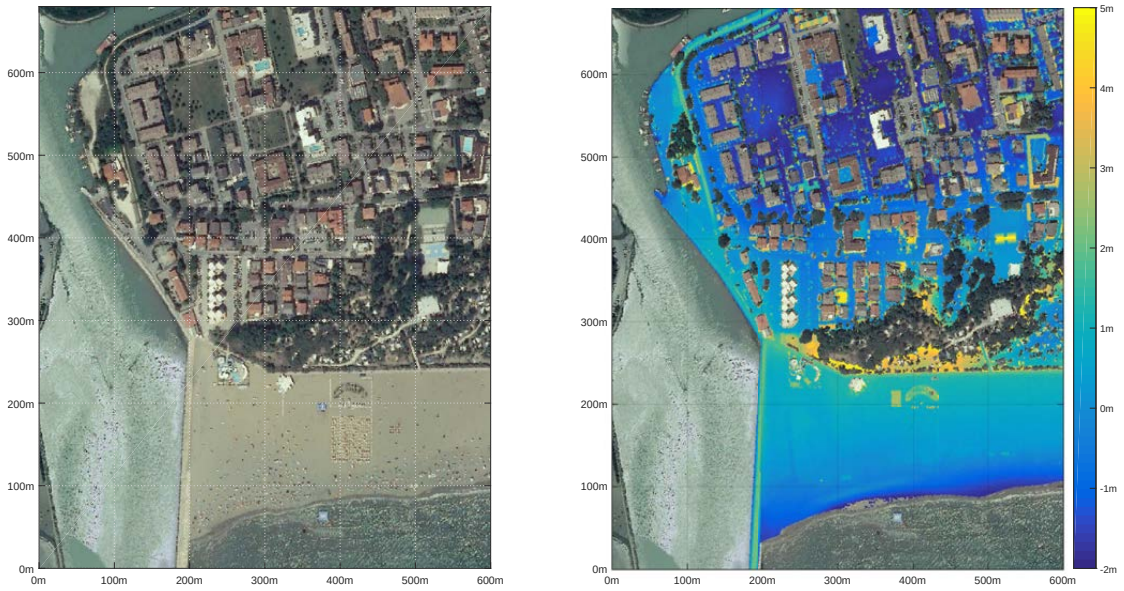

Figure 5.21: *Ortophoto (left)and Digital Elevation Model (DEM, right) of the investigated area (Livenza mouth, Caorle - VE)*

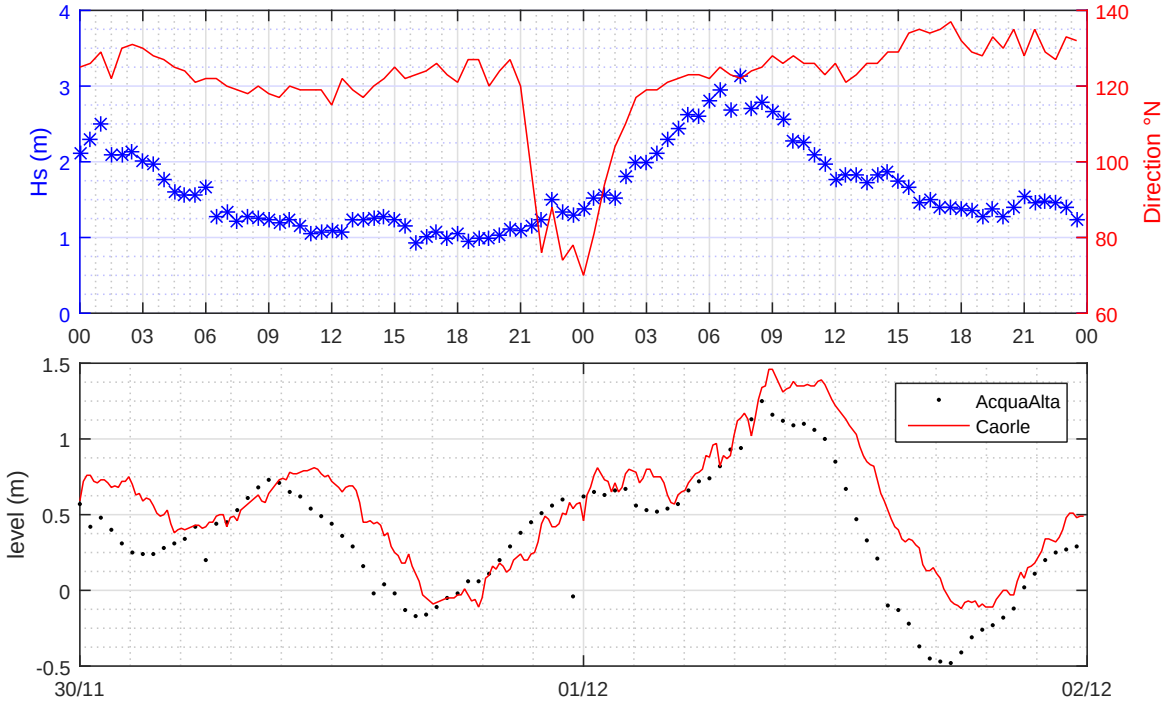

Figure 5.22: *Storm characteristics measured during the event in Caorle (Venice – Italy) in December 2008: sea levels at the Acqua Alta tower and at the Livenza river mouth (top); wave heights and wave directions at the Acqua Alta tower (bottom)*

Fig.s 5.23-5.25 shows the simulated flood extent in 6 instants (h. 7:30, h. 8:00, h. 9:00, h. 10:00, h. 11:00, h. 13:30) for the portion of the domain shown in Fig. 5.21. The simulated results (predicted water depth equal to 50 cm at 11:00 am in the blue area of Fig. 5.20)

are compatibles with the report, although in the simulation the onset of the flood is slightly earlier (around 7:30 am). Nevertheless, its subsequent progression (Fig. 5.25, h.11:00 and h.13:00) agrees with the report and the video information.
Fig. 5.23 (h.7:30 and h.8:00) show the predicted inundation at the initial stage. The locations where the over-topping occurred are in good agreement with the positions pointed out in Fig. 5.20 (video frames n°1, n°2, n°3 and n°6). In particular, the over-topping began in correspondence to the pier for ferry-boat (x = 100 m, y = 425 m in Fig. 5.21) shown in frame n°1 of Fig. 5.20.
The inundated areas shown in the snapshot of the simulation at 11.00 am (Fig. 5.25) correspond to the ones recognized by the in-depth viewing of the video taken at the same time (e.g. the areas visible in the frames no.4 and no. 5 of Fig. 5.20. The video also shows the presence of some debris already there at 11:00 am (frame n°5), proving that here the main flooding began some time before. Furthermore, the newspaper reports that the whole beach was also flooded by the sea from the shoreline, inundation well predicted by the proposed model.
In conclusion, the simulation appears to be coherent with the available information: the over-topping occurs in the same locations documented by the video taken during the storm and the extent of the flooding area and the maximum water depth are consistent with such video and with the report.
Table 5.9 reports, in the first 6 rows, the numerical results of the proposed model in terms of maximum flooded area and flooded volume together with the main input values. It is clear that the water retreats after 11:00 am, when the wave height and tide decrease. The subsequent flooding evolution, affected by several processes of anthropic (e.g. urban drainage and pumping) and natural character (e.g. filtration and evapotranspiration) is obviously not modelled.

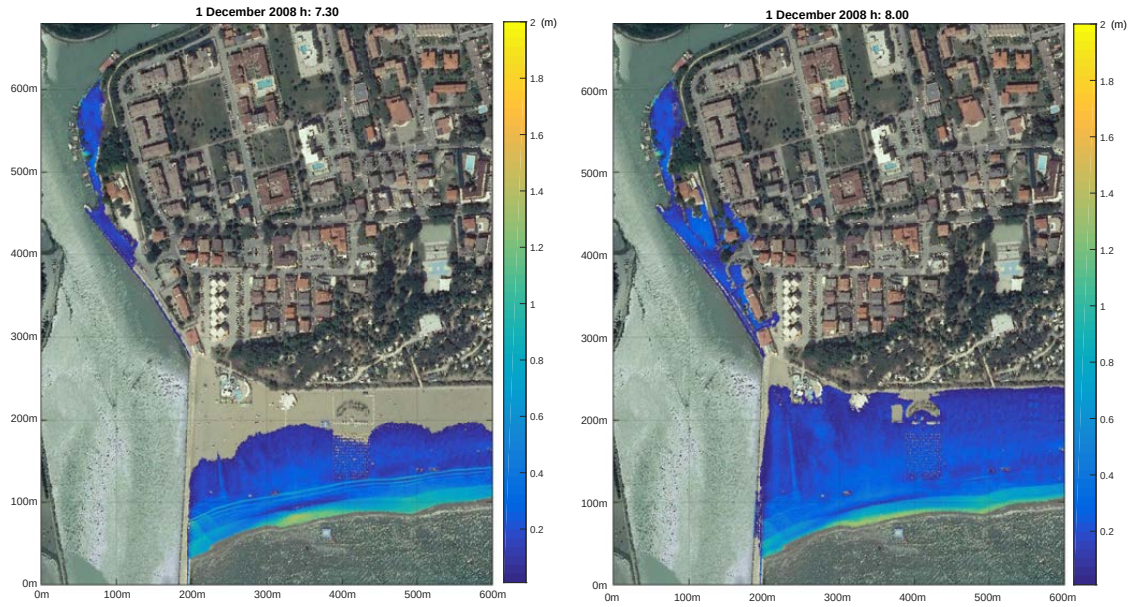

Figure 5.23: *Caorle (VE), December 2008, 7:30 am (left) and 8.00 am (right): inundation model results*

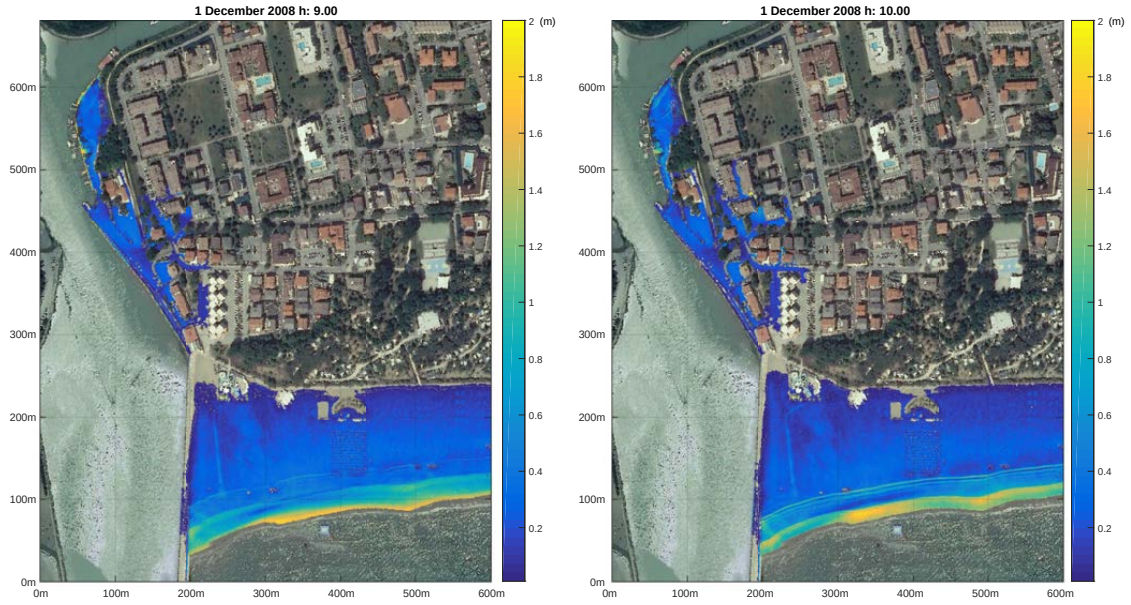

Figure 5.24: *Caorle (VE), December 2008, 9:00 am (left) and 10.00 am (right): inundation model results*

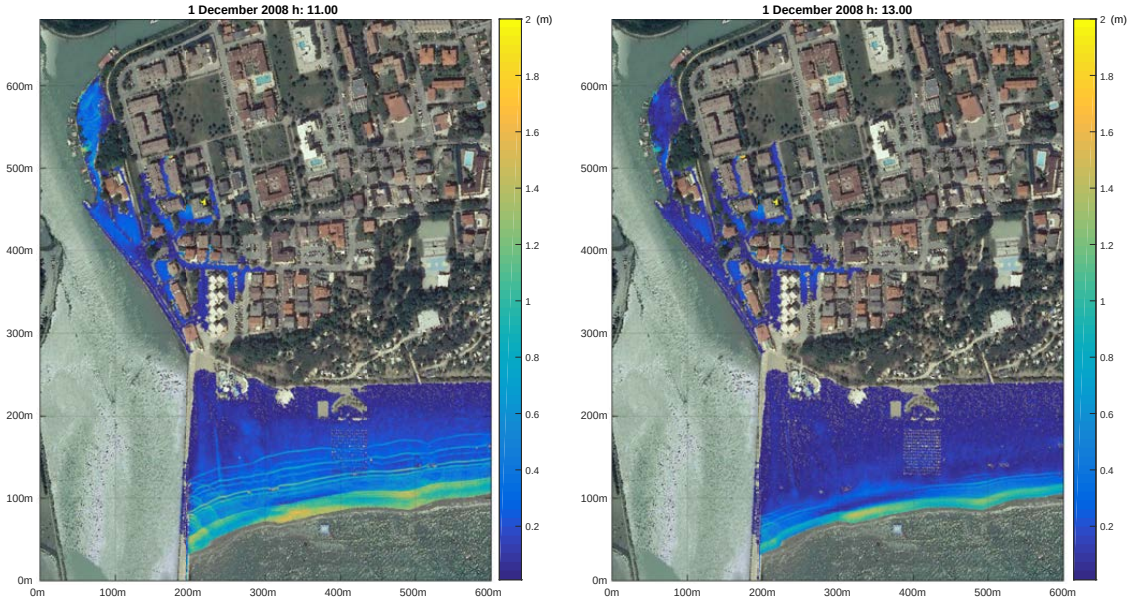

Figure 5.25: *Caorle (VE), December 2008, 11:00 am (left) and 13.00 am (right): inundation model results*

In order to better appreciate the relevance of these results, the static inundation model was applied to determine flooded locations that are hydraulically connected to the coastline and lower than the maximum elevation of the storm surge. Fig. 5.26 shows that the static model largely overestimates the flooded area, as also seen in the last row of Table 5.9. Furthermore, the static model does not appropriately point out the overtopping locations and the beach inundation.

Table 5.9: *Available information on wave and sea-level and numerical results in terms of maximum flooded area and volume*

hour 1/12/2008	7.30	8.00	9.00	10.00	11.00	13.00	Static
Hs (m)	3.13	2.71	2.66	2.27	2.1	1.83	-
"Acqua Alta" sea level (m ZMPS)	0.94	1.13	1.16	1.09	1.06	0.47	-
Livenza sea level (m ZMPS)	1.14	1.02	1.46	1.38	1.35	1.03	1.46
Simulated flooded Area (m^2)	6179	12510	14873	17299	18749	20181	476269
Simulated flooded Volume (m^3)	1269	2403	3599	3986	3878	2586	579530

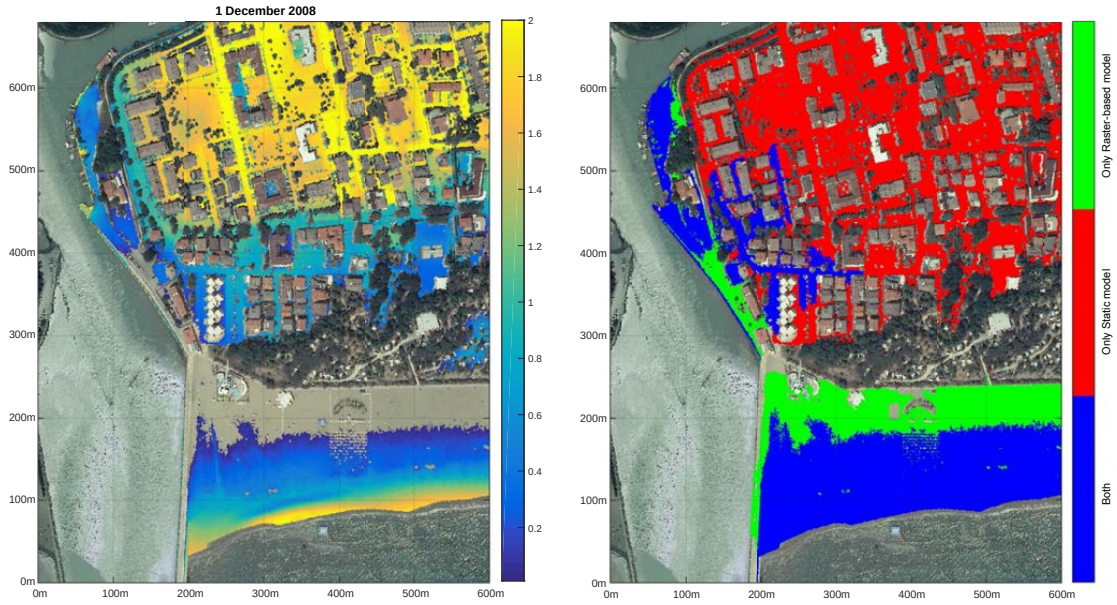

Figure 5.26: *Caorle (VE), December 2008: static inundation model results (left), comparison between static and dynamic model results in terms of inundated areas*

Chapter 6

Extensive application

6.1 Introduction

The aim of this chapter is to produce local inundation maps for some stretches of the Venetian littoral, that show the annual probability of exceedance for a given flood level. To achieve the aim, the FORM analysis is coupled with the inundation model proposed in chapter 3. The investigated littoral is firstly described through a set of variables belonging to the following main groups:

- physical conditions (shore-face width, width and height of the emerged beach, mean grain size and pressure of the use) that characterise the beach system in terms of accommodation and mitigation capacity against the inundation;
- coastline evolution (recent and historical shoreline trends and shore-face evolution) that indicates the beach system behaviour within short and long terms;
- subsidence of the coastal territory that affects coastal submersion;
- typologies of the defence structures along the coast and inland that identify the beach passive mitigation answer to flood;
- marine-weather conditions, that have a significant importance for characterising the hazard to the extreme event (e.g. for coastal flooding: significant wave height Hs, peak period Tp, sea level ζ and storm duration).

Then the whole methodology is described in detail (step by step procedure) and applied to three stretches of coast in the Venetian littoral. Finally, an example of the inclusion of the global mean sea level rise based on the Stocker et al. (2013) report is achieved.

6.2 The Venetian littoral

The Venetian coastline (Fig. 6.1) is 160 km long and faces the Northern Adriatic Sea. The coastline's borders are the mouth of the River Tagliamento to the North and the mouth of the River Po di Goro to the South. It subdivided into two provinces and ten coastal municipalities. The Venetian coastline is characterized by low beaches, lagoons (i.e. Caorle, Venice and Po River Delta) and the mouths of seven rivers: the Tagliamento, Livenza, Piave, Sile, Brenta, Adige, and Po.

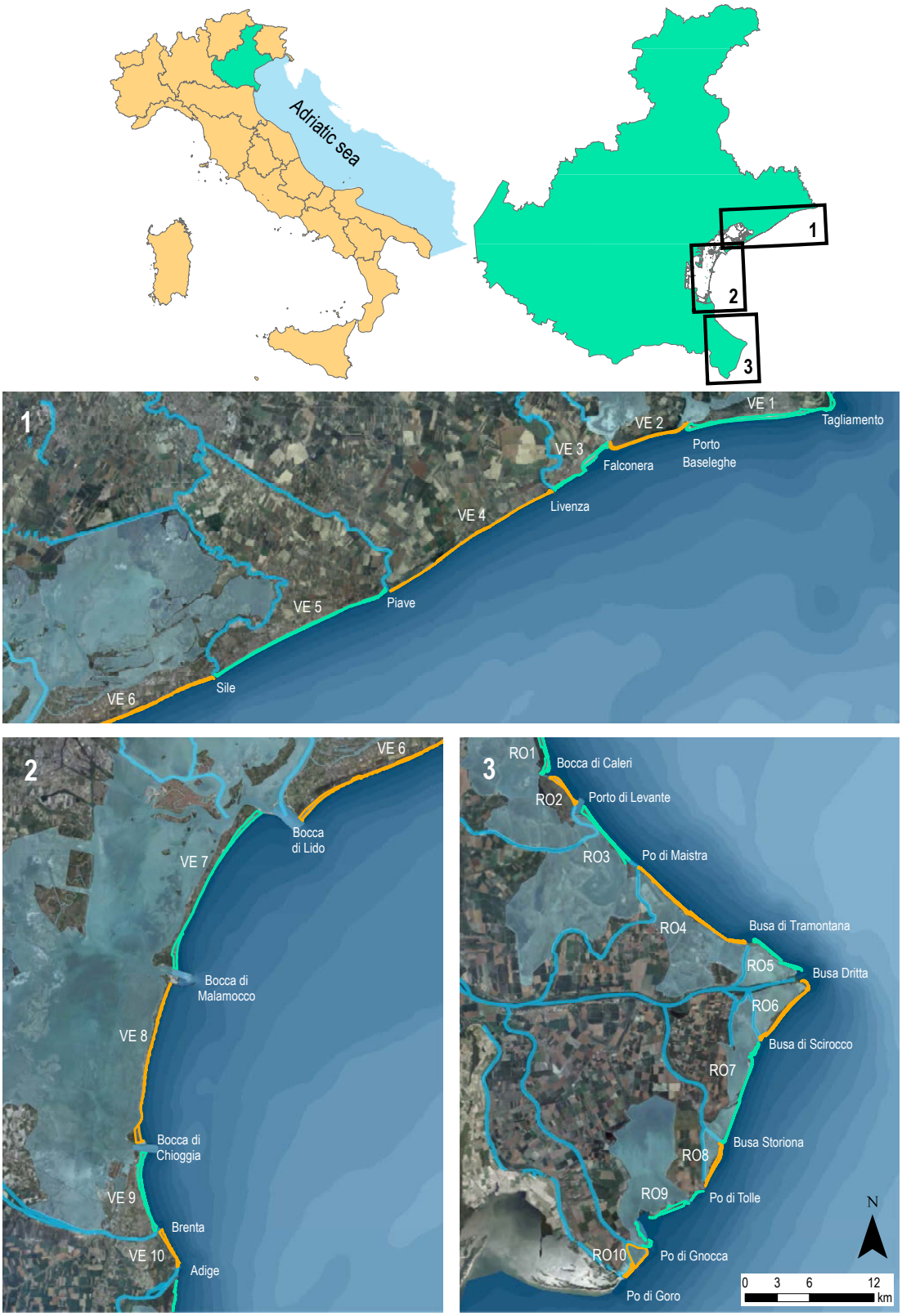

Figure 6.1: *Venetian littoral and its subdivision into coastal cells*

Along the 100 km stretch of coast from the mouth of the River Tagliamento to the Porto Caleri inlet (Ruol et al. 2016) lie a vast number of areas with a high tourist value (e.g. Bibione,

Caorle, Jesolo, Lido di Venezia, Sottomarina). Many of them are protected by coastal structures (e.g. groins, seawalls, breakwaters), and few are free of urban settlements (e.g. Valle Vecchia). Only a few, mainly discontinuous dune systems can be found along the coast because they were destroyed at various times in the past.
The remaining Venetian littoral comprises the Po Delta, which covers 610 km^2 and has 60 km of coast stretching from the Porto Caleri inlet to the mouth of the River Po di Goro. The active river branches of the River Po are (from North to South) Po di Maistra, Po di Pila, Po di Tolle, Po di Gnocca and Po di Goro. The coastal fringe is characterized by a sequence of low sandy and vulnerable barrier islands, beaches and spits that separate lagoons, fishing valleys, bays, tidal flats and marshes from the sea. Inland, ground elevation is almost completely below sea level (locally -2.5/-3.0 m.s.l.), consequently the risk of coastal flooding is very high. The morphological characteristics of the Po Delta make it Italy's largest wetland, as well as particularly unstable and very fragile when subjected to human pressure.
The Northern Adriatic coast is subject to rapidly evolving pressures from a range of drivers, including natural and anthropogenic ones: rapid morphological evolution of Po river Delta (Simeoni and Corbau 2009), human-induced subsidence caused by fluid withdrawal (Carbognin et al. 2004), changing wave climate (Pomaro et al. 2017). For a better understanding of sediment transport patterns Ruol et al. (2016) introduced the concept of "sediment cells". These cells are stretches of coast with similar characteristics bordered by morphological features, such as river mouths, inlets and port dams, meaning that, in the absence of major obstacles to long-shore currents, sediment is relatively free to move inside the morphological feature. The Venetian coast can be subdivided into 20 homogeneous littoral cells (Fig. 6.1, Table 6.1) separated by inlets or the mouths of rivers (from North to South) Tagliamento, Bocca di Porto Baseleghe, Bocca di Falconera, Livenza, Piave, Sile, Bocca di Lido, Bocca di Malamocco, Bocca di Chioggia, Brenta, Adige, Bocca di Caleri, Bocca di Porto Levante, Po di Maistra, Busa Tramontana, Busa Dritta, Busa di Scirocco, Busa Storiona, Po di Tolle, Po di Gnocca, and Po di Goro (Ruol et al. 2016).
Thanks to the work presented by Ruol et al. (2016), useful information and data for the Venetian littoral were collected, harmonised and stored in a single geographical information system (called Coastal GIS). These informations comprise offshore and near-shore wave characteristics, sediment grain size, topographic and bathymetric surveys over a range of time (bathymetry: 2005, 2007/2008, 2010, 2012/2014, DTM: 2008, 2012/2013), subsidence rate (1992-2000 and 2002-2010), shoreline position (from orthophoto: 1983, 2000, 2003, 2012), flooding risk maps (from 2007/60/EC directive), rate and direction of long-shore sediment transport, subsidence, river sediment transport of the main rivers (Tagliamento, Piave, Brenta, Adige, and Po), sediment budget results, value of the area in general (i.e. environmental relevance, urban and tourist pressure, local economy, cultural heritage, etc.) and a catalogue of areas with special legal protection or regulation, existing shore protection structures and nourishment/dredging carried out.
Table 6.2 shows the average sediment size for each littoral cell at different depths. In general, sediment on the Veneto coast is fine sand, with grain diameter ranging between 0.12 and 0.25 mm. As expected, grain size is coarser near the shoreline and decreases seawards. Deviations occur is some places, e.g. RO8, where rivers transport fine sediment that may deposit in the near-shore zone.
The spatial pattern of the net long-shore sediment transport presented in Ruol et al. (2016)

contains divergence and convergence areas that separate areas with oppositely directed net sediment fluxes (Fig. 6.2). Divergence points are located in front of the mouths of the two main rivers (Adige and Po). Convergence points are at Bocca di Lido and Bocca di Caleri. The latter, placed between cell RO1 and RO2, is a highly persistent point of convergence for net transport and thus a likely deposition area (volume $\sim$ 100,000 m^3/year). The most dynamic zone is the Po Delta area, which has a symmetric morphology with a divergence net sediment transport of $\sim$ 200,000 m^3/year.

Table 6.1: *Littoral cell boundary in the Venetian littoral*

Cell	Name	North bound	South bound
VE1	Bibione	Tagliamento	Porto Baseleghe
VE2	Valle Vecchia	Porto Baseleghe	Falconera
VE3	Caorle	Falconera	Livenza
VE4	Eraclea	Livenza	Piave
VE5	Jesolo	Piave	Sile
VE6	Cavallino-Treporti	Sile	Bocca di Lido
VE7	Lido di Venezia	Bocca di Lido	Bocca di Malamocco
VE8	Pellestrina	Bocca di Malamocco	Bocca di Chioggia
VE9	Sottomarina	Bocca di Chioggia	Foce Brenta
VE10	Isola Verde	Brenta	Adige
RO1	Rosolina	Adige	Bocca di Caleri
RO2	Isola Albarella	Bocca di Caleri	Porto di Levante
RO3	Scanno Cavallari	Porto di Levante	Po di Maistra
RO4	Scanno Boccasette	Po di Maistra	Busa di Tramontana
RO5	Scanno della Batteria	Busa di Tramontana	Busa Dritta
RO6	Scanno Boa	Busa Dritta	Busa di Scirocco
RO7	Scanno del Canarin	Busa di Scirocco	Busa Storiona
RO8	Scanno Barricata	Busa Storiona	Po di Tolle
RO9	Scanno Scardovari	Po di Tolle	Po di Gnocca
RO10	Scanno del Bacucco	Po di Gnocca	Po di Goro

Subsidence along the coast is associated with natural causes related to the area's geological history (e.g. sediment consolidation) and with anthropogenic activities, mainly fluid withdrawal. The subsidence in the Northern part is equal to 1-2 mm/year and is mainly related to natural causes. The subsidence in the Po Delta is much larger and ranges from 3-5 mm/year, with it being linked to both natural and anthropogenic causes.
After the evaluation of every source term and the computation of the sediment balance for each littoral cell, Ruol et al. (2016) drawn the following conclusions on : $\sim$ 58 km of coastline have a depositional behaviour with a volume $>$ 10,000 m^3/year; $\sim$ 62 km of coastline have an erosive behaviour with a volume $<$ -10,000 m^3/year; and $\sim$ 19 km of coastline are almost stable, with a volume in the range of $\pm$10,000 m^3/year.

Table 6.2: *Values of sediment diameter (d_{50} mm) sampled at different depths*

Cell	0m/-2m	-2m/-4m	-4m/-6m		-2m/-4m	-4m/-6m	<-6m
VE1	0.323	-	-	RO1	0.19	0.191	0.129
VE2	0.173	-	-	RO2	0.139	0.126	0.11
VE3	0.175	0.235	0.118	RO3	0.143	0.185	0.142
VE4	0.205	0.173	0.143	RO4	0.173	0.208	0.133
VE5	0.153	0.268	0.118	RO5	0.234	0.23	0.101
VE6	-	0.235	0.213	RO6	0.273	0.258	0.207
VE7	0.181	-	0.186	RO7	0.167	0.148	0.132
VE8	-	-	-	RO8	0.068	0.197	0.1
VE9	-	0.144	0.168	RO9	0.144	0.146	-
VE10	-	-	-	RO10	-	-	-

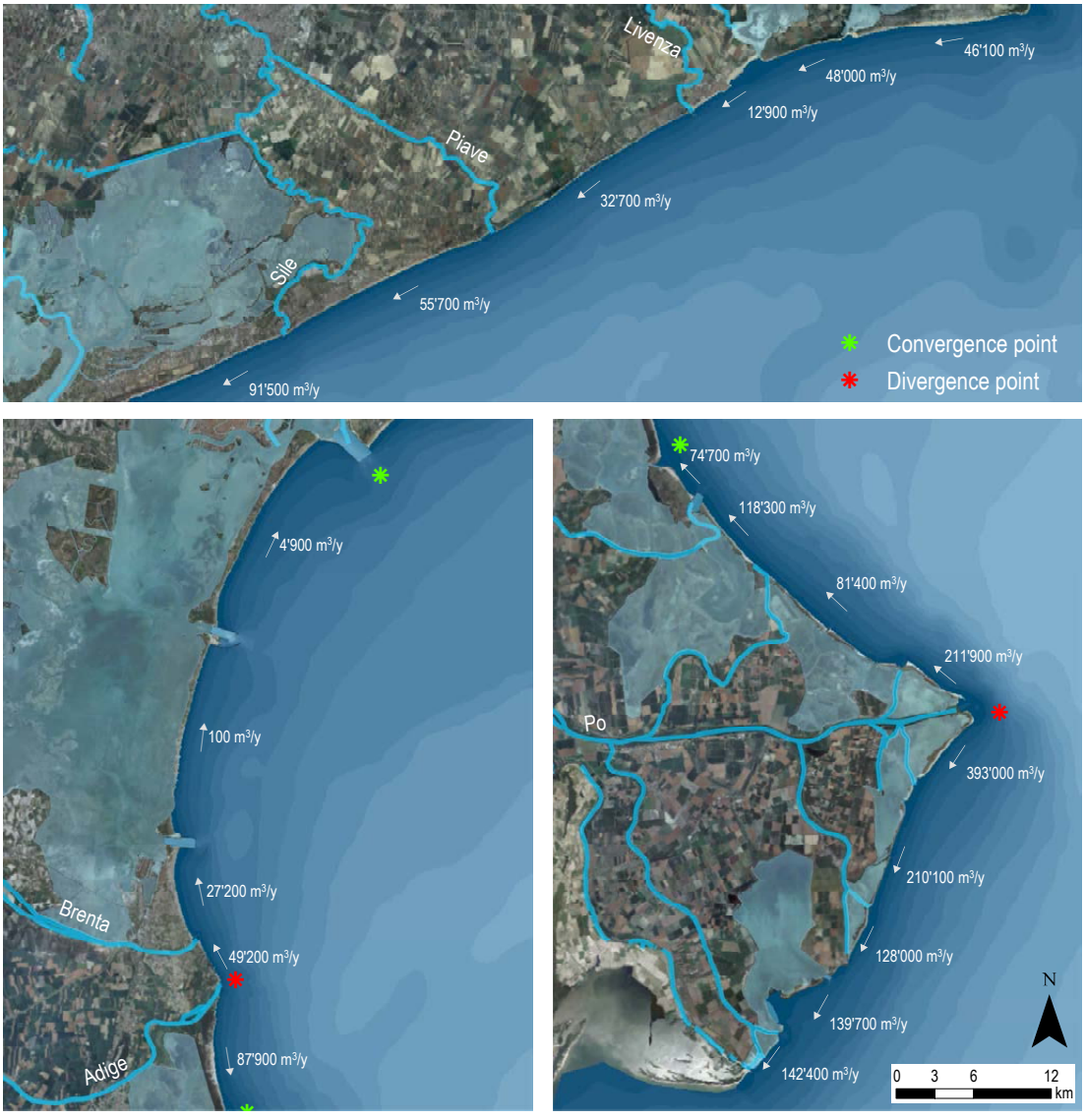

Figure 6.2: *Long-shore sediment transport for the Venetian littoral (from Ruol et al. 2018)*

6.3 Marine loads in the Northern Adriatic Sea

The Adriatic Sea is rectangular-shaped, is about 750 km long and 200 km wide, and it is connected to the Mediterranean Sea at its Southern end by the Strait of Otranto, which is about 80 km wide. Its depth is rather limited in the Northern part, where the bottom descends south-eastwards with an 1 in 1000 slope.

Figure 6.3: *Oceanographic tower "Acqua Alta"*

The Adriatic coast is plagued by a combination of high waves and storm surges, which are responsible for the flooding of coastal areas, in particular, Venice and its lagoon. The highest surge was on 4 November 1966 when the sea level rose approximately 180 cm above the mean sea level (MSL) and persisted above the 100 cm mark for more than 15 hours (Canestrelli et al. 2001). The North Adriatic Sea is characterized by two main wind (and correspondingly wave) regimes, which are primarily influenced by local orography. The prevailing winds along the Venetian coastline are the Bora and the Scirocco, which blow from the North-East and South-East respectively.
In the Venetian littoral two different datasets of waves are available. The first dataset comes from measurements (1987 - 2017) at the oceanographic tower "Acqua Alta" (Fig. 6.3) situated in 16 m of water (MLLW) in the Gulf of Venice (Lat 45° 18' 51,27" N, Lon: 12° 30' 29,93" E). Different wave gauges have been used since the start of the measurements at the Acqua Alta research tower and the instrument system has been progressively upgraded and repositioned during maintenance operations. The measured data include: significant wave height Hs (m), maximum wave height $Hmax$, mean period Tm and peak period Ts (s), mean wave direction (°N), sea level ζ (m referred to Punta della Salute).
The second dataset is formed by modelled wave data. Wave information was obtained by existing WAM simulations forced by data from the European Centre for Medium-Range Weather Forecasts (ECMWF) between June 1992 and December 2008, and were restricted to two points

in the Northern Adriatic sea (P1: Lon. 13 °00' Lat. 45°00', P2: Lon. 13°00' Lat. 45°30'). Fig. 6.4 shows the location of the three points where wave data are available. Fig. 6.5 shows the wave climates at points P1 and P2 and Fig. 6.6 illustrates the wave climate at the tower.

Figure 6.4: *Location where wave data are available*

As aforementioned, in the first dataset, the sea level is also recorded. Thanks to his length and to the combined measurements of waves and sea level, the first dataset allows to deeper investigate the long term behaviour of the marine hydrodynamics in the area under investigation and to highlight some typical phenomena. As stated previously, the long-fetch south-easterly Scirocco and the short-fetch strong north-easterly Bora wind generate waves, blowing along

the major and minor axis of the basin, respectively. Bora is the most frequent regime, but high waves are mostly associated to Scirocco direction (Fig. 6.6, b). Fig. 6.7 reports the monthly values of the 5th, 50th, 95th and 99th Hs percentiles. The long term behaviour is almost stationary; the peak of November 2012 is due to the occurrence of 2 storm with wave height bigger than 4 m.

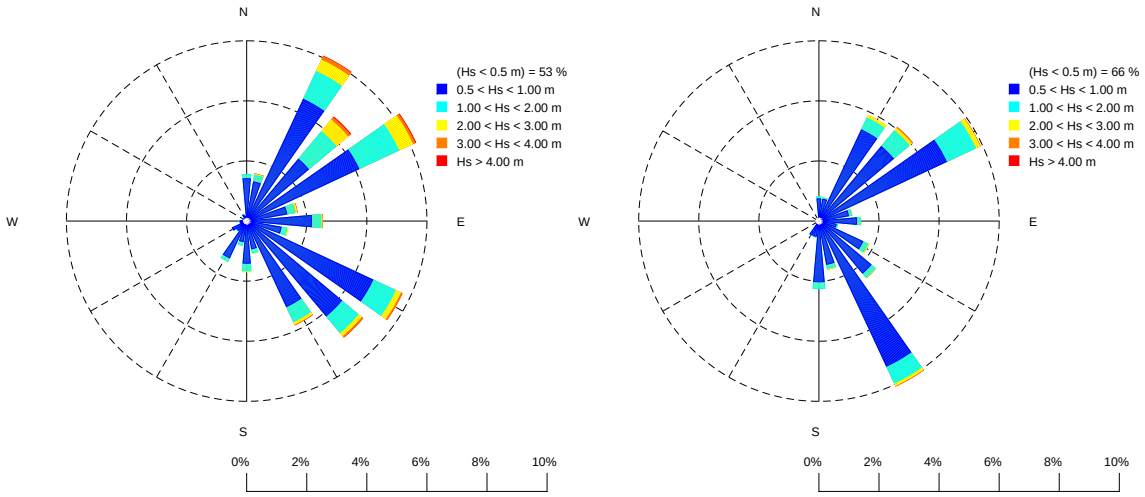

Figure 6.5: *a) Wave climate at point P1, b) Wave climate at point P2*

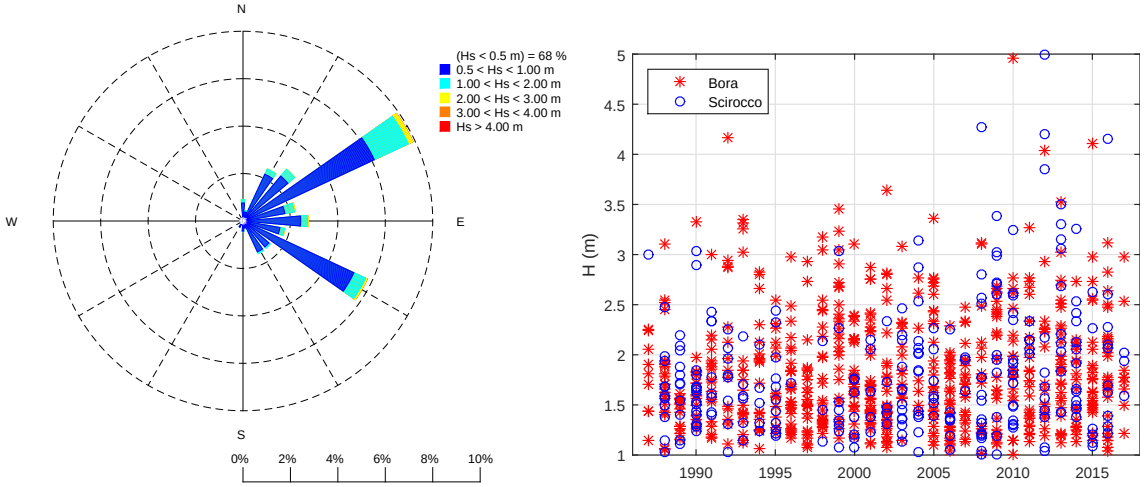

Figure 6.6: *a) Wave climate at the oceanographic tower "Acqua Alta", b) Peak over threshold 1 m subdivided into Bora and Scirocco direction*

The total water level ζ measured at "Acqua Alta" tower (Fig. 6.8) includes two independent contributions: the astronomical tide (ζ_A) and the meteorological contribution (storm surge, ζ_S). Therefore, an extreme high level can be reached in different conditions: a strong astronomical tide with a moderate surge (sufficient anyway to reach an alarm threshold), or vice versa, or with two substantial contributions at about the same time. Under these conditions, the surge value is defined, at every instant, as the observed sea level minus the astronomical tide embedding the mean sea level (d_0) trend (Fig. 6.9).

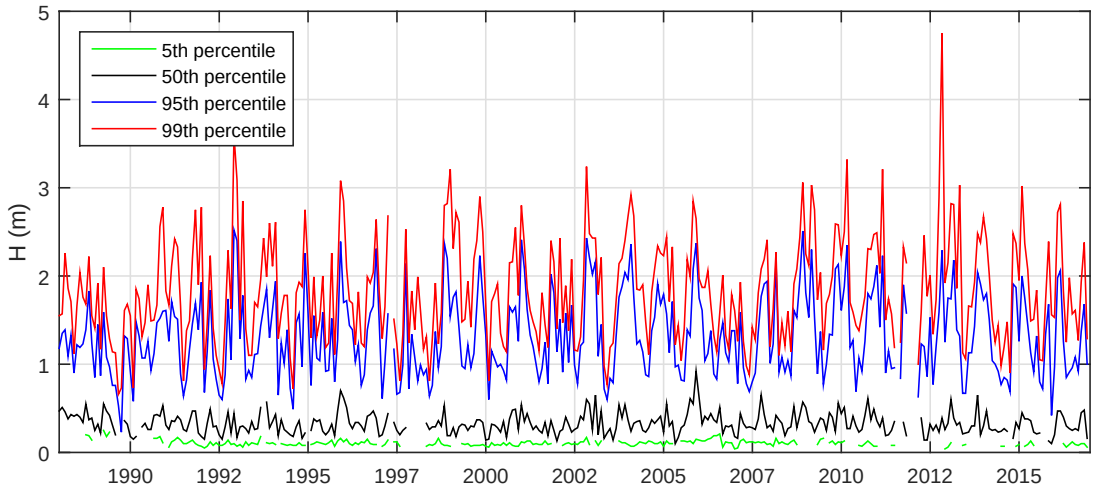

Figure 6.7: *Time series of the monthly values of the 5th, 50th, 95th and 99th Hs percentiles*

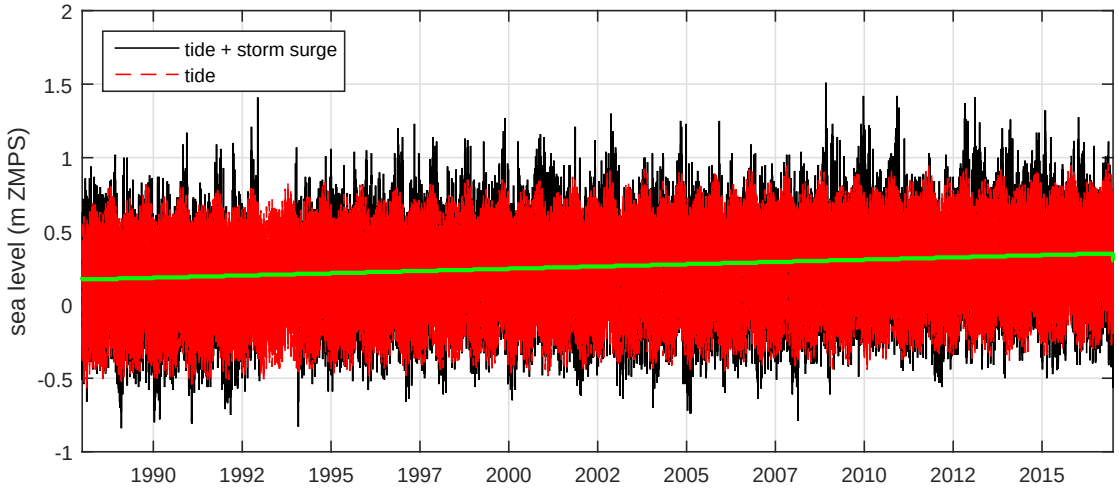

Figure 6.8: *Time series of sea level and tide at the "Acqua Alta" Oceanographic Tower*

Focusing on the observed sea water level in the Northern Adriatic sea, the record shows an oscillating behaviour (ζ_R residual sea level) not only associated to the astronomical tide (due to the daily periodicity of the Sun and the Moon in their rising and descending), but also to the meteorological contribution. This phenomenon is connected to some local condition: after a pulse due to a storm, the whole Adriatic is involved in "seiches", oscillations of a semi-closed basin. The main seiche of the Adriatic sea has a period close to 22 hours. This contribution is relevant for the possible occurrence of floods because it can magnify the effect of the surge. Fig. 6.10 shows an event recorded in December 1997: the total sea level had a peak equal to 1.11 m (referred to ZMPS) measured at 10 a.m. on 20 December 1997. The meteorological surge shows an oscillating behaviour after the peak connected to the beginning of the 22h seiche. Extracting from the surge the seiche with period equal to 22 hours (filtering the curve), the residual level is the effective storm surge (6.11). Fig. 6.12 shows the contemporary wave height measurement: a Bora storm (mean direction 90 °N) occurred in the interval under investigation with a maximum Hs of 2.15 m.

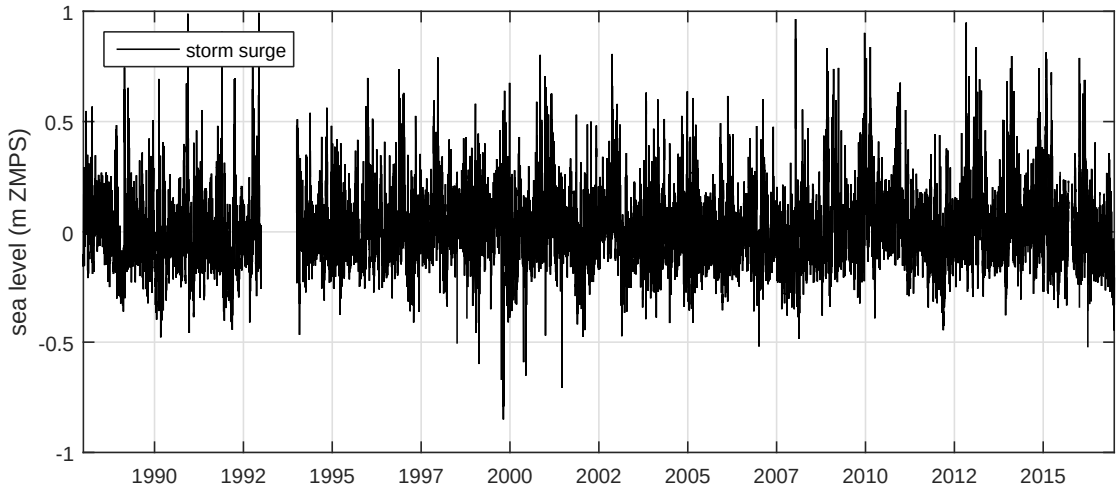

Figure 6.9: *Time series of surge at the "Acqua Alta" Oceanographic Tower*

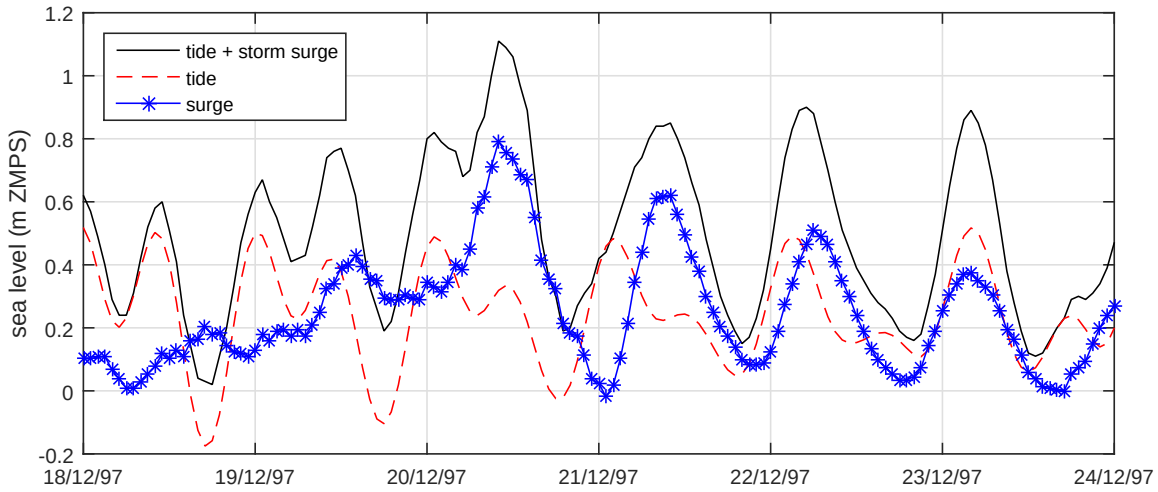

Figure 6.10: *Tide and surge level at the Oceanographic tower: 18 - 24 December 1997*

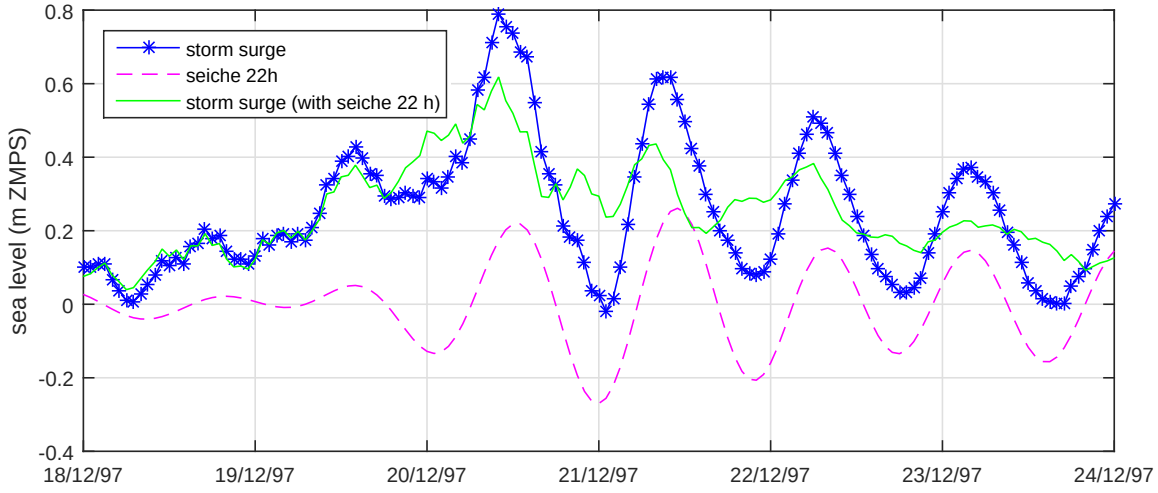

Figure 6.11: *Surge level and seiche at the Oceanographic tower: 18 - 24 December 1997*

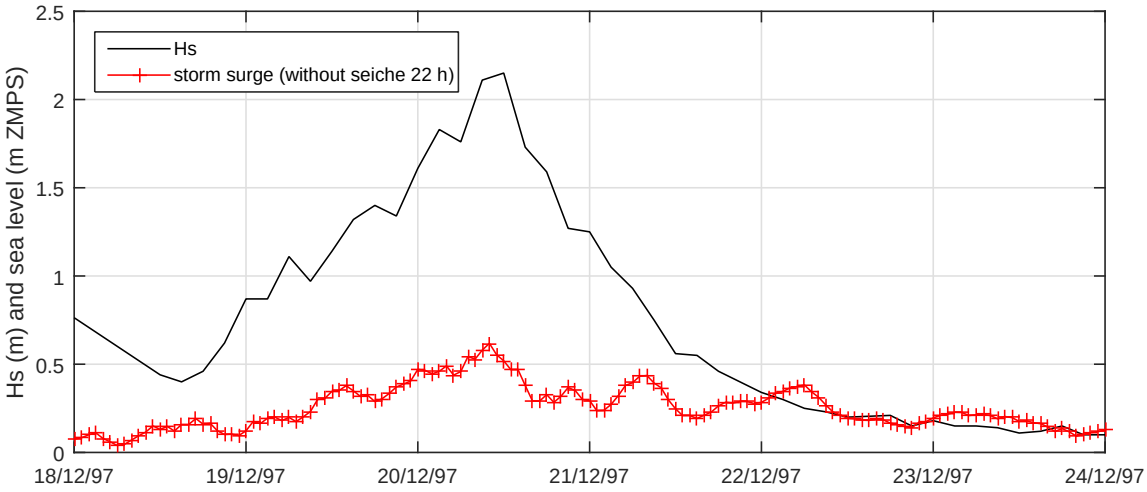

Figure 6.12: *Wave height and storm surge residual at the Oceanographic tower: 18 - 24 December 1997*

6.3.1 Identification of storm

Hazard situations mainly occur during storm conditions. Therefore, it is important to perfectly understand the physical processes that are occurring during wave storm conditions. Wave conditions must be studied in terms of significant wave height (Hs), peak period (Tp), mean wave direction, sea level (ζ=ζ_A+ζ_S+ζ_R) and storm duration. Some of these characteristics have strong correlation that could be expressed through analytical formulation, other need to be studied with a bivariate statistical analysis (e.g. waves and sea level).
In the framework of a statistical analysis, the first issue to be solved is to establish a homogeneous and independent sample representing sea storms. Boccotti (1986) defined a sea storm as a sequence of sea states during which the significant wave height is above a given threshold h_{crit} and does not fall below it for a predefined time interval. Usually the threshold h_{crit} is related to the average significant wave height Hs calculated from its time series in the considered zone, so that it depends on the characteristics of the recorded sea states.
In the Venetian littoral the h_{crit} value is approximately equal to 1 m. Therefore, the storm events were defined as periods where the significant wave height exceeds 1 m at least for 3 hours (example in Fig. 6.13). To guarantee the independence of selected storms, the minimum time interval between two storms was set as 72 h, hence two storms with time interval less than 72 h were considered as one storm event (Lin-Ye et al. 2018). The observations were selected and processed to obtain a time series of independent storm events, characterized by the maximum significant wave height (Hs_{MAX}) and his concomitant wave period (Tp), water level (ζ), wave direction (Dir), the maximum water level during storm (ζ_{MAX}) and the storm duration. Fig. 6.14 shows the selected events for the wave series measured at the oceanographic tower "Acqua Alta".
The data sample, selected from the entire population by the aforementioned procedure, includes 974 wave storms recorded from 1987 to 2017 at the "Acqua Alta" tower. In the following, this data sample is used to find some correlation among variables and for all the statistical analysis. Table 6.3 reports the annual maximum recorded at the "Acqua Alta" tower.

Table 6.3: *Annual Hs maximum at the "Acqua Alta" tower*

Date	Hs (m)	Tp (s)	ζ (m ZMPS)	Dir. °N
24/11/1987 18:00	3.0	7.7	0.46	131
21/11/1988 21:00	3.1	7.0	0.70	63
05/04/1989 09:00	2.2	7.3	0.55	132
10/12/1990 00:00	3.3	9.0	1.04	107
03/05/1991 15:00	3.0	10.0	0.71	-
08/12/1992 12:00	4.2	7.7	0.76	106
02/10/1993 18:00	3.4	7.6	-	108
13/02/1994 21:00	2.8	6.6	0.56	67
14/12/1995 00:00	3.5	7.4	0.63	-
30/01/1996 21:00	3.0	6.6	0.28	-
21/04/1997 18:00	2.9	6.6	0.43	69
22/11/1998 18:00	3.2	7.6	-0.17	69
11/01/1999 00:00	3.5	2.9	0.53	83
07/11/2000 00:00	3.1	8.8	0.71	32
14/01/2001 06:00	2.9	6.7	0.17	59
16/11/2002 15:00	3.6	8.8	0.83	63
11/01/2003 21:00	3.1	7.2	0.15	80
24/09/2004 15:00	3.4	4.0	0.59	-
23/11/2005 03:00	3.4	7.6	0.51	72
30/04/2006 06:00	2.3	6.6	-0.12	42
17/12/2007 06:00	2.5	7.0	0.31	73
10/12/2008 15:00	4.3	6.6	0.48	121
29/03/2009 18:00	3.4	5.4	0.89	122
10/03/2010 06:00	5.0	6.1	0.78	70
01/03/2011 21:00	3.3	4.6	0.72	71
11/11/2012 09:00	5.0	7.7	1.03	125
25/03/2013 09:00	3.5	4.3	0.84	71
31/01/2014 06:00	3.3	5.6	0.96	128
05/02/2015 21:00	4.1	8.4	-	88
05/03/2016 21:00	4.2	4.0	1.08	128
17/01/2017 21:00	3.0	5.3	0.27	84

In order to model coastal flooding, it is essential to analyse the correlation between different variable. Both the wave period and the duration of storms could be related to the wave height with an analytical dependency.

a) Wave height and wave period correlation: The wave period is often determined through a dependency with the wave height. The relationship used to determine the depen-

dency law between the peak period T_p and H_s is of the type:

$$T_p = aH_s^b \tag{6.1}$$

The analysis of the extreme wave height (fig. 6.14) measured at the oceanographic tower "Acqua Alta" and their concomitant wave period is shown in fig. 6.15a, where $a = 4.76$ and $b = 0.283$. However, considering also the wave steepness ($= H/L$), the correlation between H_s and T_p can differ a lot. Distinguishing every couple of H_s and T_p with their value of steepness, different correlations can be found (fig. 6.15b, the values of a and b are reported in Table 6.4).

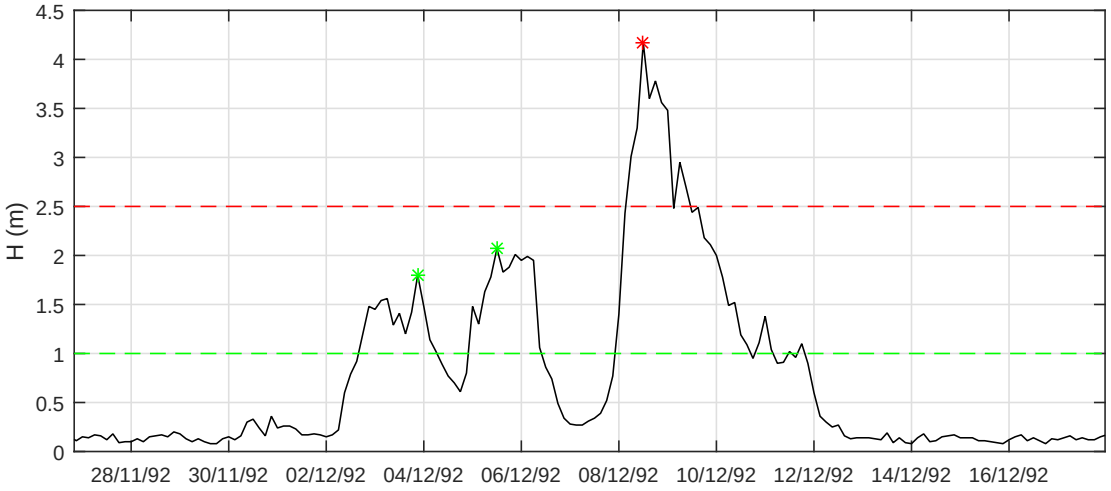

Figure 6.13: *Example of identification of storm with peak over threshold methods (1 m green, 2.5 m red)*

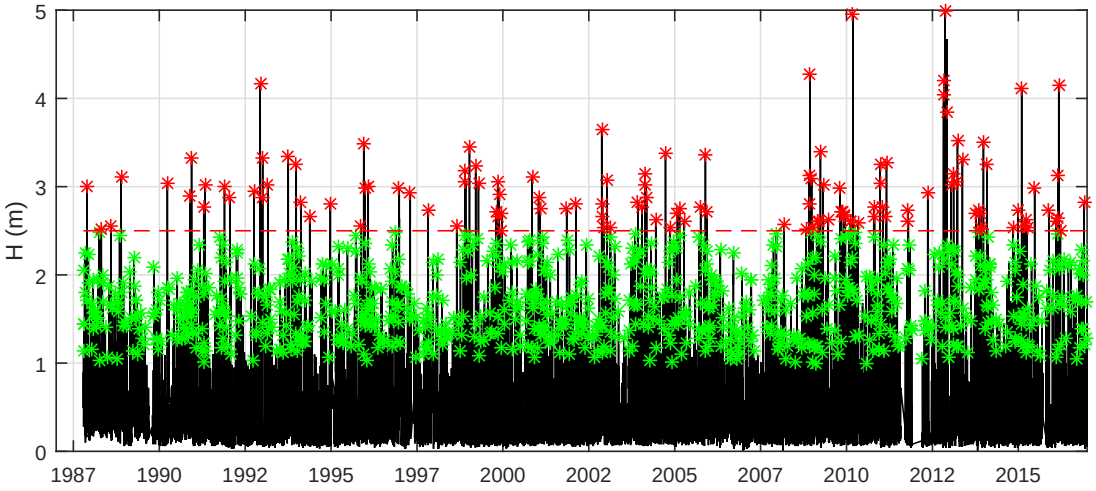

Figure 6.14: *Time series of significant wave height Hs and peak over threshold 1 m (green) and 2.5 m (red)*

b) Storm duration: The storm duration is one of the key factors in coastal flooding modelling, influencing the extension of the flooded area and the storm damage intensity. Fig. 6.16a shows the storm duration in the Northern Adriatic sea relative to different values of

Hs and Fig. 6.16b reports the duration of the storm peak, defines as the period, that includes Hs_{MAX}, where the significant wave height exceeds the 50% of Hs_{MAX}. On each box, the central mark is the median, the edges of the box are the 25th and 75th percentiles, the whiskers extend to the most extreme data points not considered outliers, and outliers are plotted individually. The results are:

1. Storm duration t_S: mean= 31.3 h, median= 24 h, 25th perc.= 12 h, 75th perc.= 45 h
2. Peak duration t_P: mean= 3.9 h, median= 3.5 h, 25th perc.= 2 h, 75th perc.= 5 h

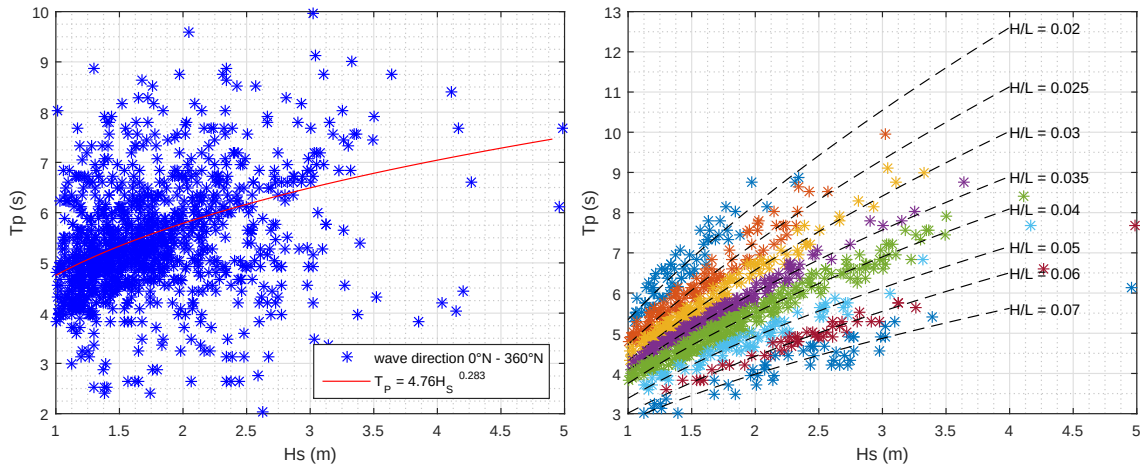

Figure 6.15: *a) Hs - period (Tp) correlation b) Hs, Tp and steepness (Hs/L) correlation*

Table 6.4: *Coefficient of Eq. 6.1 for different value of steepness*

H/L	0.02	0.025	0.03	0.035	0.04	0.05	0.06	0.07
a	5.34	4.72	4.31	4.08	3.75	3.38	3.01	2.82
b	0.619	0.619	0.609	0.563	0.554	0.540	0.555	0.496

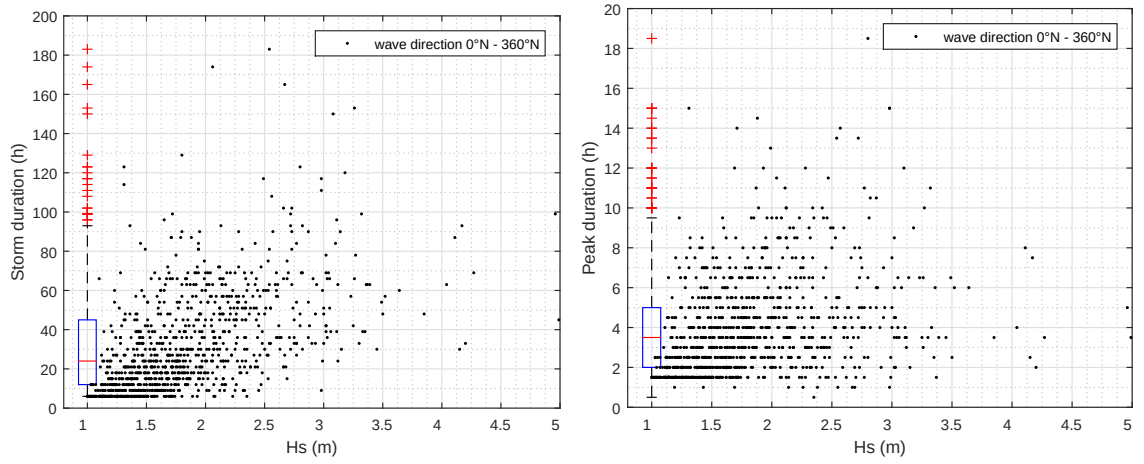

Figure 6.16: *a) Storm duration t_S vs Hs, b) Peak duration t_P vs Hs*

6.3.2 Statistical analysis of waves and sea level

The two marine conditions, that are crucial to characterize the hazard related to coastal flooding, are the wave height and the sea level. In the following, these two variables are statistically characterized to evaluate the boundary conditions for the inundation model.
Among the classical statistical methods, one of the most used is the Peak Over Threshold (PoT) (Goda 1989; Coles et al. 2001; Goda 2010).
The general concept is that only the maxima above a certain threshold are processed. The samples selected in this manner are stochastically independent. The chosen threshold plays a significant role on the quality of return value estimates. For instance, a quite low threshold may violate asymptotic basis of the statistic model, as storm peaks must be independent and identically distributed random variables. On the other hand, a quite high threshold could lead to unstable predictions due to a small sample size (Li et al. 2012).
A way to analyse peak over threshold data is to fit the data with the Generalized Pareto Distribution (GPD), which was introduced by Pickands III (1975) as a distribution of the sample excess above sufficiently high thresholds. Coles et al. (2001) proposed two different methods for threshold selection based on empirical techniques: one is based on the interpretation of the mean excess (ME) plot, which should be approximately linear in proximity of the appropriate threshold, and the other on the stability of shape and modified scale parameter of GPD in the vicinity of the threshold. Hereinafter, this procedure is applied to both wave and sea level, in order to characterize this two variables in the Northern Adriatic sea.

a) Univariate statistical analysis of waves: The data sample of Hs used for the POT methods is the one described in section 6.3.1. Fitting the data with a GPD for increasing thresholds, the resulting mean excess plot is shown in Fig. 6.17a. Fig. 6.17b shows the values of Hs associated with different return period, varying the thresholds. Fig. 6.18a shows the results of three performance index (NSE, Eq. 2.74; D, Eq. 2.75; RMSE, Eq. 2.76), that are used to estimate the reliability between the GPD distribution and the Hazen plotting position formula (Eq. 2.73). All these methodologies tend to indicate that the best threshold is ~ 2.5 m. The results of the univariate statistical analysis on waves, setting a threshold equal to 2.5 m are shown in Fig. 6.18b and in Table 6.5.

Table 6.5: *Results of GPD for H_S, selected threshold = 2.5 m*

$T_R(y)$	1	2	5	10	50	100
$H(m)$	3.2	3.5	3.9	4.3	4.9	5.2
lowerbound	-0.0060	-0.0095	-0.0176	-0.0267	-0.0561	-0.0721
upperbound	0.0061	0.0095	0.0179	0.0264	0.0581	0.0726

b) Univariate statistical analysis of sea level: The same procedure is applied also to the sea levels ζ (astronomical tide ζ_A + meteorological surge ζ_S + residual level ζ_R). Fig. 6.19a shows the three performance indexes, indicating that the best thresholds is ~ 1.3 m ZMPS. The results of the univariate statistical analysis on ζ, setting a threshold equal to 1.3 m are shown in Fig. 6.19b and in Table 6.6.

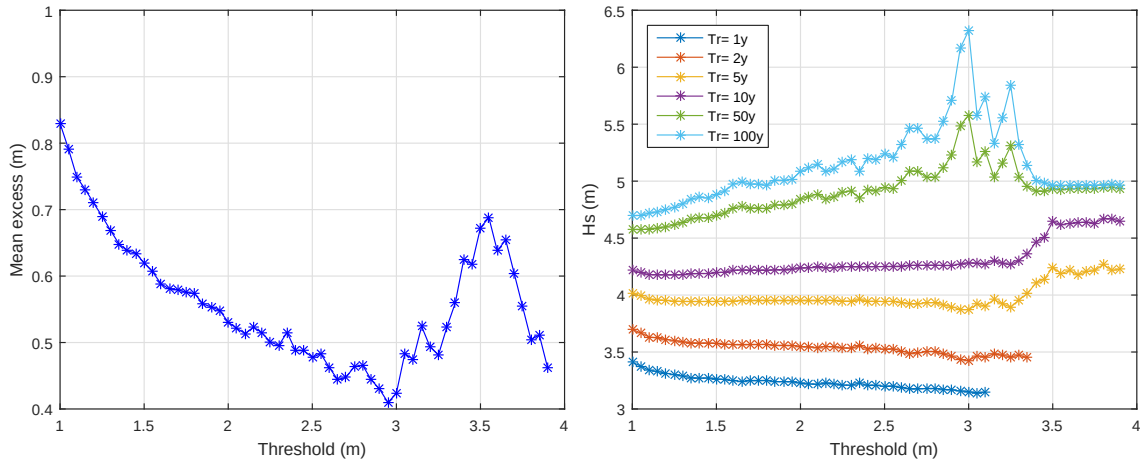

Figure 6.17: *a) Mean excess plot, b) H_S associated to 6 different return period T_R, varying the threshold*

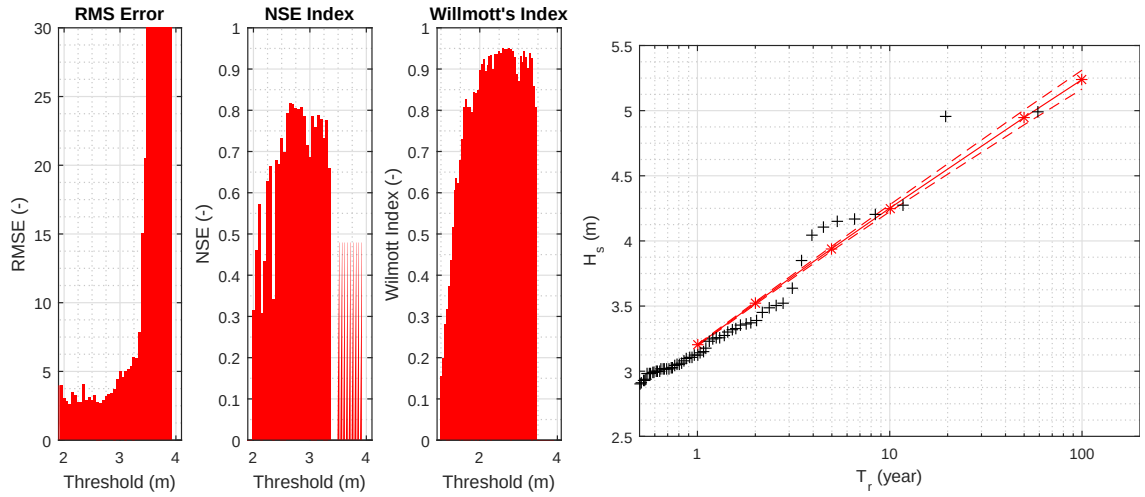

Figure 6.18: *a) Performance indexes (RMSE, NSE, D) used to estimate the reliability, b) Results of GPD for H_S, selected threshold = 2.5 m*

6.3.3 Bivariate statistical analysis

On coasts both still water levels and waves can be important in assessing flood risk. The simultaneous occurrence of large waves and a high still water level is therefore important in estimating their combined effect on sea defences. Therefore, more than one random variable must be considered in the extreme analysis. While it is convenient to assume that the relevant random variables are independent, this is often inappropriate. For instance, the significant-wave-height (Hs) is the most frequently used wave-storm component. It is usually regarded as being independent of other storm components, such as sea level (ζ) or storm-duration. However, the univariate analysis lead to an inaccurate estimation of marine drivers (Salvadori et al. 2014), so these cannot describe coastal processes adequately.
Multivariate extremes are difficult to predict directly from observational data, as there may be too few events of the relevant type amongst the observations. In the past, the fitting and extrapolation of the dependence functions between the variables as well as their marginal

Table 6.6: *Results of GPD for sea level ζ, selected threshold = 1.3 m)*

$T_R(y)$	1	2	5	10	50	100
$\zeta(mZMPS)$	1.54	1.64	1.74	1.81	1.94	1.99
lowerbound	-0.0010	-0.0024	-0.0047	-0.0068	-0.0121	-0.0147
upperbound	0.0011	0.0025	0.0049	0.0072	0.0127	0.0149

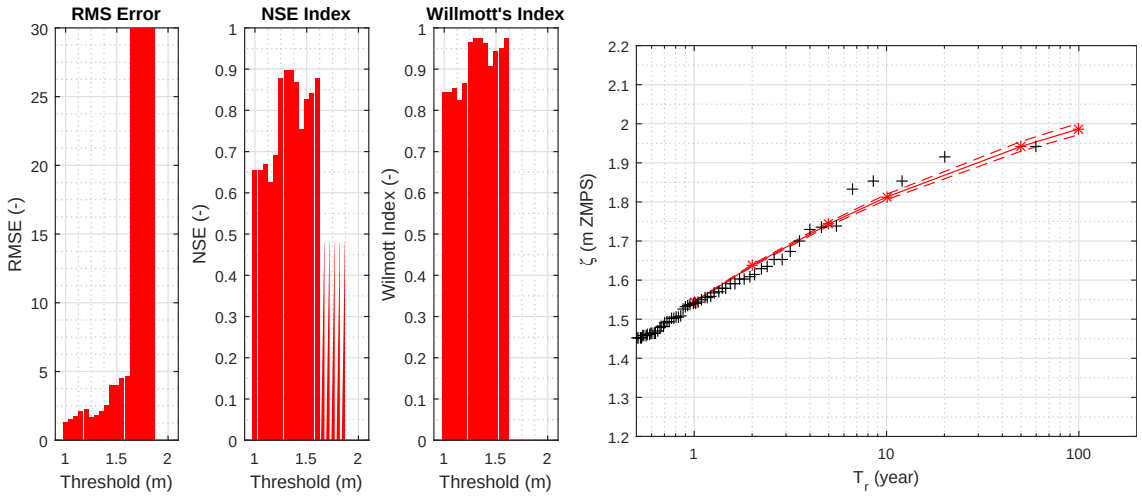

Figure 6.19: *a) Performance indexes (RMSE, NSE, D) used to estimate the reliability, b) Results of GPD for ζ, selected threshold = 1.3 m*

distributions have often involved complicated and/or subjective approaches.
Copulas are functions that describe dependencies among variables (see paragraph 2.3.2), and provide a way to create distributions that model correlated multivariate data (Dupuis and Jones 2006). The calibration of copulas on real data allow generating random sample that have the same dependence of the real quantities, in order to obtain a larger population and perform a more reliable multivariate statistical analysis.
To generate data with a distribution "just like" (in terms of marginal distributions and correlations) the distribution of real events, the following procedure must be done:

1. Transform the real data to the copula scale (unit square) using a kernel estimator of the cumulative distribution function;

2. Fit a copula, maximizing the log likelihood function (Bouyé et al. 2000);

3. Generate a random sample from the fitted copula;

4. Transform the random sample back to the original scale of the real data.

Fig. 6.20a shows the original events (red dots, Hs and ζ) and the samples (blue dots) generated according to the aforementioned procedure. Fig. 6.20 b) shows the bivariate pdf of wave heights and sea levels in blue scale. Black lines are the contours of equal joint exceedance probability (expressed as return period $Tr = 1/P$).
The establishment of coastal flooding risk maps is performed with the FORM method. This

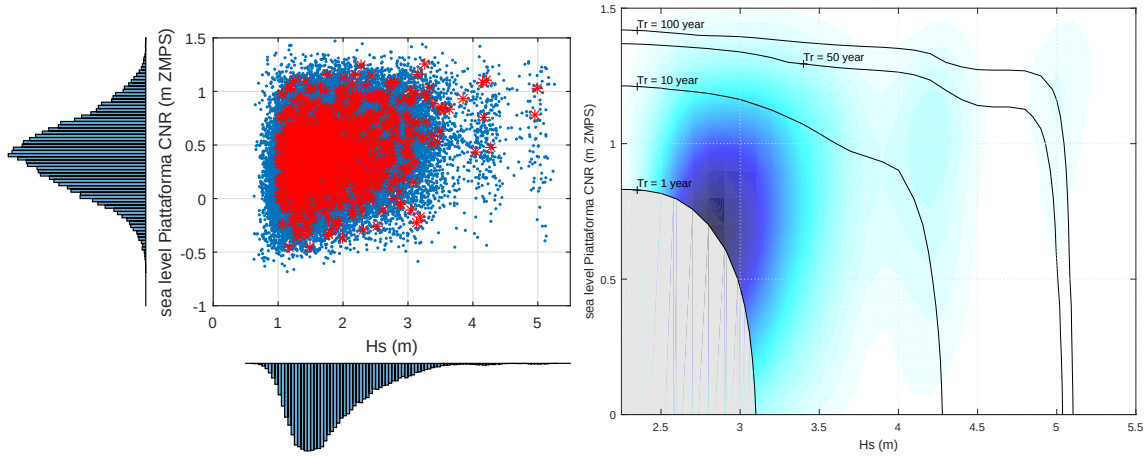

Figure 6.20: *a) Original events and generated samples b) Bivariate analysis shown as contours of equal joint exceedence probability.*

reliability method requires the transformation of the random variables $\mathbf{X} = [Hs, \zeta]$ to an equivalent standard normal random variable space $\mathbf{U} = [\mathrm{X}_H, X_\zeta]$. The procedure is described in paragraph 2.4. Fig. 6.21 shows the marginal distribution of the two selected variables in physical and standard space. The transformation is achieved through the Nataf transformation (explained in paragraph 2.4) and Fig. 6.22 shows the samples (Hs and ζ) in physical (red) and standard spaces (blue).

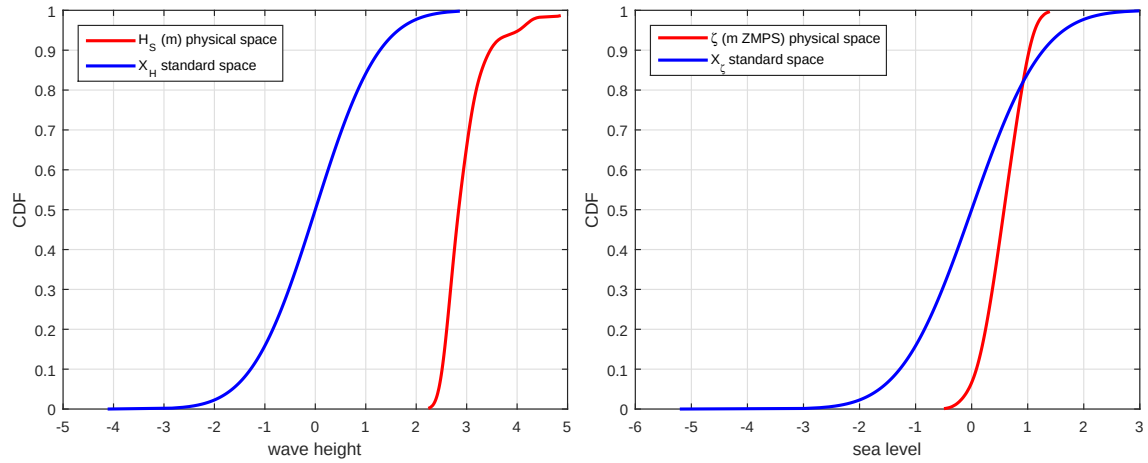

Figure 6.21: *a) Marginal distribution of Hs in physical and standard spaces, b) Marginal distribution of ζ in physical and standard spaces*

6.4 Coastal flooding in the Venetian littoral

The proposed inundation model (chapter 4) and the FORM analysis are applied in three different littoral cells in order to obtain flooding hazard maps. The failure mechanism associated to these maps is the flooding caused by the overtopping. The model does not take into account other failure mechanism, such as dunes breaching, infiltrations, etc. The selected stretches of the Venetian coast are: the Valle Vecchia coastline (littoral cell n°VE2), the Caorle coastline

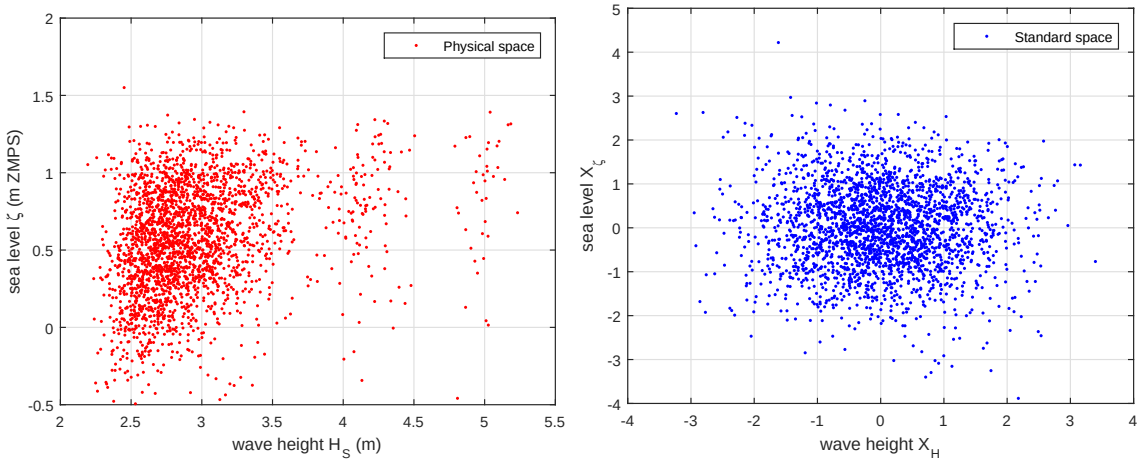

Figure 6.22: *Samples (Hs and ζ) in physical and standard spaces (Nataf transformation)*

(littoral cell n° VE3) and the Cavallino-Treporti coastline (n° VE6). The modelling steps and inputs are described in the following:

1) Definition of the offshore marine loads. 20 couple of wave heights Hs and sea levels ζ were chosen as offshore input and are reported in Fig. 6.23. The wave steepness is assumed to be $Hs/L = 0.04$ so the wave period Tp is estimated with the formula and the coefficient evaluated in paragraph 6.3.1(a): $Tp = 3.75Hs^{0.554}$. The total storm duration is assumed equal to 4 hours (peak duration, paragraph 6.3.1(b)), with 30 min of ramping up and 30 min of ramping down.

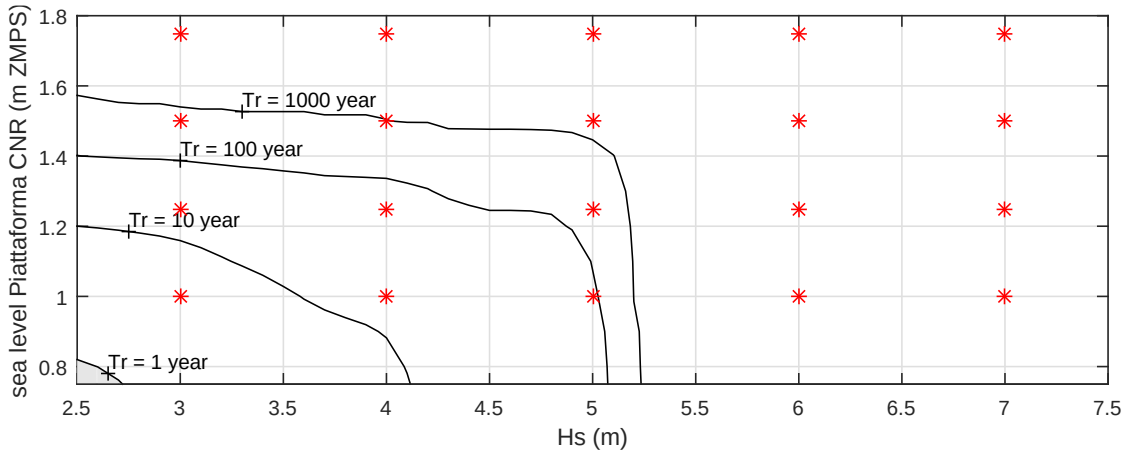

Figure 6.23: *Red dots are the couple Hs - ζ chosen as input for the models*

2) Definition of the boundary conditions at the shoreline. The wave transformation model from offshore to onshore (described in paragraph) is applied to each of the chosen couple Hs-ζ in order to estimate the value of the set-up Z and the residual wave height at the shoreline refereed to the Mean Sea Level MSL (an example is shown in Fig. 6.24). The final boundary condition is composed by a constant value $\zeta_{TOT} = \zeta + Z$ and an irregular impulsive signal with height equal to $H_{Residual}$ and period equal to the offshore period Tp (example in Fig. 6.25). The offshore value of ζ (initially given in m over the local datum Punta della

Salute) are now given in m (so 23 cm are subtracted from ζ) because bathymetry (levelled for the Venetian littoral in 2014) are referred to the world datum.

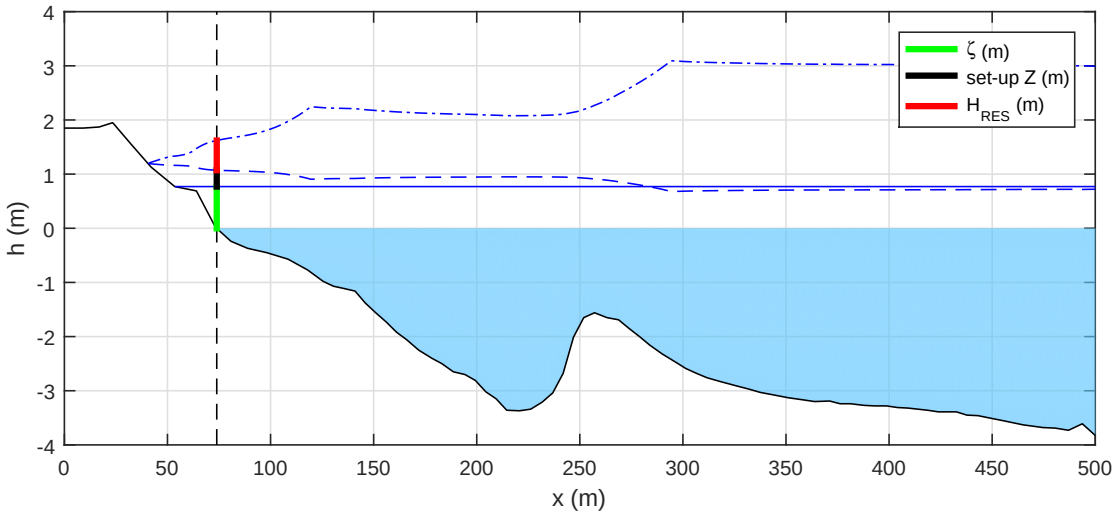

Figure 6.24: *Example of the wave transformation model results and definition of the boundary conditions at the depth 0 m (offshore loads are $Hs = 3$ m and $\zeta = 1$ m ZMPS = 0.77 m)*

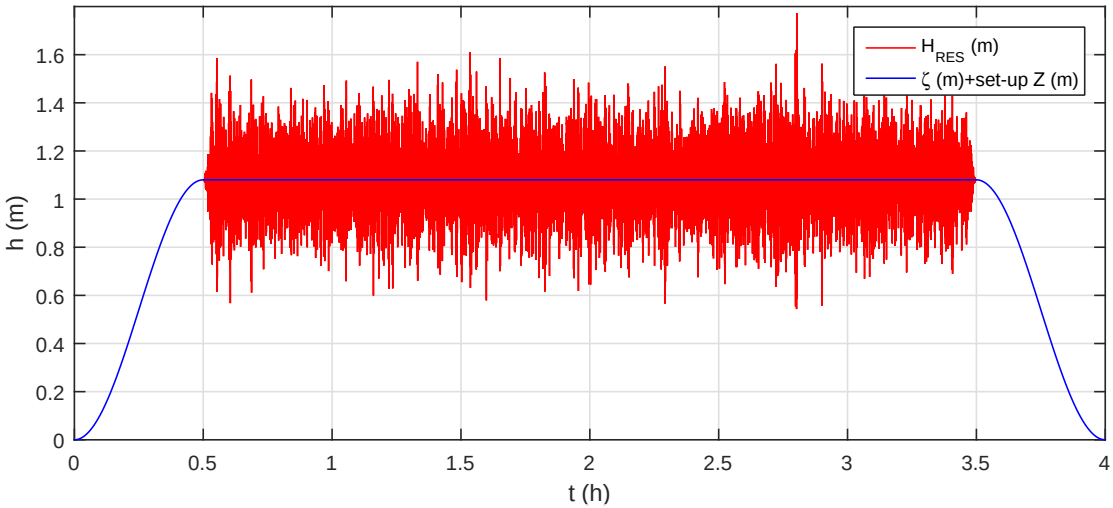

Figure 6.25: *Example of final boundary condition at the shoreline*

3) Coastal inundation modelling. The model for coastal flooding propagation, presented in paragraph 4.4, is applied. The essential data are: the position of the shoreline refereed to the MSL (or the position of the depth equal to 0 m MSL); the inland topography, here defined as the Digital Terrain Model DTM (levelled in 2012) from Lidar survey, with a grid size equal to 1 m; the roughness. Since maps of the land uses are not available, a uniform friction coefficient is applied $K_s = 33 m^3 s^{-1}$. For each of the 20 boundary conditions selected, the propagation model is run. The maximum water depth reached in each grid cell of the domain is saved and the obtained maps are flooding map relative to each couple of Hs and ζ.

4) Reliability analysis. The reliability analysis is performed with the FORM method

(paragraph 2.4). The probability of failure is defined as the probability that a portion of inland is flooded (with a least $h_F = 0.2$ m or 0.5 m of water depth) under certain values of wave height and sea level. Therefore, the limit state (explained in paragraph 2.4) is evaluated through an interpolation with the obtained results. In each cell of the domain the maximum water level reached during the simulation for a fixed value of ζ is plotted against the different values of Hs (Fig. 6.26a); then two couples that correspond to a water level in the cell equal to h_F (in Fig. 6.26a $h_F = 0.5$ m) are extrapolated. Finally, the transformation of the two couples from the physical space to the standard space is applied and the minimum distance β from the limit state to the origin of the standard space is computed (Fig. 6.26b).
The distance β is also called reliability index and it allow to easily evaluate the probability of failure p_f (Eq. 2.91).
The last step is the fulfilment of the hazard maps in terms of return period:

$$T_R = \frac{1}{N_y * p_f} \tag{6.2}$$

where N_y are the number of extreme events recorded in each year of observation (based on the data available in the Venetian littoral $N_y \approx 3.9677$). Maps will be also displayed in terms of probability of failure in a decade $p_{10} = 1 - (1 - T_R^{-1})^{T_L}$ (where $T_L = 10$ years).

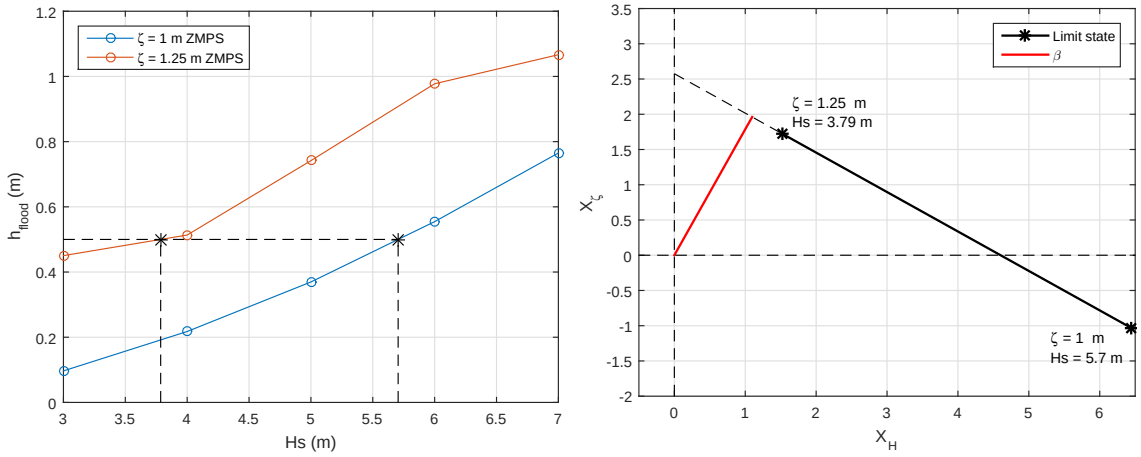

Figure 6.26: *a) Example of evaluation of the limit state in the physical space, b) Limit state in standard space g(**U**) and evaluation of the distance β*

6.4.1 Example of application to the Valle Vecchia coastline

The Valle Vecchia coastline (VE2 cell in Fig. 6.1) is 5.5 km long, its borders are the mouth of the lagoon's channel Baseleghe (Fig. 6.27, bottom left) to the North-East and the mouth of the lagoon's channel Falconera to the South-West. The entire cell is a major environmental area, protected and designated as Natura 2000 sites (SCI IT3250033 and SPA IT3250041), free of urban and tourist settlements and without any coastal defence structure. In the back-shore, a system of dunes is present. Behind the dunes, there are valleys and crop fields. The long-shore sediment transport, coming from the Northern cell (VE1) is equal to $\sim$ 50'000 m^3/year. Analysing the recent evolution of the shoreline, it is possible to verify that the cell is substantially in accretion, even if damages in the dunes, due to erosion, are present. In fact,

the risk of coastal flooding is very high and inundation occurred in the back-shore valley. The water has always entered through some interruptions (used mainly for transit) on the dunes (Fig. 6.27, top).

Figure 6.27: *Aerial photograph of Valle Vecchia (Caorle, Venezia - IT) with a path to access the beach; photograph of the mouth of the lagoon's channel Baseleghe and photograph of the beach "Spiaggia di Levante"*

Some available information and data concerning this littoral cell are drawn in a summary maps (Fig. 6.28) arranged by Ruol et al. (2016). The topography highlights different dunes, with crest high in the range 2m - 5m.
The aforementioned steps for the coastal flooding risk assessment are applied to the Valle Vecchia coastline. The figure 6.29 shows an example of flooding maps for Hs = 4 m and ζ = 1.75 m ZMPS: few areas are inundated, mainly next to the mouth of the lagoon's channel Falconera. The figure 6.30 shows the flooding maps for Hs = 6 m, ζ = 1.75 m ZMPS: the South-West area is partly flooded and the breaching occur along the dunes.
The figure 6.35 shows the flooded area and volume in the Valle Vecchia coastline for the 20 boundary conditions. Following the FORM methods, present hazard maps and ten-years failure probability maps are arranged. The chosen limit states are 0.2 m (present map Fig. 6.31 and ten-year map Fig. 6.33) and 0.5 m (present map Fig. 6.32 and ten-year map Fig. 6.34).

Figure 6.28: *Summary maps for the Valle Vecchia coastline (cell VE2) from Ruol et al. (2016)*

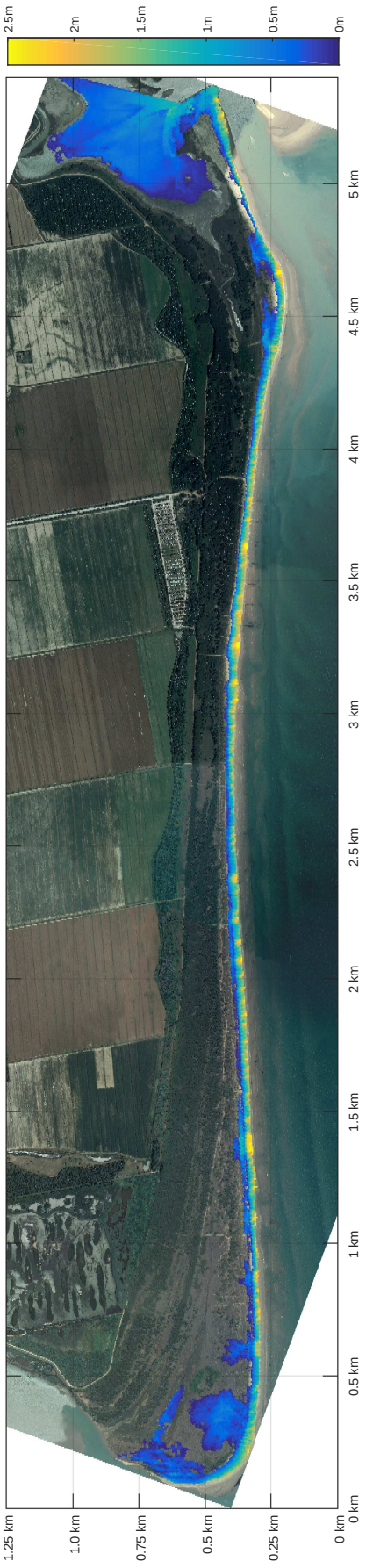

Figure 6.29: *Flooding map (cell VE2): $Hs = 4\ m$, $\zeta = 1.75\ m$ ZMPS*

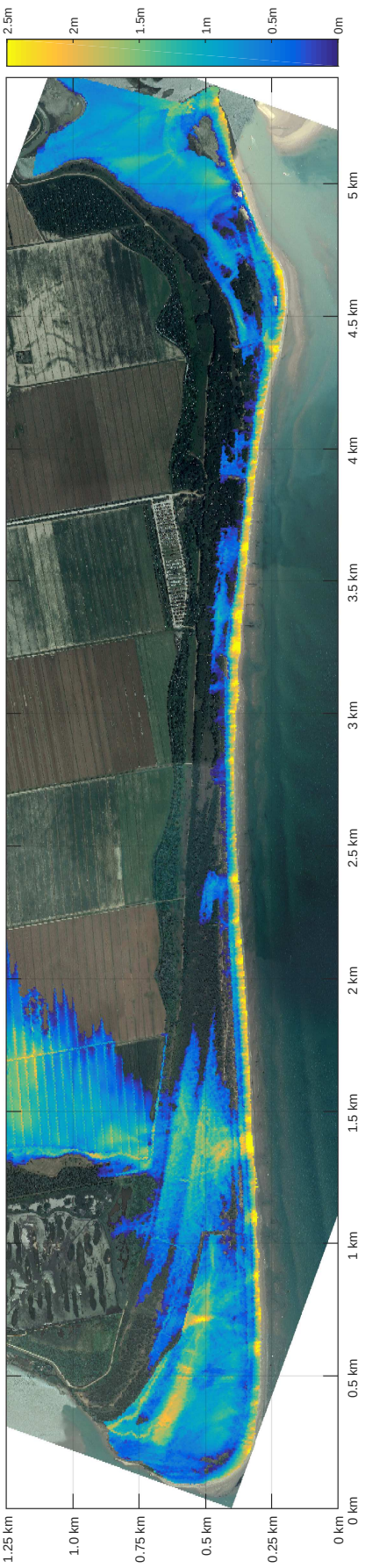

Figure 6.30: *Flooding map (cell VE2): $Hs = 6\ m$, $\zeta = 1.75\ m$ ZMPS*

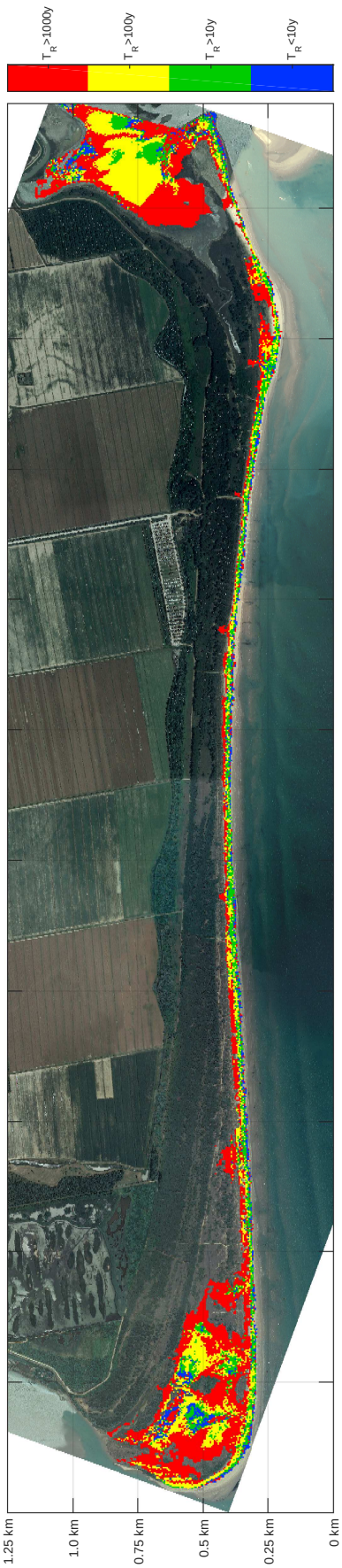

Figure 6.31: *Present hazard map (cell VE2): Probability that flooding level 0.2 m is exceeded, expressed as return period T_R*

Figure 6.32: *Present hazard map (cell VE2): Probability that flooding level 0.5 m is exceeded, expressed as return period T_R*

Figure 6.33: *Ten-years failure probability map (color-scale p_f =[0 1]) for a flooding level equal 0.2 m (cell VE2)*

Figure 6.34: *Ten-years failure probability map (color-scale p_f =[0 1]) for a flooding level equal 0.5 m (cell VE2)*

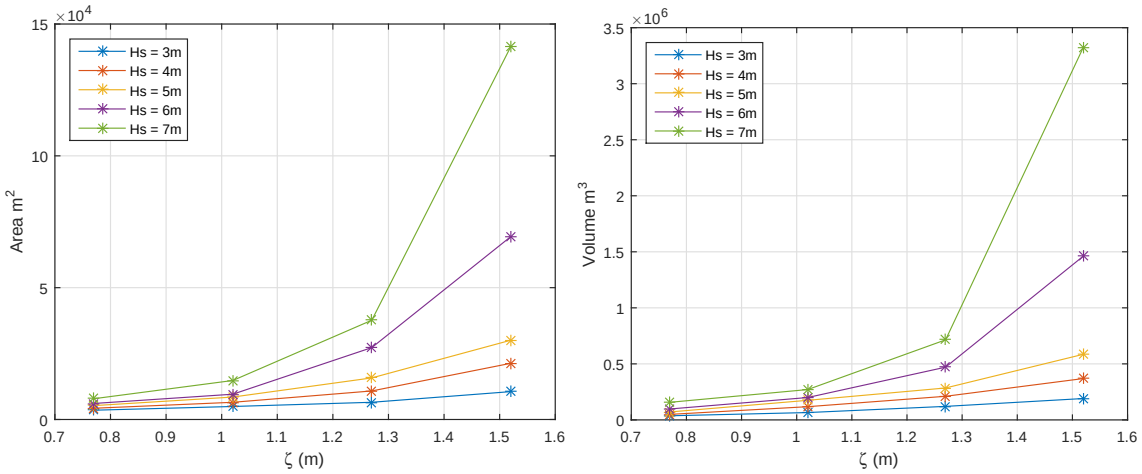

Figure 6.35: *Flooded area and volume for the VE2 cell for all the simulated conditions*

6.4.2 Example of application to the Caorle coastline

The Caorle coastline (VE3 cell in Fig.6.1) is 5 km long, its borders are the mouth of the lagoon's channel Falconera to the North and the mouth of the River Livenza to the South, both armoured with jetties. The economy is based mainly on tourism ($\sim$ 4'500'000 visitors in 2017) and fishing. The cell can be subdivided into three main part: i) "Spiaggia di Levante" at North East, ii) "Murazzi" in the central part; iii) "Spiaggia di Ponente" at South-West (Fig. 6.36). The first stretch of this coast at North-East (named "Spiaggia di Levante", Fig. 6.36) has a normal shoreline direction equal to 140° N, very different from the adjacent ones. This coast is characterized by very fine sediments, with silty fraction that causes drainage problems and occasionally, during the most intense precipitation, the formation of puddles. The emerged beach is very wide and the submerged beach is characterized by gentle slopes. The longshore sediment transport is $\sim$ 20,000 m^3/year, South-West directed.
In the central part, it is located the historic centre of Caorle. This stretch of coast (800 m long) is bordered at North by a cusp, where it is located a church named "Chiesa della Madonna dell'Angelo" (Fig. 6.36). In order to mitigate the risk to human health, economic activities and cultural heritage, the shoreline position in the central area is stabilized by a sea wall (named "Murazzi").
In the Southern part, the longshore sediment transport remains approximately equal to 20,000 m^3/year, directed from North-East to the South-West. This sand nourishes partly the beach named "Spiaggia di Ponente", partly deposits in the area next to the jetty of the mouth of the river Livenza and only a few thousand m^3 goes to the Southern cell (VE4).
Some available information and data concerning this littoral cell are drawn in a summary maps (Fig. 6.38) arranged by Ruol et al. (2016). The topography shows that the city is partially lower than 0.5 m and no system of dunes are present.
The aforementioned steps for the coastal flooding risk assessment are applied to the Caorle coastline. The figure 6.39 shows an example of flooding maps for Hs = 4 m and ζ = 1.75 m ZMPS: the city is only partly inundated and the flooded areas are next to the two river mouth. The figure 6.40 shows the flooding maps for Hs = 6 m, ζ = 1.5 m ZMPS: the historic town is partly flooded and the breaching occur at the Southern bound of the seawall. The figure 6.37 shows the flooded area and volume in the Caorle coastline for the 20 boundary conditions.

Following the FORM methods, present hazard maps and ten-years failure probability maps are arranged. The chosen limit states are 0.2 m (present Fig. 6.41 and ten-year Fig. 6.43) and 0.5 m (present Fig. 6.42 and ten-year Fig. 6.44).

Figure 6.36: *Aerial photograph of Caorle (Venezia - IT); photograph of the North-East beach "Spiaggia di Levante" and photograph of the "Chiesa della Madonna dell'Angelo"*

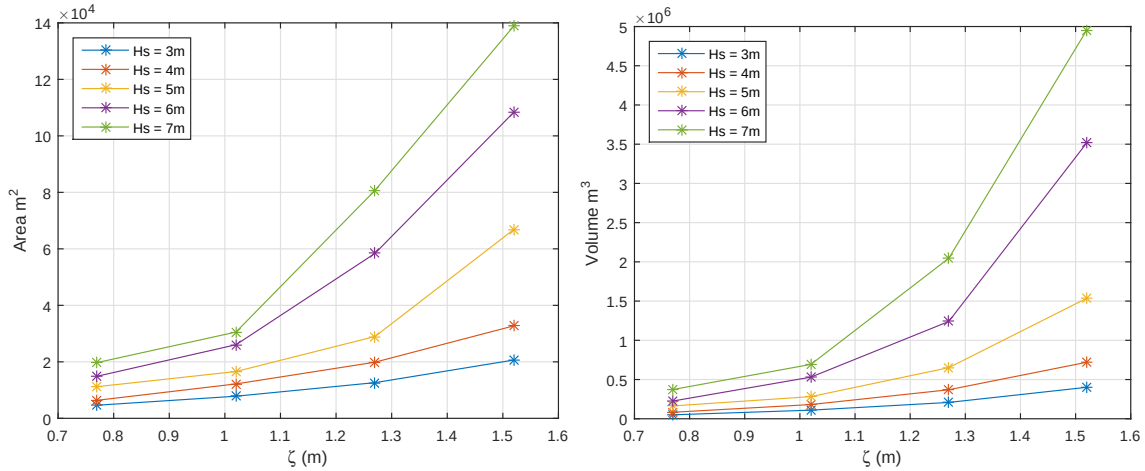

Figure 6.37: *Flooded area and volume for the Caorle coastline for all the simulated conditions*

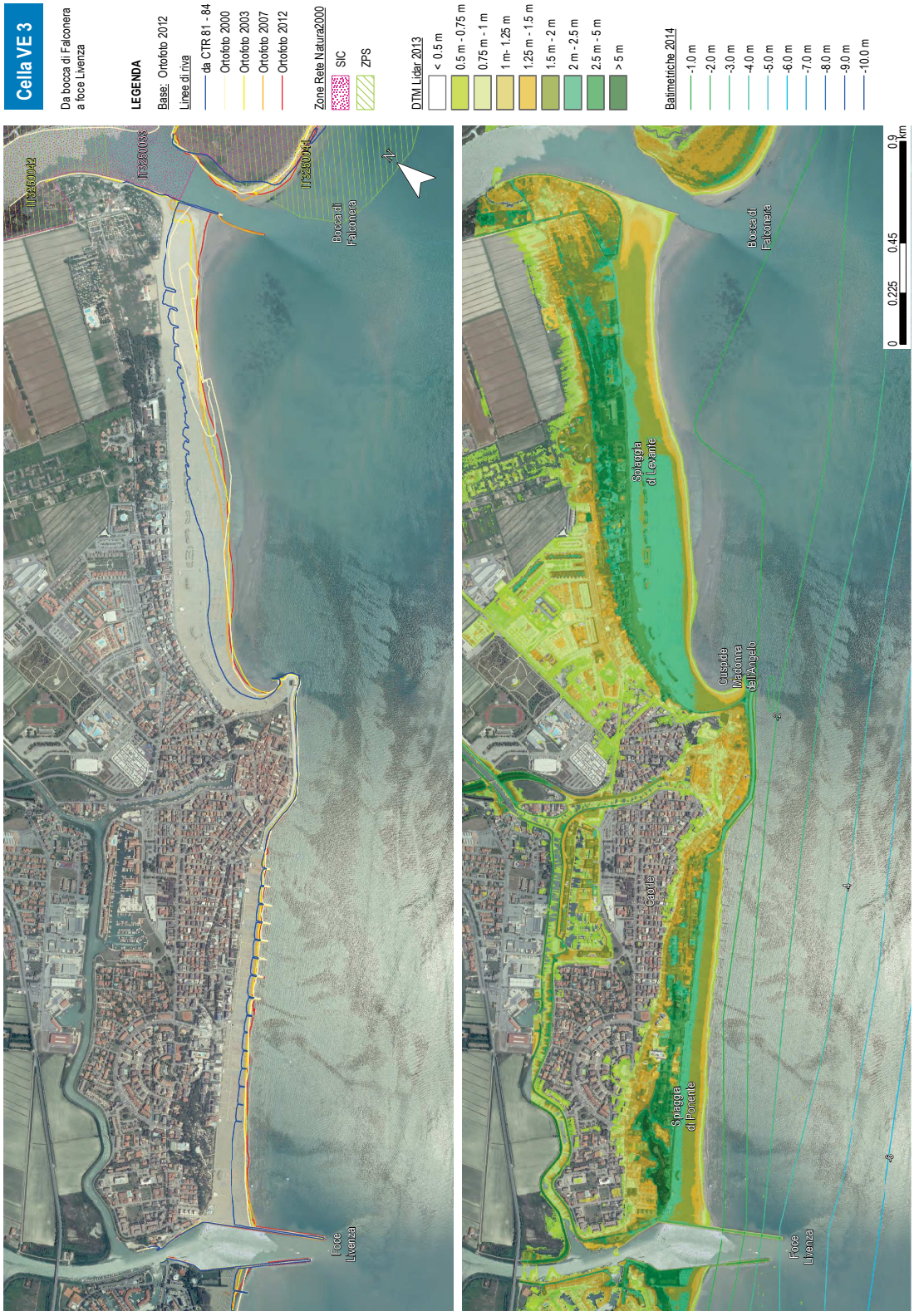

Figure 6.38: *Summary maps for the Caorle coastline (cell VE3) from Ruol et al. (2016)*

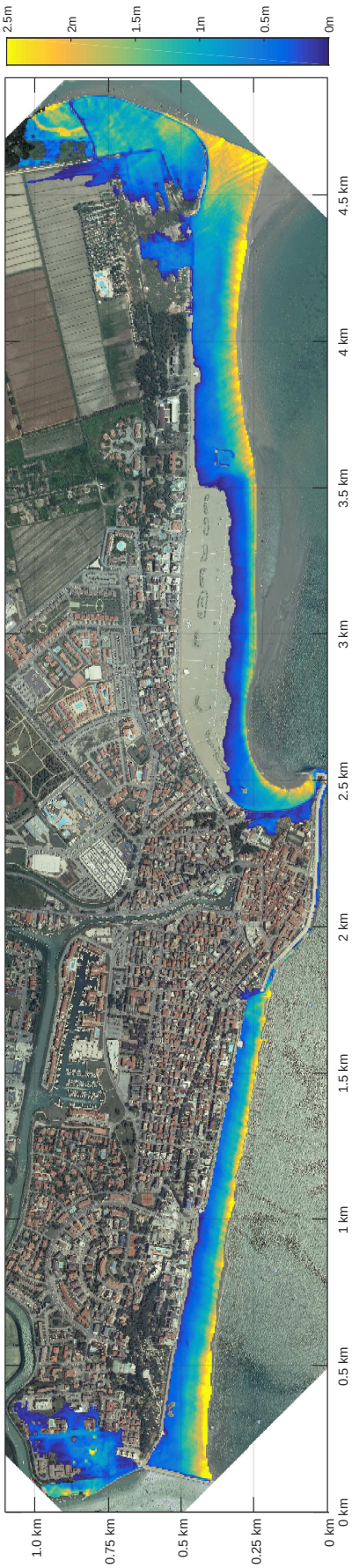

Figure 6.39: *Flooding map (cell VE3): $Hs = 4$ m, $\zeta = 1.75$ m ZMPS*

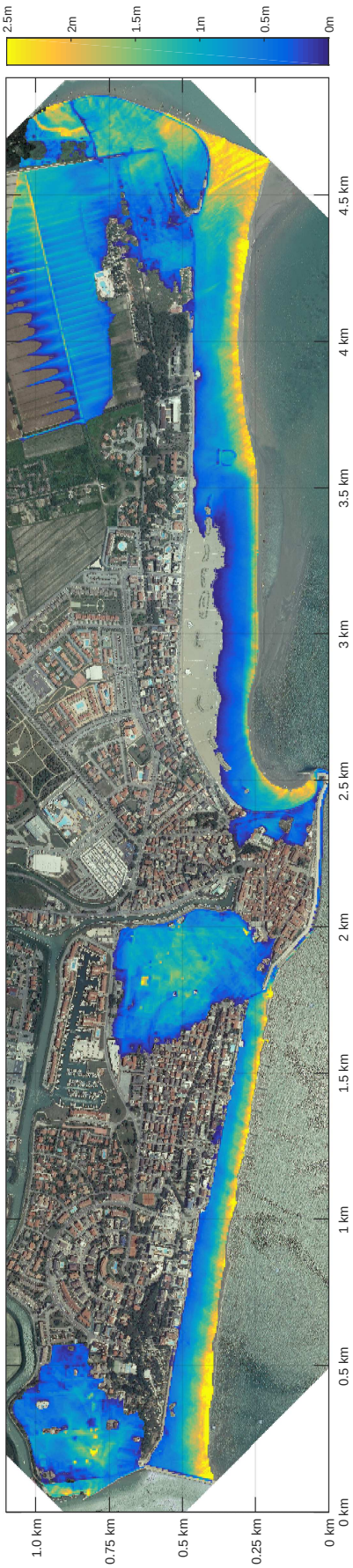

Figure 6.40: *Flooding map (cell VE3): $Hs = 6$ m, $\zeta = 1.5$ m ZMPS*

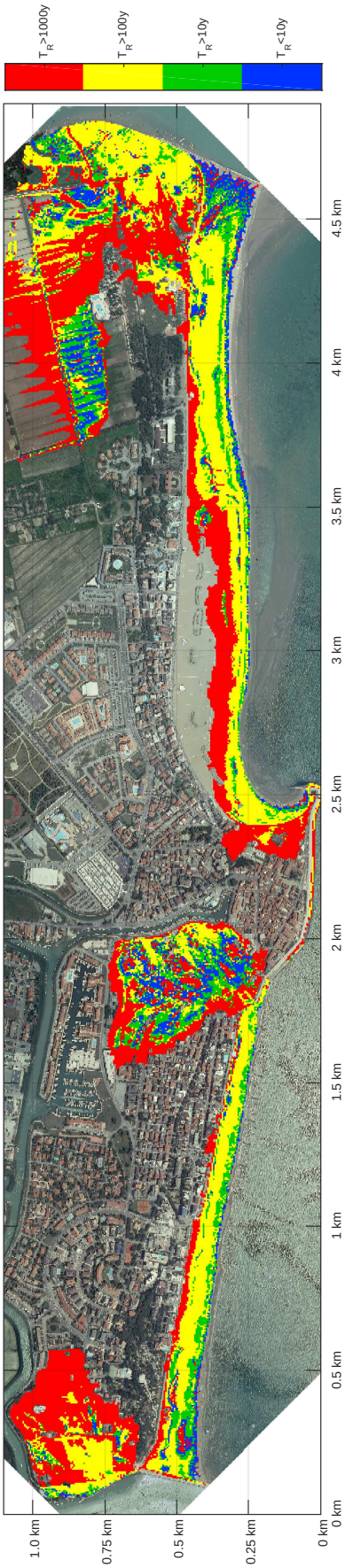

Figure 6.41: *Present hazard map (cell VE3): Probability that flooding level 0.2 m is exceeded, expressed as return period T_R*

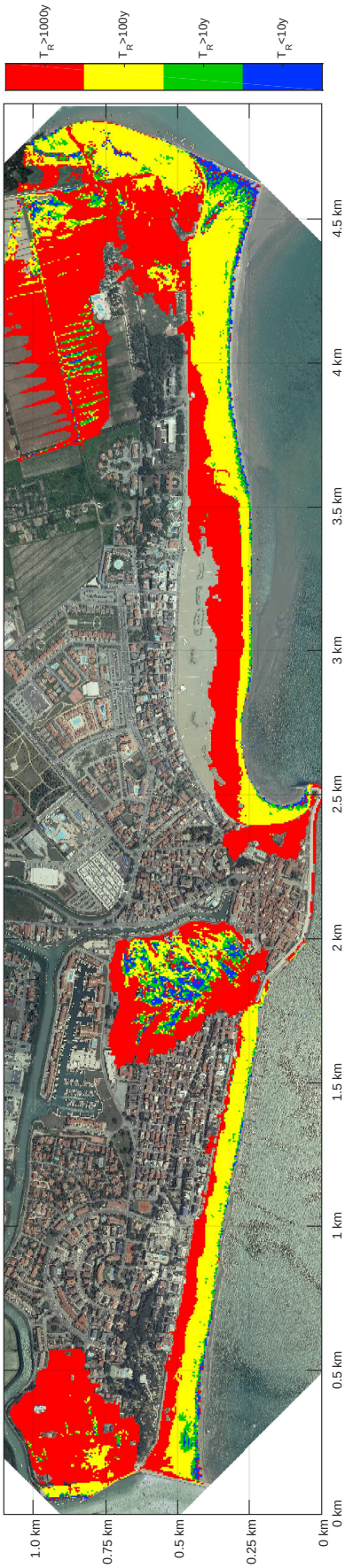

Figure 6.42: *Present hazard map (cell VE3): Probability that flooding level 0.5 m is exceeded, expressed as return period T_R*

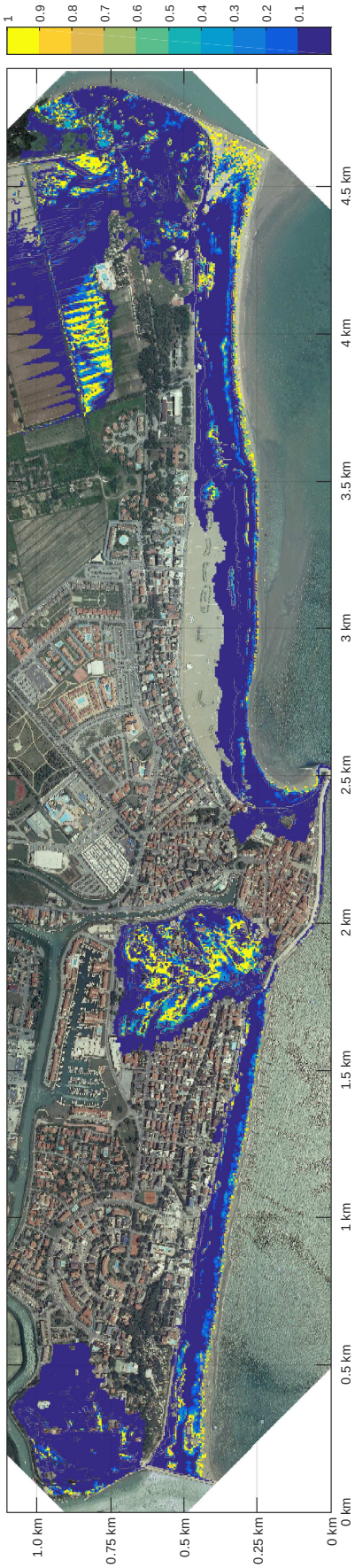

Figure 6.43: *Ten-years failure probability map (color-scale p_f =[0 1]) for a flooding level equal 0.2 m (cell VE3)*

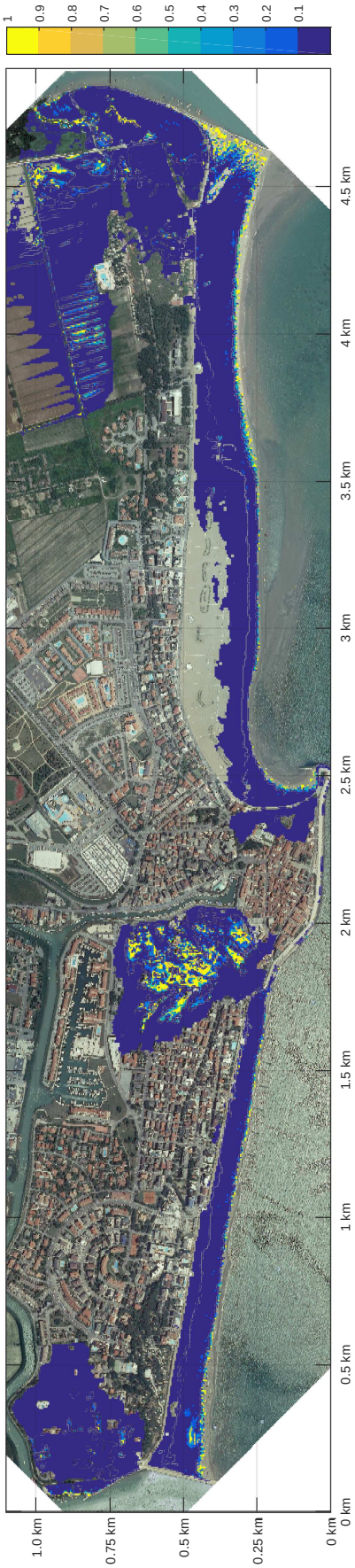

Figure 6.44: *Ten-years failure probability map (color-scale p_f =[0 1]) for a flooding level equal 0.5 m (cell VE3)*

6.4.3 Example of application to the Cavallino-Treporti coastline

The Cavallino-Treporti coastline (VE6 cell in Fig. 6.1) is 15 km long peninsula between the Adriatic Sea and the Venice lagoon. Its borders are the mouth of the River Sile (Fig. 6.45, bottom left) to the North-East and one of the mouths of the lagoon of Venice (named Bocca di Lido) to the South-West. The mouths are both armoured with jetties and the latter is one of the channels involved in the Mose project. Along the coast, the economy is based mainly on tourism (∼6'000'000 visitors in 2016, Fig. 6.45, top), while the inner part is dedicated to intensive agriculture (Fig. 6.45, bottom right).

Figure 6.45: *Cavallino-Treporto beach, Aerial photograph of mouth of the river Sile; Aerial photograph of the Cavallino-Treporti (Venice - IT)*

Thanks to an extensive nourishment completed at the end of the 90s and to periodic nourishment (20'000 m^3/year), the coastline is stable. The jetty at the Bocca di Lido intercepts about 60% of the longshore sediment transport, which is equal to 50'000 m^3/year directed from NE to SW. In fact, the shoreline variation in the last 30 years highlights an advance of 100 m.
The planning of mitigation actions against coastal flooding is essential on this coastline in order to defend the tourist activities (e.g. camp-grounds) and the Venice lagoon. Some available information and data concerning this littoral cell are drawn in a summary map (Fig. 6.46) arranged by Ruol et al. (2016). The topography highlight different dunes, with crest high in the range 2m - 5m.
The aforementioned steps for the coastal flooding risk assessment are applied to the Valle Vecchia coastline. The figure 6.48 shows an example of flooding maps for $Hs = 4$ m and $\zeta = 1.75$ m ZMPS: few areas (with camp-grounds) are inundated, mainly in the North-East side.

Figure 6.46: *Summary maps for the Cavallino-Treporti coastline (cell VE6) from Ruol et al. (2016)*

The figure 6.49 shows the flooding maps for $Hs = 6$ m, $\zeta = 1.25$ m ZMPS: while with a lower value of ζ, some camp-grounds are inundated. The figure 6.37 shows the flooded area and volume in the Cavallino-Treporti coastline for the 20 boundary conditions.
Following the FORM methods, present hazard maps and ten-years failure probability maps are arranged. The chosen limit states are 0.2 m (present Fig. 6.50 and ten-year Fig. 6.52) and 0.5 m (present Fig. 6.51 and ten-year Fig. 6.53).

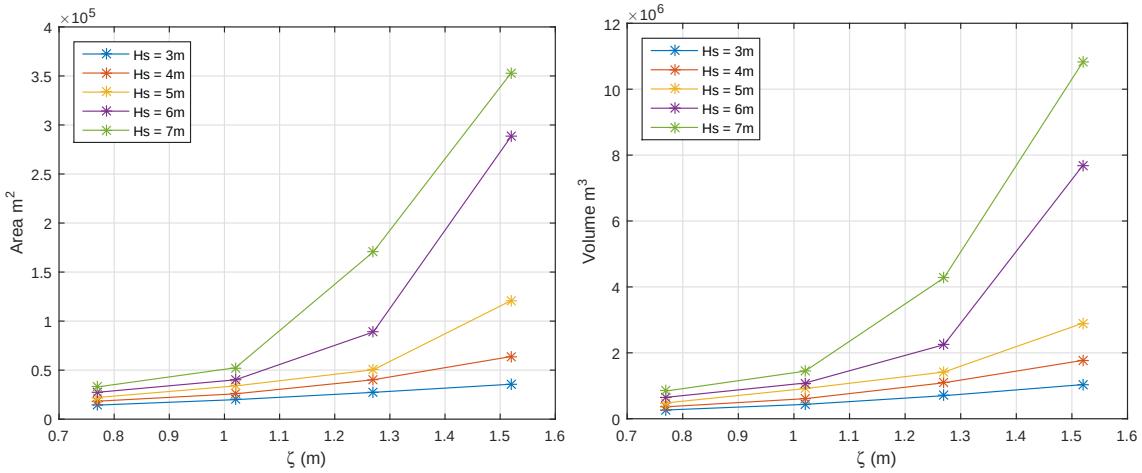

Figure 6.47: *Flooded area and Volume for the Cavallino-Treporti coastline (cell VE6) for all the simulated conditions*

6.5 Future scenario of coastal flooding in the Venetian littoral (IPCC projection of Global Mean Sea Level Rise)

The same analysis was repeated considering a projection of the sea level rise in the next years, in order to obtain some information on the future hazard.

The fifth Assessment Report (AR5, Stocker et al. 2013) adopted four greenhouse gas concentration trajectories, named Representative Concentration Pathways (RCPs). The pathways are used for climate modeling and research activities and describe four possible climate futures, all of which are considered possible depending on how much greenhouse gases are emitted in the years to come.
The four RCPs, RCP2.6, RCP4.5, RCP6.0, and RCP8.5, are named after a possible range of radiative forcing values in the year 2100 relative to pre-industrial values (+2.6, +4.5, +6.0, and +8.5 W/m^2, respectively). The RCPs are consistent with a wide range of possible changes in future anthropogenic (i.e., human) greenhouse gas (GHG) emissions, and aim to represent their atmospheric concentrations.
The four RCPs are also consistent with certain socio-economic assumptions but are to be substituted with the Shared Socio-economic Pathways which are anticipated to provide flexible descriptions of possible futures within each RCP. Mid- and late-21st century (2046-2065 and 2081-2100 averages, respectively) projections of global warming and global mean sea level rise from the IPCC Fifth Assessment Report (IPCC AR5 WG1) are tabulated in Table 6.7 and shown in Fig. 6.54 for the four scenarios considered.

Figure 6.48: *Flooding map (cell VE6): $Hs = 4$ m, $\zeta = 1.75$ m ZMPS*

Figure 6.49: *Flooding map (cell VE6): $Hs = 6$ m, $\zeta = 1.25$ m ZMPS*

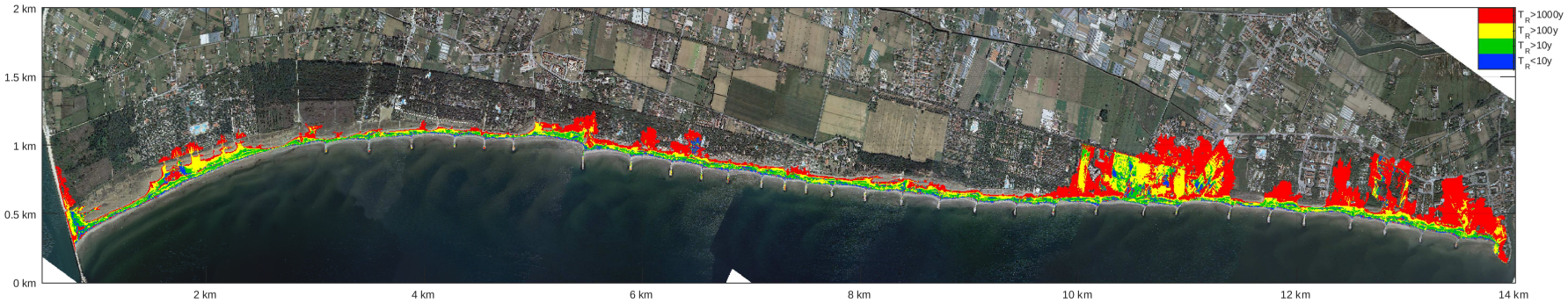

Figure 6.50: *Present hazard map (cell VE6): Probability that flooding level 0.2 m is exceeded, expressed as return period* T_R

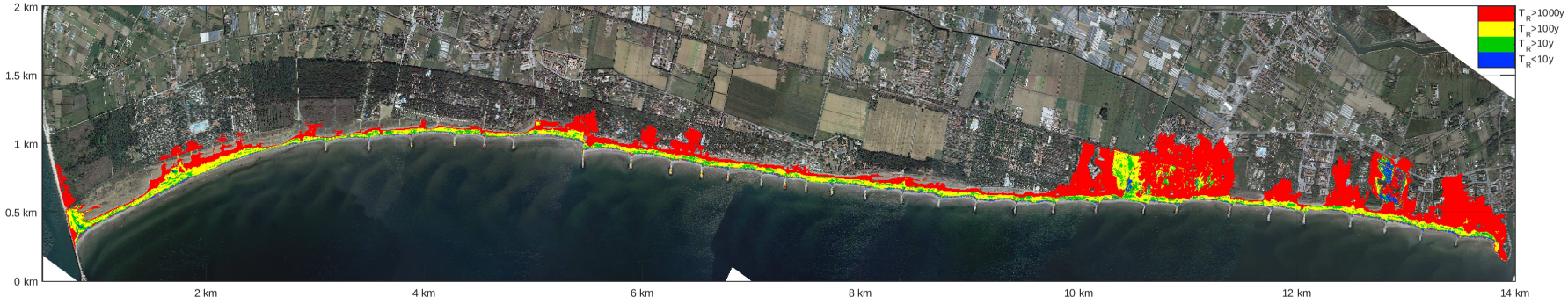

Figure 6.51: *Present hazard map (cell VE6): Probability that flooding level 0.5 m is exceeded, expressed as return period* T_R

Figure 6.52: *Ten-years failure probability map (color-scale p_f =[0 1]) for a flooding level equal 0.2 m (cell VE6)*

Figure 6.53: *Ten-years failure probability map (color-scale p_f =[0 1]) for a flooding level equal 0.5 m (cell VE6)*

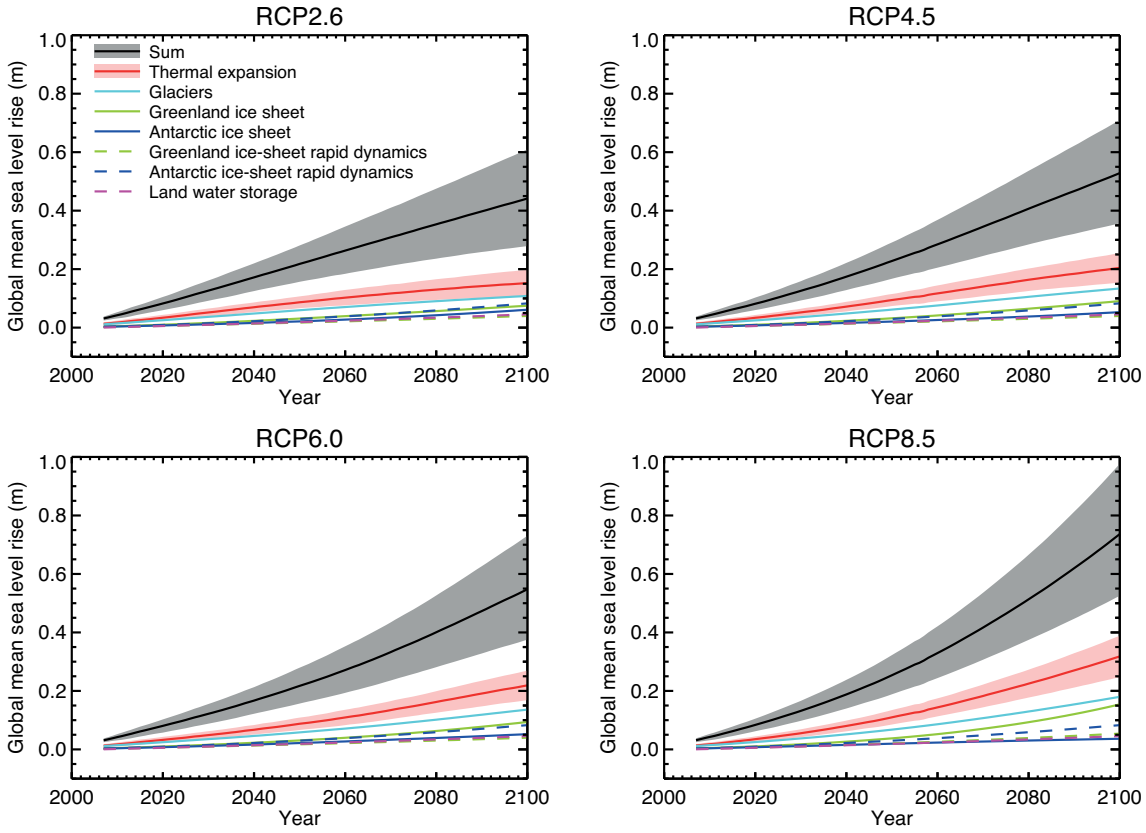

Figure 6.54: *Projections from process-based models of global mean sea level (GMSL) rise relative to 1986–2005 and its contributions as a function of time for the four RCP scenarios (from Stocker et al. 2013).*

Table 6.7: *AR5 Stocker et al. (2013) global mean sea level (m) increase projections, starting from 2013*

Scenario	2046 - 2065 Mean and likely range	2081 - 2100 Mean and likely range
RCP2.6	0.24 [0.17 to 0.32]	0.40 [0.26 to 0.55]
RCP4.5	0.26 [0.19 to 0.33]	0.47 [0.32 to 0.63]
RCP6.0	0.25 [0.18 to 0.32]	0.48 [0.33 to 0.63]
RCP8.5	0.30 [0.22 to 0.38]	0.63 [0.45 to 0.82]

The projections are relative to temperatures and sea levels in the late-20th to early-21st centuries (1986-2005 average).The lines show the median projections and for GMSL rise (black line) and the thermal expansion contribution (red line), the likely range is shown as a shaded band. The contributions from ice sheets include the contributions from ice-sheet rapid dynamical change, which are also shown separately.
The coastal flooding model was rerun only for the VE2 littoral cell (Valle Vecchia coastline) considering the mean sea level rise projection in 2050 for the RPC8.5 scenario (mean GMSL

rise $\sim$ 0.3m starting from 2013, the same year of the topography survey).
Fig. 6.55 shows the results of this analysis in terms of variation of area relative to different return periods. Obviously, the area that is characterized by a return period lower than 10 years increases in the future, reaching the almost total area that can be flooded.

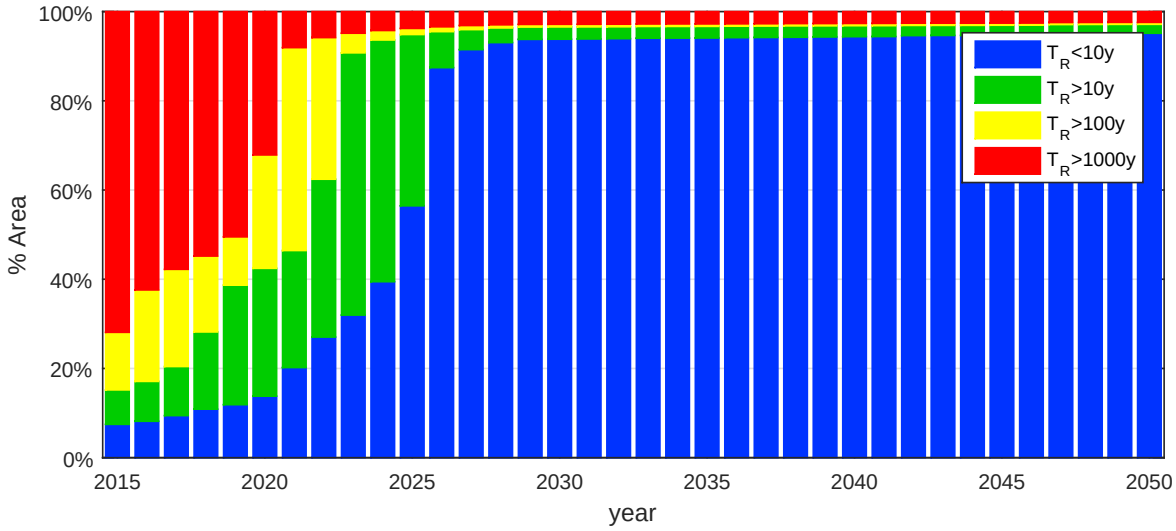

Figure 6.55: *Variation of area relative to 4 values of return period* T_R

Chapter 7

Conclusions

This thesis presents a numerical model for the inland flood propagation and an approach for the assessment of coastal flooding vulnerability. The proposed model is a novel 2D model that solves the shallow-water equations using a linearised friction term and assumes negligible convective accelerations. The formulation takes advantage of a grid-based vectorization and a positivity preserving scheme. The key feature of this model is the fast computational speed obtained by means of a formulation suited to GPU cards, thus making it ideal for handling high-resolution maps on a regional scale. In a typical coastal flooding simulation, the computational time using a GPU was found to be 3% of the time using a CPU.

The performance of the proposed model was verified by comparing the results with some well-known benchmarks. The good agreement found between the model results and the analytical solution of an oscillatory flow in a parabolic basin (Nash-Sutcliffe index $NSE > 0.996$), highlights the ability of the model to simulate a phenomenon that involves wet/dry interfaces in a very large domain (diameter of the basin equal to 10 km). The magnitude of the advection terms was studied through the comparison with a set of experiments that investigate the solitary wave run-up on a simple beach (Synolakis 1987), where the length scale of the phenomena is very small. In this test, advection terms were found 500 times smaller than the other terms (inertial and friction terms), proving that the achievable improvement including convection for inland coastal flooding (so in absence of small-scale features) is not significant. The model, together with a wave transformation model, was also applied to a real case study of a flooding event on the Venetian littoral in December 2008. The results show a good match between the simulations and the real flooded area documented by a video and a report.

The final goal is to provide a robust and reliable tool for the assessment of coastal flooding hazard along the littoral. An extensive application to the Venetian coast was carried out, thanks to a wide geomorphological and hydraulic knowledge of this regional area. The statistical analysis of the main marine drivers acting on this coast was carried out in order to force the wave transformation model and obtain the boundary condition to be imposed at the shoreline. Finally, a reliability analysis was applied to the results gained through the flooding propagation model, establishing the desired hazard maps.
The methodology seems promising and meets the requirements of local stakeholders for a flexible tool that predicts coastal flooding and highlights the more exposed and vulnerable areas, as the hardware required (GPU) to run the model is certainly well within the financial

and technical means of local administrations, unlike the large cluster of CPUs needed to run the existing operational dynamic models.

7.1 Recommendations for future work

From a more general perspective, the methodology can be easily coupled with other models in order to include other key aspects of the coastal flooding assessment. For example, the boundary conditions can be linked with meteorological models to include the effects of hurricanes, typhoons and cyclones and/or with riverine models. In fact, the combinations of multiple phenomena, not only related to sea conditions, frequently exacerbate the effect of marine inundation. For instance, the simultaneous occurrence of intense precipitations or river overflows (in areas such as deltas and estuaries) with extreme waves and sea levels could contribute to coastal flooding. Similarly, the presence of a drainage system could be less efficient than expected during sea storm (Fig. 7.1).

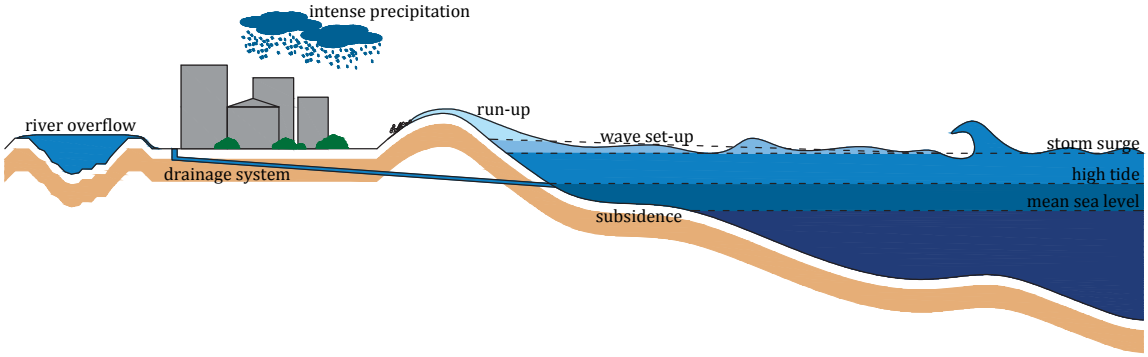

Figure 7.1: *Combinations of multiple phenomena that exacerbate coastal flooding*

It must be underlined that only a single failure mechanism is taken into account, i.e. the overtopping. However, other features, that influence failure in the long term, are, for example, erosion and, more generally, morphological changes in the topography (for example the breaching of coastal defence structures such as dunes and dikes). The inclusion of this mechanism is not straightforward since involves a deep knowledge of sea-dike/dune resistance and, in the long term, its maintenance strategy (e.g nourishment, dunes reinforcement).
Finally, the produced hazard maps could be integrated with information on the exposed values in the coastal area (e.g. number of inhabitants potentially affected, type of economic activity of the area potentially affected, etc.) in order to prepare flood risk maps that show the potential adverse consequences for human health, the environment, cultural heritage and economic activity associated with coastal flooding.

Appendix A

Wave and sea level data

The waves and sea levels dataset used for the statistical analyses are here reported. Data comes from measurements (1987 - 2017) performed at the oceanographic tower "Acqua Alta" situated in 16 m of water (MLLW) in the Gulf of Venice (Lat 45° 18' 51,27" N, Lon: 12° 30' 29,93" E). Different wave gauges have been used since the start of the measurements at the Acqua Alta research tower and the instrument system has been progressively upgraded and repositioned during maintenance operations. The measured data include: significant wave height Hs (m), maximum wave height $Hmax$, mean period Tm and peak period Ts (s), mean wave direction (°N), sea level z (m referred to Punta della Salute).
Fig. A.1 shows an interval of the measurements and Fig.s A.2 - A.7 show the whole time series of waves and sea levels for three time periods. The figures highlight the storms with a maximum larger than 1 m (green dots, 974 storms) and larger than 2.5 m (red dots, 126 storms). The independent storm (forming the data sample for the statistical analyses) were selected following the procedure described in paragraph 6.3.1. In the sea levels series, the red dots indicate the simultaneous measures to the $Hs > 2.5$ m.
Tab.s A.1 report the 126 storms with maximum larger than 2.5m.

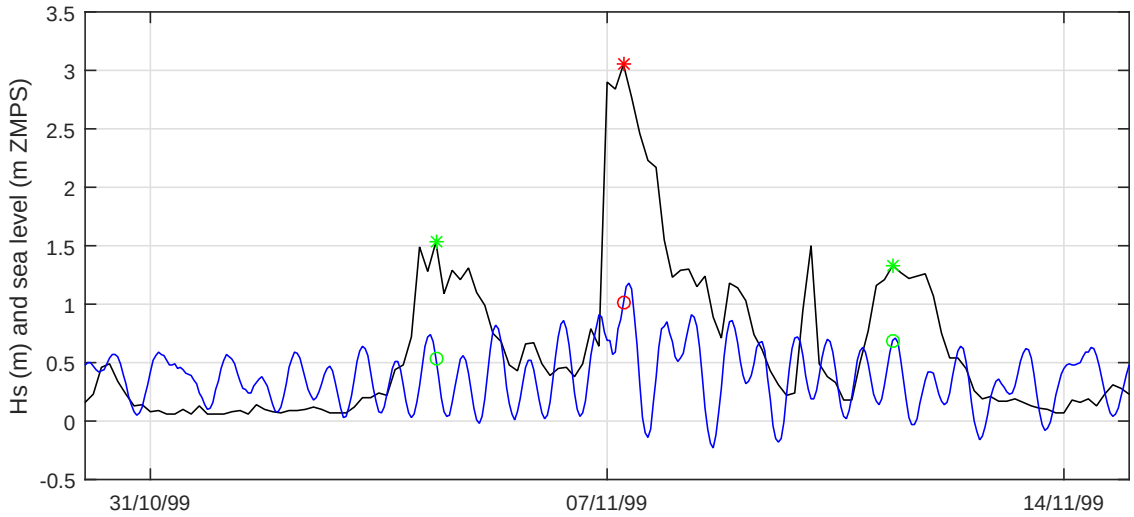

Figure A.1: *Example of portion of the time series of significant wave height Hs (black) and sea levels (blue) measured at the "Acqua Alta" tower*

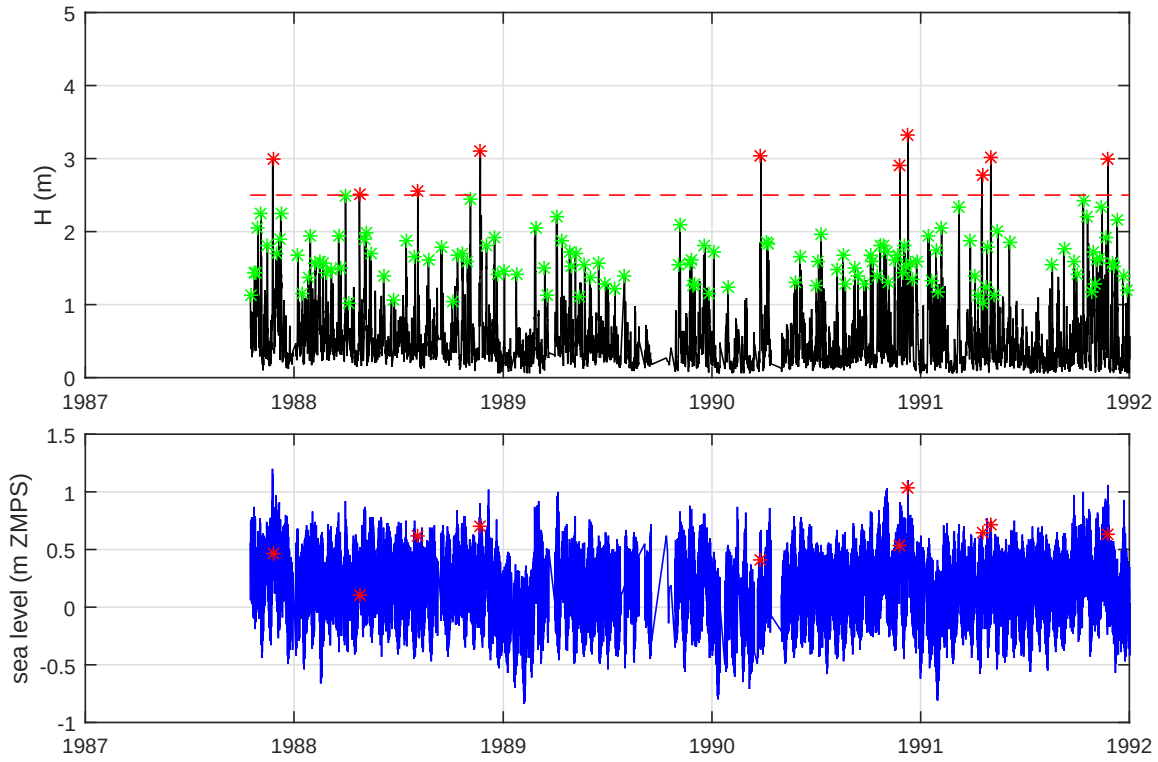

Figure A.2: *Time series (1987 - 1992) of significant wave height Hs and peak over threshold 1 m (green) and 2.5 m (red) and sea levels (below) measured at the "Acqua Alta" tower*

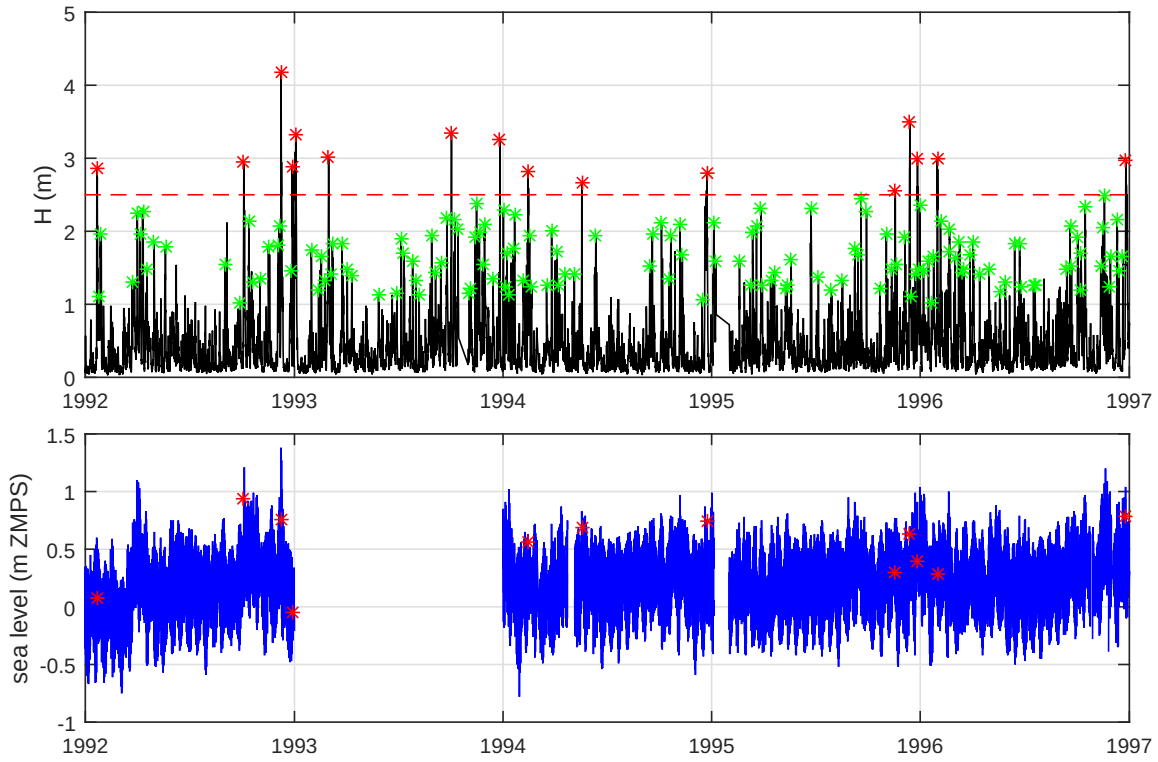

Figure A.3: *Time series (1992 - 1997) of significant wave height Hs and peak over threshold 1 m (green) and 2.5 m (red) and sea levels (below) measured at the "Acqua Alta" tower*

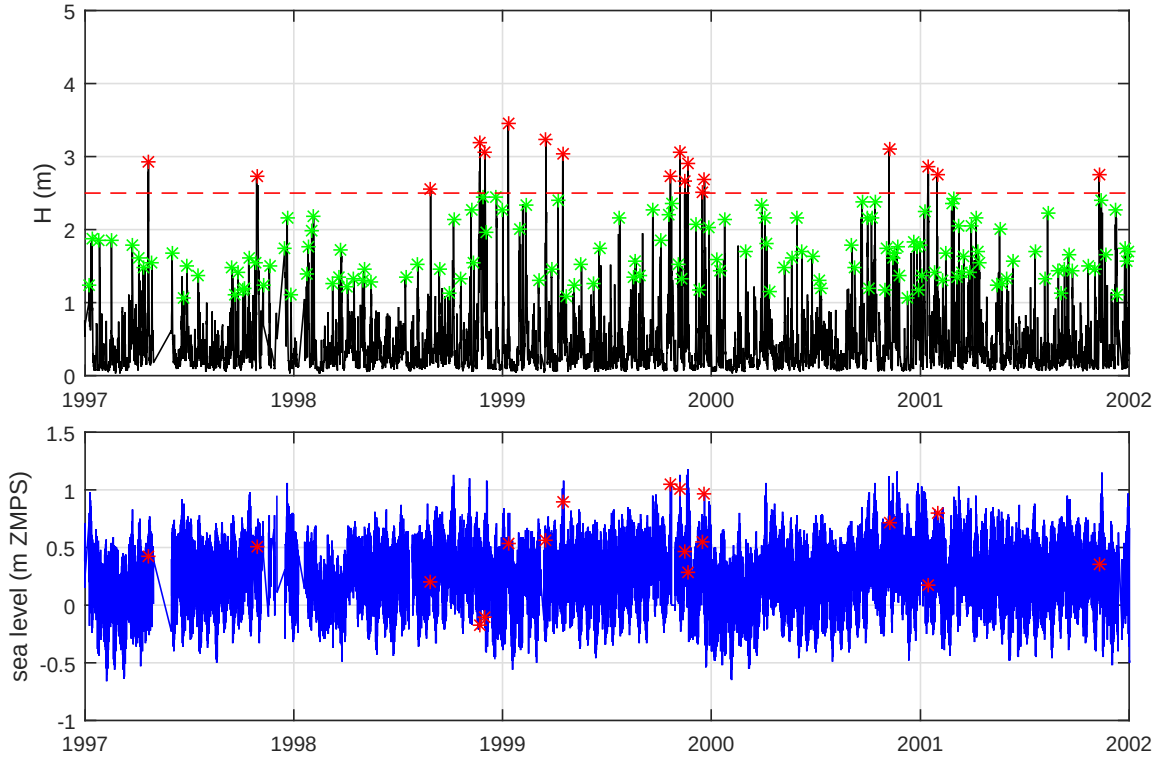

Figure A.4: *Time series (1997 - 2002) of significant wave height Hs and peak over threshold 1 m (green) and 2.5 m (red) and sea levels (below) measured at the "Acqua Alta" tower*

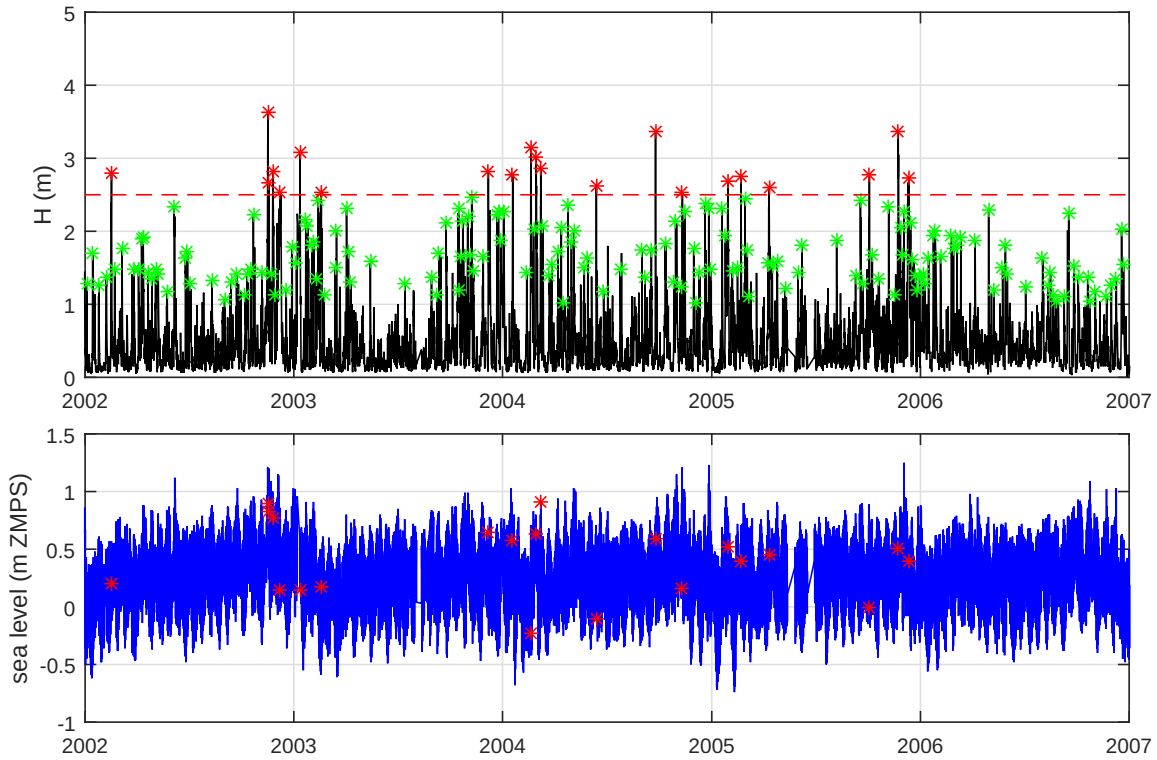

Figure A.5: *Time series (2002 - 2007) of significant wave height Hs and peak over threshold 1 m (green) and 2.5 m (red) and sea levels (below) measured at the "Acqua Alta" tower*

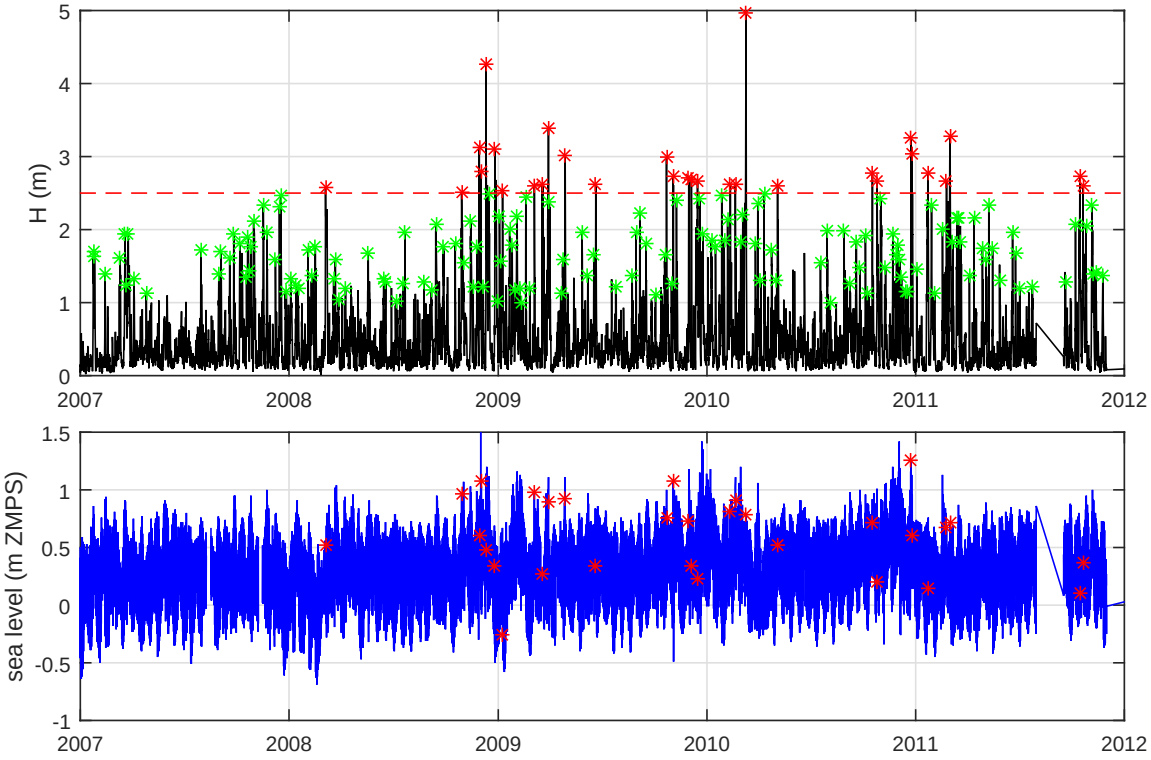

Figure A.6: *Time series (2007 - 2012) of significant wave height Hs and peak over threshold 1 m (green) and 2.5 m (red) and sea levels (below) measured at the "Acqua Alta" tower*

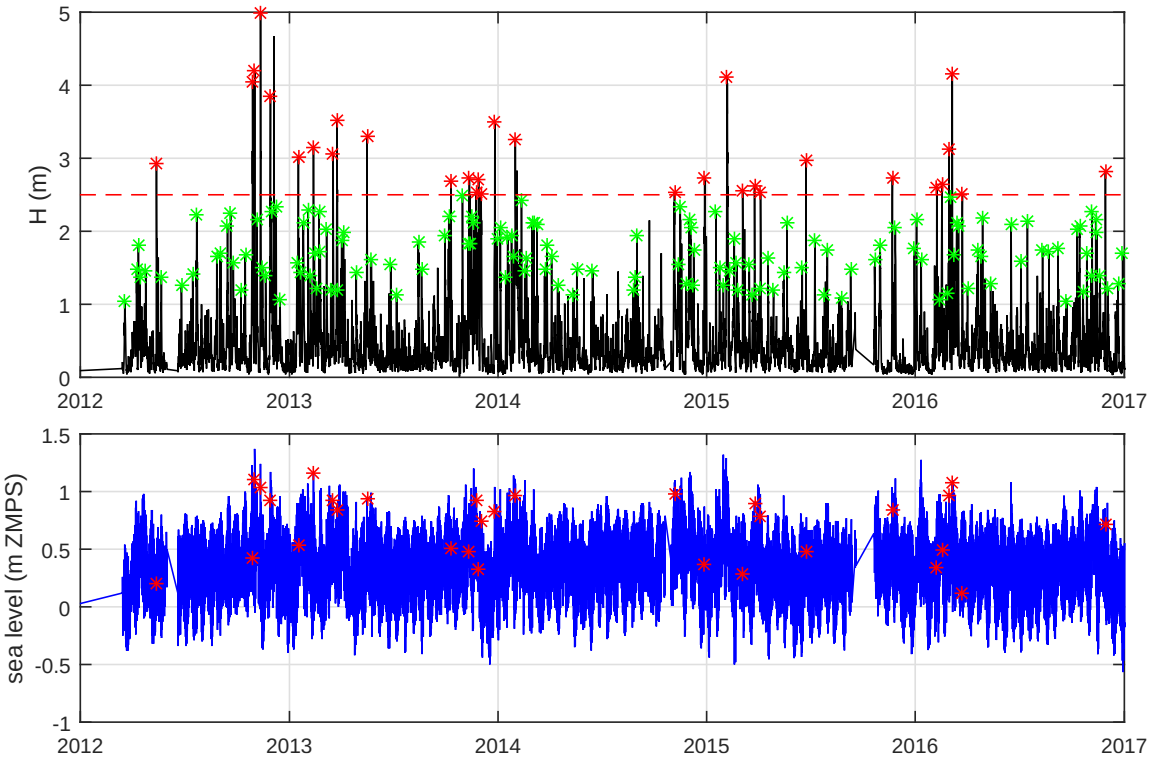

Figure A.7: *Time series (2012 - 2017) of significant wave height Hs and peak over threshold 1 m (green) and 2.5 m (red) and sea levels (below) measured at the "Acqua Alta" tower*

Table A.1: *Storms with maximum larger than 2.5 m, measured at the "Acqua Alta" tower*

Date	time	Hs (m)	Tp (s)	ζ (m ZMPS)	*duration* (h)
23/11/1987	18:00	3.00	7.7	0.46	48
23/04/1988	09:00	2.52	6.0	0.10	27
03/08/1988	12:00	2.55	5.8	0.62	51
20/11/1988	21:00	3.11	7.0	0.70	96
26/03/1990	18:00	3.03	7.2	0.41	66
24/11/1990	21:00	2.90	7.8	0.53	33
09/12/1990	00:00	3.33	9.0	1.04	39
17/04/1991	12:00	2.77	6.6	0.64	33
02/05/1991	15:00	3.02	10.0	0.71	39
23/11/1991	21:00	3.00	6.8	0.63	33
20/01/1992	03:00	2.87	6.6	0.07	54
03/10/1992	09:00	2.94	6.7	0.94	63
07/12/1992	12:00	4.17	7.7	0.76	93
27/12/1992	06:00	2.88	6.7	-0.05	42
02/01/1993	12:00	3.32	6.8	-	99
28/02/1993	18:00	3.02	6.7	-	78
01/10/1993	18:00	3.35	7.6	-	39
25/12/1993	12:00	3.26	7.4	-	66
12/02/1994	21:00	2.82	6.6	0.56	69
17/05/1994	18:00	2.66	7.9	0.69	21
23/12/1994	03:00	2.80	6.2	0.74	123
17/11/1995	09:00	2.55	6.6	0.30	51
13/12/1995	00:00	3.49	7.4	0.63	54
26/12/1995	06:00	2.99	7.1	0.39	24
29/01/1996	21:00	3.00	6.6	0.28	51
24/12/1996	21:00	2.98	6.8	0.78	111
20/04/1997	18:00	2.93	6.6	0.43	48
26/10/1997	21:00	2.73	6.6	0.51	90
27/08/1998	06:00	2.55	6.6	0.20	33
21/11/1998	18:00	3.18	7.6	-0.17	120
30/11/1998	12:00	3.05	7.0	-0.11	66
10/01/1999	00:00	3.45	2.9	0.53	30
16/03/1999	21:00	3.23	6.8	0.56	57
15/04/1999	09:00	3.04	9.1	0.90	69
20/10/1999	18:00	2.72	6.8	1.05	30
06/11/1999	06:00	3.05	7.2	1.01	51
15/11/1999	00:00	2.67	6.5	0.46	27

Table A.2: *Storms with maximum larger than 2.5 m, measured at the "Acqua Alta" tower*

Date	time	Hs (m)	Tp (s)	ζ (m ZMPS)	*duration* (h)
20/11/1999	12:00	2.91	5.3	0.28	66
19/12/1999	06:00	2.69	5.6	0.96	66
06/11/2000	00:00	3.11	8.8	0.71	39
13/01/2001	06:00	2.87	6.7	0.17	90
29/01/2001	00:00	2.75	6.4	0.80	36
08/11/2001	12:00	2.75	7.2	0.36	45
15/02/2002	03:00	2.80	6.4	0.20	42
15/11/2002	15:00	3.64	8.8	0.83	60
17/11/2002	18:00	2.66	7.8	0.89	21
24/11/2002	06:00	2.81	8.3	0.77	69
07/12/2002	15:00	2.54	6.4	0.14	183
10/01/2003	21:00	3.08	7.2	0.15	150
16/02/2003	06:00	2.54	6.1	0.17	81
06/12/2003	06:00	2.82	7.0	0.64	93
17/01/2004	18:00	2.77	4.9	0.57	27
18/02/2004	15:00	3.14	3.4	-0.23	90
28/02/2004	00:00	3.02	4.2	0.63	69
06/03/2004	21:00	2.87	6.4	0.91	36
12/06/2004	03:00	2.62	4.3	-0.11	42
23/09/2004	15:00	3.37	4.0	0.59	63
09/11/2004	15:00	2.53	4.9	0.16	60
28/01/2005	12:00	2.69	6.5	0.52	75
20/02/2005	03:00	2.75	4.3	0.40	33
10/04/2005	09:00	2.60	6.8	0.45	57
02/10/2005	15:00	2.77	4.0	0.00	33
22/11/2005	03:00	3.36	7.6	0.51	63
10/12/2005	18:00	2.72	6.7	0.39	93
03/03/2008	21:00	2.57	8.5	0.52	90
27/10/2008	21:00	2.51	5.6	0.96	51
27/11/2008	18:00	3.12	5.8	0.61	24
30/11/2008	06:00	2.80	5.3	1.08	48
09/12/2008	15:00	4.27	6.6	0.48	69
25/12/2008	03:00	3.10	5.3	0.34	84
07/01/2009	12:00	2.53	5.4	-0.26	27
04/03/2009	03:00	2.60	6.5	0.98	36
19/03/2009	03:00	2.61	4.9	0.27	57
28/03/2009	18:00	3.39	5.4	0.89	63

Table A.3: *Storms with maximum larger than 2.5 m, measured at the "Acqua Alta" tower*

Date	time	Hs (m)	Tp (s)	ζ (m ZMPS)	*duration* (h)
27/04/2009	00:00	3.02	4.9	0.93	42
19/06/2009	12:00	2.63	2.0	0.34	30
21/10/2009	06:00	2.99	4.9	0.75	60
01/11/2009	21:00	2.72	5.0	1.08	99
29/11/2009	03:00	2.71	5.8	0.73	36
03/12/2009	18:00	2.68	5.3	0.34	21
14/12/2009	12:00	2.66	4.2	0.23	102
09/02/2010	21:00	2.61	5.3	0.81	63
18/02/2010	15:00	2.61	5.2	0.91	36
09/03/2010	06:00	4.96	6.1	0.78	99
03/05/2010	12:00	2.59	2.8	0.52	63
16/10/2010	09:00	2.77	4.9	0.71	54
24/10/2010	15:00	2.66	5.2	0.20	66
23/12/2010	00:00	3.25	8.0	1.26	42
24/12/2010	21:00	3.03	3.5	0.61	36
21/01/2011	06:00	2.77	4.6	0.15	84
23/02/2011	00:00	2.67	3.1	0.67	165
28/02/2011	21:00	3.27	4.6	0.72	78
14/10/2011	03:00	2.73	4.2	0.10	81
19/10/2011	12:00	2.60	4.2	0.37	60
12/05/2012	06:00	2.93	8.2	0.20	33
27/10/2012	12:00	4.04	4.2	0.43	63
31/10/2012	03:00	4.20	4.4	1.11	33
10/11/2012	09:00	4.99	7.7	1.03	45
27/11/2012	18:00	3.85	3.8	0.93	48
15/01/2013	15:00	3.02	5.2	0.54	42
11/02/2013	00:00	3.15	7.8	1.16	30
17/03/2013	12:00	3.06	6.0	0.93	39
24/03/2013	09:00	3.52	4.3	0.84	57
15/05/2013	15:00	3.30	7.3	0.94	33
09/10/2013	21:00	2.69	4.0	0.50	15
10/11/2013	21:00	2.74	4.9	0.48	51
22/11/2013	12:00	2.54	4.7	0.93	63
27/11/2013	00:00	2.70	4.4	0.32	69
01/12/2013	09:00	2.51	5.4	0.74	60
25/12/2013	09:00	3.50	7.9	0.83	48
30/01/2014	06:00	3.26	5.6	0.96	153

Table A.4: *Storms with maximum larger than 2.5 m, measured at the "Acqua Alta" tower*

Date	time	Hs (m)	Tp (s)	ζ (m ZMPS)	*duration* (h)
04/11/2014	18:00	2.53	5.6	0.98	75
27/12/2014	15:00	2.73	5.8	0.37	102
04/02/2015	21:00	4.11	8.4	-	87
04/03/2015	00:00	2.56	5.0	0.28	108
24/03/2015	21:00	2.63	5.9	0.89	36
04/04/2015	09:00	2.54	5.7	0.78	33
22/06/2015	21:00	2.98	4.5	0.48	9
21/11/2015	03:00	2.73	5.5	0.83	63
06/02/2016	18:00	2.60	3.8	0.35	69
15/02/2016	18:00	2.64	4.5	0.50	36
28/02/2016	03:00	3.12	5.8	0.97	63
04/03/2016	21:00	4.15	4.0	1.08	30
27/11/2016	21:00	2.82	5.5	0.71	30
16/01/2017	21:00	2.98	5.3	0.27	117
24/02/2017	00:00	2.53	5.6	0.23	15

Appendix B

Additional information on cells VE2, VE3, VE6

Some information on the three littoral cells of the Veneto region analysed in Chapter 6 are here reported and illustrated. Fig. B.2 shows the North-Eastern Venetian littoral, where the three analysed cells are located: VE2 Valle Vecchia, VE3 Caorle and VE6 Cavallino-Treporti. In the following, for each cell, geographical information and results of the sediment budget analysis are given together with the shoreline variation and some bathymetric profile.
Regarding the sediment budget data, the assessment method is described (and performed) in Ruol et al.(2016,2018). The sediment budget is essentially a mass balance equation applied to a specified time interval. Subdividing the coastline into a number of small stretches, the balance is applied to each stretch i:

$$\varepsilon_i = \partial V_i - Q_i \Delta t = 0 \tag{B.1}$$

where ∂V_i is the volume of accretion or erosion estimated by a comparison of the bathymetries surveyed at the beginning and at the end of the time range Δt, and Q_i is the net sediment discharge shown in Fig. B.1 and given by:

$$Q_i = Q_{LS(North)i} + Q_{LS(South)i} + Q_{Fi} - Q_{CRi} + Q_{Ni} - Q_{Di} \tag{B.2}$$

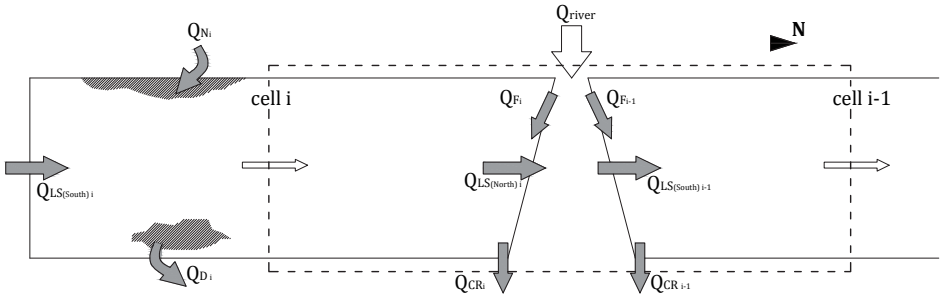

Figure B.1: *Sediment balance diagram. Littoral cells are limited by morphological features (continuous line). The inclusion of river sediment transport in the balance equations would be straightforward if the cell control volume extended to the dash-dot box (from Ruol et al. 2018)*

where Q_{LS} is the long-shore sediment transport; Q_F is the additional river sediment supply;

Q_{CR} is the cross-shore sediment transport; and Q_N and Q_D are the volumes added or subtracted due to nourishment or dredging respectively. Subsidence and sea level rise do not affect the sediment balance directly, but they have the same effect as generalized erosion.

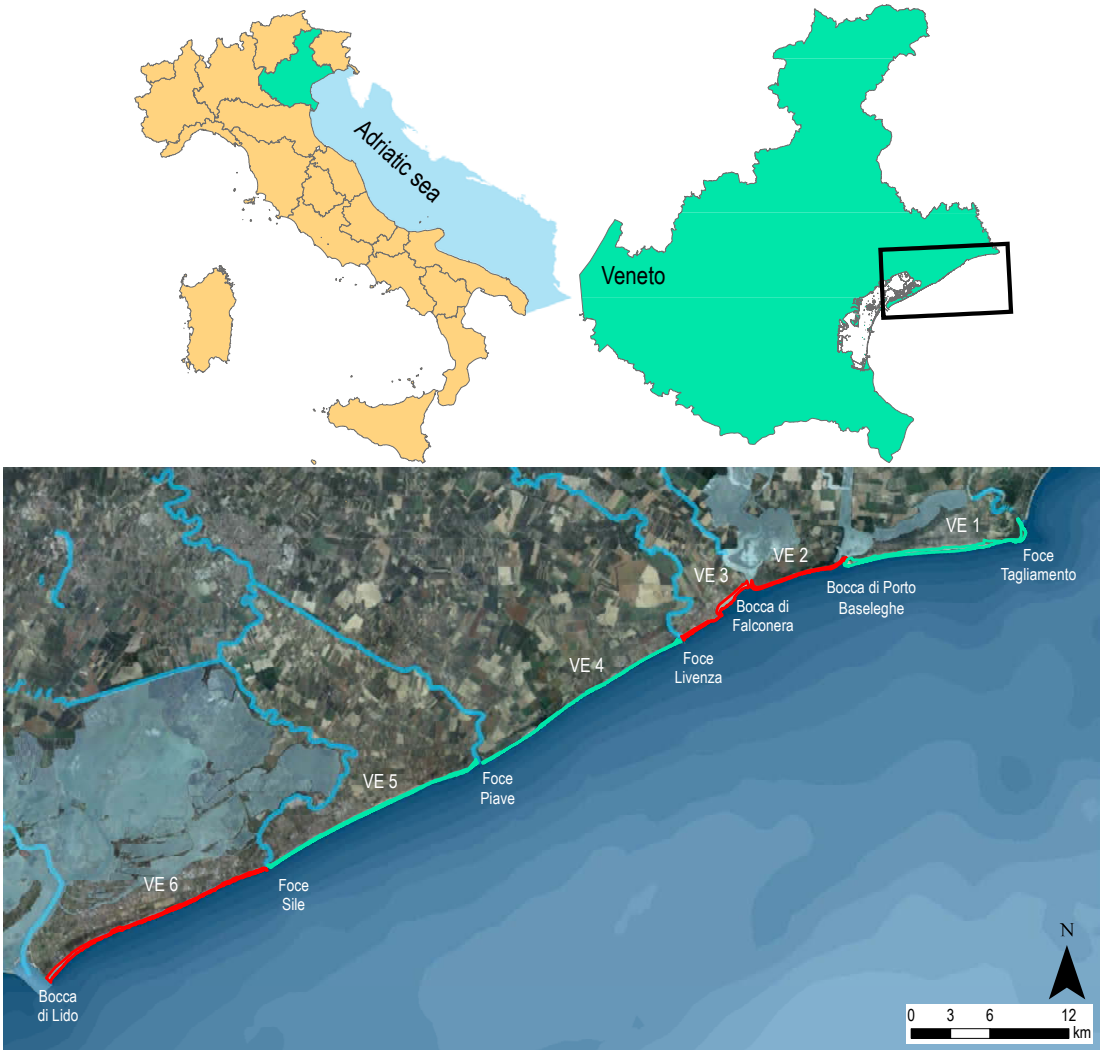

Figure B.2: *North-Eastern Venetian littoral: VE2, VE3 and VE6 cells in red*

LITTORAL CELL VE2: Valle Vecchia coastline

Cell boundaries	from *Porto Baseleghe* to *Bocca di Falconera*
Municipality	Caorle (Venice - Italy)
Cell length	5515 m
Direction orthogonal to the shoreline	165 °N
Environmental site	SCI IT3250033 (Laguna di Caorle - Foce del Tagliamento) SPA IT3250041 (Valle Vecchia - Zumelle - Valli di Bibione)

Table B.1: *Sediment balance (volume m^3/year * 1000)*

Cell	part	Q_{LS} (1) Long-shore	Q_{LS} (2) Long-shore	Q_{CR} Cross-shore	Q_F Fluvial	Q_N Nourished	Q_D Dredged	∂V
VE2	N	-67.9	-48.0	4.4	-	-	-	15.6
VE2	S	-48.0	-36.4	3.0	-	22.8	17.2	14.1

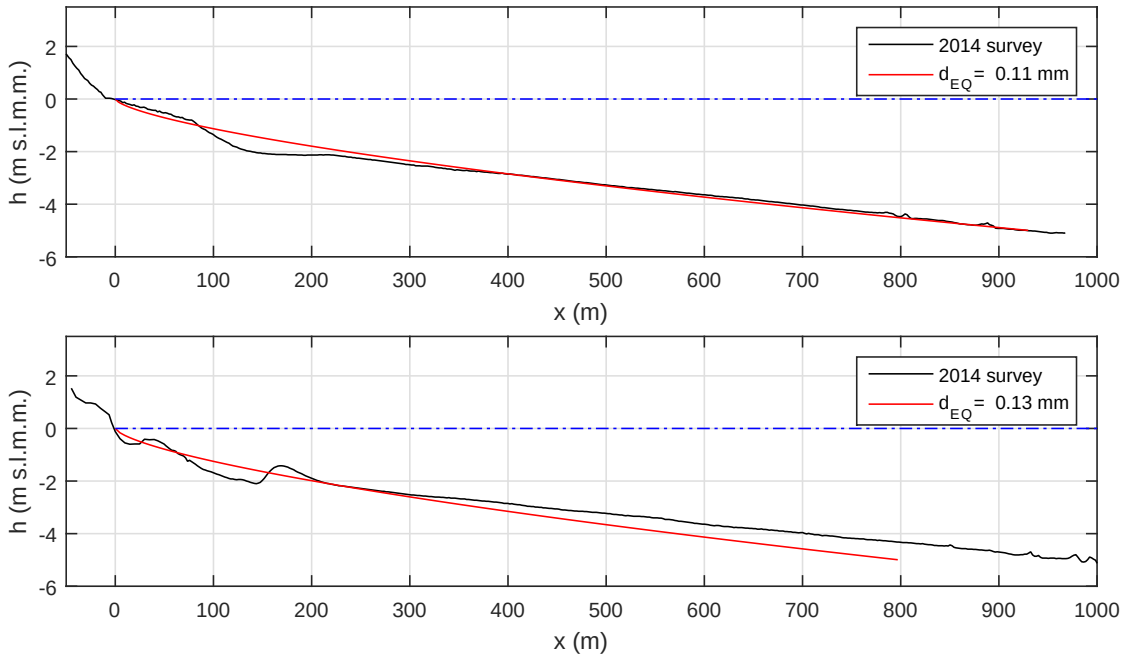

Figure B.3: *Bathymetric profile, form survey 2014: profile next to "Porto Baseleghe" North-East (above), profile next to "Bocca di Falconera" South-West (below)*

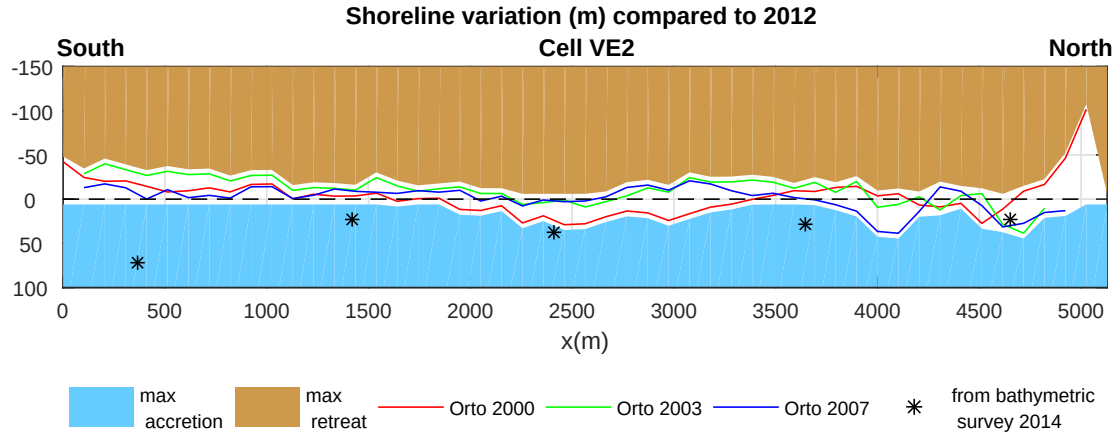

Figure B.4: *Shoreline variation for cell VE2, data from Orthophoto and bathymetric survey*

LITTORAL CELL VE3: Caorle coastline

Cell boundaries	from *Bocca di Falconera* to *Foce Livenza*
Municipality	Caorle (Venice - Italy)
Cell length	5168 m
Direction orthogonal to the shoreline	140 °N

Table B.2: *Sediment balance (volume m^3/year * 1000)*

Cell	part	Q_{LS} (1) Long-shore	Q_{LS} (2) Long-shore	Q_{CR} Cross-shore	Q_F Fluvial	Q_N Nourished	Q_D Dredged	∂V
VE3	N	-20.3	-12.9	4.6	-	24.0	0.0	26.9
VE3	S	-12.9	-10.0	3.8	-	22.4	5.1	16.3

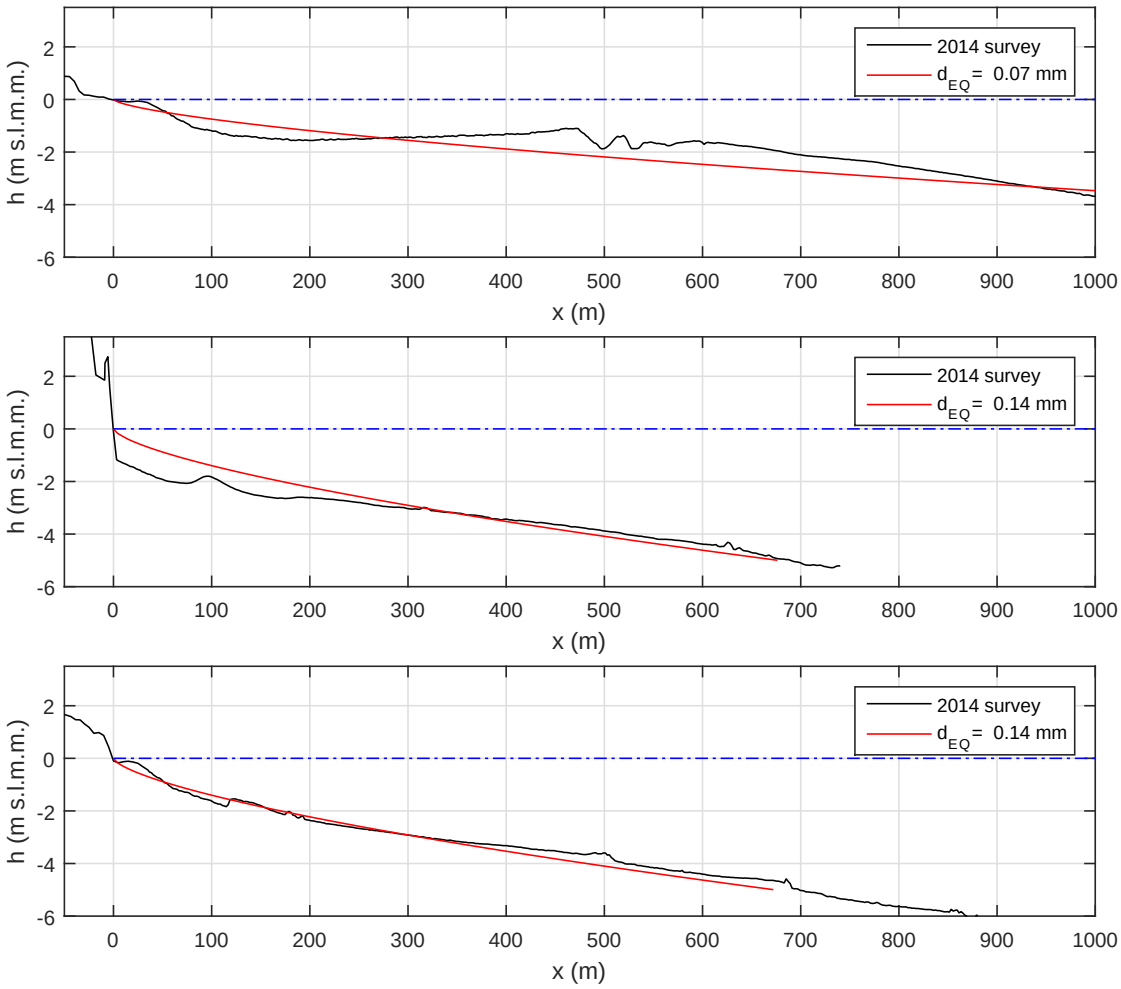

Figure B.5: *Bathymetric profile, form survey 2014: profile at the "Spiaggia di Levante" (above) North-East, profile at "Murazzi" (middle) and profile at the "Spiaggia di Ponente" South-West(below)*

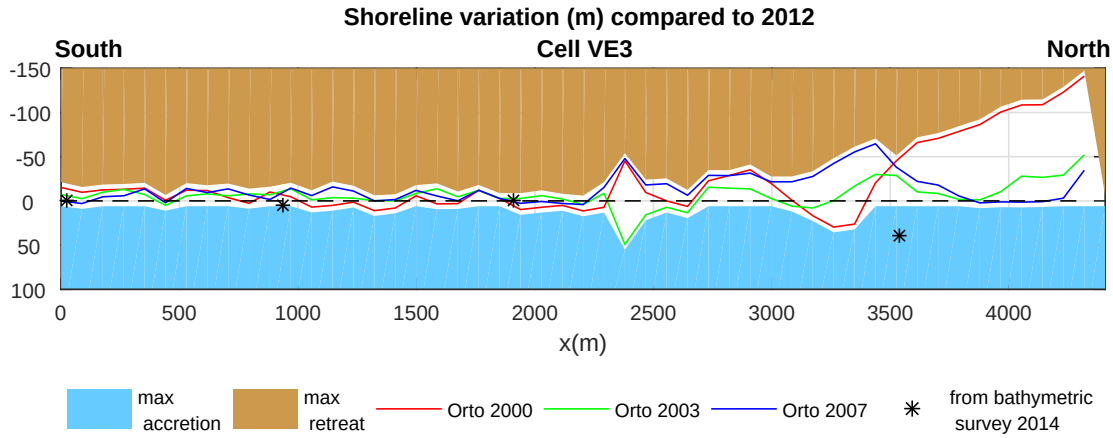

Figure B.6: *Shoreline variation for cell VE3, data from Orthophoto and bathymetric survey*

LITTORAL CELL VE6: Cavallino-Treporti coastline

Cell boundaries	from *Foce Sile* to *Bocca di Lido*
Municipality	Cavallino - Treporti ((Venice - Italy)
Cell length	13682 m
Direction orthogonal to the shoreline	150 °N
Environmental site	SCI/SPA IT3250003 (Penisola Cavallino)

Table B.3: *Sediment balance (volume m^3/year * 1000)*

Cell	part	Q_{LS} (1) Long-shore	Q_{LS} (2) Long-shore	Q_{CR} Cross-shore	Q_F Fluvial	Q_N Nourished	Q_D Dredged	∂V
VE6	N	-75.6	-91.5	22.1	-	20.1	-	-17.9
VE6	S	-91.5	-24.3	17.2	-	-	20.2	29.8

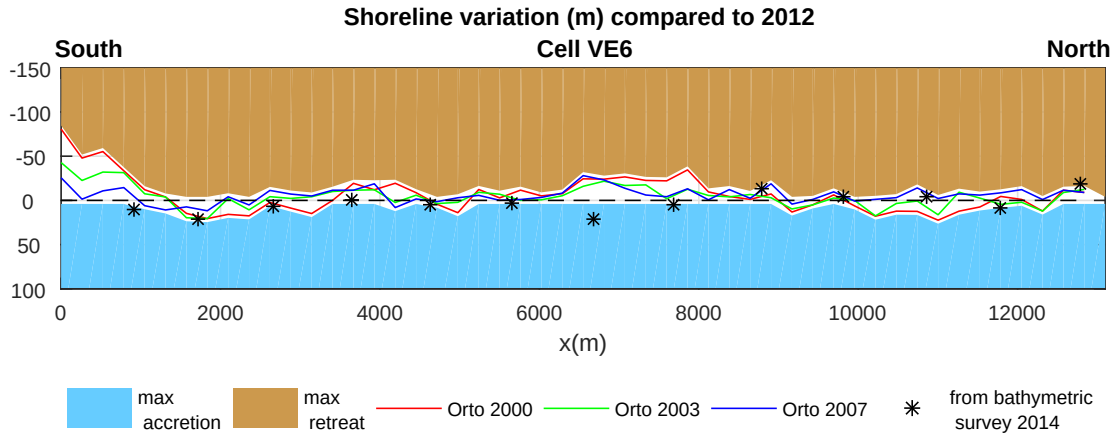

Figure B.7: *Shoreline variation for cell VE6, data from Orthophoto and bathymetric survey*

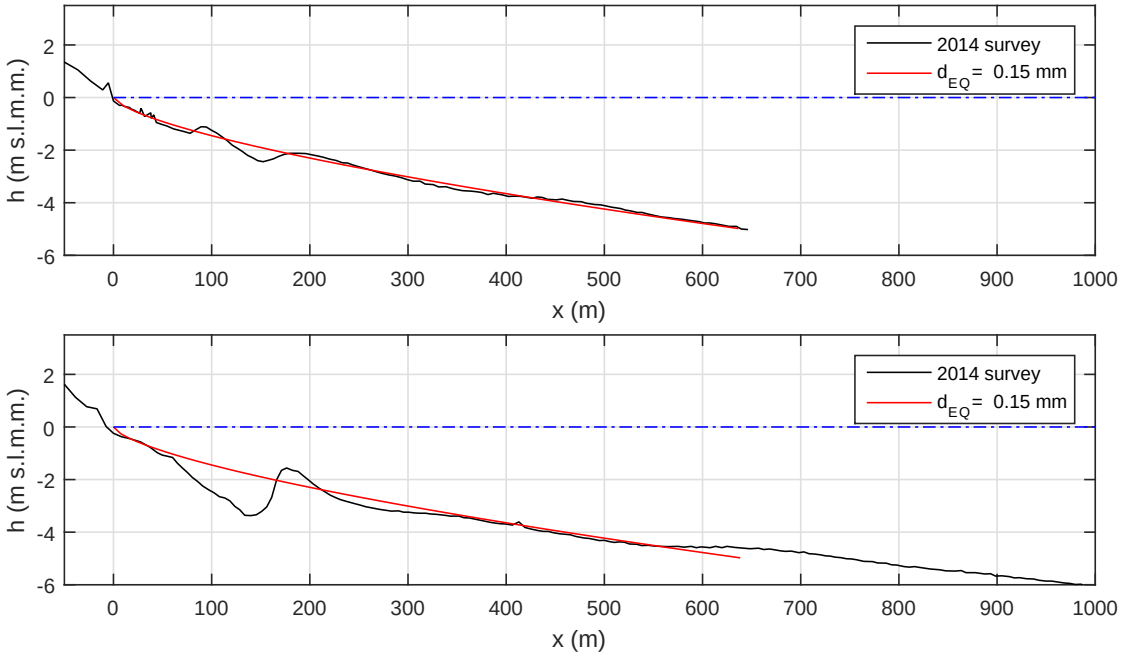

Figure B.8: *Bathymetric profile, form survey 2014: profile next to the mouth of river Sile (above) North-East, profile next to "Bocca di Lido" South-West(below)*

Acknowledgements

I would like to thank my supervisor Prof. Piero Ruol for his knowledge and support of my Ph.D. studies. Undertaking this experience has been a challenge for me and I am thankful for the guidance and motivation I received from him.

My sincere thanks go to Prof. Luca Martinelli for his helpfulness, knowledge and patience. He believed in my capabilities, encouraged me to engage the doctoral program and shared with me the most of the work I did. Without his precious support it would not have been possible to widen my research from various perspectives.

I gratefully thank the continuous moral and/or scientific support provided by Ing. Matteo Volpato, Prof. Marco Favaretti and all the professors, researchers, PhD colleagues, technicians and students of the University of Padova, who always proved to be kind and friendly to me.

I wish to acknowledge Regione del Veneto, especially Ing. Patti, Ing. Simonin and Ing. Selvi, for their knowledge of the Venetian littoral which gave the impulse and allowed the development of this PhD thesis.

Finally, special thanks to my husband Francesco, my parents Olga and Gianangelo and my sister Francesca for their encouragement during my study.

Chiara Favaretto

List of Publications

Journal papers:

[1] Ruol P, Martinelli L, Favaretto C. (2018). Vulnerability Analysis of the Venetian Littoral and Adopted Mitigation Strategy. *Water*. 10(8):984

[2] Martinelli, L., Ruol, P., Volpato, M., Favaretto, C., Castellino, M. , De Girolamo, P., Franco, L., Romano, A., Sammarco, P. (2018). Experimental investigation on non-breaking wave forces and overtopping at the recurved parapets of vertical breakwaters. *Coastal Engineering*, 141:52-67

[3] Favaretto, C., Martinelli, L., Ruol, P. (2018). A model of coastal flooding using linearized bottom friction and its application to a case study in Caorle, Venice (IT). *International Journal of Offshore and Polar Engineering* (accepted)

[4] Favaretto, C., Martinelli, L., Ruol, P. Coastal flooding hazard due to overflow using a Level II method. Application to the Venetian littoral. (submitted to *Water*)

Conference proceedings (peer reviewed, Scopus indexed):

[5] Favaretto, C., Martinelli, L., Ruol, P. (2018). Raster Based Model of Inland Coastal Flooding Propagation Using Linearized Bottom Friction and Application to a Real Case Study in Caorle, Venice (IT). *Proc. of the 28th International Ocean and Polar Engineering Conference*, 1335-1342

[6] Ruol, P., Martinelli, L., Favaretto, C., Scroccaro, D. (2018). Innovative Sand Groin Beach Nourishment with Environmental, Defense and Recreational Purposes. *Proc. 28th International Ocean and Polar Engineering Conference*, 1320-1329

[7] Favaretto, C., Martinelli, L., Ruol, P., Cortellazzo, G. (2017). Investigation on Possible Layouts of a Catamaran Floating Breakwater behind a Wave Energy Converter *Proc. 27th International Ocean and Polar Engineering Conference*, 140-145

[8] Martinelli, L., Ruol, P., Favaretto, C. (2016). Hybrid structure combining a wave energy converter and a floating breakwater. *Proc. 26th International Ocean and Polar Engineering Conference*, 622-628

Conference proceedings:

[9] Martinelli, L., Ruol, P., Favaretto, C., Volpato, M. (2018). Overtopping and stability of a rubble mound breakwater with coreloc armour under oblique cyclonic waves. *Proc. 36th Coastal Engineering Conference* (abstract)

[10] Martinelli, L., Ruol, P., Favaretto, C., Volpato, M. (2018). Experimental investigation on the dynamics of a Floating WEC with PTO phase control. *Proc. of the 13th SWEDES conference*

[11] Favaretto, C., Martinelli, L., Ruol, P., (2018). Sulla disposizione ottimale di frangiflutti galleggianti a catamarano combinati a convertitori di energia ondosa. *Proc. XXXVI Convegno Nazionale di Idraulica e Costruzioni Idrauliche - IDRA*, 350

[12] Castellino, M. ,Sammarco, P., Romano, A., Martinelli, L., Ruol, P., Volpato, M., Favaretto, C., Franco, L., De Girolamo, P. (2018). Forze impulsive e sormonti su muri ricurvi soggetti ad onde non frangenti. *Proc. XXXVI Convegno Nazionale di Idraulica e Costruzioni Idrauliche - IDRA*, 308

[13] Ruol, P., Martinelli, L., Favaretto, C. (2016). Una metodologia per la valutazione di criticità e priorità di intervento: il caso del litorale Veneto. *Proc. XXXV Convegno Nazionale di Idraulica e Costruzioni Idrauliche - IDRA*, 907-910

[14] Martinelli, L., Ruol, P., Favaretto, C., Marini, F. (2016). Interazioni tra componenti elettriche e idrodinamiche per un convertitore di energia ondosa. *Proc. XXXV Convegno Nazionale di Idraulica e Costruzioni Idrauliche - IDRA*, 237-240

[15] Ruol, P., Favaretto, C., Martinelli, L. (2015). A structured approach for the assessment of sediment budget in coastal management: the case of the Venetian littoral. *Proc. 7th International Short Conference on Applied Coastal Research – SCACR*, 437-448

Book:

[16] Ruol, P., Martinelli, L., Favaretto, C. (2016). Gestione integrata della zona costiera. Studio e monitoraggio per la definizione degli interventi di difesa dei litorali dall'erosione nella Regione Veneto - Linee guida. *Edizioni Libreria Progetto*, pp 335. ISBN 978-88-96477-84-7

Bibliography

Armaroli, C. and Duo, E. (2017). Validation of the coastal storm risk assessment framework along the emilia-romagna coast. *Coastal Engineering*.

Aucelli, P. P. C., Di Paola, G., Incontri, P., Rizzo, A., Vilardo, G., Benassai, G., Buonocore, B., and Pappone, G. (2017). Coastal inundation risk assessment due to subsidence and sea level rise in a mediterranean alluvial plain (volturno coastal plain–southern italy). *Estuarine, Coastal and Shelf Science*, 198:597–609.

Bates, P. D., Dawson, R. J., Hall, J. W., Horritt, M. S., Nicholls, R. J., Wicks, J., and Hassan, M. A. A. M. (2005). Simplified two-dimensional numerical modelling of coastal flooding and example applications. *Coastal Engineering*, 52(9):793–810.

Bates, P. D. and De Roo, A. (2000). A simple raster-based model for flood inundation simulation. *Journal of hydrology*, 236(1-2):54–77.

Bates, P. D., Horritt, M. S., and Fewtrell, T. J. (2010). A simple inertial formulation of the shallow water equations for efficient two-dimensional flood inundation modelling. *Journal of Hydrology*, 387(1):33–45.

Begnudelli, L. and Sanders, B. F. (2006). Unstructured grid finite-volume algorithm for shallow-water flow and scalar transport with wetting and drying. *Journal of hydraulic engineering*, 132(4):371–384.

Begnudelli, L. and Sanders, B. F. (2007). Simulation of the st. francis dam-break flood. *Journal of Engineering Mechanics*, 133(11):1200–1212.

Begnudelli, L., Sanders, B. F., and Bradford, S. F. (2008). Adaptive godunov-based model for flood simulation. *Journal of Hydraulic Engineering*, 134(6):714–725.

Boccotti, P. (1986). On coastal and offshore structure risk analysis. *Excerpta of the Italian Contributions to the Field of Hydraulic Engineering*, 1:19–36.

Bolle, A., das Neves, L., Smets, S., Mollaert, J., and Buitrago, S. (2017). An impact-oriented early warning and bayesian-based decision support system for flood risks in zeebrugge harbour. *Coastal Engineering*.

Boussinesq, J. (1871). Théorie de l'intumescence liquide appelée onde solitaire ou de translation se propageant dans un canal rectangulaire. *CR Acad. Sci. Paris*, 72(755–759).

Bouyé, E., Durrleman, V., Nikeghbali, A., Riboulet, G., and Roncalli, T. (2000). Copulas for finance-a reading guide and some applications.

Bradbrook, K. (2006). Jflow: a multiscale two-dimensional dynamic flood model. *Water and Environment Journal*, 20(2):79–86.

Breilh, J., Chaumillon, E., Bertin, X., and Gravelle, M. (2013). Assessment of static flood modeling techniques: application to contrasting marshes flooded during xynthia (western france). *Natural Hazards and Earth System Sciences*, 13(6):1595–1612.

Briere, C., Abadie, S., Bretel, P., and Lang, P. (2007). Assessment of telemac system performances, a hydrodynamic case study of anglet, france. *Coastal engineering*, 54(4):345–356.

Briggs, M. J., Synolakis, C. E., Harkins, G. S., and Green, D. R. (1995). Laboratory experiments of tsunami runup on a circular island. *Pure and applied geophysics*, 144(3-4):569–593.

Brodtkorb, A. R., Sætra, M. L., and Altinakar, M. (2012). Efficient shallow water simulations on gpus: Implementation, visualization, verification, and validation. *Computers & Fluids*, 55:1–12.

Canestrelli, P., Mandich, M., Pirazzoli, P., and Tomasin, A. (2001). Wind, depression and seiches: tidal perturbations in venice (1951–2000). *Citta di Venezia, Centro Previsioni e Segnalazioni Maree, Comune di Venezia*, pages 1–104.

Carbognin, L., Teatini, P., and Tosi, L. (2004). Eustacy and land subsidence in the venice lagoon at the beginning of the new millennium. *Journal of Marine Systems*, 51(1-4):345–353.

Cazenave, A. and Cozannet, G. L. (2014). Sea level rise and its coastal impacts. *Earth's Future*, 2(2):15–34.

Coles, S., Bawa, J., Trenner, L., and Dorazio, P. (2001). *An introduction to statistical modeling of extreme values*, volume 208. Springer.

Dally, W. R., Dean, R. G., and Dalrymple, R. A. (1985). Wave height variation across beaches of arbitrary profile. *Journal of Geophysical Research: Oceans*, 90(C6):11917–11927.

Dawson, R. J., Hall, J., Bates, P., and Nicholls, R. (2005). Quantified analysis of the probability of flooding in the thames estuary under imaginable worst-case sea level rise scenarios. *Water resources development*, 21(4):577–591.

Dean, R. G. (1977). *Equilibrium beach profiles: US Atlantic and Gulf coasts*. Department of Civil Engineering and College of Marine Studies, University of Delaware.

Di Luccio, D., Benassai, G., Di Paola, G., Rosskopf, C., Mucerino, L., Montella, R., and Contestabile, P. (2018). Monitoring and modelling coastal vulnerability and mitigation proposal for an archaeological site (kaulonia, southern italy). *Sustainability (Switzerland)*, 10(6).

Di Risio, M., Bruschi, A., Lisi, I., Pesarino, V., and Pasquali, D. (2017). Comparative analysis of coastal flooding vulnerability and hazard assessment at national scale. *Journal of Marine Science and Engineering*, 5(4):51.

Dottori, F., Martina, M. L. V., and Figueiredo, R. (2016). A methodology for flood susceptibility and vulnerability analysis in complex flood scenarios. *Journal of Flood Risk Management*.

Du, X. (2005). First order and second reliability methods. *Probabilistic engineering design*, pages 1–33.

Dupuis, D. J. and Jones, B. L. (2006). Multivariate extreme value theory and its usefulness in understanding risk. *North American Actuarial Journal*, 10(4):1–27.

Favaretto, C., Martinelli, L., and Ruol, P. (2018). A model of coastal flooding using linearized bottom friction and its application to a case study in caorle, venice italy. *International Journal of Offshore and Polar Engineering*.

Fisher, R. A. and Tippett, L. H. C. (1928). Limiting forms of the frequency distribution of the largest or smallest member of a sample. In *Mathematical Proceedings of the Cambridge Philosophical Society*, volume 24, pages 180–190. Cambridge University Press.

Formentin, S. M. and Zanuttigh, B. (2018). A new method to estimate the overtopping and overflow discharge at over-washed and breached dikes. *Coastal Engineering*, 140:240–256.

Fréchet, M. (1927). Sur les ensembles compacts de fonctions mesurables. *Fundamenta Mathematicae*, 9(1):25–32.

Galland, J.-C., Goutal, N., and Hervouet, J.-M. (1991). Telemac: A new numerical model for solving shallow water equations. *Advances in Water Resources*, 14(3):138–148.

Gallien, T. (2016). Validated coastal flood modeling at imperial beach, california: Comparing total water level, empirical and numerical overtopping methodologies. *Coastal Engineering*, 111:95–104.

Gallien, T., Sanders, B., and Flick, R. (2014). Urban coastal flood prediction: Integrating wave overtopping, flood defenses and drainage. *Coastal Engineering*, 91:18–28.

Gnedenko, B. (1943). Sur la distribution limite du terme maximum d'une serie aleatoire. *Annals of mathematics*, pages 423–453.

Goda, Y. (1989). On the methodology of selecting design wave height. In *Coastal Engineering 1988*, pages 899–913.

Goda, Y. (2010). *Random seas and design of maritime structures*, volume 33. World Scientific Publishing Company.

Goda, Y. and Kobune, K. (1991). Distribution function fitting for storm wave data. In *Coastal Engineering 1990*, pages 18–31.

Grilli, S., Svendsen, I., and Subramanya, R. (1997). Breaking criterion and characteristics for solitary waves on slopes. *Journal of waterway, port, coastal, and ocean engineering*, 123(3):102–112.

Gumbel, E. (1958). Statistics of extremes. 1958. *Columbia Univ. press, New York*, page 247.

Haines, P. (2013). Hydrological modelling of tidal re-inundation of an estuarine wetland in south-eastern australia. *Ecological engineering*, 52:79–87.

Hanson, H. and Kraus, N. C. (1989). Genesis: Generalized model for simulating shoreline change. report 1. technical reference. Technical report, Coastal Engineering Research Center Vicksburg MS.

Hasofer, A. M. and Lind, N. C. (1974). Exact and invariant second-moment code format. *Journal of the Engineering Mechanics division*, 100(1):111–121.

Hasselmann, D. E., Dunckel, M., and Ewing, J. A. (1980). Directional wave spectra observed during JONSWAP 1973. *Journal of physical oceanography*, 10(8):1264–1280.

Hervouet, J.-M. (2000). Telemac modelling system: an overview. *Hydrological processes*, 14(13):2209–2210.

Hinkel, J. (2005). Diva: an iterative method for building modular integrated models. *Advances in Geosciences*, 4:45–50.

Hinkel, J., Lincke, D., Vafeidis, A. T., Perrette, M., Nicholls, R. J., Tol, R. S., Marzeion, B., Fettweis, X., Ionescu, C., and Levermann, A. (2014). Coastal flood damage and adaptation costs under 21st century sea-level rise. *Proceedings of the National Academy of Sciences*, 111(9):3292–3297.

Hunt, J. N. (1979). Direct solution of wave dispersion equation. *Journal of the Waterway, Port, Coastal and Ocean Division*, 105(4):457–459.

Hunter, N. M., Bates, P. D., Horritt, M. S., and Wilson, M. D. (2007). Simple spatially-distributed models for predicting flood inundation: a review. *Geomorphology*, 90(3-4):208–225.

Hunter, N. M., Horritt, M. S., Bates, P. D., Wilson, M. D., and Werner, M. G. (2005). An adaptive time step solution for raster-based storage cell modelling of floodplain inundation. *Advances in Water Resources*, 28(9):975–991.

Kalyanapu, A. J., Shankar, S., Pardyjak, E. R., Judi, D. R., and Burian, S. J. (2011). Assessment of gpu computational enhancement to a 2d flood model. *Environmental Modelling & Software*, 26(8):1009–1016.

Khorshid, S., Mohammadian, A., and Nistor, I. (2017). Extension of a well-balanced central upwind scheme for variable density shallow water flow equations on triangular grids. *Computers & Fluids*, 156:441–448.

Kovanen, J., Oksanen, J., and Sarjakoski, T. (2018). Near real-time coastal flood inundation simulation with uncertainty analysis and gpu acceleration in a web environment. *Computers & Geosciences*.

Lamon, L., Rizzi, J., Bonaduce, A., Dubois, C., Lazzari, P., Ghenim, L., Gana, S., Somot, S., Li, L., Canu, D. M., et al. (2014). An ensemble of models for identifying climate change scenarios in the gulf of gabes, tunisia. *Regional environmental change*, 14(1):31–40.

Le Roy, S., Pedreros, R., André, C., Paris, F., Lecacheux, S., Marche, F., and Vinchon, C. (2015). Coastal flooding of urban areas by overtopping: dynamic modelling application to the johanna storm (2008) in gâvres (france). *Natural Hazards and Earth System Sciences*, 15(11):2497.

Lerma, A., Bulteau, T., Elineau, S., Paris, F., Durand, P., Anselme, B., and Pedreros, R. (2018). High-resolution marine flood modelling coupling overflow and overtopping processes: Framing the hazard based on historical and statistical approaches. *Natural Hazards and Earth System Sciences*, 18(1):207–229.

Lhomme, J., Sayers, P., Gouldby, B., Samuels, P., Wills, M., and Mulet-Marti, J. (2008). Recent development and application of a rapid flood spreading method. flood risk 2008.

Li, F., Bicknell, C., Lowry, R., and Li, Y. (2012). A comparison of extreme wave analysis methods with 1994–2010 offshore perth dataset. *Coastal Engineering*, 69:1–11.

Li, Y. and Raichlen, F. (2002). Non-breaking and breaking solitary wave run-up. *Journal of Fluid Mechanics*, 456:295–318.

Liang, W.-Y., Hsieh, T.-J., Satria, M. T., Chang, Y.-L., Fang, J.-P., Chen, C.-C., and Han, C.-C. (2009). A gpu-based simulation of tsunami propagation and inundation. In *International Conference on Algorithms and Architectures for Parallel Processing*, pages 593–603. Springer.

Lin-Ye, J., García-León, M., Gràcia, V., Ortego, M. I., Stanica, A., and Sánchez-Arcilla, A. (2018). Multivariate hybrid modelling of future wave-storms at the northwestern black sea. *Water*, 10(2):221.

Longuet-Higgins, M. S. (1970). Longshore currents generated by obliquely incident sea waves: 1 and 2. *Journal of geophysical research*, 75(33):6778–6801.

Longuett-Higgins, M. S. (1952). On the statistical distribution of the heights of sea waves. *J. Mar. Research*, 11(3):245–266.

Lynett, P. J., Wu, T.-R., and Liu, P. L.-F. (2002). Modeling wave runup with depth-integrated equations. *Coastal Engineering*, 46(2):89–107.

Martinelli, L., Zanuttigh, B., and Corbau, C. (2010). Assessment of coastal flooding hazard along the emilia romagna littoral, it. *Coastal Engineering*, 57(11):1042–1058.

MathWorks, I. (2018). *Parallel Computing Toolbox^{TM}: User's Guide*. Mathworks, Incorporated.

Merkens, J.-L., Reimann, L., Hinkel, J., and Vafeidis, A. T. (2016). Gridded population projections for the coastal zone under the shared socioeconomic pathways. *Global and Planetary Change*, 145:57–66.

Miche, M. (1951). Le pouvoir réfléchissant des ouvrages maritimes exposés à l'action de la houle. *Annales de Ponts et Chaussées, 121 (285-319)*.

Nash, J. E. and Sutcliffe, J. V. (1970). River flow forecasting through conceptual models part i—a discussion of principles. *Journal of hydrology*, 10(3):282–290.

Nataf, A. (1962). Determination des distribution don't les marges sont donnees. *Comptes rendus de l'Académie des Sciences*, 225:42–43.

Neal, J., Fewtrell, T., and Trigg, M. (2009). Parallelisation of storage cell flood models using openmp. *Environmental Modelling & Software*, 24(7):872–877.

Nelsen, R. B. (1999). An introduction to copulas, volume 139 of lecture notes in statistics.

Neumann, B., Vafeidis, A. T., Zimmermann, J., and Nicholls, R. J. (2015). Future coastal population growth and exposure to sea-level rise and coastal flooding-a global assessment. *PloS one*, 10(3):e0118571.

Nicholls, R. J. and Cazenave, A. (2010). Sea-level rise and its impact on coastal zones. *science*, 328(5985):1517–1520.

Penney, W. G. and Price, A. T. (1944). Diffraction of sea waves by breakwaters. *Technical History*, 26(3-4).

Pickands III, J. (1975). Statistical inference using extreme order statistics. *the Annals of Statistics*, pages 119–131.

Pomaro, A., Cavaleri, L., and Lionello, P. (2017). Climatology and trends of the adriatic sea wind waves: analysis of a 37-year long instrumental data set. *International Journal of Climatology*, 37(12):4237–4250.

Poulter, B. and Halpin, P. N. (2008). Raster modelling of coastal flooding from sea-level rise. *International Journal of Geographical Information Science*, 22(2):167–182.

Rahmstorf, S. (2017). Rising hazard of storm-surge flooding. *Proceedings of the National Academy of Sciences*, page 201715895.

Roelvink, D., Reniers, A., Van Dongeren, A., de Vries, J. v. T., McCall, R., and Lescinski, J. (2009). Modelling storm impacts on beaches, dunes and barrier islands. *Coastal engineering*, 56(11-12):1133–1152.

Rosenblatt, M. (1952). Remarks on a multivariate transformation. *The annals of mathematical statistics*, 23(3):470–472.

Ruol, P., Favaretto, C., and Martinelli, L. (2015). A structured approach for the assessment of sediment budget in coastal management: the case of the venetian littoral. In *Proceeding of SCACR*, pages 437–448.

Ruol, P., Martinelli, L., and Favaretto, C. (2016). *Gestione integrata della zona costiera. Studio e monitoraggio per la definizione degli interventi di difesa dei litorali dall'erosione nella Regione Veneto - Linee guida*. Edizioni Libreria Progetto, Padova.

Ruol, P., Martinelli, L., and Favaretto, C. (2018). Vulnerability analysis of the venetian littoral and adopted mitigation strategy. *Water*, 10(8):984.

Salvadori, G., Tomasicchio, G., and D'Alessandro, F. (2014). Practical guidelines for multivariate analysis and design in coastal and off-shore engineering. *Coastal Engineering*, 88:1–14.

Sampson, J., Easton, A., and Singh, M. (2006). Moving boundary shallow water flow above parabolic bottom topography. *Anziam Journal*, 47:373–387.

Şen, O. and Kahya, E. (2017). Determination of flood risk: A case study in the rainiest city of turkey. *Environmental Modelling & Software*, 93:296–309.

Simeoni, U. and Corbau, C. (2009). A review of the delta po evolution (italy) related to climatic changes and human impacts. *Geomorphology*, 107(1-2):64–71.

Small, C. and Nicholls, R. J. (2003). A global analysis of human settlement in coastal zones. *Journal of coastal research*, pages 584–599.

Sommerfeld, A. (1896). Mathematische theorie der diffraction. *Mathematische Annalen*, 47(2-3):317–374.

Stocker, T. F., Qin, D., Plattner, G., Tignor, M., Allen, S., Boschung, J., Nauels, A., Xia, Y., Bex, V., and Midgley, P. (2013). Climate change 2013: The physical science basis, working group 1 (wg1) contribution to the intergovernmental panel on climate change (ipcc) 5th assessment report (ar5). *Cambridge, UK and New York, New York, USA*.

Synolakis, C. (1987). The runup of solitary waves. 185:523 – 545.

Tavakkol, S. and Lynett, P. (2017). Celeris: A gpu-accelerated open source software with a boussinesq-type wave solver for real-time interactive simulation and visualization. *Computer Physics Communications*, 217:117–127.

Teng, J., Jakeman, A., Vaze, J., Croke, B. F., Dutta, D., and Kim, S. (2017). Flood inundation modelling: A review of methods, recent advances and uncertainty analysis. *Environmental Modelling & Software*, 90:201–216.

Teng, J., Vaze, J., and Dutta, D. (2013). Simplified methodology for floodplain inundation modelling using lidar dem. *Climate and land surface changes in hydrology, IAHS Red Book, by Boegh E, Blyth E, Hannah DM, Hisdal H, Kunstmann H, Su B, Yilmaz KK (eds) pp*, pages 198–204.

Thacker, W. C. (1981). Some exact solutions to the nonlinear shallow-water wave equations. *Journal of Fluid Mechanics*, 107:499–508.

Torresan, S., Critto, A., Rizzi, J., and Marcomini, A. (2012). Assessment of coastal vulnerability to climate change hazards at the regional scale: the case study of the north adriatic sea. *Natural Hazards and Earth System Sciences*, 12(7):2347.

Torresan, S., Critto, A., Rizzi, J., Zabeo, A., Furlan, E., and Marcomini, A. (2016). Desyco: a decision support system for the regional risk assessment of climate change impacts in coastal zones. *Ocean & Coastal Management*, 120:49–63.

Vafeidis, A. T., Nicholls, R. J., McFadden, L., Tol, R. S., Hinkel, J., Spencer, T., Grashoff, P. S., Boot, G., and Klein, R. J. (2008). A new global coastal database for impact and vulnerability analysis to sea-level rise. *Journal of Coastal Research*, pages 917–924.

Van Dongeren, A., Ciavola, P., Martinez, G., Viavattene, C., Bogaard, T., Ferreira, O., Higgins, R., and McCall, R. (2017). Introduction to risc-kit: Resilience-increasing strategies for coasts. *Coastal Engineering*.

Vincent, L. (1993). Morphological grayscale reconstruction in image analysis: Applications and efficient algorithms. *IEEE transactions on image processing*, 2(2):176–201.

Vousdoukas, M. I., Voukouvalas, E., Annunziato, A., Giardino, A., and Feyen, L. (2016). Projections of extreme storm surge levels along europe. *Climate Dynamics*, 47(9-10):3171–3190.

Wang, J., Yi, S., Li, M., Wang, L., and Song, C. (2018). Effects of sea level rise, land subsidence, bathymetric change and typhoon tracks on storm flooding in the coastal areas of shanghai. *Science of The Total Environment*, 621:228–234.

Wang, Y., Liang, Q., Kesserwani, G., and Hall, J. W. (2011). A 2d shallow flow model for practical dam-break simulations. *Journal of Hydraulic Research*, 49(3):307–316.

WBM-BMT (2010). Tuflow user manual-gis based 2d/1d hydrodynamic modelling. Technical report, Report.

Weibull, W. (1939). A statistical theory of the strength of materials. *Ing. Vet. Ak. Handl.*

Weisse, R., Bellafiore, D., Menéndez, M., Méndez, F., Nicholls, R. J., Umgiesser, G., and Willems, P. (2014). Changing extreme sea levels along european coasts. *Coastal engineering*, 87:4–14.

Willmott, C. J., Ackleson, S. G., Davis, R. E., Feddema, J. J., Klink, K. M., Legates, D. R., O'donnell, J., and Rowe, C. M. (1985). Statistics for the evaluation and comparison of models. *Journal of Geophysical Research: Oceans*, 90(C5):8995–9005.

Yu, D. (2010). Parallelization of a two-dimensional flood inundation model based on domain decomposition. *Environmental Modelling & Software*, 25(8):935–945.

Zanuttigh, B. (2011). Coastal flood protection: what perspective in a changing climate? the theseus approach. *Environmental science & policy*, 14(7):845–863.

Zanuttigh, B., Simcic, D., Bagli, S., Bozzeda, F., Pietrantoni, L., Zagonari, F., Hoggart, S., and Nicholls, R. J. (2014). Theseus decision support system for coastal risk management. *Coastal Engineering*, 87:218–239.

Development of a model for the assessment of Coastal Flooding vulnerability: An application to the Venetian littoral
November 2018

Chiara Favaretto
chiara.favaretto@dicea.unipd.it

Dept. Civil, Environmental and Architectural Engineering - ICEA
University of Padova